Universidad Zaragoza
1474

Instituto Universitario de Investigación en Ingeniería de Aragón
Universidad Zaragoza

Ph.D. Thesis

Cardiac Digital Twins To Aid In Repairing Damaged Hearts

Gemelos Digitales Cardíacos para Ayudar a Reparar Corazones Dañados

Author

Ricardo Maximiliano Rosales Veliz

Supervisor

Esther Pueyo Paules

Ph.D. Program in Biomedical Engineering
Doctoral School

Instituto de Investigación en Ingeniería de Aragón
Universidad de Zaragoza
2025

Cardiac Digital Twins To Aid In Repairing Damaged Hearts

Ricardo Maximiliano Rosales Veliz, 2025
Cardiac Digital Twins To Aid In Repairing Damaged Hearts

Date of current version: Tuesday 28th April, 2026

This Ph.D. thesis belongs to the inter-universitary Biomedical Engineering Ph.D. Program of the University of Zaragoza and Polytechnic University of Cataluña, and has been developed within the Biomedical Signal Interpretation and Computational Simulations (BSICoS) group of the Aragón Institute for Engineering Research (I3A), and the Department of Electronic Engineering and Communications at the University of Zaragoza (Zaragoza, Spain).

The research presented in this thesis was supported by EU H2020 Program under G.A. 874827 (BRAVƎ), by Agencia Estatal de Investigación - Ministerio de Ciencia e Innovación (Spain) through projects PID2022-140556OB-I00, TED2021-130459B-I00 and CARDIOPRINT (PLEC2021-008127), by European Social Fund (EU) and Aragón Government through project LMP94_21 and BSICoS group T39_23R and by the European Research Council under G.A. 638284. Computations were performed using ICTS NANBIOSIS (HPC Unit at University of Zaragoza).

This thesis was printed thanks to the financial support of BSICoS Group at University of Zaragoza.

Non potevano cambiare i sentimenti. Anzi, neppure voi potevate cambiarli, neanche volendo. Potevano portare allo scoperto, fino all'ultimo dettaglio, tutto ciò che avevate detto, fatto o pensato, ***ma ciò che giaceva in fondo al cuore e che seguiva percorsi sconosciuti anche a voi stessi, restava inespugnabile.***

George Orwell, 1984

ABSTRACT

Human induced pluripotent stem cell-derived cardiomyocytes (hiPSC-CMs) have emerged as a promising cell source for the fabrication of engineered heart tissues (EHTs) intended to remuscularize the infarcted myocardium and restore cardiac function. However, their immature electrophysiological phenotype, characterized by prolonged action potential and reduced intercellular coupling, poses risks of post-transplantation arrhythmias, as local gradients in depolarization and repolarization may facilitate reentrant activity. Culturing hiPSC-CMs within three-dimensional scaffolds represents an effective strategy to promote their structural alignment and functional maturation.Yet, the impact of scaffold architecture on the global electrophysiology of *in vitro* and engrafted EHTs remains insufficiently characterized, partly due to the high experimental costs and time demands.

To address this gap, we employed computational modeling and simulation to investigate how scaffold geometry, hiPSC-CMs alignment, EHT implantation site, electrical maturation, and degree of attachment of the EHT to the host myocardium influence arrhythmic risk following epicardial remuscularization.

First, we developed our *in silico* EHT models and calibrated them using optical mapping (OM) recordings of *in vitro* EHTs. We computationally characterized their electrophysiological activity across scaffolds with varying pore geometries and sizes. Among the tested *in vitro* configurations, scaffolds with small, elongated hexagonal pores exhibited the most biomimetic behavior, reducing activation times (ATs), while scaffold thickness had only a minor effect. Following engraftment, a minimum EHT conductivity of 5% of that in healthy myocardium was required to sustain bidirectional EHT-myocardium electrical propagation. Above this threshold, small elongated hexagonal pores produced the lowest ATs. Moreover, when biomimetic EHT conductivity was combined with hiPSC-CMs alignment following that of epicardial myocytes, ATs and

repolarization gradients decreased, thereby mitigating arrhythmic risk.

To extend our analysis to realistic biventricular (BiV) geometries and address data variability and scarcity, we developed a three-dimensional (3D) cardiac magnetic resonance (CMR) segmentation pipeline that combines synthetic data augmentation (SA) via generative adversarial networks and topological correction (TC) using persistent homology, and introduces a novel method to quantify uncertainty in measured volumes from voxel-level predictions. When applied to anisotropic, topologically inconsistent cine and late gadolinium-enhanced (LGE) CMRs, and isotropic, topologically consistent *ex vivo* CMRs, it improved segmentation accuracy and topological consistency, with enhanced identification of the thin right ventricle (RV) apex in *ex vivo* data and infarction in LGE data. Generally, SA increased the prediction overlap with expert-derived manual segmentations, while TC reduced the topological discrepancies, across all datasets. Additionally, the method accurately detected microvascular obstructions and quantified prediction uncertainty, enhancing robustness and interpretability.

Next, we constructed a cohort of cardiac digital twins representing healthy and infarcted pigs. These models were generated by integrating multi-modal CMRs, electrocardiograms (ECGs), OM and electroanatomical mapping data acquired from 5 healthy and 10 infarcted animals. Ventricular conduction system (CS) architectures were built from OM and ECG recordings. Myocardial fiber orientation, action potential characteristics, and cell-to-cell conductivity in infarcted tissue were defined from OM and CMR data. Simulated ECGs for healthy and diseased models of left anterior descending (LAD) and left circumflex (LCx) occlusions were compared to experimental ECGs and used to assess infarction-induced changes. While fiber orientation personalization had limited electrophysiological impact, accurate modeling of the CS and spatial repolarization heterogeneities was essential to reproduce realistic depolarization and repolarization dynamics. Incorporating experimentally guided infarction-induced alterations enabled faithful reproduction of depolarization patterns, ATs, T-wave morphologies, and ECG features characteristic of artery-specific occlusions.

Subsequently, we extended the analysis to graft EHT models into our validated set of 9 porcine-specific infarcted BiV models (LCx: 4, LAD: 5). Using an S1-S2 stimulation protocol, we evaluated ventricular tachycardia (VT) incidence across different pacing sites and coupling intervals, accounting for infarction characteristics, EHT implantation site and conductivity, and the CS. *In silico* reentries reproduced experimental arrhythmias, with LAD infarcts showing higher arrhythmic propensity, likely due to their larger infarct size.

The CS architecture critically influenced post-infarction arrhythmicity, with the introduced electrical shortcuts either facilitating or suppressing reentry. Direct EHT engraftment over dense, transmural scars increased VT inducibility, whereas lateral implantation substantially reduced it compared to direct implantation. In non-transmural scars, VT inducibility varied with EHT implantation location, highlighting the usefulness of digital twins to accurately assess arrhythmic risk case by case. Notably, biomimetic EHT conductivity mitigated post-engraftment arrhythmogenicity.

Finally, we introduced *Cocoro*, a web-based solver designed for efficient graphical processing unit (GPU) computation and rendering of cardiac electrophysiological simulations. Benchmarking against a gold-standard solver using BiV models under anisotropic and isotropic conditions demonstrated high agreement, with 90^{th}-percentile node-wise AT differences of 11 ms (anisotropic) and 4 ms (isotropic), and negligible repolarization discrepancies. Five-second simulations executed in 9.54 min (RTX 2070) and 22.13 min (Titan V), with minimal overhead from computation and rendering of simulated ECGs and cellular outputs. *Cocoro*-simulated QRS complexes closely matched experimental data.

Overall, by integrating extensive multimodal datasets, we advanced preclinical cardiac digital twin modeling and elucidated how structural and electrophysiological parameters shape both healthy and diseased cardiac behavior. Our findings reveal latent arrhythmic risk following EHT-based remuscularization and identify infarction substrate, EHT conductivity, and implantation site as key determinants, emphasizing the importance of accurate CS representation. This integrative framework, spanning scaffold-guided EHT maturation, robust and topologically consistent CMR segmentation, swine digital twin modeling, and high-performance, web-accessible simulation, establishes a mechanistic, data-driven platform for evaluating the arrhythmogenic risk of post-infarction remodeling and EHT-mediated therapies. It provides a translational pipeline to optimize scaffold design, refine personalized infarct characterization, and improve the clinical safety of EHT-based cardiac repair.

Keywords: Cardiac Electrophysiology, Cardiac Magnetic Resonance Segmentation, Digital Twins, Engineered Heart Tissue, Modeling and Simulation.

RESUMEN Y CONCLUSIONES

Los cardiomiocitos derivados de células madre pluripotentes inducidas humanas (hiPSC-CMs, por sus siglas en inglés) han surgido como una materia prima celular prometedora para la construcción de tejidos cardíacos bioingenierizados (EHTs, por sus siglas en inglés) destinados a remuscularizar el miocardio infartado y restaurar la función cardíaca. Sin embargo, su inmadurez electrofisiológica, que se asocia con un potencial de acción prolongado y un acoplamiento reducido entre células, plantea riesgos de arritmogénesis tras el trasplante, ya que los gradientes locales de despolarización y repolarización pueden facilitar la aparición de reentradas. El cultivo de hiPSC-CMs en matrices tridimensionales representa una estrategia para promover su maduración y alineamiento estructural. No obstante, la influencia del diseño de la matriz de cultivo en la electrofisiología global, tanto *in vitro* como en EHTs injertados, sigue siendo poco comprendida, en parte debido a los costes y los tiempos que requiere esta experimentación. Para mejorar dicho conocimiento, en esta tesis investigamos computacionalmente cómo el diseño de la matriz de cultivo, el alineamiento de los hiPSC-CMs, la localización del implante, la maduración eléctrica del EHT y el grado de acoplamiento del EHT al miocardio huésped afectan el riesgo arrítmico tras la remuscularización epicárdica.

En primer lugar, desarrollamos modelos *in silico* de EHTs y los calibramos mediante el análisis de registros de mapeo óptico (OM) de su actividad eléctrica *in vitro*. Caracterizamos computacionalmente el comportamiento electrofisiológico de los EHTs para distintos tamaños y formas de poros, antes y después del injerto. Los resultados indicaron que las matrices de cultivo con poros hexagonales pequeños y alargados, alineados con la anisotropía miocárdica, reducían los tiempos de activación, preservando la sincronía en la conducción, mientras que el grosor de la matriz de cultivo ejercía solo un efecto menor en las simulaciones *in vitro*. De forma importante, el injerto de EHT en tejido infartado mostró que la conductividad del EHT debía ser al menos un 5%

de la del tejido sano para permitir la propagación eléctrica bidireccional EHT-miocardio. Para conductividades por encima de dicho umbral, la matriz de cultivo de pequeños hexágonos alargados produjo el menor tiempo de activación en el sistema acoplado EHT-miocardio. Al seguir aumentando la conductividad del EHT y al orientar los hiPSC-CMs en paralelo a las células epicárdicas, el tiempo total de activación y el gradiente de repolarización disminuyeron sustancialmente, minimizando la probabilidad de arritmias tras el trasplante del EHT.

Con el fin de extender nuestro análisis al dominio biventricular y abordar la escasez y variabilidad de los datos de resonancia magnética cardíaca (CMR), desarrollamos métodos para la segmentación tridimensional cardíaca mediante algoritmos de aprendizaje profundo. Estos métodos automáticos integran el aumento de datos, a través de la generación sintética de los mismos (SA) mediante redes generativas antagónicas, y la corrección topológica (TC) basada en homología persistente. Además, propusimos un método para cuantificar la incertidumbre en los volúmenes medidos a partir de predicciones a nivel de vóxel. Analizamos imágenes CMR cine y con realce tardío de gadolinio (LGE), anisotrópicas y topológicamente inconsistentes, así como imágenes CMR *ex vivo* isotrópicas y topológicamente consistentes. Los resultados mostraron mejoras firmes en la segmentación para los datos *ex vivo*, tanto en el solapamiento con la segmentación de referencia como en la precisión topológica al aplicar TC y SA de manera individual y combinada. Al usar SA y TC, se obtuvo una mejor identificación del ápice del ventrículo derecho y del infarto en las imágenes *ex vivo* y LGE, respectivamente. En general, SA aumentó el solapamiento de las predicciones con las segmentaciones manuales realizadas por expertos, mientras que TC redujo las discrepancias topológicas en todos los conjuntos de datos. Más allá de la precisión en la segmentación, detectamos de manera consistente la presencia o ausencia de obstrucciones microvasculares en infartos agudos en las imágenes LGE y estimamos la incertidumbre de los volúmenes derivados de las predicciones, lo que mejora la robustez y la interpretabilidad clínica.

A continuación, construimos una cohorte de gemelos digitales cardíacos que representan cerdos sanos e infartados, integrando datos multi-modales para analizar la terapia de remuscularización en un contexto preclínico realista. Esta cohorte se construyó a partir de CMRs, electrocardiogramas (ECGs), OM y mapeos electroanatómicos, adquiridos en 5 cerdos sanos y 10 cerdos infartados, cuyo corazón es un modelo preclínico bien establecido por su estrecha semejanza anatómica y funcional con el corazón humano. Las arquitecturas del sistema de conducción ventricular (CS) se construyeron a partir de registros

de OM y ECG. La orientación de las fibras miocárdicas, las características del potencial de acción y la conductividad intercelular en el tejido infartado se definieron a partir de datos de OM y CMR. Los ECGs simulados para modelos sanos y enfermos con oclusiones de la arteria coronaria descendente anterior izquierda (LAD) y circunfleja izquierda (LCx) se compararon con ECGs experimentales y se usaron para evaluar los cambios inducidos por el infarto. Nuestros resultados demostraron que la orientación personalizada de las fibras desempeña un papel menor en la electrofisiología cardíaca, mientras que una representación precisa del CS y las heterogeneidades espaciales de la repolarización fueron esenciales para reproducir las características de despolarización y repolarización. La incorporación de alteraciones inducidas por el infarto, guiadas experimentalmente, permitió que los modelos reprodujeran patrones de despolarización, tiempos de activación, morfologías de la onda T y patrones de ECG específicos de la arteria ocluida.

Seguidamente, los modelos de EHT se injertaron en nuestro conjunto validado de 9 modelos biventriculares infartados de cerdo (4 LCx y 5 LAD). Se aplicó un protocolo de estimulación S1-S2 con lugares de estimulación e intervalos S2 variables para evaluar la incidencia de taquicardia ventricular (VT) en relación con las características del infarto, el lugar de implantación y la conductividad del EHT, así como el papel del CS. Se observó actividad reentrante en modelos biventriculares infartados, cuyos patrones arrítmicos se asemejan a los observados experimentalmente en cerdos. La vulnerabilidad a VT fue marcadamente mayor en cerdos LAD comparados con LCx, probablemente debido a su mayor tamaño de infarto. La inclusión del CS alteró la incidencia de VT, ya que los atajos eléctricos introducidos facilitaron o suprimieron la reentrada. Tras la remuscularización con EHTs, la incidencia de VT aumentó en cicatrices densas y altamente transmurales. Sin embargo, este efecto se mitigó cuando el EHT se implantó lateralmente en lugar de directamente sobre el infarto. En cicatrices no transmurales, la incidencia de VT tuvo una fuerte dependencia con el sitio de implantación del EHT, resaltando la utilidad de los gemelos digitales para evaluar con precisión el riesgo arrítmico caso por caso. De manera destacable, una conductividad del EHT similar a la del tejido miocárdico sano redujo de manera consistente y robusta las arritmias posteriores al injerto.

Finalmente, en la tesis introdujimos *Cocoro*, un software basado en la web para el cálculo y visualización eficiente de simulaciones electrofisiológicas cardíacas, que aprovecha el uso de unidades de procesamiento gráfico. Evaluamos su exactitud y rendimiento usando una malla biventricular de cerdo bajo configuraciones anisotrópicas e isotrópicas. *Cocoro* mostró una estrecha concordancia al comparar sus resultados con un software de referencia. Es-

pecíficamente, el percentil 90 de las diferencias de tiempo de activación nodo a nodo fue de 11 ms (anisotrópico) y 4 ms (isotrópico), mientras que las diferencias en la duración de la repolarización fueron inferiores a 6 ms en ambos casos. Las simulaciones de cinco segundos de actividad eléctrica se ejecutaron en 9.54 min (RTX 2070) y 22.13 min (Titan V), sin apenas retraso adicional debido al cálculo y visualización de gráficas tales como ECGs simulados y datos celulares. Los complejos QRS simulados reprodujeron con precisión morfologías y duraciones experimentales, indicando el potencial de nuestra solución para el modelado y simulación cardíaca rápida, portátil y clínicamente relevante.

En conjunto, esta tesis integra gran cantidad de datos multi-modales para avanzar en el desarrollo de gemelos digitales cardíacos porcinos, mostrando la influencia de parámetros estructurales y electrofisiológicos clave en la función cardíaca, tanto en condiciones sanas como patológicas. Los resultados permiten además caracterizar el riesgo arrítmico latente tras la remuscularización mediada por EHT en corazones infartados, identificando el sustrato del infarto, la conductividad del EHT y el lugar de implantación como factores clave, mientras enfatizan que una modelización *in silico* precisa requiere una representación exacta del CS. El marco integrador propuesto, que abarca la maduración de EHTs guiada por matrices de cultivo, la segmentación robusta y topológicamente consistente de CMR y el modelado con gemelos digitales porcinos ofrece una plataforma mecanicista y basada en datos experimentales para evaluar el riesgo arrítmico tras un infarto y después de la aplicación de terapias basadas en EHT. Al unir avances en ingeniería tisular, procesado de señal e imagen y cardiología computacional de alto rendimiento y amplio acceso, esta tesis proporciona una estrategia traslacional para optimizar el diseño de matrices de cultivo, refinar la caracterización del infarto específica de cada paciente y predecir los resultados postrasplante, avanzando así en la aplicación clínica segura de la terapia cardíaca basada en EHTs.

Palabras clave: Electrofisiología Cardíaca, Segmentación de Resonancia Magnética Cardíaca, Gemelos Digitales, Tejido Cardíaco Bioingenierizado, Modelado y Simulación.

ACKNOWLEDGEMENTS

“Es de bien nacido ser agradecido”. O, como yo lo siento, en el agradecimiento continuo uno construye su felicidad.

En primer lugar, quiero expresar mi gratitud a mis guías. A Konstantinos Mountris, por ser ese primer referente tan cercano, algo esencial, sobre todo, en una ciudad nueva y en el ocaso de una pandemia. A Ana Mincholé, quien me brindó consejos invaluables, siempre acompañados de un positivismo inquebrantable ante cualquier adversidad. A Manuel Doblaré, por su atento y constante seguimiento, que supo brindarme su experiencia con recomendaciones, claves para enaltecer la calidad de este trabajo. Y a Esther Pueyo, a quien admiro profundamente por su incansable búsqueda de la excelencia y su templanza en la tormenta, transformada en una serena humildad en sus triunfos. Gracias, Esther, por permitirme recorrer este camino del que he aprendido tanto.

A cada integrante del grupo *BSICoS*, gracias por cada ayuda, cada palabra de aliento, cada tarde deportiva, cada excursión, cada salida de fin de semana y cada comida compartida durante este apasionante trayecto. Especialmente a mis compañeros de laboratorio, por saber anestesiar las horas grises y multiplicar las increíbles.

A los integrantes del proyecto BRAVƎ y CARDIOPRINT, por su calidez y respeto en cada reunión, así como por las interesantes jornadas científicas compartidas, que me han permitido crecer tanto en conocimiento como así también, a nivel personal.

A mi familia de España, gracias por tanto y perdón por tan poco. Aunque no lo parezca, se han convertido en un apoyo indispensable en los momentos de incertidumbre.

A mi familia y amigos en Argentina o que están lejos, esparcidos por el globo, por estar siempre presentes y recordarme que la distancia no puede erosionar los recuerdos compartidos.

A Sofia, por tener la mágica cualidad de sonreír y hacerme feliz.

A mis primeros maestros, mis abuelos.

A mi hermano, por su silencioso pero inconmensurable acompañamiento.

Y a mis padres, por haberme dado, con su esfuerzo y sacrificio, las oportunidades que ellos no tuvieron; por enseñarme que la vida se persigue cada día; y por su inclaudicable amor y compañía.

CONTENTS

Abstract **iii**

Resumen y conclusiones **vii**

Acknowledgements **xi**

List of Acronyms **xix**

1 Introduction **1**
1.1 Motivation 2
1.2 The heart 4
1.2.1 Anatomy and physiology 4
1.2.2 The myocardium 8
1.2.3 Electrophysiology 12
1.2.4 Myocardial infarction 16
1.2.5 Human versus porcine heart 19
1.3 Imaging and electrical mapping 21
1.3.1 Magnetic resonance 21
1.3.2 Electrophysiological data 23
1.4 Stem cell-derived cardiomyocytes 29
1.4.1 Fundamentals 29
1.4.2 Origin and maturity 30
1.4.3 Towards adult-like cells 31
1.4.4 Applications 32
1.4.5 Challenges 33

1.5 Segmentation via DL 34
1.5.1 Cardiac segmentation 34
1.5.2 Introduction to DL 35
1.5.3 Generative adversarial networks 38
1.5.4 Persistent homology 39
1.5.5 Miscalibration and uncertainty 40
1.6 Electrophysiological modeling and simulation 42
1.6.1 Bidomain and monodomain models 43
1.6.2 Cell-scale modeling 46
1.6.3 Tissue- and organ-scale simulations 51
1.7 Objectives 71
1.8 Structure of the thesis 72

2 State of the art **79**
2.1 Segmentation of cardiac magnetic resonances 80
2.1.1 Convolutional neural networks 80
2.1.2 Synthetic data augmentation 81
2.1.3 Anatomical consistency 83
2.1.4 Uncertainty estimation 83
2.2 Post-MI remuscularization therapy 85
2.2.1 Preclinical evidence of EHT therapy 85
2.2.2 Early clinical translation 85
2.2.3 Cell survival and paracrine mechanisms 86
2.2.4 Immature phenotype and arrhythmogenic risk 86
2.2.5 Outstanding challenges and future directions 87
2.3 Modeling and simulation of chronic and remuscularized MI 87
2.3.1 Personalization 87
2.3.2 Arrhythmic risk 88
2.3.3 Remuscularization 89
2.3.4 Future directions for digital twin–guided regeneration . . . 92
2.4 Parallel computation of *in silico* electrophysiology 92
2.5 Chapter summary 94

3 Experimentally-guided *in silico* design of EHT **97**
3.1 Methodology 98
3.1.1 Experimental analysis of *in vitro* EHTs 98
3.1.2 *In silico* analysis of EHTs 102
3.2 Results 109
3.2.1 EHT models *in vitro*-based calibration 109
3.2.2 *In silico* assessment of EHT designs 110

3.2.3 *In silico* analysis of the EHT-MI interaction 113
3.3 Discussion 118
3.3.1 *In silico* replication of *in vitro* electrophysiology 118
3.3.2 Small elongated pores accelerate EHT activation 119
3.3.3 EHT thickness role *in vitro* 120
3.3.4 EHT design determines activation of MI-coupled EHTs . 120
3.3.5 Higher EHT conductivity lowers arrhythmic risk in MI-coupled EHTs 121
3.4 Limitations 123
3.5 Conclusion 125

4 3D segmentation of multi-contrast CMRs 127
4.1 Methodology 128
4.1.1 Data description and processing 128
4.1.2 Baseline training 132
4.1.3 GAN-based data augmentation 134
4.1.4 Topological correction and priors definition 135
4.1.5 Inference and postprocessing 137
4.2 Results 138
4.2.1 *Ex vivo* dataset 138
4.2.2 Cine dataset 139
4.2.3 LGE dataset 141
4.3 Discussion 143
4.4 MYOSAIQ challenge 147
4.4.1 Preprocessing, synthetic augmentation, segmentation and confidence estimation 147
4.4.2 Results 150
4.5 Conclusion 153

5 Data-driven modeling of healthy and MI porcine hearts 155
5.1 Methodology 156
5.1.1 Experiments 156
5.1.2 Structural data 159
5.1.3 Functional data 161
5.1.4 Electrophysiological modeling 165
5.1.5 Numerical simulations 171
5.2 Results 174
5.2.1 Effective CS-BiV coupling 174
5.2.2 BiV activation and QRS 175
5.2.3 BiV repolarization and T wave 176

5.2.4 Personalized CM orientation . . . 178
5.2.5 Post-MI alterations . . . 180
5.2.6 Post-MI activation and the ECG . . . 181
5.2.7 Location and morphology of MI and the ECG . . . 181
5.3 Discussion . . . 183
5.3.1 CS-myocardial coupling . . . 184
5.3.2 CS and HERP determine QRS complex . . . 185
5.3.3 Small APDSH shapes repolarization . . . 186
5.3.4 Limited impact of CM orientation . . . 187
5.3.5 Post-MI remodeling . . . 188
5.3.6 Post-MI ECG replication . . . 189
5.3.7 MI-induced ECG changes . . . 190
5.3.8 Limitations . . . 191
5.4 Conclusion . . . 192

6 Arrhythmic risk following EHT implantation 195
6.1 Methodology . . . 196
6.1.1 Arrhythmia inducibility . . . 196
6.1.2 BiV-EHT modeling . . . 198
6.1.3 BiV and EHT electrophysiology . . . 200
6.1.4 Numerical simulations . . . 201
6.2 Results . . . 204
6.2.1 Cell alignment, conductivity and attachment . . . 204
6.2.2 Real and virtual VT . . . 207
6.2.3 Baseline VT . . . 208
6.2.4 CS and post-MI VT . . . 209
6.2.5 EHT location and VT . . . 212
6.2.6 EHT maturation and VT . . . 214
6.2.7 MI substrate and VT . . . 216
6.3 Discussion . . . 217
6.3.1 Cell alignment, conductivity and attachment . . . 217
6.3.2 Models replicate arrhythmicity . . . 218
6.3.3 Arrhythmia vulnerability protocol . . . 219
6.3.4 CS modulates arrhythmicity . . . 220
6.3.5 EHT conductivity affects arrhythmicity . . . 221
6.3.6 MI substrate modulates arrhythmicity . . . 221
6.4 Limitations . . . 222
6.5 Conclusion . . . 225

7 Fast and portable electrophysiological simulation 227
7.1 *ELECTRA* extension 228
7.2 *Cocoro*: implementation and validation 228
7.2.1 Implementation 230
7.2.2 Accuracy and performance evaluation 231
7.2.3 Results and discussion 232
7.3 Conclusion 235

8 Conclusions and future work 237
8.1 Main findings 238
8.2 Major contributions 241
8.3 Perspectives for future work 242

Appendix 247

A MI characterization and arrhythmicity before and after EHT implantation 249
A.1 Table: arrhythmicity for varying MI locations 250
A.2 Table: arrhythmicity with and without the conduction system . 251
A.3 Table: arrhythmicity for different EHT locations 252
A.4 Table: arrhythmicity for different EHT maturation states 253
A.5 Table: characterization of the MI substrate 253

Bibliography 255

List of Publications 277

List of Figures 281

List of Tables 285

LIST OF ACRONYMS

1D	one-dimensional	55
2D	two-dimensional	31
3D	three-dimensional	iv
ADP	adenosine diphosphate	12
AIP	arrhythmia inducibility protocol	72
AP	action potential	11
APD	action potential duration	3
APD_{90}	action potential duration at 90% repolarization	108
APDSH	action potential duration spatial heterogeneity	170
ATP	adenosine triphosphate	12
AT	activation time	iii
AVN	atrioventricular node	7
AZ	affected zone	17
BE	Betti error	138
BiV	biventricular	iv
BZ	border zone	18
Ca^{2+}	calcium	10
CDF	cumulative density function	42
CA	cellular alignment	98
CM	cardiomyocyte	2
CMR	cardiac magnetic resonance	iv
CNN	convolutional neural network	36

CRPS continuous ranked probability score 42
CS conduction system iv
CV conduction velocity 27
CVD cardiovascular disease 2
D discriminator 39
DA data augmentation 35
DL deep learning 2
DSC dice similarity score 138
DW diffusion-weighted 21
EAM electro-anatomical mapping 20
ECE expected calibration error 41
ECG electrocardiogram iv
EHT engineered heart tissue iii
FDM finite difference method 54
FEM finite element method 54
G generator 38
GAN generative adversarial network 37
GPU graphical processing unit v
GTL ground truth label 42
HD Hausdorff distance 138
HF heart failure 2
HERP heart-electrodes relative position 163
hiPSC human induced pluripotent stem cell 30
hiPSC-CF human induced pluripotent stem cell-derived cardiac fibroblast 100
hiPSC-CM human induced pluripotent stem cell-derived cardiomyocyte iii
IHD ischemic heart disease 2
IS inducibility score 198
I_{CaL} L-type calcium current 13
I_f inward, hyperpolarization-activated funny current 50

I_{K1}	inward rectifier potassium current	21
I_{Kr}	rapid delayed rectifier potassium current	14
I_{Ks}	slow delayed rectifier potassium current	14
I_{Na}	sodium current	13
I_{NaCa}	sodium/calcium exchange current	14
I_{NaK}	sodium/potassium pump current	14
I_{to}	transient outward potassium current	13
K^+	potassium	12
KUL	Katholieke Universiteit Leuven	156
LAD	left anterior descending	iv
LAx	long axis	35
LCA	longitudinal cellular alignment	105
LCx	left circumflex	iv
LDC	longitudinal diffusion coefficient	98
LGE	late gadolinium-enhanced	iv
LV	left ventricle	2
MI	myocardial infarction	2
MVO	microvascular obstruction	17
Na^+	sodium	12
ODE	ordinary differential equation	47
OM	optical mapping	iii
PDE	partial differential equation	45
PDF	probability density function	84
pECG	pseudo-ECG	173
PH	persistent homology	38
PMJ	Purkinje-muscular junctions	18
RBM	rule-based model	62
RTG	repolarization time gradient	91
RV	right ventricle	iv
SAN	sinoatrial node	7

SA	synthetic data augmentation	iv
SAx	short axis	22
SCD	sudden cardiac death	2
SERMAS	Servicio Madrileño de Salud	156
SR	sarcoplasmic reticulum	10
SZ	scar zone	18
TC	topological correction	iv
VARP	Virtual Heart Arrhythmic Risk Predictor	88
V_m	transmembrane potential	13
VT	ventricular tachycardia	iv

CHAPTER 1

INTRODUCTION

1.1 Motivation

1.2 The heart

1.2.1 Anatomy and physiology

1.2.2 The myocardium

1.2.3 Electrophysiology

1.2.4 Myocardial infarction

1.2.5 Human versus porcine heart

1.3 Imaging and electrical mapping

1.3.1 Magnetic resonance

1.3.2 Electrophysiological data

1.4 Stem cell-derived cardiomyocytes

1.4.1 Fundamentals

1.4.2 Origin and maturity

1.4.3 Towards adult-like cells

1.4.4 Applications

1.4.5 Challenges

1.5 Segmentation via DL

1.5.1 Cardiac segmentation

1.5.2 Introduction to DL

1.5.3 Generative adversarial networks

1.5.4 Persistent homology

1.5.5 Miscalibration and uncertainty

1.6 Electrophysiological modeling and simulation

1.6.1 Bidomain and monodomain models

1.6.2 Cell-scale modeling

1.6.3 Tissue- and organ-scale simulations

1.7 Objectives

1.8 Structure of the thesis

This chapter establishes the foundation of the thesis by outlining its aims and structure, introducing the key concepts of cardiac anatomy, function, vascularization, and electrophysiology, all of which are crucial for the development of this thesis across scales ranging from subcellular to the whole organ. It discusses myocardial infarction (MI), highlighting both its pathological features and the physiological differences between the human and porcine heart, and reviews the experimental techniques commonly employed to characterize cardiac structure and electrophysiology. An overview is then provided on the generation of stem cell-derived cardiomyocytes (CMs), emphasizing the associated challenges and opportunities for cardiac repair. This chapter further introduces the deep learning (DL) framework, with particular attention to generative models as well as topological and uncertainty-based evaluations in the context of CMR image segmentation. Finally, it presents *in silico* modeling and simulation approaches used to represent cardiac electrophysiology, spanning from ionic mechanisms to organ-level behavior.

1.1 Motivation

Cardiovascular diseases (CVDs) remain the leading cause of death worldwide. Within this group of diseases, ischemic heart disease (IHD) is the largest single contributor to mortality, accounting for 33% CVD-related deaths in women and 40% in men each year. In recent years, IHD-related mortality has risen particularly in low- and middle-income countries, adding to the already substantial global health and economic burden. This includes not only direct healthcare expenditures, which represented 11% of total European healthcare in 2021, but also considerable indirect costs, such as productivity losses caused by patient disability and caregiver absenteeism, estimated at €140.6 billion annually in Europe [1]. With the progressive aging of the global population, the incidence and socioeconomic impact of IHD are expected to increase further, highlighting the urgent need for effective therapeutic strategies, particularly for its most frequent complication, MI [1].

Following MI, the necrotic myocardium is replaced by non-contractile fibrotic tissue through an inflammatory remodeling process, ultimately impairing cardiac function [2]. This adverse remodeling increases the risk of heart failure (HF) and sudden cardiac death (SCD), frequently linked to persistent post-MI VT. Current therapeutic options for patients with end-stage disease include cardiac transplantation and left ventricle (LV) assist devices [3,4]. However, both strategies face significant limitations: transplantation is limited by

donor scarcity and numerous post-operative complications, including graft failure, allograft rejection, and the need for lifelong immunosuppression [5], while LV assist devices, often used as a bridge to transplantation, require invasive implantation surgery and long-term anticoagulation therapy [3, 4].

Tissue engineering has emerged as a promising alternative, with particular focus on remuscularizing the infarct scar using hiPSC-CMs. Preclinical studies in rodents and macaques have shown that implanting EHTs composed of hiPSC-CMs can improve post-MI ejection fraction [6, 7]. Yet, these constructs remain functionally immature compared to adult myocardium, displaying weaker intercellular coupling and prolonged action potential durations (APDs), even when cultured under biomimetic conditions [6, 8]. Consequently, EHT-based therapy may introduce additional electrophysiological heterogeneities, potentially increasing arrhythmogenic risk.

Over the past decades, advances in biological data acquisition and computational power have enabled the rise of *in silico* modeling and simulation as a powerful tool for studying cardiac electrophysiology and assessing new therapies [9–12]. By integrating structural and electrophysiological information, these models can reproduce cardiac electrical activity across cellular, tissue, and organ scales. Compared to preclinical and clinical trials, computational approaches are faster, less costly, and more flexible, making them attractive for therapy development and safety assessment [9, 13].

Crucially, *in silico* studies complement preclinical experiments where swine models are considered the gold standard due to their close similarity to humans in coronary circulation, hemodynamics, cardiac dimensions, and electromechanical behavior [14]. Detailed computational models of pigs have already demonstrated their value in evaluating cardiac conditions and therapies, while also helping to reduce animal use in preclinical research [15, 16].

Despite these advances, the clinical adoption of digital twins remains limited [13]. The main barriers are the complexity of generating and using these models, and the slow pace of experimental validation. However, recent progress in machine learning for automated patient-specific model generation [17–19], combined with faster simulations enabled by optimized software and high-performance computing [20–23], is paving the way for their broader implementation in clinical practice.

Altogether, the *in silico* assessment of EHT-mediated remuscularization after MI provides a unique opportunity to explore the therapeutic potential and safety of this approach, which would otherwise be challenging in the clinic. While recent studies have shown the feasibility and efficacy of EHT implan-

tation in improving ejection fraction [6, 7, 24], a systematic evaluation of how EHT design, implantation, and engraftment variability affect cardiac electrophysiology is still lacking. Critically, ensuring the arrhythmic safety of this therapy requires large-scale analyses across diverse, experimentally validated digital twins representing a wide range of MI substrates.

1.2 The heart

The heart is the central organ of the cardiovascular system. By rhythmically contracting, it maintains continuous blood flow through the vascular network, thereby delivering oxygen and nutrients to metabolically active tissues [25]. Structurally, the heart is a hollow muscular organ composed of specialized muscle tissue, the myocardium, which is internally lined by the endocardium and externally covered by the epicardium [25,26]. During relaxation (diastole), venous blood enters the heart due to pressure gradients. During contraction (systole), the heart ejects blood into the arteries through the aorta and the pulmonary trunk.

1.2.1 Anatomy and physiology

1.2.1.1 Location

In both humans and pigs, the heart is located in the thoracic cavity, between the lungs, surrounded by their pleurae, above the diaphragm, and anterior to the spine. It lies behind the sternocostal wall, in the lower mediastinum, a central thoracic compartment between the right and left pleuropulmonary cavities (Figure 1.1). The pericardium, a fibrous serous membrane, encloses the heart and separates it from neighboring organs [26].

1.2.1.2 External anatomy

Externally, the heart has four faces (anterior or sternocostal, inferior or diaphragmatic, and left and right pulmonary), three borders (inferior, superior, and left), a base and an apex. As shown in Figure 1.1, the anterior face features the coronary sulcus, separating atria from ventricles, and the anterior interventricular sulcus, which divides the ventricles and descends toward the antero-inferior border of the heart, ending one to two cm behind the apex. The inferior face rests on the diaphragm and shows two distinct regions: the ventricular portion, crossed by the posterior interventricular sulcus, which originates

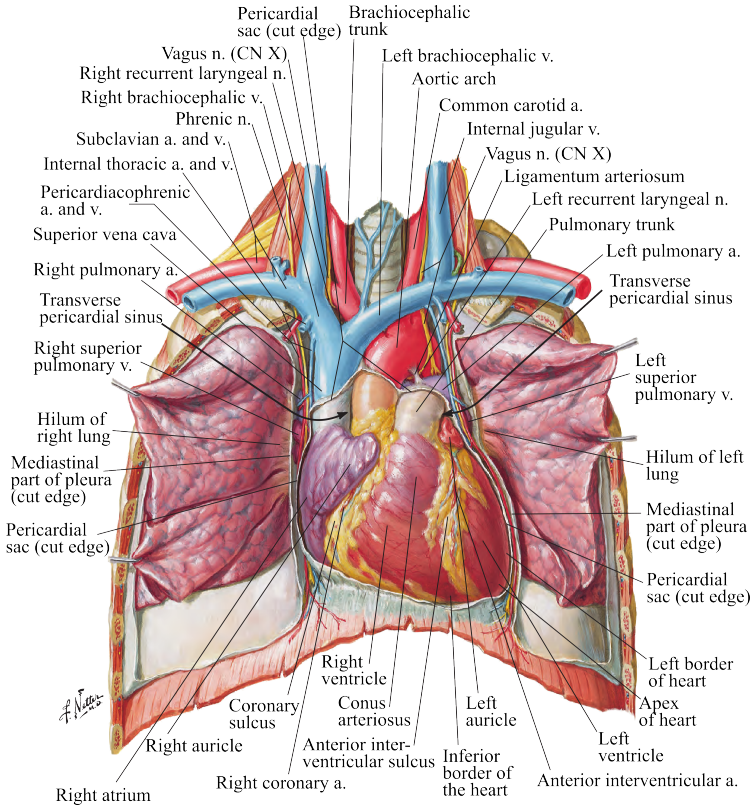


Figure 1.1: Anterior exposure of the heart without the pericardial sac. Adapted from Plate 232 in [27]. n.: nerve, a.: artery and v.: vein.

slightly to the right of the apex and extends backward toward the coronary sulcus, and the right atrial portion [26].

1.2.1.3 Internal anatomy

Internally, the heart is divided by the cardiac septum into the right and left halves, each composed of an atrium and a ventricle, separated by an opening known as the atrioventricular orifice, which is equipped with an atrioventricular valve, as can be seen in Figure 1.2 [26]. The atria act as weak primer pumps, assisting ventricular filling, while the ventricles provide the main contractile force: the RV propels blood to the lungs, and the LV to the systemic circulation [25].

Blood enters the atria via the coronary sinus and the superior and infe-

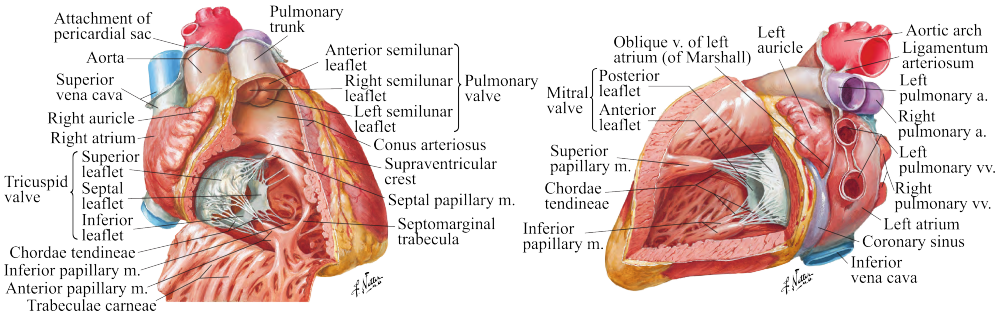


Figure 1.2: Internal anatomy of the right (left panel) and left (right panel) ventricles. Adapted from Plates 241 and 242 in [27]. m.: muscle, a.: artery, v.: vein, vv.: *venae* or veins.

1

rior vena cava into the right atrium, and through the four pulmonary veins, two from each lung, into the left atrium. It then flows from the atria to the ventricles through the respective atrioventricular orifices, a process that occurs during the diastolic phase of the cardiac cycle. Lastly, blood exits the ventricles through a large arterial trunk: the pulmonary trunk for the RV, and the aorta for the LV. The inlet and outlet orifices of the ventricles are equipped with valve mechanisms.

Left (mitral) and right (tricuspid) atrioventricular valves prevent backflow from the ventricles to the atria during ventricular systole, whereas semilunar valves (aortic and pulmonary valves) prevent backflow from the great arteries (aorta and pulmonary arteries) to ventricles during diastole [25]. The atrioventricular valves are anchored to the ventricles by chordae tendineae, which connect the free edges and ventricular surfaces of the valve leaflets to the papillary muscles, as shown in Figure 1.2. These papillary muscles, also termed first-order pillars, are part of the valvular apparatus. They are conical muscular projections with their bases attached to the ventricular wall and their apices extending freely into the ventricular cavity. Typically, they are grouped as anterior, posterior, or lateral, each corresponding to a particular valve leaflet (see Figure 1.2). Ventricular walls also contain muscular reinforcements, called trabeculae carneae, which form muscular bridges or thickenings of the ventricular wall. The former is characterized by a central portion that is free between two relatively distant points of attachment (as an example, see the septomarginal trabecula in Figure 1.2) [26].

1.2.1.4 Vascularization

The arteries and veins that supply and drain blood from the heart encircle the organ and are collectively called the coronary vessels (Figure 1.3). The main arteries are the left and right coronary arteries.

The left coronary artery originates from the aorta at the level of the free edge of the left semilunar (aortic) valve cusp, within the corresponding aortic sinus. Its initial course runs posteriorly to the pulmonary trunk, then to its left, and finally downward and anteriorly. It is hidden beneath the left auricle and, after a short course, it bifurcates into the LAD branch and the LCx branch. The LAD follows a very sinuous path along the anterior interventricular sulcus, reaching the anteroinferior border of the heart, emitting numerous branches along the way that gradually reduce in caliber. It curves around the inferior border of the heart to reach the inferior surface, where it enters the posterior interventricular sulcus and usually ends after a few centimeters. Embedded in adipose tissue, this artery runs close to the great cardiac vein [26]. The LCx follows the left portion of the coronary sulcus, running in the subepicardial adipose tissue, close to the left fibrous ring. Its initial portion is hidden beneath the base of the left auricle. It is accompanied by the great cardiac vein. The LCx terminates in atrioventricular branches that supply the inferior surface of the LV, typically not reaching the posterior interventricular sulcus. In some cases, it provides irrigation to the sinoatrial node (SAN) through a collateral atrial branch (45% of cases) [26].

The right coronary artery originates from the aorta, specifically at the level of the edge of the right semilunar valve cusp and the corresponding aortic sinus. It courses downward, forward, and to the right. It extends from its origin to the anteroinferior border of the heart (preatrial segment), continues along the right portion of the coronary sulcus (infratrial segment) and bends at a right angle from the previous segment (posterior interventricular segment), where it becomes known as the posterior interventricular branch, which is its terminal branch. This terminal branch is in close relationship with the posterior interventricular vein and the coronary sinus, into which this vein drains. The collateral branches of this artery provide irrigation to the SAN (55% of cases) and the atrioventricular node (AVN) [26].

Generally, the left coronary artery irrigates the anterior and lateral LV, while the right coronary artery irrigates most of the RV and the posterior LV in 80-90% of individuals [25].

Venous drainage occurs mainly via the great cardiac vein, which becomes the coronary sinus, and a group of independent veins. The anterior interven-

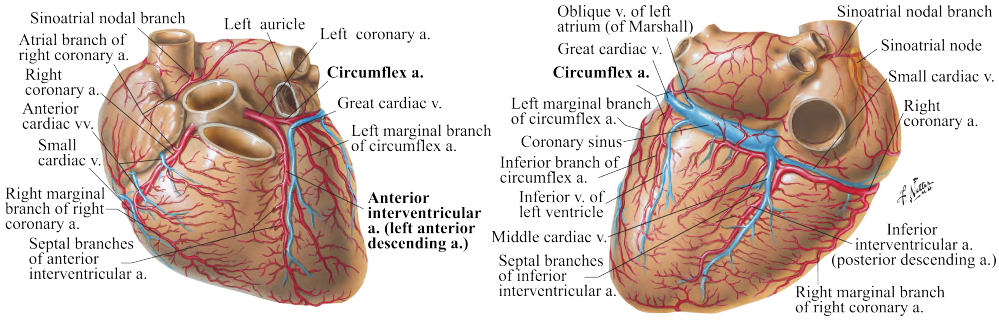


Figure 1.3: Sternocostal (left) and diaphragmatic (right) faces of the heart showcasing its vascularization. Adapted from Plate 239 in [27]. a.: artery, v.: vein, vv.: *venae* or veins.

tricular vein originates to the right of the apex of the heart, in the anterior interventricular sulcus, near the LAD. It follows the artery, crosses it anteriorly and then deviates to reach the LCx, continuing as the great cardiac vein. Then it runs along the coronary sulcus, above the LCx. Shortly before reaching the junction of the posterior and anterior interventricular sulci on the inferior surface, it dilates abruptly, forming the coronary sinus [26].

1.2.2 The myocardium

1.2.2.1 Macroscopic view

Cardiac tissue is composed of muscle fibers arranged in a lattice-like network, spiraling around the heart in a double helix [25]. The ventricular myocardium is particularly thick, especially in the LV (see Figure 1.2). Its architecture includes both common (superficial) fibers and specialized fibers that form deeper layers. The superficial fibers, anchored to the connective tissue around the orifices, extend toward the apex, where they reflect around the cardiac vortex, as depicted in Figure 1.4. From there, they fan out toward the interventricular septum, the papillary muscles, or the fibrous rings. The specialized fibers, also attached to the fibrous rings, are shorter and oriented obliquely in the RV, but nearly circular in the LV (see Figure 1.4). They form two distinct planes: a middle circular layer and a deeper layer corresponding to the papillary muscles and subendocardial trabeculae carneae [26]. In contrast, the atrial myocardium is considerably thinner. Nevertheless, it also contains common and specialized fibers: the latter form rings around the venous orifices, while the common fibers extend in loop-like trajectories across the atrial walls [26].

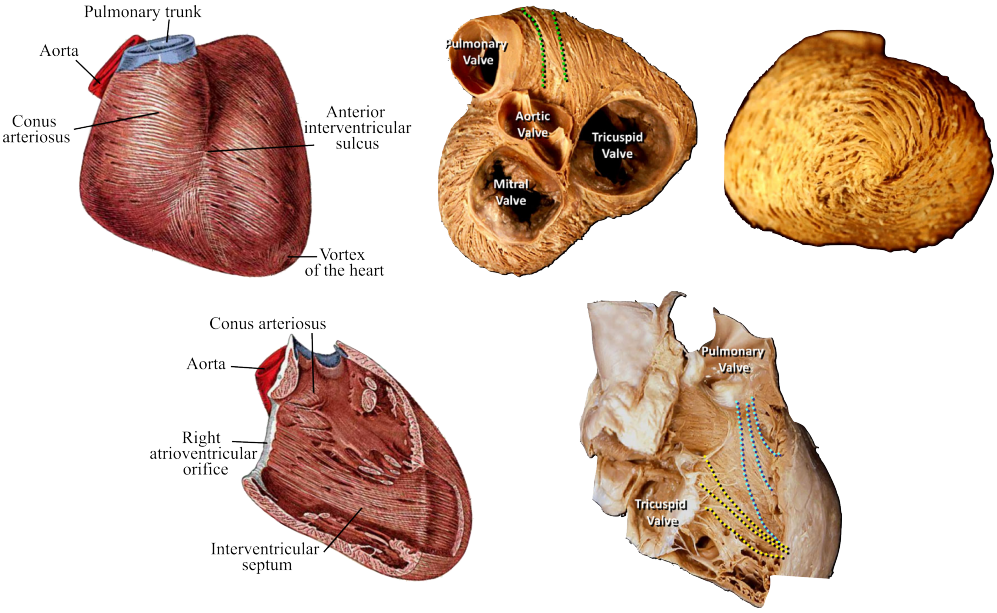


Figure 1.4: Illustration (left) and experimental data (right) of the myocardial fibers arrangement in the heart. Illustrations are from [26] and images from [28].

1.2.2.2 Microscopic view

The myocardium is composed of cardiac muscle, whose functional unit is the CM. Myocardium is structurally and functionally similar to skeletal muscle, which powers voluntary movement. As shown in Figure 1.5, each CM is surrounded by a sarcolemma, consisting of collagen fibrils, polysaccharides, and its plasma membrane [25, 29]. CMs can be mononucleated or binucleated.

1.2.2.3 Contractile machinery

Each CM contains numerous myofibrils composed of thousands of actin and myosin molecules (see Figure 1.5). The spatial arrangement of these thick (myosin) and thin (actin) filaments produces the striated appearance typical of both cardiac and skeletal muscles when viewed under polarized light. As illustrated in Figure 1.5b, the dark anisotropic (A) bands represent areas of overlap between the two filaments, whereas the bright isotropic (I) bands contain only actin. Actin filaments are anchored to Z discs and extend toward adjacent myosin filaments. The region between two Z discs defines a sarcomere, the fundamental contractile unit. During contraction, sarcomeres shorten

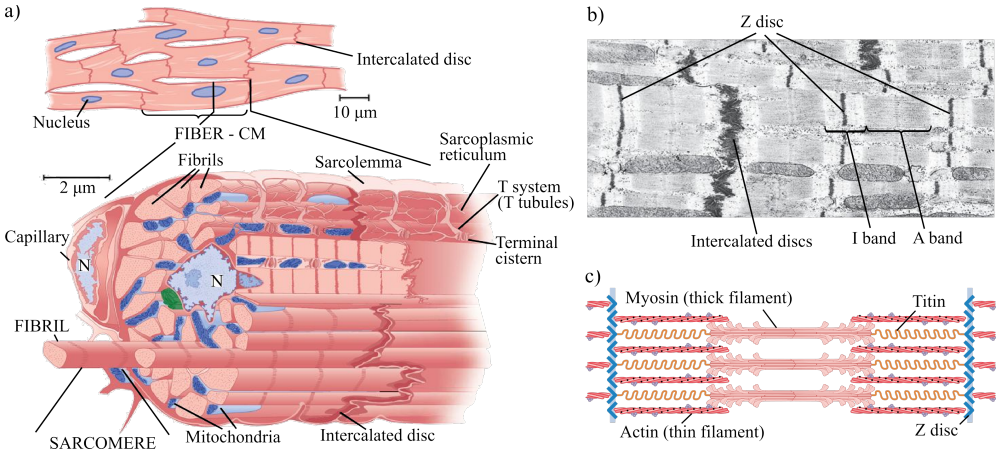


Figure 1.5: Microstructure of the cardiac muscle. a- Illustration of the cardiac muscle and its inner structure. b- Electron photomicrograph of cardiac tissue. c- Sarcomere microstructure depicting the myosin and actin filaments. Image created from images in [29] and [25].

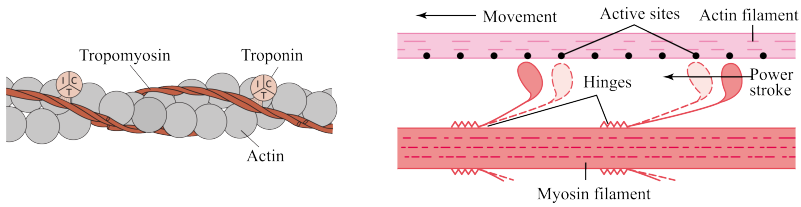


Figure 1.6: Actin-tropomyosin-troponin complex (left) and tilting and pulling of the myosin heads on the active sites of the actin filament (right). Image created from images in [29] and [25].

as actin and myosin overlap increases (see Figure 1.5c).

Additional components enable contraction. The sarcoplasmic reticulum (SR), a specialized endoplasmic reticulum, serves as a reservoir for calcium (Ca^{2+}), releasing or sequestering the ion depending on membrane polarization. As observed in Figure 1.6, two other proteins are also essential: *tropomyosin*, which blocks myosin-binding sites on actin at rest, and *troponin*, a three-subunit complex. Troponin I anchors the molecule to actin, troponin T binds to tropomyosin, and troponin C binds Ca^{2+}, initiating contraction [25, 29].

1.2.2.4 Cell-to-cell coupling

Cardiac muscle fibers are interconnected by intercalated discs, specialized junctions that ensure functional synchronization. Each fiber is composed of nu-

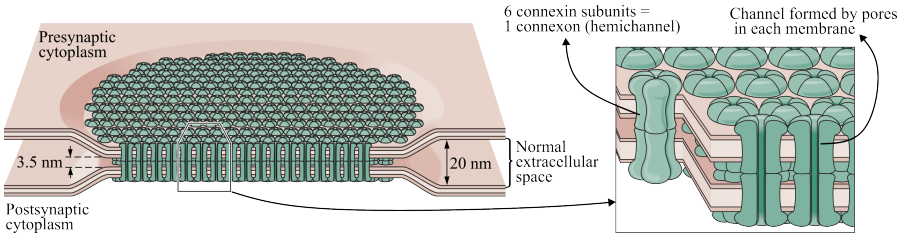


Figure 1.7: Gap junction structure connecting two cells. Multiple gap junctions connecting the cytoplasm of two cells (left) and close view of the 6 connexin proteins forming a connexon (right). Image adapted from [29].

merous CMs, connected both in series and in parallel. At intercalated discs, adjacent cell membranes fuse to form gap junctions, which allow rapid ionic diffusion between cells (see Figure 1.7) [25]. Within gap junctions, the intercellular space narrows from 20-25 nm to only 3-3.5 nm [25, 29]. Each junction consists of paired connexons, with each connexon made of six connexin subunits forming a central pore (see Figure 1.7). When connexons from neighboring cells align, they create continuous channels for direct ion exchange, bypassing the extracellular space [29].

In cardiac muscle, gap junctions are predominantly located at the fiber ends, producing anisotropic conduction. This connectivity allows action potentials (APs) to propagate efficiently, enabling the myocardium to act as a functional syncytium in which the excitation of a single cell activates the entire network.

Functionally, the myocardium consists of two syncytia: atrial and ventricular, separated by fibrous tissue surrounding the atrioventricular orifices. Under normal conditions, electrical impulses cannot directly cross this barrier, but are relayed through the specialized electrical CS (see Section 1.2.3.2). This delay ensures that atrial contraction precedes ventricular contraction, a timing critical for effective cardiac output [25].

1.2.2.5 Mechanisms of contraction

Excitation-contraction coupling in cardiac muscle describes how an AP initiates contraction (Figure 1.8). Like in skeletal muscle, the AP propagates through T tubules, which are invaginations of the sarcolemma, and triggers Ca^{2+} release from the SR. However, in cardiac cells, extracellular Ca^{2+} entering through voltage-gated channels in the T tubules further stimulates Ca^{2+} release from the SR. The binding of Ca^{2+} to troponin C induces a conformational change

in the troponin-tropomyosin complex, exposing actin's binding sites. Myosin heads then attach to actin, reducing the distance between the Z discs and generating the movement associated with pulling the filaments together (see Figure 1.6).

The energy that myosin heads need for this process is obtained from adenosine triphosphate (ATP) hydrolysis into adenosine diphosphate (ADP) and phosphate. When depolarization ceases, Ca^{2+} is pumped back into the SR, and the tilt of the myosin heads to generate the pulling of actin filaments enables ADP and phosphate release from the myosin head. As this site is now empty, a new ATP molecule binds and myosin-actin detachment occurs, terminating contraction. Because the SR in cardiac cells is less developed than in skeletal muscle, extracellular Ca^{2+} influx is essential to achieve sufficient contraction strength. T tubules, which are larger in cardiac muscle, also store Ca^{2+}, making cardiac muscle contraction particularly dependent on extracellular Ca^{2+} levels [25].

1.2.3 Electrophysiology

1.2.3.1 Action potentials and ionic currents

Cardiac electrical activity arises from specialized action potentials. Nodal cells generate spontaneous depolarizations due to pacemaker currents, whereas atrial and ventricular myocytes exhibit a rapid sodium-driven upstroke followed by a plateau phase sustained by calcium influx and potassium efflux. Electrical excitation of cardiac tissue, in turn, triggers mechanical contraction.

As in neurons and skeletal muscle, CMs maintain ionic gradients between intracellular and extracellular spaces. The difference in electrical potential at the CM membrane is mainly determined by three ions: sodium (Na^+), potassium (K^+) and Ca^{2+} (see Figure 1.8b) [29]. K^+ ions are more concentrated inside the cell, whereas Na^+ and Ca^{2+} ions are more concentrated outside the cell. These gradients are maintained by active transport mechanisms that ensure electrochemical stability. The resting membrane potential of mammalian CMs is about –80 mV, determined primarily by K^+ ions, which have the highest resting permeability [25, 29].

When stimulated, the membrane depolarizes (i.e., electrically activates) rapidly. Like neurons and skeletal muscle fibers, cardiac cells exhibit an overshoot of zero potential. However, unlike other excitable tissues, depolarization of CMs is followed by a prolonged plateau before repolarization (i.e., before the membrane potential returns to its resting value). In mammals, the entire de-

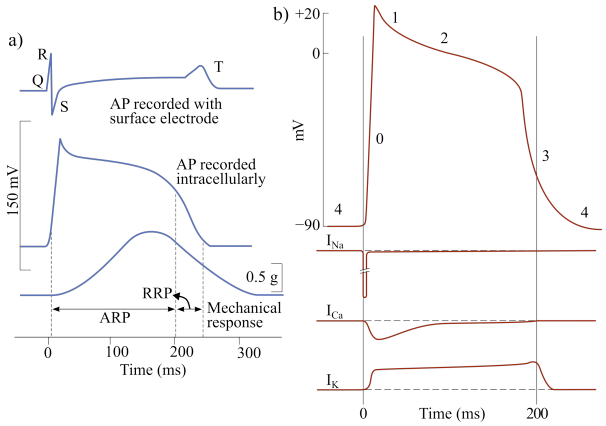


Figure 1.8: AP phases and relation with contraction. a- AP compared with contractile response. ARP: absolute refractory period, RRP: relative refractory period. b- AP phases in relation with main ionic currents. Image adapted from [29].

polarization and repolarization process lasts 200 ms or more [29]. The resting membrane potential of CMs is sensitive to changes in extracellular K^+, while the AP amplitude depends mainly on extracellular Na^+ levels.

The cardiac AP consists of five distinct phases (Figure 1.8b):

- *Phase 0* (rapid depolarization): It is triggered by the opening of voltage-gated Na^+ channels, which allows Na^+ to enter the cytoplasm of the CM. This positive flow generates the sodium current (I_{Na}), producing an abrupt increase in the transmembrane potential (V_m) to around 20 mV.

- *Phase 1* (initial repolarization): It is caused by the closure of Na^+ channels and the opening of the transient K^+ channels that produces the transient outward potassium current (I_{to}). These ion flows allow a net, brief efflux of K^+ out of the cell and a slight drop in V_m.

- *Phase 2* (plateau phase): It results from the slow and sustained opening of voltage-gated Ca^{2+} channels, allowing Ca^{2+} influx to maintain a stable V_m near 0 mV. This plateau supports sustained myocardial contraction, essential for effective blood ejection. CMs have two main types of Ca^{2+} channels: T-type and L-type. Most Ca^{2+} influx during the AP comes from the slower and longer-lasting L-type channels, generating the L-type calcium current (I_{CaL}).

- *Phase 3* (final repolarization): It occurs due to closure of Ca^{2+} channels and delayed K^+ efflux through the increasing activation of the delayed rectifier K^+ channels. The rapid delayed rectifier potassium current (I_{Kr}), together with the slow delayed rectifier potassium current (I_{Ks}), restore negative V_m.

- *Phase 4* (resting potential): V_m stabilizes near –80 mV. Ca^{2+} is pumped back into the SR (see Section 1.2.2.5) via the Ca^{2+}-ATPase, also known as the SERCA (Sarcoendoplasmic Reticulum Calcium ATPase) pump, and extruded from the cell by the Na^+/Ca^{2+} exchanger, which generates the sodium/calcium exchange current (I_{NaCa}). Na^+ is subsequently removed by the Na^+/K^+-ATPase, generating the sodium/potassium pump current (I_{NaK}) and restoring ionic homeostasis until the next AP.

Cardiac muscle exhibits a refractory period during which it cannot be re-excited. This prevents premature reactivation during an ongoing AP. In ventricular tissue, the absolute refractory period lasts about 250–300 ms, corresponding to the duration of the plateau phase, followed by a brief relative refractory period of approximately 50 ms, during which only stimuli stronger than normal can elicit responses (Figure 1.8a). Atrial muscle has a shorter refractory period [25, 29].

1.2.3.2 Conduction system and pacemaking

The heart continues to beat even when isolated from external neural input. Contraction of the atria and ventricles follows an intrinsic rhythm coordinated by the cardiac CS, which consists of specialized myocardial cells located subendocardially. The two main components are the SAN and the atrioventricular complex, which includes the AVN, the His bundle, and Purkinje fibers (Figure 1.9) [26].

SAN: The SAN, the primary pacemaker of the heart, is a thin, flattened, spindle-shaped structure. Its upper end is located anteriorly and to the right of the opening of the superior vena cava, within the right atrium, descending vertically along the inner side of the crista terminalis [26].

Atrioventricular complex: The AVN, or node of Aschoff-Tawara, lies in the right atrial wall, within a triangular region bounded posteriorly by the opening of the coronary sinus, inferiorly and to the left by the insertion of the septal leaflet of the tricuspid valve, and medially by the tendon of the inferior vena cava valve. It lies in the atrioventricular septum. The AVN includes a

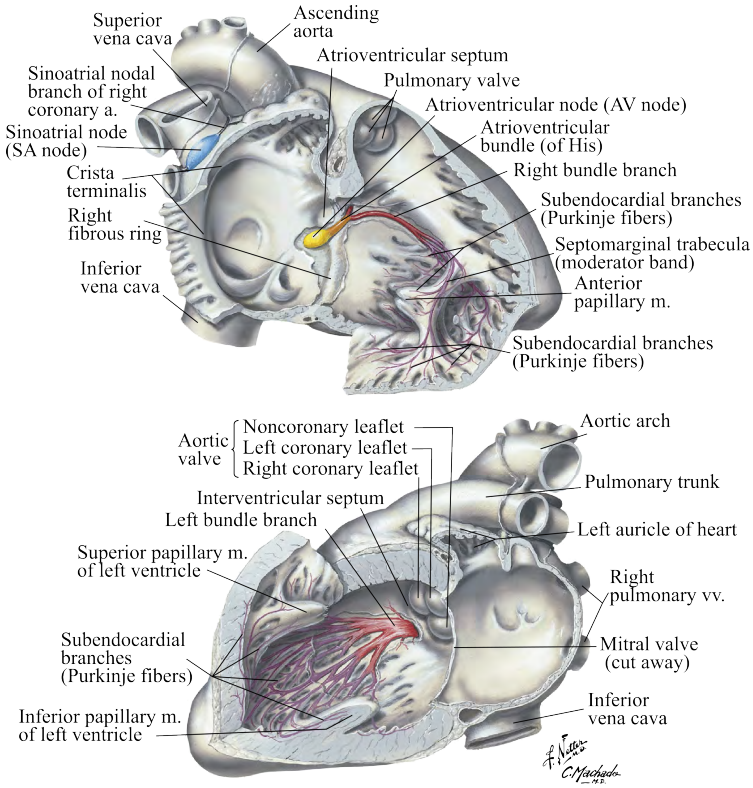


Figure 1.9: Opened RV (top) and LV (bottom) depicting the CS of the heart. Image adapted from plate 248 in [27].

portion of fibers arranged in a fan-like shape (Zahn's node) situated to the right, which condense into a denser group on the left. From here it transitions into the atrioventricular bundle, better known as the His bundle. The trunk of this bundle, approximately 3 mm wide and 10–12 mm long, extends forward, upward, and to the left. It runs along the right side of the heart septum, at the insertion of the septal leaflet of the tricuspid valve, reaching the anterior and inferior part of the membranous portion of the interventricular septum, where it divides into two branches: right and left bundle branches.

The right branch follows the course of the septomarginal trabecula (moderator band), beneath the endocardium. The septomarginal trabecula is a muscular bridge inserted inferiorly and anteriorly at the base of the anterior papillary muscle, as can be seen in the top of Figure 1.9. After exiting the septomarginal trabecula, it extends upward, slightly posteriorly, and to the left, to reach the medial wall near the septal papillary muscle. The left branch

traverses the interventricular septum and emerges beneath the endocardium on its left face, aligned vertically with the space between the right and posterior (non-coronary) aortic semilunar valve leaflets, as depicted at the bottom of Figure 1.9. Difficult to isolate, this branch appears to divide into anterior and posterior fascicles directed toward the papillary muscles of the LV. At the insertion of the papillary muscles, both branches give rise to Purkinje fibers, which arborize throughout the ventricular walls. Some Purkinje fibers run freely beneath the endocardium, occasionally resembling tendinous cords (false chordae tendineae) [26].

Impulse propagation: Electrical impulses originate in the SAN and spread through the atria with moderate velocity. Transmission slows markedly in the AVN, introducing a delay of more than 0.1 s before entering the His bundle. From there, conduction accelerates through the Purkinje fibers (150 and 400 cm/s), ensuring nearly simultaneous ventricular activation. Propagation through ventricular myocardium proceeds more slowly to the epicardial surfaces (around 50 cm/s), completing the coordinated contraction required for effective pumping [25]. Under pathological conditions, such as impaired conduction between the SAN and AVN, latent pacemaking activity of the AVN and Purkinje fibers may emerge. This ectopic activity disrupts the normal activation sequence and can significantly compromise cardiac efficiency [25].

1.2.4 Myocardial infarction

As outlined in Section 1.1, MI represents one of the most frequent outcomes of various CVDs. When cardiac muscle is deprived of oxygen and nutrients for several minutes, irreversible CM death occurs. Most commonly MI arises from persistent ischemia without timely reperfusion in the context of IHD. As illustrated in Figure 1.10, this irreversible damage triggers an orchestrated inflammatory cascade, ultimately replacing necrotic myocardium with fibrotic, non-contractile tissue. The resulting structural remodeling impairs both systolic and diastolic function [2].

1.2.4.1 Acute stage

During the acute phase of MI, previously viable myocardium undergoes necrosis, leading to loss of contractile capacity. This functional decline increases LV volume, which further elevates wall stress and myocardial oxygen demand [2].

Rapid coronary reperfusion in patients with ST-elevation MI is unequivocally beneficial, as it salvages myocardium, limits infarct size, and attenuates

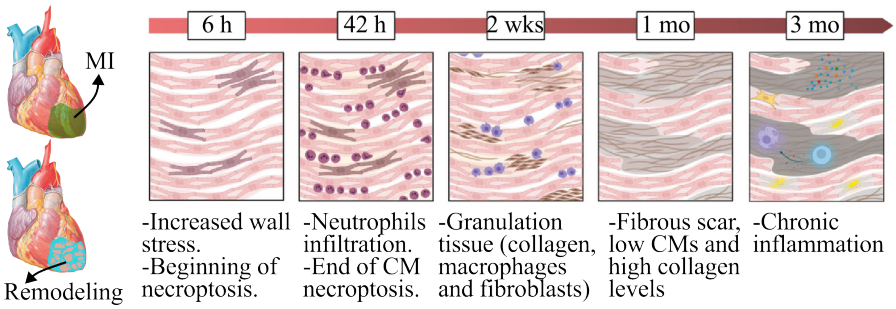


Figure 1.10: Progression of MI from acute to chronic phases. Image adapted from [2] and plate 233 in [27].

adverse remodeling, particularly when performed within the 12 hours of coronary occlusion [2, 30]. Paradoxically, however, restoring blood flow can itself exacerbate injury, a process termed reperfusion injury.

Reperfusion can severely compromise microvascular integrity due to structural and functional alterations in the microcirculation. Although the precise sequence of events underlying anatomic no-reflow remains uncertain, multiple mechanisms have been implicated (Figure 1.11). Experimental studies show that endothelial swelling, cytoplasmic blebbing, and intraluminal obstructions from platelets, erythrocytes, and neutrophils contribute to capillary plugging. Additional compression from edematous myocytes and subsarcolemmal blebs worsens obstruction. These abnormalities, coupled with reduced perfusion, delineate regions of anatomic no-reflow, which can be quantified as a microvascular obstruction (MVO) through limited dye penetration in ischemic tissue [30, 31].

In patients, clinical no-reflow is further complicated by microembolization and inflammation. Spontaneous plaque rupture or mechanical intervention can release atherosclerotic and thrombotic debris, which obstruct distal microvessels. Beyond mechanical blockage, this debris also activates inflammatory and pro-thrombotic cascades, aggravating microvascular injury. Consequently, perfusion to peripheral, still-viable CMs is reduced, resulting in additional cell loss [30, 31].

1.2.4.2 Chronic stage

In the weeks to months following MI, the heart undergoes sustained increases in workload as it adapts to elevated pre-load and after-load conditions [2]. Within the chronically infarcted region, here referred to as the affected zone (AZ),

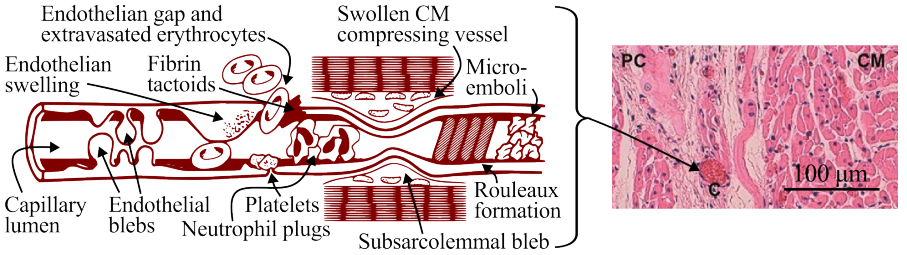


Figure 1.11: Illustration of mechanisms generating MVO (left) and microscopic view of an occluded capillary produced after acute reperfusion (right). C: capillary, PC: Purkinje cell and CM: cardiomyocyte. Image created from images in [31] and [32].

1

necrotic non-renewable CMs are progressively replaced with fibrotic connective tissue [2]. The AZ is typically subdivided into the scar zone (SZ) and the border zone (BZ). The SZ is a dense, non-excitable collagen-rich fibrotic scar characterized by wall thinning and stiffening, whereas the BZ forms a transition region from the SZ to the healthy tissue characterized by disrupted myocardial organization and increased collagen deposition [33, 34].

This long-term remodeling not only escalates healthcare costs associated with ischemic heart disease [1], but also increases the risk of HF and SCD, as discussed in Section 1.1. The severity of post-MI cardiomyopathy is strongly influenced by MI location. Preclinical studies often induce proximal occlusions of the LAD or LCx coronary arteries, but the distinct damage patterns they produce can markedly affect outcomes. As shown in Figure 1.12, LAD occlusion tends to cause apical infarcts, whereas LCx occlusion predominantly affects the basal region. Consequently, LAD-MI models generally develop larger scars, undergo more extensive remodeling, and exhibit greater functional impairment compared to LCx-MI models. The greater dysfunction in LAD-MI has been linked to both larger infarct size and impaired longitudinal contraction [35].

Importantly, MI also disrupts the CS. Purkinje cells show greater ischemic tolerance than typical CMs, surviving longer under ischemia-reperfusion conditions. For instance, Figure 1.12b shows their persistence even one month after MI. In acute MI, both the density and spatial distribution of Purkinje-muscular junctionss (PMJs) differ from healthy states, as shown in histological studies of LAD-MI pig hearts [32]. Reduced PMJ density persists into the chronic stage, with redistribution from the midmyocardium to the subendocardium and epicardium. This spatial remodeling has been proposed as an anatomic substrate for reentrant VTs in chronic MI [32]. Supporting evidence includes reports of Purkinje fiber involvement in sustained VT in post-MI patients [36],

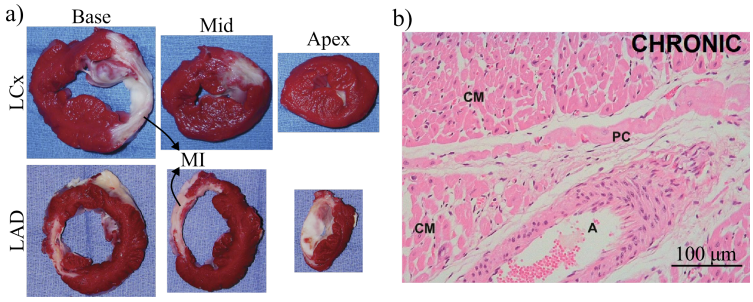


Figure 1.12: a- Macroscopic view of MI on LAD and LCx. The septal side is always at the left margin of the images. b- Microscopic image of a chronic MI induced on the LAD of a pig. Image created with images from [35] and [32].

as well as reduced VT recurrence in IHD patients receiving combined endocardial–epicardial ablation compared with endocardial ablation alone [37].

As discussed in Section 1.1, the current gold-standard approaches to preventing severe post-MI cardiac dysfunction are heart transplantation and LV assist devices [3, 4]. Heart transplantation, while highly effective in select end-stage HF cases, is constrained by limited donor availability and is associated with substantial risks, including graft dysfunction, rejection, life-long immunosuppression, and cardiac allograft vasculopathy [5]. LV assist devices, on the other hand, are primarily used as a bridge to transplantation. However, implantation requires invasive surgeries and long-term anticoagulation therapy [3, 4].

1.2.5 Human versus porcine heart

1.2.5.1 Pigs in cardiovascular research

Animals are widely used for preclinical evaluation of therapies and as organ donors for transgenic xenotransplantation. Over recent decades, pigs have largely replaced dogs in cardiovascular research due to closer similarities of their coronary circulation to that of humans [14]. In the setting of post-MI remuscularization, studies in small non-human primates (3-8 kg) have been limited by their markedly higher sinus heart rates compared with humans. This elevated intrinsic rate is a crucial limitation, as it can alter the behavior of transplanted stem cells or obscure graft-induced arrhythmias that would be more apparent in the slower human heart.

In contrast, pigs exhibit a heart-to-body weight ratio similar to humans, and their coronary anatomy, hemodynamics, cardiac size, and electromechan-

ical function closely replicate human physiology [14, 38]. Their larger size allows greater experimental throughput, reduced costs compared with primates, and the application of standard clinical tools such as catheter-based electroanatomical mapping (EAM) (see Section 1.3.2.3) [38]. Consequently, large white domestic pigs (*Sus scrofa domestica*) have become the gold-standard large-animal model for CVDs investigation. Still, despite these advantages, notable inter-species differences remain [14].

1.2.5.2 Anatomical differences between pigs and humans

The most prominent anatomical distinctions between humans and pigs stem from posture and thoracic configuration. The porcine heart has a classic "Valentine-shaped" form, influenced by the pig's unguligrade stance and lateral thoracic compression, whereas the human heart appears more trapezoidal, reflecting an upright (orthograde) posture and dorsoventral thoracic compression [14, 39].

Specific chamber differences also exist. In pigs, the right atrium has a tubular appendage, in contrast to the left atrial appendage in humans. The superior and inferior vena cava enter the atrium at right angles rather than aligned, and a large left azygous vein drains into the coronary sinus, compared with only a small oblique vein in humans. The porcine left atrium typically receives two pulmonary veins, while the human left atrium generally receives four (see Figure 1.2). In the ventricles, pigs display coarser and more prominent trabeculations. The septomarginal trabecula, which carries part of the right His bundle branch, is located more basally in pigs than in humans [14, 39].

1.2.5.3 Electrophysiological differences between pigs and humans

Electrophysiologically, pigs exhibit denser autonomic innervation than humans. The SAN lies in a slightly different position, though the AVN occupies a similar location in both species. The porcine His bundle is shorter due to its earlier bifurcation into the left and right bundle branches. Together with the thicker and more basally positioned septomarginal trabecula, these differences contribute to distinct porcine ECG features, including a faster sinus rhythm and shorter PR interval (see Section 1.3.2.2). While sinus rate decreases with pig maturation, it generally remains above that of age-matched humans [14].

Another key distinction lies in ventricular conduction. Purkinje cells in pigs penetrate deeper into the ventricular wall than in humans, which has been proposed to explain the near-simultaneous activation of the endocardium and epi-

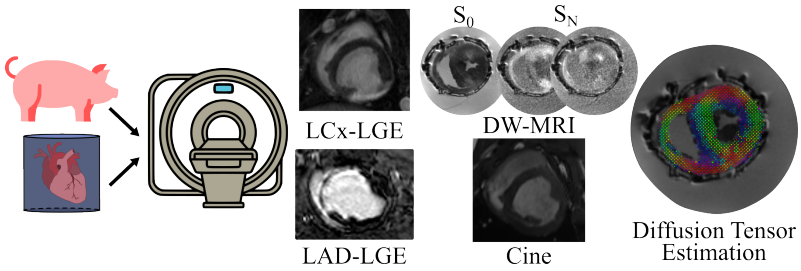


Figure 1.13: Different *in vivo* and *ex vivo* CMRs employed. Cine-CMR, LGE-CMR and DW-CMR obtained from pigs. The diffusion tensor estimation showcases an CMR slice with glyphs representing the diffusion tensor. The colors of the glyphs depict the direction of the primary eigenvector. Red: right-left, Green: anterior-posterior and Blue: apico-basal directions.

cardium observed in swine ventricles [14, 32, 40]. At the cellular level, porcine and human AP also diverge. Porcine myocytes show APs with a deeper notch, longer APD at 50% repolarization, and higher plateau potentials. These differences are underpinned by ion channel properties: humans exhibit larger I_{Kr} and smaller inward rectifier potassium current (I_{K1}) currents. Furthermore, porcine Ca^{2+} handling involves two distinct transient sources, one defined by T-tubular and another one by non-T-tubular subcellular regions, unlike the more uniform transients in humans [16].

1.3 Cardiac imaging and electrical mapping

CMR is now a well-established tool for the evaluation of CVDs. It provides comprehensive insights into cardiac morphology, function, blood flow, and tissue characteristics, supporting both clinical decision-making and the development of *in silico* models [41–43]. Complementary to this, detailed electrophysiological data are essential for the accurate diagnosis of cardiac disorders and for enabling patient-specific modeling of tissue- and organ-level electrical activity [42].

1.3.1 Magnetic resonance

The most widely applied CMR techniques in cardiology are cine CMR, diffusion-weighted (DW)-CMR and LGE-CMR, illustrated in Figure 1.13 and briefly outlined below.

1.3.1.1 Cine CMR

Cine CMR provides detailed anatomical and functional information and is typically acquired with a balanced steady-state free precession sequence, which ensures strong contrast between myocardium and blood pools [41]. It captures systolic-diastolic motion by repeatedly imaging a cardiac slice over the full cardiac cycle, enabling 3D reconstruction when multiple slices are combined after aligning them. Spatial resolution is high ($\sim$1 mm) in the short axis (SAx) plane of the heart, but lower (5-10 mm) across planes [44].

Since images are acquired during repeated breath-holds (typically 15–20), slice misalignment from respiratory motion is common [44]. Arrhythmias further complicate acquisition, as they prevent consistent cycle averaging. To mitigate this, arrhythmic beats can be excluded, at the expense of prolonged scan time, or prospective ECG triggering to the R wave can be used, though this may compromise end-diastolic accuracy. Moreover, focusing solely on regular cycles risks missing dynamic variations that reflect specific pathologies. Unlike echocardiography, cine CMR is not inherently real-time. Current advances aim to reduce breath-hold requirements, limit reliance on ECG synchronization, and achieve real-time 3D volumetric coverage [41].

1.3.1.2 Diffusion-weighted CMR

In DW-CMR, voxel intensities represent the diffusion rate of water molecules in a specific direction in which an electromagnetic gradient was applied. Thus, this technique characterizes the 3D micro-architecture of tissues with different diffusion properties, such as the brain, where cellular architectures and proportions of intracellular and extracellular compartments vary throughout the space [45]. In the heart, DW-CMR faces challenges both when performed *in vivo* and *ex vivo*. *In vivo*, cardiac motion introduces severe noise, limiting acquisition to a few slices. *Ex vivo*, motion artifacts are avoided, but the absence of intrathoracic pressure and myocardial active and passive tension leads to deformation [46, 47].

In DW-CMR, signal attenuation due to diffusion follows the Stejskal-Tanner model: $S(d(\boldsymbol{g}))/S_0 = e^{-bd(\boldsymbol{g})}$, where $d(\boldsymbol{g})$ is the diffusion along the gradient, S/S_0 the signal attenuation, b the scalar weighting value and S_0 the signal value without the sensitizing gradients. From this formulation and the DW-CMR data, it is possible to estimate the diffusion function as a positive-valued Cartesian tensor with even order and full symmetry (see right side of Figure 1.13) [48]. In a specific spatial location covered with voxels, the principal

eigenvector of the diffusion tensor corresponds to the direction with the highest water diffusivity, which matches the longitudinal axis of CMs in that region [47].

Although still primarily research-focused, DW-derived markers have shown promise. Fractional anisotropy measures the alignment of CMs within a voxel, while mean diffusivity captures overall diffusion magnitude. Both are sensitive to fibrosis and CM disarray, making them relevant for detecting remodeling in hypertrophic cardiomyopathy and post-MI border zones [43].

1.3.1.3 Late gadolinium-enhanced CMR

LGE-CMR employs gadolinium as a paramagnetic contrast agent to detect scar, fibrosis, and infiltration in cardiac tissue. After injection into the bloodstream, gadolinium rapidly enters blood pools but accumulates preferentially in damaged regions due to easier penetration and delayed washout. Ten to twenty min after injection, elevated concentrations yield hyperintense signals on T1-weighted images, clearly delineating pathological regions such as infarct zones [30, 41].

In acute MI, uptake occurs as gadolinium diffuses into the intracellular space, facilitated by the initial rupture of cell membranes, whereas MVO prevents delivery, appearing as hypoenhanced areas surrounded by hyperenhancement. MVO in LGE-CMRs signals reperfusion injury, poor prognosis, and higher remodeling risk [30, 41]. In chronic MI, contrast accumulation occurs due to increased uptake and delayed washout arising from expanded extracellular space within fibrotic tissue, particularly in the BZ and SZ. Figure 1.13 illustrates how AZ is associated with high signal intensity in LGE-CMRs, both in acute and chronic MI. The extent of hyperenhancement correlates with adverse outcomes, regardless of the underlying cause or LV ejection fraction [41,49]. In the context of MI, the likelihood of functional recovery after coronary revascularization decreases as transmural hyperenhancement increases [30,41]. Today, LGE-CMR is the clinical gold standard for defining infarct regions in patient-specific digital twin models [10, 15, 50]

1.3.2 Electrophysiological data

Cardiac electrophysiology can be studied across multiple scales. At the cellular scale, patch-clamp recordings quantify transmembrane ionic currents and inform biophysically detailed cellular models [16, 51, 52]. In this thesis, we focus on tissue- and organ-scale electrophysiology. At these scales, depolarization-repolarization dynamics can be measured using micro-electrode arrays, needle

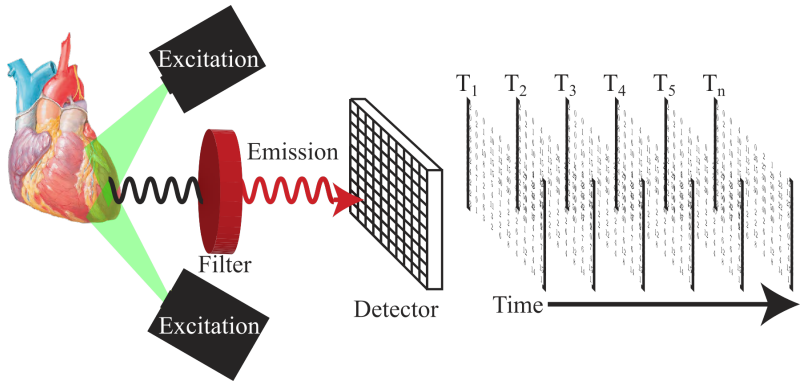


Figure 1.14: Simplified scheme of an OM system. Image created from an image in [56] and the plate 233 in [27].

electrodes, OM, EAM, or non-invasive body-surface potentials, including the ECG [53, 54]. The specific techniques applied here are introduced below.

1.3.2.1 Optical mapping

Principles: OM is an imaging technique that uses voltage- or Ca^{2+}-sensitive dyes to convert V_m changes and Ca^{2+} transients into a fluorescent signal, enabling high-resolution spatio-temporal mapping of cardiac activity. It has been instrumental in elucidating arrhythmia mechanisms and assessing therapies [55–57]. The setup includes a dye, light source, filters, and detectors (Figure 1.14) [56]. Upon illumination at the dye's absorption wavelength, fluorescence is emitted, filtered, and captured by detectors. Each pixel records optical signals reflecting changes in V_m or Ca^{2+}, enabling quantification of electrophysiological dynamics [55–57].

Artifacts: Artifacts must be carefully managed when analyzing OM data. Motion is commonly suppressed using cardiac electro-mechanical uncouplers. Uniform illumination and precise filtering improve accuracy, with light-emitting diodes offering better stability, energy efficiency, portability, flexibility, and lower costs compared with traditional light sources [57]. Since continuous illumination may result in photobleaching, illumination is limited to recording intervals. This reduction in the fluorescence of the dye can be mitigated by high-quality filtering of the excitation light and filtering to reduce background light and allow only selected wavelengths to reach the detector [55,57]. Another effect observed in OM measurements is photon scattering. Due to the thickness

of the ventricular wall and the inherently large depth of focus in typical macroscopic OM setups, fluorescence originates not only from the surface, but also from the subsurface layers. Activation wavefronts originating below the epicardial surface can reach the surface at varying angles and can blur the epicardial signals. Thus, optical data should be compared not directly to surface V_m, but to depth-averaged V_m values to account for subsurface contributions [57].

1.3.2.2 Electrocardiography

Principles: The ECG non-invasively records the electrical activity of the heart through body-surface electrodes. Because the torso is an efficient volume conductor, surface electrodes can capture electrical signals that are generated during cardiac depolarization-repolarization cycles. The ECG represents the spatial summation of time-dependent electrical changes across the myocardium. The amplitude of the recorded signals is directly related to the mass of the cardiac tissue that is depolarized (or repolarized). These characteristics make the ECG a cost-effective and widely used diagnostic tool [25, 29].

Lead configurations: Electrocardiographic signals can be recorded using unipolar or bipolar surface electrode configurations, which lead to varying ECG waveforms corresponding to specific views of cardiac electrical activity (so-called leads). Unipolar recordings use an active (exploring) electrode paired with an indifferent (reference) electrode, while bipolar recordings measure the voltage difference between two active electrodes. Importantly, the direction of depolarization relative to an electrode determines the waveform polarity. When depolarization moves toward an electrode, a positive deflection appears in the ECG. In contrast, when it moves away, a negative deflection is recorded. This relationship between wave direction and electrode orientation is essential for ECG interpretation [25, 29].

The 12-lead ECG is the gold-standard configuration, which combines three types of leads recorded from 10 electrodes placed on the body (see Figure 1.15):

- Bipolar limb leads (I, II, III): They measure voltage differences between pairs of limbs (right arm, left arm, and left leg) and correspond to the corners of Einthoven's triangle, with the heart at its center, as shown in the left side of Figure 1.15. These leads view the heart in the frontal plane.
- Augmented unipolar limb leads (aVR, aVL, aVF): They use the same limb electrodes, but each lead records the voltage at one limb relative

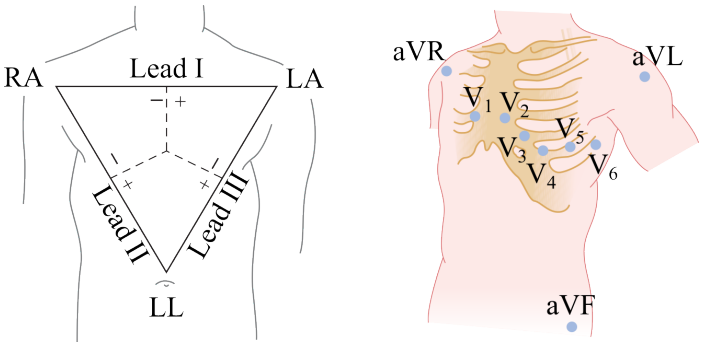


Figure 1.15: Bipolar (left) and unipolar (right) electrode positioning of the 12-lead ECG in a human. Image created from images in [29].

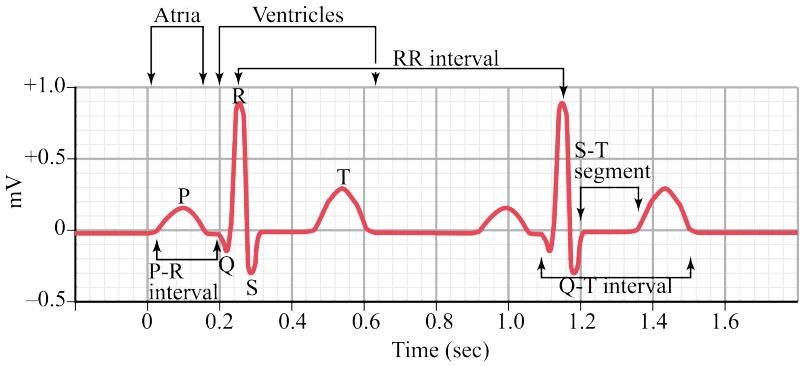


Figure 1.16: The normal ECG waveform and its segments and intervals. Image adapted from [25].

to the average of the other two. These leads also represent the frontal plane.

- Unipolar precordial (chest) leads (V1–V6): Electrodes are placed across the chest and view the heart in the transverse plane (see the right side of Figure 1.15). Each unipolar measurement is referenced to the Wilson central terminal, calculated as the average voltage of the electrodes in the left arm, right arm, and left leg.

Waveforms: The normal ECG (Figure 1.16) consists of the P wave, QRS complex, and T wave, each reflecting a specific phase of cardiac electrical activity [25, 29].
- *P wave:* The P wave represents atrial depolarization, originating from the

SAN and propagating across both atria. Its duration is typically 80–120 ms with a monophasic, positive morphology in most leads. Variations in P wave shape and duration may indicate atrial enlargement or conduction disturbances.
- *PR interval:* Following the P wave, the isoelectric PQ segment reflects the slow conduction through the AVN, where no electrical activity is detected. The PR interval, measured from the onset of the P wave to the onset of the QRS complex, typically ranges from 120 to 200 ms and indicates the time taken for the electrical impulse to travel from the atria to the ventricles.
- *QRS complex:* The QRS complex corresponds to ventricular depolarization, generated by the summation of the activation of APs from both ventricles. It consists of three deflections. The first, the Q wave, is commonly defined as an initial negative deflection. The R wave represents a subsequent positive deflection, whereas the S wave is a second negative deflection. The normal QRS duration is in the 80–110 ms range, and its amplitude is the highest among all ECG waveforms, reflecting the greater myocardial mass and faster conduction velocity (CV) of the ventricles compared to the atria. A prolonged QRS (>120 ms) may suggest intraventricular conduction abnormalities. Atrial repolarization is not visible in the ECG, as it is masked by the dominant QRS complex.
- *ST segment:* After the QRS complex, the ST segment represents the time interval when the ventricles are uniformly depolarized and corresponds to phase 2 (plateau) of the ventricular APs. This segment, which extends from the end of the S wave (J point) to the start of the T wave, is isoelectric under normal conditions. Abnormalities such as ST elevation or depression are indicators of IHD or MI.
- *T wave:* The T wave reflects ventricular repolarization (phase 3 of APs) and has a smooth, positive, and low-amplitude profile compared to the QRS complex. Repolarization usually occurs 250–350 ms after depolarization. The QT interval, from the onset of the QRS complex to the end of the T wave, includes both ventricular depolarization and repolarization phases. It ranges from 200 to 400 ms depending on the heart rate, as it shortens at higher heart rates due to abbreviated ventricular APs.
- *U wave:* Occasionally, a U wave may appear in the ECG after the T wave. Its origin remains uncertain, but it is believed to be related to afterpotentials or late repolarization phenomena in certain ventricular cells, such as from the papillary muscles.

In sinus rhythm, each P wave precedes a QRS complex, indicating that ventricular activation is triggered by atrial depolarization via the AVN. Heart rate is typically governed by the SAN, with resting values usually found between

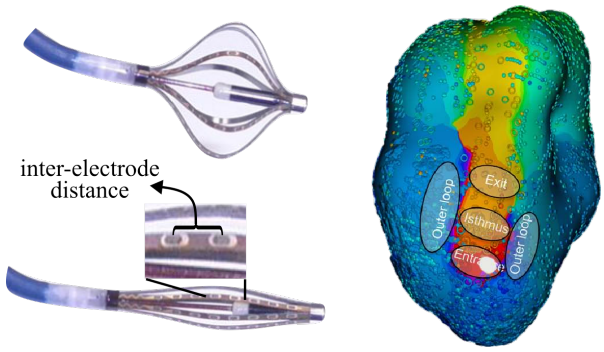


Figure 1.17: At the left side, an example of a mapping catheter, Orion catheter (Boston Scientific, Cambridge, MA, USA), is shown at its open and close configuration together with the inter-electrode distance. At the right side, a post-MI EAM-derived AT map of the porcine LV during VT is shown. The reentrant circuit is individualized. Image created from images in [60] and [54].

60 and 100 beats per minute [25, 29].

Pig-human differences: As discussed in Section 1.2.5, species-specific anatomy and posture affect ECG morphology. In 10-15 week old pigs (30-40 kg), higher heart rates (91-167 beats per minute), shorter PR intervals (50-120 ms), and shorter QT intervals (150-340 ms) are consistently observed compared with humans [14].

1.3.2.3 Electroanatomical mapping

Principles: Originally developed to improve catheter guidance during ablation, EAM now enables real-time reconstruction of cardiac anatomy with superimposed electrograms [58]. Mapping (left side of Figure 1.17) and reference electrodes track catheter position using electromagnetic signals. By sequentially sampling, reconstruction of structures such as LV endocardium can be generated (right side of Figure 1.17).

This minimally invasive approach links electrophysiological measurements to cardiac geometry, enhancing understanding of arrhythmias, guiding targeted ablations, and supporting detailed substrate characterization [58,59] (right side of Figure 1.17).

Signal interpretation: Multi-electrode mapping catheters record unipolar and bipolar electrograms (left side of Figure 1.17). Bipolar amplitudes can

provide valuable information about the presence of arrhythmogenic fibrotic substrates, but are influenced by factors such as the distance between electrodes (left side of Figure 1.17), electrode size, and orientation relative to activation wavefronts. Unipolar electrograms are more robust to catheter orientation and are not affected by interelectrode spacing, but are more sensitive to noise and far-field activity, requiring advanced filtering techniques to ensure reliable interpretation [59]. Recent advances use high-density mapping catheters (2 mm interelectrode distance) for high-resolution data collection, enabling accurate identification of low-voltage areas and narrow isthmuses in conditions such as chronic MI [54, 59–61]. These improvements allow precise electrophysiological substrate characterization, which not only improves the effectiveness of arrhythmia ablation but also enables detailed patient-specific electrical modeling, paving the way for digital twin applications.

1.4 Stem cell-derived cardiomyocytes

1.4.1 Fundamentals

Embryonic stem cells can be derived from the inner cell mass of mammalian blastocysts, possessing unlimited self-renewal capacity and pluripotency. They are able to differentiate into derivatives of the three germ layers, endoderm, mesoderm, and ectoderm [62, 63]. Embryonic stem cells have long been explored in regenerative medicine, pharmacological testing, and basic mechanistic studies. However, their use has raided substantial ethical concerns, especially in humans, limiting their translation to clinical and research applications. In addition, xenogeneic and allogeneic immune rejection after transplantation further questioned the feasibility of embryonic stem cell-based therapies, motivating the search for alternative sources of pluripotent cells [62].

In the late 20^{th} century, it was discovered that certain transcription factors could reprogram somatic cells to acquire pluripotent or totipotent states. In 2006, Takahashi and Yamanaka [62] introduced 20 candidate factors into mouse embryonic fibroblasts using retroviral transduction, and identified four key regulators: Oct3/4, Sox2, c-Myc, and Klf4. Their combined expression conferred pluripotency, giving rise to induced pluripotent stem cells [62]. These reprogrammed cells resembled embryonic stem cells in gene expression, morphology, and proliferation, and demonstrated the capacity to form derivatives of all three germ layers and to generate teratomas *in vivo* [62]. Comparable results were subsequently obtained using fibroblasts from the tails of 7-week-old male

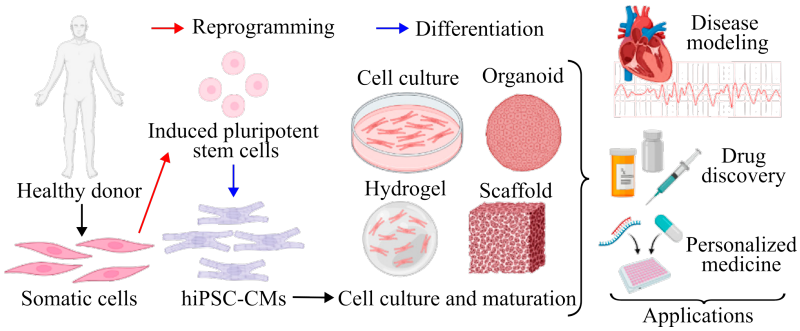


Figure 1.18: Schematic pipeline depicting the generation of hiPSC-CMs and their applications. Image adapted from [64].

mice [62].

1.4.2 Origin and maturity

One year later, Takahashi et al. [63] extended this approach to human cells, generating the first human induced pluripotent stem cells (hiPSCs). The same four transcription factors were introduced into dermal fibroblasts from the facial dermis of a 36-year-old Caucasian female, fibroblast-like synoviocytes from a 69-year-old Caucasian male, and BJ neonatal fibroblasts via retroviral transfection. The resulting hiPSCs closely resembled human embryonic stem cells in gene expression, morphology, proliferation, and *in vitro* teratoma formation [63], and could differentiate into neural and cardiac tissues. Directed differentiation toward the cardiac lineage employed mesoderm-related growth factors activin A and bone morphogenetic protein 4. After 12 days, beating clusters expressing cardiac markers such as troponin T and myosin isoforms were observed (see Section 1.2.2.2) [63]. Figure 1.18 shows a schematic workflow for generating hiPSC-CMs.

Despite these advances, hiPSC-CMs remain developmentally immature. Their fetal-like phenotype is evident at structural, electrical, mechanical, and metabolic levels. They lack fully developed T-tubules, efficient calcium handling, and oxidative metabolism [65]. By contrast, adult ventricular CMs are highly specialized for contraction, with tightly packed sarcomeres, abundant mitochondria strategically located near energy-demanding sites for efficient ATP delivery, a well-organized SR to quickly release Ca^{2+} for muscle contraction, and T-tubules coordinating calcium-induced contraction by bringing Ca^{2+} channels close to receptors that release Ca^{2+} from the SR. This archi-

tecture, along with a shift from glycolysis to oxidative metabolism to meet the energy needs that occur in the postnatal maturing heart, remains underdeveloped in immature hiPSC-CMs [8] and results in weaker, shorter contractions, spontaneous automaticity, elevated diastolic V_m, prolonged APs, and slower upstroke velocity compared to adult CMs [3, 65, 66]. Their sarcomeric structure, mitochondrial distribution, and expression of connexin 43 (a connexin found mainly in ventricular tissue) are illustrated in Figure 1.19a.

1.4.3 Towards adult-like cells

The lack of maturation has been largely attributed to culturing of hiPSC-CMs in non-biomimetic milieus that lack the stromal, vascular and biomechanical complexity of the native myocardium [65]. Early two-dimensional (2D) monoculture systems were therefore unable to replicate the structural and functional properties of the adult heart. To bridge this gap, tissue engineering strategies have been developed to promote maturation of hiPSC-CMs toward more adult-like phenotypes (Figure 1.18) [3, 8, 65, 67, 68].

Prolonged culture, electrical and mechanical stimulation, and co-culture with stromal cells are among the most studied approaches [3]. Simultaneous electromechanical stimulation during early spontaneous beating improves sarcomere organization, mitochondrial density, T-tubule formation, oxidative metabolism, calcium handling, anisotropic gap junctions, and AP morphology and propagation (CV of 25 cm/s) [3, 8]. Extended culture periods, lasting up to six months, have also been shown to improve morphology and subcellular organization, including increased myofibril density, alignment, and Z-disc organization [3, 67]. Likewise, co-culture with hiPSC-derived cardiac stromal cells, such as endothelial cells and fibroblasts, further promotes maturation [3,8]. For example, the presence of fibroblasts, particularly those expressing gap junctions, facilitates the appearance of T-tubules, stronger contractility, enhanced mitochondrial respiration, and more mature electrophysiological properties in hiPSC-CMs [3, 65].

More recently, maturation has been advanced by culturing cells in 3D engineered patches [3, 68–72]. Additive manufacturing techniques, such as melt electrowriting, enable the fabrication of scaffolds resembling the extracellular matrix (Figure 1.19b) [6,73]. When seeded onto such scaffolds, hiPSC-CM show morphological changes toward more adult-like forms, higher cellular alignment, and improved organization, particularly in close proximity to scaffold fibers (Figure 1.19d) [6, 69, 71, 72, 72, 74]. In 3D bioprinted scaffolds, cells aligned along scaffold fibers exhibited greater expression of connexin 43 and higher

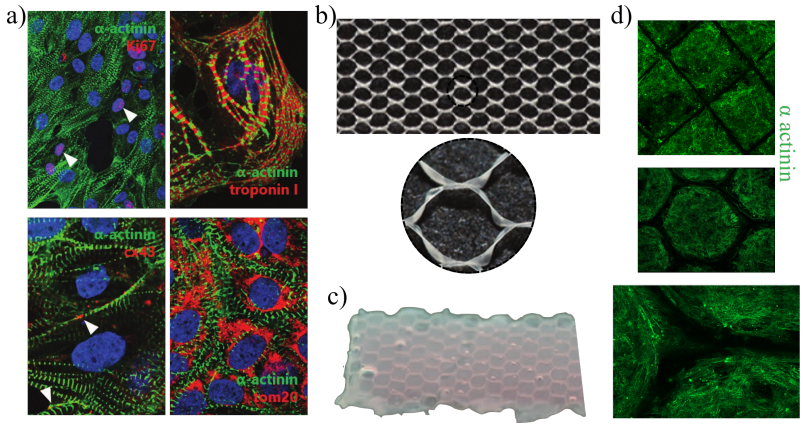


Figure 1.19: Characterization of hiPSC-CMs before and after the seeding onto the scaffold. a- Example of hiPSC-CMs previous the scaffold-mediated culturing depicting their nuclei and actin based structures, together with cellular proliferation (top-left), sarcomeric structure (top-right) and connexin 43 (bottom-left) and mitochondria (bottom-right) localizations. b- Melt electrowriting scaffold with hexagonal pore shapes. c- Cell-laden scaffold with hexagonal pore shape. d- Microscopic view of the structure of hiPSC-CMs when cultured in square (top) and hexagonal (mid and bottom) pore-shaped scaffolds. Image contains images from [70] and the BRAVƎ project [75].

CV than in 2D cultures [71, 74]. Furthermore, advanced printing technologies allow the creation of scaffolds with bio-inspired pore shapes and sizes (Figure 1.19b-c). For example, scaffolds with diamond-shaped pores have been shown to drive cell orientation, enabling the generation of highly anisotropic EHTs [6].

In addition to bioprinted scaffolds, hydrogels that mimic the extracellular matrix, both natural (e.g., collagen type I, fibrin) and synthetic (e.g., GelMA), have been extensively investigated for their ability to provide structural support and enhance cellular alignment [3, 73, 74]. As shown in Figures 1.19c and 1.19d, highly matured EHTs can be achieved by encapsulating hiPSC-CMs with cardiac stromal cells in hydrogels before seeding them into bioprinted scaffolds [6, 70, 74]. Once built, EHT are maintained in bioreactors, where electromechanical and biochemical cues further promote maturation [3].

1.4.4 Applications

As illustrated in Figure 1.18, hiPSC-CMs have broad applications across three main domains: cardiotoxicity screening in drug development, mechanistic studies of healthy and diseased myocardium, and personalized cell-based cardiac therapies [3, 68]. A key advantage of hiPSC-CMs is the ability to derive them

from donors carrying defined genetic backgrounds or disease-associated mutations. In combination with genome-editing tools, this enables the dissection of genetic contributions to inherited cardiac diseases and improves the predictive value of preclinical drug safety and efficacy testing [3, 68].

Given the high mortality associated with post-MI HF and SCD, regenerative strategies have increasingly focused on hiPSC-CMs as a source for remuscularization therapies [68]. One of the most promising approaches involves repopulating infarcted regions with EHTs, as shown in Figures 1.20a and 1.20b. Engraftment of hiPSC-CMs within the injured myocardium has been reported to improve ejection fraction, reduce infarct size, and restore ventricular wall thickness, while aiming to avoid exacerbation of arrhythmias [3, 6, 69, 71]. Importantly, when generated from autologous or patient-matched stem cells, EHTs reduce the likelihood of immune rejection [3, 68].

1.4.5 Challenges

Despite their promise, the translation of hiPSC-CMs faces several challenges in terms of reproducibility, scalability, and cost, all of which limit their widespread adoption in research and pharmaceutical applications [3, 68]. Differentiation protocols guide pluripotent cells through mesodermal lineages toward a CM state, but outcomes remain variable. This variability arises from differences in donor genetic background, disease mutations, and epigenetic reprogramming, leading to inconsistent efficiency and reduced reproducibility across laboratories [3, 68]. Even with the same donor, clone-to-clone differences or batch-to-batch variation can introduce further inconsistency. As a result, parameters such as APD, contractile function, and oxygen consumption rates often display higher variability in hiPSC-CMs compared to adult CMs. Standardized cryopreservation and transport protocols are also urgently needed to ensure quality and reproducibility as the field expands [3, 68].

In the context of myocardial repair with robust *de novo* force-producing tissue, additional challenges arise. Implantation of EHTs frequently suffers from limited post-engraftment cell survival [3, 68]. Co-culture of hiPSC-CMs with endothelial and other stromal cardiac cells has been proposed to promote angiogenesis and improve graft viability [3, 71]. However, achieving consistent electromechanical coupling between the graft and host myocardium remains a major barrier [6]. Technical difficulties during surgery can further compromise engraftment. For example, incomplete adhesion of the engraftment can be observed due to air bubbles, scar tissue formation from suturing can impair EHT-myocardium contact, or shear stresses generated during contraction-relaxation

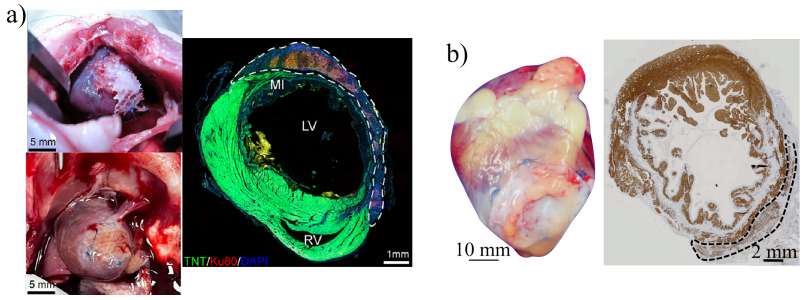


Figure 1.20: Macroscopic and microscopic views of preclinical EHT implantation. a- EHT implantation on an athymic rat at day 0 (top-left) and after 28 days (bottom-left). At the right side, a microscopic view showcases the MI region and the engrafted hiPSC-CM-based EHT (white dashed line). b- At the left side, a rhesus macaque heart is shown with its MI region covered by the stitched EHT. At the right side, a microscopic view with Desmin staining depicts the implanted EHT in a black dashed line. Image created with images from [6] and [7].

cycles can detach the graft (Figure 1.20) [11].

Finally, even when cultured under biomimetic conditions using bioprinted scaffolds with hydrogels, electromechanical stimulation, and biochemical factors, hiPSC-CMs remain immature compared with adult CMs [6,70,74]. Their incomplete electrophysiological development leads to weaker intercellular coupling and longer APDs, resulting in functional heterogeneity [6,8]. Such heterogeneities may in turn heighten the risk of arrhythmogenesis following EHT implantation [3,6,11,76–78].

1.5 Cardiac segmentation via DL

1.5.1 Cardiac imaging and segmentation

1.5.1.1 CMR

CMR is a leading non-invasive imaging technique to assess the structure and function of the heart. As mentioned in Section 1.3.1, key CMR modalities include cine and LGE sequences, widely used clinically, and DW imaging, primarily used in research modeling and simulation pipelines. Accurate segmentation of CMRs data is critical for extracting patient-specific information across cardiac pathologies. Traditionally performed manually by experts, segmentation is laborious and resource-intensive. DL-based methods now enable efficient, accurate, and automated segmentation [79,80].

1.5.1.2 Challenges in cardiac segmentation

Cardiac image segmentation presents unique challenges such as:
- Data scarcity and heterogeneity from multi-center, multi-vendor, and multi-type nature of images [81–84].
- Motion artifacts due to cardiac contraction-relaxation cycles and respiration in *in vivo* CMRs, such as long axis (LAx) inter-slice misalignment [44].

To address these challenges, researchers evaluate segmentation approaches using per slice (2D), multi-slice (2.5D), or volumetric (3D) images with preprocessing and postprocessing. Preprocessing usually involves image intensity normalization, spatial cropping, padding, and resampling. Postprocessing can include multi-segmentation averaging, smoothing, all-but-largest connected component suppression, and geometrical deformation guided by high-resolution atlases. Moreover, the model's generalization capacity can be enhanced by artificially increasing the number of data samples, either through the use of similar data or by applying data augmentation (DA) techniques such as brightness variations, random contrast adjustments, and rigid or non-rigid geometric transformations [80].

1.5.2 Introduction to DL

For more than half a century, scientists have developed mathematical algorithms to enable machines to perform tasks that resemble human reasoning. Today, artificial intelligence supports medical diagnosis, text and image analysis, and the automation of repetitive processes. A core branch of artificial intelligence is machine learning, where algorithms extract patterns from raw data and progressively build knowledge. A further specialization of machine learning is DL, which builds hierarchical representations by composing complex concepts from simpler ones. Unlike earlier approaches, DL systems can accumulate knowledge from past experiences, reducing the need for human supervision [85].

1.5.2.1 Neural networks

The most common DL architecture is the neural network, also known as a deep feedforward network. These models approximate functions f that map some input $\boldsymbol{x}$ to a certain output $\boldsymbol{y}$ and can be expressed as $\boldsymbol{y} = f(\boldsymbol{x}, \boldsymbol{\theta})$, where $\boldsymbol{\theta}$ represents the trainable parameters.

The architecture is made from the concatenation of multiple layers, where

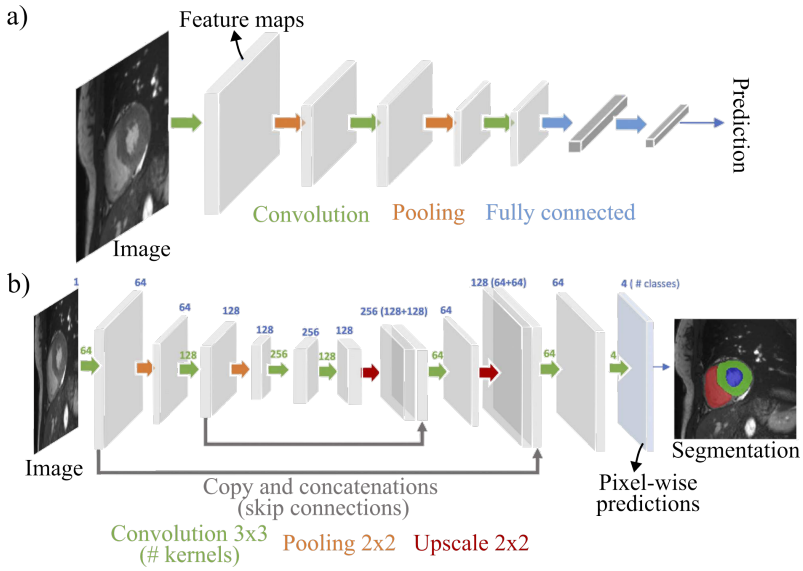


Figure 1.21: a- CNN generic architecture for prediction. b- UNet architecture for cardiac segmentation. Image adapted from [80].

the first and last layers are called input and output layers, and the inner layers are called hidden layers. The number of hidden layers defines the depth of the network. The term neural originates from an analogy with biological neurons, with hidden layers consisting of many units that work in parallel, take several inputs (dendrites) and provide one output (axon). However, neural networks should be regarded as flexible models for statistical generalization rather than biological models of brain function.

Training occurs by presenting input-output pairs ($\boldsymbol{x}$, $\boldsymbol{y}$) to the model and adjusting the trainable parameters in the vector $\boldsymbol{\theta}$ to minimize prediction error [80, 85].

1.5.2.2 Convolutional neural networks

A convolutional neural network (CNN) is a neural network that applies convolution operations in at least one of its layers [85]. Convolutions are often combined with normalization and nonlinear activations to extract feature maps (Figure 1.21a), which are then downsampled by pooling operations. Pooling reduces redundancy and improves generalization by summarizing local regions, typically using maximum or average values [80, 85].

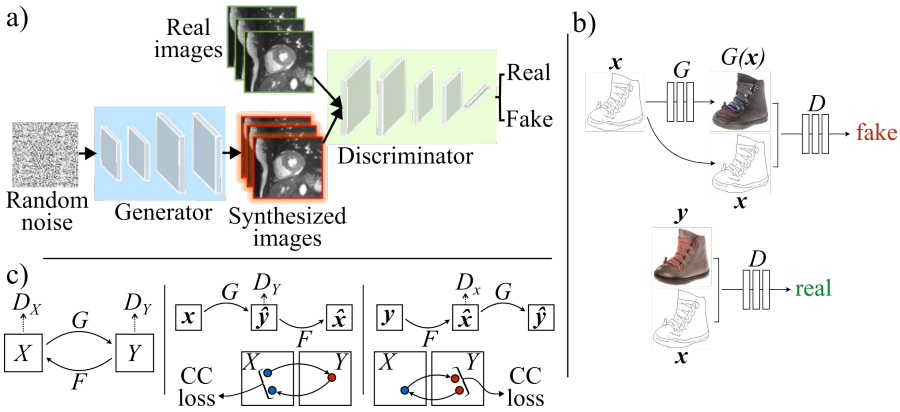


Figure 1.22: Different approaches for generative adversarial network (GAN)-based SA. a- Generic GAN-based SA from random noise. b- Conditional GAN-based paired image-to-image translation. c- Conditional GAN-based unpaired image-to-image translation with cycle consistency. CC: cycle-consistency. Image created from images in [80], [86] and [87].

Receptive field, overfitting, and regularization: The receptive field defines the portion of the input (e.g., an image region) influencing a particular neuron's output (e.g., one pixel of the output image). Deeper networks enlarge the receptive field and often improve performance, albeit with some potential risks. The most critical is overfitting, which occurs when the model memorizes the features of the training data, improving its capacity to treat training data but failing to generalize on new unseen data. Overfitting is more likely when deeper models are used with scarce data, excessive training, and weak regularization [80, 85]. A common regularization strategy is dropout, which improves generalization by randomly disregarding neuron activations during training [88] to encourage robustness and reduce overfitting. A comprehensive discussion of regularization methods is beyond the scope of this thesis (see [85] for further details).

UNet for biomedical segmentation: The quintessential CNN architecture in biomedical image segmentation is the UNet, which is depicted in Figure 1.21b [81]. It consists of a U-shape encoder-decoder design. In the encoder phase, the CNN applies convolutions, normalizations, activations, and downsampling to obtain high-level representations of the features in the input image. These high-level representations forming the latent space of the net are interpreted back by the decoder into an output image of the same resolution but in a new domain, such as the semantical domain for image segmentation. Skip

connections between encoder and decoder layers preserve spatial information lost in the encoder, enabling precise segmentation (see Figure 1.21b). Today, UNet variants form the backbone of state-of-the-art biomedical segmentation pipelines [79–83].

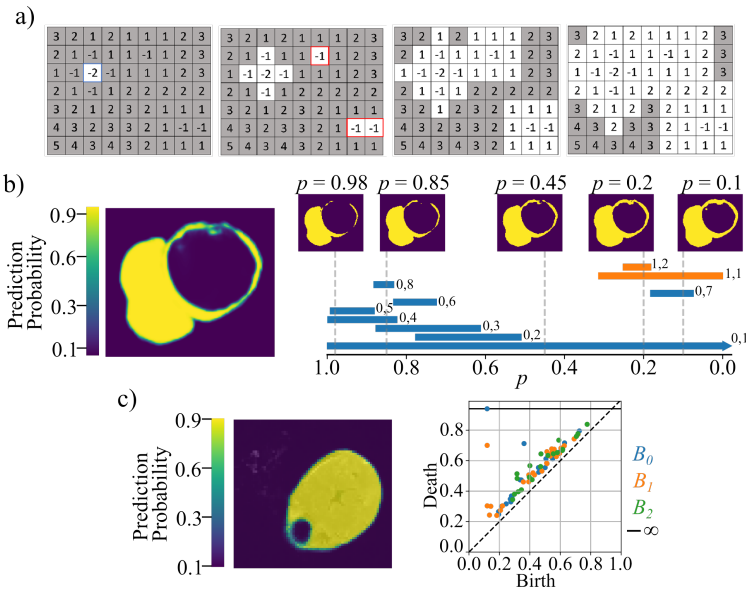


Figure 1.23: Calculation of persistent homology (PH). a- Simple numerical example. When the threshold p is varied from -2 to 2 for filtration, several connected components (white regions) are created and merged together. b- CNN output for cardiac segmentation and its PH plotted as persistent barcodes. Blue bars represent connected components and orange bars depict loops. c- CNN output for cardiac segmentation and its PH plotted as a lifetime plot. Image was created from images in [89], [19] and from our own research.

1.5.3 Generative adversarial networks

1.5.3.1 Introduction to GANs

A major obstacle in medical DL is the limited availability of annotated training data. GANs address this by synthesizing realistic samples from random noise [80, 85]. In 2014, one year before the UNet implementation, Goodfellow et al. [90] presented a generative model, termed GAN. During training, two CNNs compete to fool one another in a two-player minimax game. GANs train two CNN in competition (adversarial training): a generator (G) produces synthetic data by learning a generative model of real data that is trained to fool

a discriminator (D), while D is simultaneously trained to accurately distinguish between real and G-created synthetic data. Through this adversarial training, G is capable of generating new samples out of random noise at the end of the training (Figure 1.22a) [80, 85].

1.5.3.2 Conditional GANs and image translation

Conditional GANs extend this framework by conditioning synthetic data generation and discrimination on an input image, and the resulting G is capable of mapping data from this input image domain to another (Figures 1.22b and 1.22c). This allows image-to-image translation, i.e., mapping between imaging domains when paired input and target images are available during training (Figure 1.22b) [86] and even when unpaired input-target images are only available [87]. As depicted in Figure 1.22c, a reverse mapping function $F : Y \rightarrow X$ from the synthetic target $\hat{\boldsymbol{y}} = G(\boldsymbol{x})$ to input is learned and an objective function considering consistency between the original input $\boldsymbol{x}$ and the reverse mapped synthetic target $\hat{\boldsymbol{x}}$ is measured and optimized. In this thesis, conditional GANs are explored to generate synthetic cardiac images. A broader review of GAN-based augmentation in biomedical imaging is provided in Chapter 2.

1.5.4 Persistent homology in image segmentation

Topological data analysis applies algebraic topology to extract qualitative features from complex data. PH is particularly relevant, as it can be computed using linear algebra, is robust to small variations of input data, and can be applied to different types of data, such as point clouds and digital images. PH can be used to drive generative DL algorithms to achieve topologically reasonable results in segmentation [91–93].

In CNN-based image segmentation, PH is used to study topological properties of probabilistic outputs. Initially, the image to be segmented can be represented as a cubical complex, which is a set of points, segments, squares, cubes, and/or their hyper-dimensional counterparts. The topology of the cubical complex is determined by the calculation of its Betti numbers B_0, B_1, and B_2 whose values indicate the presence of connected components, tunnels, or voids in the topological space, respectively. In the context of PH, the Betti numbers are calculated for different cubical complexes obtained by the modification of a single variable, a procedure known as filtration. As an example, consider $\hat{\mathbf{Y}}$ being a 3D probabilistic output of a CNN performing binary segmentation. $\hat{\mathbf{Y}}$ has shape $i \times j \times k$ and per-voxel probability $\hat{\mathbf{Y}}_{ijk} \in [0, 1]$ of

belonging to the foreground class. In this case, filtration involves the variation of a threshold $p \in [0, 1]$ to obtain level sets $\mathbf{S}(p)$ that contain all voxels with $\hat{\mathbf{Y}}_{ijk} \geqslant p$. During filtration, topological entities can be created and destroyed, as shown in Figure 1.23a for a simple numerical example. Filtration can be encoded in a birth-death diagram, which can be represented by horizontal persistent barcodes or lifetime plots. In the former, every topological entity is represented with a bar and its left and right endings correspond to birth and death (Figure 1.23b), while in the latter, every topological entity is a dot in a scatter plot and its axes correspond to its birth and death (Figure 1.23c). Topological entities with longer lifetimes, that is, with longer bars in persistent barcodes (Figure 1.23b) or with dots far from the diagonal in lifetime plots (Figure 1.23c), correspond to meaningful topological characteristics of $\hat{Y}$ [91, 94]. Thus, PH offers a principled way to remove topological noise from the segmentation outputs [94].

1.5.5 Miscalibration and uncertainty in DL models

1.5.5.1 Miscalibration of predictions

As CNNs grew deeper and less regularized, their accuracy improved, but their predicted probabilities became miscalibrated. Today, CNN-based predictions are not well-modeled probabilities, i.e., they are not true probabilities, and CNNs are overconfident in their predictions [88, 95]. For example, Figure 1.24 presents a simple early CNN (left) and a complex modern CNN (right) tested on a common dataset. Although the modern CNN outperforms the simpler one in accuracy, its average confidence exceeds its actual accuracy, indicating reduced reliability due to overconfidence.

Temperature scaling is a simple post-processing calibration technique [95] that rescales the logits of the CNN by a scalar (temperature), which is learned after training on the validation set by employing an objective function relying on the uncertainty, such as the cross-entropy loss. This technique improves calibration while preserving accuracy [88, 95].

Calibration of a CNN is visualized with reliability diagrams (bottom part of Figure 1.24), comparing the accuracy (acc) and confidence ($conf$) across a group of M bins in which the predictions have been separated:

$$acc(B_m) = \frac{1}{|B_m|} \sum_{i \in B_m} \mathbf{1}(\hat{y}_i = y_i) \tag{1.1}$$

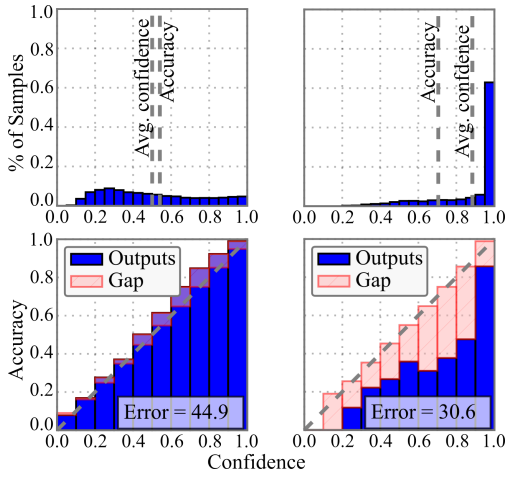


Figure 1.24: Miscalibrated modern CNNs. Confidence histograms (top) and reliability diagrams (bottom) obtained from evaluating a simple early (left) and a modern complex (right) CNNs on the well-known CIFAR-100 dataset. Image adapted from [95].

$$conf(B_m) = \frac{1}{|B_m|} \sum_{i \in B_m} \hat{p}_i \tag{1.2}$$

where B_m is the set of indices of, for example, pixels of a predicted segmentation image whose prediction values ($\hat{p}_i$) fall into the confidence interval, $I_m = (\frac{m-1}{M}, \frac{m}{M}]$, of the m^{th} bin, with $m = 1, ..., M$. Then, $|B_m|$ is the total number of elements in B_m. In addition, $\hat{y}_i$ and y_i are the predicted and true class labels, respectively, and $\mathbf{1}$ is an indicator function with value 1 when the condition is fulfilled, and 0 otherwise. As shown in Figure 1.24, the reliability diagrams of the well-calibrated models (left) have the same accuracy and confidence value, leading to diagram bars representing the identity or diagonal function. In contrast, models with poor calibration (right) present discrepancies between accuracy and confidence. Higher differences between *acc* and *conf* yield higher red gaps, signaling a poorly calibrated network [95]. The discrepancy between the two defines the expected calibration error (ECE) [95]:

$$\text{ECE} = \sum_{m=1}^{M} \left(\frac{|B_m|}{N} \left| \text{acc}(B_m) - \text{conf}(B_m) \right| \right) \tag{1.3}$$

where N is the total number of predicted samples.

1.5.5.2 Uncertainty quantification

For clinical deployment, predictions must be not only accurate, but also trustworthy. Uncertainty quantification determines the trustworthiness of the predictions, which improves the analysis by highlighting unreliable outputs, guides user interventions (e.g., by directing attention to regions of greater uncertainty), and reveals model weaknesses such as insufficient training data [88].

Uncertainty can be classified as [88]:
- Epistemic: model-related, due to limited training data (e.g. when complex multi-center and multi-vendor data are used only for testing).
- Aleatoric: data-related, due to noise and artifacts present in the image and/or the ground truth labels (GTLs).

A recent evaluation metric for segmentation confidence is the continuous ranked probability score (CRPS) [96]. By estimating distributions of derived clinical parameters, e.g. ventricular volume obtained from a semantic segmentation of a patient CMR, CRPS quantifies the accuracy of probabilistic predictions against ground truth volumes:

$$CRPS = \frac{1}{NI} \sum_{i=1}^{I} \sum_{n=0}^{N-1} \left(P(y \leqslant n) - \mathbf{1}(n \geqslant V_i) \right)^2 , \tag{1.4}$$

where $P(y \leqslant n)$ is the predicted cumulative density function (CDF) of the random variable volume y, I the total number of patients, N is the total number of discrete volume values considered, V_i is the reference volume, and n is a value extracted from the discrete volume range ($n = 0, ..., N-1$).

1.6 Electrophysiological modeling and simulation

In silico modeling and simulation of cardiac electrical activity have become powerful approaches to investigate the mechanisms underlying cardiac function in both physiological and pathophysiological states, as well as in response to pharmacological interventions and tissue engineering therapies [9–13]. Earlier studies relied on generic models parameterized with averaged electrophysiological values, providing general-purpose simulations with limited specificity. Advances in computational power, memory capacity, and the availability of high-resolution biochemical and imaging data have since enabled the development of biophysically detailed mathematical models that can accurately reproduce a wide variety of conditions and experimental scenarios [9, 13, 42, 97].

A major step forward has been the emergence of patient-specific models, which have been shown to have superior ability to capture inter-individual variability in arrhythmia generation compared to generic formulations [10, 15]. Current research, therefore, focuses on the personalization of key electrophysiological parameters in order to replicate specific pathological conditions more faithfully [15, 50, 98].

The following sections introduce the principal modeling frameworks used to represent cardiac electrophysiology at the cellular and tissue scales, as well as the numerical techniques employed to solve the governing mathematical equations. Particular attention is given to the bidomain and monodomain models, cellular electrophysiological representations, ventricular CS models, and organ-level considerations including anisotropy, spatial heterogeneity, and numerical solvers.

1.6.1 Bidomain and monodomain models of cardiac electrical propagation

The bidomain model provides a rigorous mathematical framework capable of accurately representing the depolarization-repolarization dynamics of cardiac tissue. Since the early 2000s, it has become the reference standard for *in silico* electrophysiological simulations, supported by extensive validation against both preclinical and clinical studies [99]. In this bidomain formulation, myocardial tissue is represented as two overlapping, continuous domains, the intracellular and extracellular space, linked by the transmembrane current across the capacitive cell membrane, thereby replacing discrete cell-to-cell connections with a syncytial representation [99, 100]. Each domain is modeled as a volumetric conductor with its own conductivity tensor and electric potential, while the membrane serves as the interface mediating ionic flux (Figure 1.25) [101].

The extracellular (ϕ_e) and intracellular (ϕ_i) potentials are coupled through the transmembrane current density I_m, which is equal to the sum of the capacitive, ionic, and stimulation current densities [99, 101]:

$$\nabla \cdot (\boldsymbol{\sigma_i} \nabla \phi_i) = \beta I_m, \tag{1.5}$$

$$\nabla \cdot (\boldsymbol{\sigma_e} \nabla \phi_e) = -\beta I_m, \tag{1.6}$$

$$I_m = C_m \frac{\partial V_m}{\partial t} + I_{ion} + I_s, \tag{1.7}$$

where $\boldsymbol{\sigma_i}$ and $\boldsymbol{\sigma_e}$ denote the intracellular and extracellular conductivity tensors, β is the surface-to-volume ratio of the cell membrane, C_m is the membrane

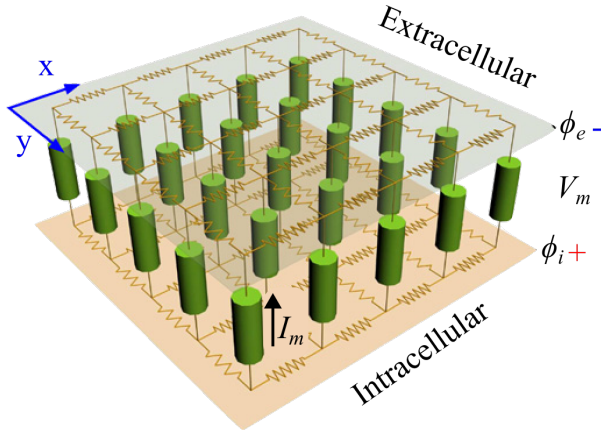


Figure 1.25: Electrical representation of the bidomain model in 2D. Intracellular and extracellular (interstitial) domains are represented by the orange and gray planes, respectively, while different resistances in each direction illustrate the anisotropic conductivity in each domain. The potentials in each domain are related between them by the transmembrane current density. Each green cylinder represents a segment of membrane characterized by a model-specific nonlinear relationship between current and voltage. Image adapted from [99].

capacitance per unit area, $V_m = \phi_i - \phi_e$ is the V_m, and I_s represents the applied stimulation current density. The ionic current density I_{ion} is determined by the specific cellular model adopted [99, 101].

Boundary conditions are required to complete the system. Typically, no-flux boundary conditions are assumed for the intracellular space, while the extracellular space may be either extended to a surrounding conductive bath (representing the conductive property of body components around the heart) [99] or may be assumed to be isolated. In most studies, both domains are treated as electrically insulated [99, 100], leading to homogeneous Neumann boundary conditions:

$$\boldsymbol{n} \cdot (\boldsymbol{\sigma_i} \nabla \phi_i) = 0, \tag{1.8}$$

$$\boldsymbol{n} \cdot (\boldsymbol{\sigma_e} \nabla \phi_e) = 0, \tag{1.9}$$

where $\boldsymbol{n}$ is the outward-facing unit normal vector at the boundary. By summing Equations 1.5 and 1.6 and using the definitions of V_m and I_m, the bidomain formulation can be expressed in terms of V_m and ϕ_e, which are experimentally measurable and thus convenient for validation:

$$\nabla \cdot (\boldsymbol{\sigma_i} \nabla V_m) + \nabla \cdot (\boldsymbol{\sigma_i} \nabla \phi_e) = \beta (C_m \frac{\partial V_m}{\partial t} + I_{ion} + I_s), \tag{1.10}$$

$$\nabla \cdot (\boldsymbol{\sigma_i} \nabla V_m) + \nabla \cdot ((\boldsymbol{\sigma_i} + \boldsymbol{\sigma_e}) \nabla \phi_e) = 0, \tag{1.11}$$

This formulation of the bidomain equations is valid under the assumption that no extracellular current density is applied. If an extracellular current density I_e is applied, an additional term $-I_e$ is included on the right-hand side of Equations 1.6 and 1.11 [99]. The bidomain formulation is thus suited to represent phenomena such as loading effects from surrounding conductive media and extracellular stimulation (e.g., from defibrillation) [99, 100].

Despite its accuracy, the bidomain formulation is computationally demanding, motivating the use of the simplified monodomain model in many applications [100]. The monodomain model assumes proportionality between the intracellular and extracellular conductivities, $\boldsymbol{\sigma_e} = \lambda \boldsymbol{\sigma_i}$. Under this condition, the extracellular and intracellular domains can be combined into a single effective medium. By replacing the definition of $\boldsymbol{\sigma_e}$ as a function of $\boldsymbol{\sigma_i}$ in Equation 1.11, the following equation is derived [100, 101]:

$$\nabla \cdot (\boldsymbol{\sigma_i} \nabla \phi_e) = -\frac{1}{1+\lambda} \nabla \cdot (\boldsymbol{\sigma_i} \nabla V_m), \tag{1.12}$$

Substituting Equation 1.12 into Equation 1.10 and reordering, the final expression for the monodomain model is obtained:

$$\frac{\partial V_m}{\partial t} = \frac{1}{\beta C_m} \nabla \cdot (\boldsymbol{\sigma_m} \nabla V_m) - \frac{1}{C_m} (I_{ion} + I_s), \tag{1.13}$$

with effective conductivity tensor $\boldsymbol{\sigma_m} = \lambda \boldsymbol{\sigma_i} / (1 + \lambda)$, which can be expressed as a function of the intracellular and extracellular conductivities as:

$$\boldsymbol{\sigma_m} = \frac{\boldsymbol{\sigma_i} \boldsymbol{\sigma_e}}{\boldsymbol{\sigma_i} + \boldsymbol{\sigma_e}}. \tag{1.14}$$

The first term on the right-hand side of Equation 1.13 represents the diffusion due to intercellular coupling, while the second term is the reaction term describing local ionic dynamics and stimulation. Equation 1.13 is a parabolic partial differential equation (PDE) with a single dependent variable, V_m, making it computationally less expensive than the bidomain system. As in the bidomain case, zero-flux Neumann boundary conditions are typically imposed [100, 101]:

$$\boldsymbol{n} \cdot (\boldsymbol{\sigma_m} \nabla V_m) = 0. \tag{1.15}$$

In this thesis, the monodomain model is employed to simulate cardiac wave propagation, given its reported equivalence with the bidomain model in scenarios without external stimulation or defibrillation [100].

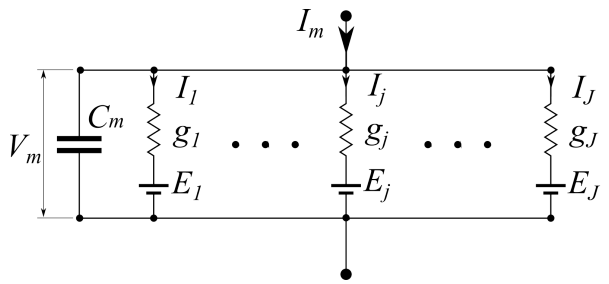


Figure 1.26: Electrical circuit model for the plasmatic membrane of the cell. Image adapted from [101].

1.6.2 Models of cellular electrophysiology

The ionic current term I_{ion} in Equation 1.13 is defined by a cellular-level model. The mathematical description of the AP traces back to the pioneering work of Hodgkin and Huxley in 1952, who demonstrated the ionic foundations of excitability in a squid giant axon. By modeling the observed electrical dynamics, they established mathematical rules for V_m as a function of the Na^+, K^+ and leakage currents. Their formulation not only laid the foundation for modern electrophysiological modeling but also enabled subsequent developments in neuronal and CM models as experimental and computational resources advanced [13, 102, 103].

1.6.2.1 Membrane representation

The plasmatic membrane can be conceptualized as an electrical circuit (Figure 1.26). Owing to its semipermeable nature, ionic concentration gradients across the membrane generate a transmembrane potential, giving rise to a capacitive current that acts to reduce these gradients. In parallel, selective ion channels regulate transmembrane flux and maintain the resting potential during phase 4 of the AP. The total membrane current is thus the sum of capacitive and ionic current contributions, as expressed in Equation 1.7.

In general, the ionic current density I_{ion} can be expressed as [13]:

$$I_{ion} = \sum_{j=1}^{J} I_j = \sum_{j=1}^{J} g_j \times op_j \times (V_m - E_j), \tag{1.16}$$

where I_j is the current carried by the j^{th} ion species, g_j is the maximal conductance density for the j^{th} ion, J is the total amount of ionic species moving

through the membrane, op_j is the probability that the channel is open (as a function of V_m), and the difference $V_m - E_j$ is the driving force, which moves the ions from one side to another of the cell membrane. E_j is the Nernst potential for ion j, which is the theoretical membrane potential at which there is no net movement of ion j across the membrane. E_j is defined by the transmembrane concentration gradient [25, 29, 101, 103]:

$$E_j = \frac{RT}{z_j F} ln(\frac{c_e^j}{c_i^j}), \tag{1.17}$$

where R is the gas constant, T the absolute temperature, F Faraday's constant (number of coulombs per mole of charge), and z_j, c_e^j and c_i^j are the valence, extracellular, and intracellular concentrations of ion j, respectively [25, 29].

1.6.2.2 Gating dynamics

During the AP, membrane permeability varies dynamically as ion channels, which act like bridges communicating the intracellular and extracellular spaces, open and close in response to V_m. In mechanistic models, three approaches are commonly employed to describe the open probability op_j [13]:

1. Instantaneous models, in which gating transitions are assumed to occur much faster than variations in V_m. Here, op_j is directly modeled as a function of V_m, without involving ordinary differential equations (ODEs). This approach may work for simple ionic dynamics, but fails to capture more complex cardiac behaviors in which ion channels experience V_m-mediated complex conformational changes.

2. Hodgkin-Huxley models, where op_j is expressed as the product of gating variables, each governed by a first-order ODE [103]:

$$op_j = \prod_{k=1}^{K} v_j^k, \tag{1.18}$$

   where v_j^k is the k^{th} gating variable for ion j.

   These variables can be conceptualized as gates that regulate ion flow. Ions are able to cross the cell membrane only when all associated gates are at least partially open. Each gate alternates between two possible states, open and closed, with the transition rates in each direction typically influenced by V_m or intracellular ion concentrations. Thus, gating

variables represent activation or inactivation probabilities of an ion, and their values oscillate between 0 and 1, representing the proportion of ion channels in a specific conformational state. The most common way to define the temporal evolution of a specific gating variable v (representing v_j^k for given values of j and k) is by an ODE of the form [102, 103]:

$$\frac{dv}{dt} = \alpha_v(1 - v) - \beta_v v, \tag{1.19}$$

where α_v and β_v are the opening and closing transition rates of gate v, typically defined by exponential functions of V_m. Thus, variations in V_m along the AP selectively and progressively modify ion permeability, which modulates I_{ion} and this, in turn, closes the loop by altering V_m. Thereby, by appropriately combining multiple gating variables with specific kinetics, Hodgkin–Huxley models can accurately replicate the biophysical behavior of various ion channels.

3. Markov models, which generalize Hodgkin–Huxley schemes by explicitly modeling multiple states and transitions, enabling the representation of channel kinetics such as state-dependent drug binding. Although biophysically richer because they can represent more complex scenarios in which the transitions from one state to another depend on the current state of the ionic channel, they significantly increase computational cost and often require parameters that cannot be fully constrained experimentally [13, 103]. More information on Markov models can be found in [13].

In addition to gating dynamics, ionic concentrations themselves evolve as a function of ionic fluxes, typically described by ODEs of the form:

$$\frac{dZ_j}{dt} = f_j(I_j; V_m; Z_j), \tag{1.20}$$

where Z_j denotes the intracellular or extracellular concentration of ion j [104].

The Hodgkin–Huxley framework and its derivatives form the mathematical foundation for the cellular electrophysiological models employed in this thesis. Also known as ionic cellular models, they follow a biophysically detailed definition of the AP, leading to highly detailed mechanistic models. Simpler phenomenological formulations also exist, which focus on macroscopically reproducing AP morphology and duration without explicitly resolving ionic detail [105]. Phenomenological models can be used to investigate phenomena such

as spiral wave dynamics, but are limited in their ability to capture disease- or drug-related effects and are therefore not considered in this thesis [13].

1.6.2.3 Models of ventricular cells

Following the Hodgkin–Huxley paradigm, several ventricular models were developed, initially based on animal data owing to the scarcity of human recordings. The first human ventricular CM model was introduced in 1998 by Priebe and Beuckelmann, who adapted the guinea pig model of Luo-Rudy to human data, particularly focusing on Ca^{2+} transients from CMs of patients with HF [103].

Subsequent developments in the early 2000s included the Iyer et al. [106] and ten Tusscher et al. [107] models, which incorporated frequency-dependent APD variations, Ca^{2+} dynamics, and transmural repolarization heterogeneities, successfully reproducing spiral wave behavior in 2D tissue simulations [13,103].

A major advance came with the O'Hara-Virág-Varró-Rudy model in 2011, which integrated extensive human experimental data, involving biophysical details of I_{CaL}, I_{to}, I_{Kr}, I_{NaCa}, and I_{K1}, AP and APD characteristics at physiological cycle lengths, and transmural gradients of genetic and protein human data. This model, defined for subendocardial, subepicardial and midmyocardial cells, reproduces transmural AP morphology, rate-dependent APD, Ca^{2+} cycling, and intracellular Na^{+} dynamics, while also capturing pathological behaviors such as early afterdepolarizations and AP and Ca^{2+} alternans [13,51]. The O'Hara et al. [51] model has since become the reference standard for simulating human ventricular electrophysiology [13,103].

More recently, Gaur et al. [16] presented the first porcine ventricular model, based on the O'Hara et al. model [51] but calibrated with species-specific data. This model reproduces porcine ionic currents, Ca^{2+} handling, AP morphology, APD restitution, and arrhythmic behaviors such as alternans. It incorporates fast and slow Ca^{2+} release from T-tubular and non-T-tubular subcellular regions, respectively, thereby replicating porcine Ca^{2+} transients. When compared with the human model of O'Hara et al. [51], the authors found that early afterdepolarizations are predominantly influenced by I_{K1} in pigs and I_{Kr} in humans. They also showed that rapid pacing triggers arrhythmicity in the human CM, whereas the porcine model remained stable under the same conditions [16]. Prior to this, swine studies were conducted *in silico* using other ventricular models, such as the ten Tusscher et al. [52] model, with ionic currents adjusted to approximate porcine AP characteristics [15]. In contrast, the Gaur et al. [16] ionic model provides a more accurate description of porcine cellular

electrophysiology, enabling computational investigation of complex phenomena, including arrhythmicity, in preclinical settings.

1.6.2.4 Models of Purkinje cells

Purkinje cells exhibit distinct electrophysiological features, including faster AP upstroke velocity, more negative plateau potentials due to reduced I_{CaL}, and longer APD relative to ventricular CMs owing to slow inactivation of I_{Na}. Their sparse T-tubule network also produces spatial heterogeneity in intracellular Ca^{2+} handling [13, 108].

The first Purkinje cell model was developed by Denis Noble in 1962, adapting the Hodgkin–Huxley framework to reproduce K^+ currents and pacemaking behavior. However, this model lacked the representation of I_{CaL} and late Na^+, which were discovered a decade later [103]. Later refinements introduced Ca^{2+} kinetics and the pacemaker inward, hyperpolarization-activated funny current (I_f) [13, 103].

In 2009, Stewart et al. [108] published a human Purkinje model based on experimental data from the human failing myocardium and extensions of the ten Tusscher et al. [52] ventricular model. Key features included I_f and a sustained K^+ current (I_{sus}). The formulation of I_{sus} was similar to that of I_{to}, but it lacked inactivation [103]. To account for HF-related alterations observed in their experimental data, the authors adjusted I_{to} and I_{K1}, which led to the emergence of a more pronounced phase-1 repolarization while leaving resting potential, AP amplitude, and APD unchanged [108]. As a result, the model successfully reproduced AP morphology, characterized by this distinct phase-1 repolarization, along with I_f-mediated automaticity, all-or-nothing repolarization, and overdrive suppression [108].

More recently, Trovato et al. [109] developed a human Purkinje cellular model based on undiseased human data, including detailed Ca^{2+} handling, lower density of T tubules, and Purkinje-specific ion currents [13,103,109]. The model reproduces AP morphology, CV (160 cm/s), I_f-related automaticity, and arrhythmic behaviors such as early and delayed afterdepolarizations [109].

1.6.2.5 Models of hiPSC-CMs

The advent of hiPSC-CMs has opened opportunities in disease modeling, drug screening, tissue engineering, and personalized medicine (see Section 1.4.4). However, hiPSC-CMs retain a fetal-like phenotype characterized by spontaneous automaticity, immature Ca^{2+} handling, and prolonged APs.

The first ionic models for hiPSC-CMs were introduced by Paci et al. in 2013 [110], representing atrial- and ventricular-like cells. These models integrated human and guinea pig ionic formulations, calibrated with experimental data of hiPSC-CMs. They reproduced baseline APs, automaticity (due to an interplay of I_{Na}, I_f, and I_{K1}), and responses to pharmacological blockade [110].

Subsequent refinements improved intracellular Na^+ and Ca^{2+} dynamics and incorporated inter-cellular variability by integrating diverse datasets [13, 103, 111, 112, 112]. In 2020, Paci et al. [110] updated their model to the Paci2020 model [113], which included enhanced I_{Na} and I_f kinetics, with optimized values of model parameters fitted against experimental *in vitro* data of the AP and Ca^{2+} transients. This version identified an essential role for the Na^+/Ca^{2+} exchanger in spontaneous activity, consistent with experimental findings [113].

1.6.3 Computational approaches to tissue- and organ-scale simulations

Numerical methods are required to solve the coupled systems of PDEs and ODEs arising from the monodomain and bidomain formulations (see Sections 1.6.1 and 1.6.2). This section reviews the most common approaches used in cardiac electrophysiology simulation, including operator splitting schemes, time and space discretization strategies, and linear solvers.

1.6.3.1 Numerical methods for reaction-diffusion systems

The bidomain equations form a system of elliptic-parabolic PDEs and ODEs, while the monodomain model reduces this to a parabolic PDE coupled to ODEs. To facilitate numerical solution, operator splitting techniques are frequently applied to decouple reaction (ionic currents) and diffusion (electrical propagation) terms [99,101]. This strategy, introduced by Qu and Garfinkel in 1999 [104], allows each subsystem to be solved sequentially, improving computational efficiency.

For the monodomain equation, this decouples Equation 1.21 of diffusion and Equations 1.22-1.24 for reaction, yielding:

$$\frac{\partial V_m}{\partial t} = \frac{1}{\beta C_m} \nabla \cdot (\boldsymbol{\sigma_m} \nabla V_m), \tag{1.21}$$

$$\frac{dV_m}{dt} = -\frac{1}{C_m}(I_{ion} + I_s), \tag{1.22}$$

$$\frac{dv}{dt} = \alpha_v(1 - v) - \beta_v v, \tag{1.23}$$

$$\frac{dZ_j}{dt} = f_j(I_j; V_m; Z_j), \tag{1.24}$$

A typical splitting scheme, widely implemented in previous studies [104, 114, 115], proceeds as follows:

- Step 1: The diffusion term 1.21 is solved for a $\Delta t/2$ time step, with V_m and all state variables initialized to their values at time t.
- Step 2: Using the results of Step 1 as the initial condition, the reaction system 1.22-1.24 is solved for a full Δt step.
- Step 3: The results of Step 2 are then used as the initial condition, and the diffusion term 1.21 is solved again for a $\Delta t/2$ step.

Here, Δt denotes the chosen finite integration step. Therefore, this procedure yields the solution at $t + \Delta t$. Notably, Step 1 needs to be computed only in the first simulation iteration; afterwards, it can be merged with Step 3 by solving Step 3 for a full Δt step [104].

Regardless of whether operator splitting is applied, the monodomain and bidomain equations are highly complex and lack analytical solutions. Therefore, numerical approximations are required. This is achieved by applying temporal and spatial discretizations to approximate the derivatives in time of the reaction term and the derivatives in both time and space of the diffusion term [101, 104].

1.6.3.2 Temporal integration

Time discretization schemes can be explicit or implicit. In the forward (explicit) Euler method, the new solution depends only on the current value:

$$V_m^{t+\Delta t} = V_m^t + \Delta t \frac{dV_m^t}{dt}, \tag{1.25}$$

where $\frac{dV_m}{dt}$ is obtained by finding I_{ion} in Equation 1.22.

In contrast, implicit methods incorporate dependence on the future state, e.g., backward Euler:

$$V_m^{t+\Delta t} = V_m^t + \Delta t \frac{dV_m^{t+\Delta t}}{dt}. \tag{1.26}$$

A generalized scheme is given by [101]:

$$V_m^{t+\Delta t} = V_m^t + \Delta t[(1-\theta)\frac{dV_m^t}{dt} + \theta\frac{dV_m^{t+\Delta t}}{dt}] \tag{1.27}$$

where $\theta \in [0, 1]$ defines the method [114]:

- $\theta = 0$ Forward Euler (explicit, conditionally stable)
- $\theta = 0.5$ Crank-Nicolson (unconditionally stable)
- $\theta = 1$ Backward Euler (implicit, unconditionally stable)

Explicit methods are simple but require small Δt for stability, while implicit methods are more robust but computationally more demanding. In general, the above methods with $\theta >= 0.5$ are unconditionally stable but computationally more expensive than the explicit method. The Crank-Nicolson method has second-order accuracy, while forward and backward Euler methods have first-order accuracy [99, 114].

The major computational bottleneck arises from solving the ODEs for gating variables. These can be efficiently integrated using the Rush-Larsen method [116], which provides an analytical solution under the assumption of constant transition rates during Δt. By applying this approach, Equation 1.19 can be rewritten as:

$$\frac{dv}{dt} = \alpha_v - v(\alpha_v + \beta_v), \tag{1.28}$$

which takes the form of the system $\frac{dy}{dt} = -\frac{y-y_\infty}{\tau}$. In this representation, τ is the system's time constant, determining how quickly y converges to its equilibrium value y_∞. For the gating variable ODE, the time constant is given by $\tau = \frac{1}{\alpha_v+\beta_v}$. The equilibrium value y_∞ corresponds to the steady-state solution, i.e., the value of y when $\frac{dy}{dt} = 0$.

In the case of a gating variable, substituting into 1.19 yields $\alpha_v - v_\infty(\alpha_v + \beta_v) = 0$, which simplifies to $v_\infty = \frac{\alpha_v}{\alpha_v+\beta_v}$. If α_v and β_v vary slowly or can be treated as constant over the time step Δt, then Equation 1.19 admits the closed-form solution [104, 116]:

$$v_{t+\Delta t} = v_\infty - (v_\infty - v_t)e^{-\frac{\Delta t}{\tau}}. \tag{1.29}$$

Adaptive time stepping is also widely employed, allowing smaller time steps during the rapid upstroke of the AP and larger steps during plateau and repolarization, thereby balancing accuracy and computational cost [101, 104]. The

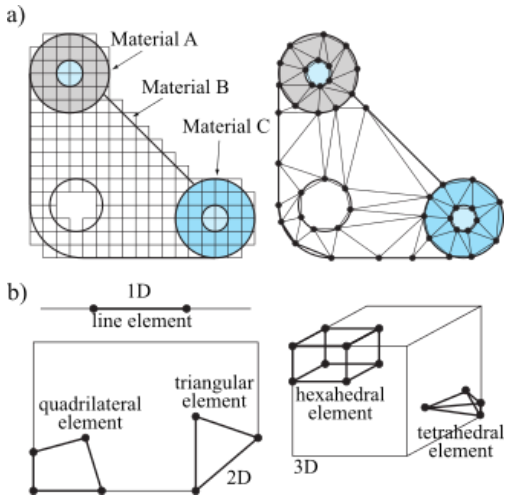


Figure 1.27: Spatial discretization of the domain of integration. a- A 2D domain with complex geometry and non-homogeneous composition discretized with a structured, regular (left) and unstructured (right) grids which are generally used for solving the FDM and the FEM, respectively. b- Elements used for the multi-dimensional discretization in the FEM and FDM. Lines, squares and hexahedrons are commonly used in FDM, while lines, triangles and tetrahedrons are normally employed in FEM. Image created from images in [117].

use of the operator splitting technique enables the reaction term to be integrated separately, thereby allowing the use of a distinct time integration scheme for its solution. The integration step is defined as $\Delta t = \Delta T/k$ with $k = 1, ..., K$ and both k and K are integers chosen to synchronize the evaluation of the reaction term with the diffusion term, which advances using steps of size ΔT. The parameter k is dynamically adjusted during integration according to the time derivative of V_m: when the derivative is small, k tends towards 1, while larger derivatives drive k toward K. In this way, the rapid upstroke of the AP is resolved with smaller Δt, avoiding divergence, whereas the slower phases (2, 3, and 4) are integrated with larger Δt, improving efficiency [101, 104]. It is important to note, however, that an excessively large ΔT results in higher per-iteration error, even if convergence is ensured.

1.6.3.3 Spatial integration and boundary conditions

Spatial integration is typically performed using either the finite difference method (FDM) or finite element method (FEM).

FDM: It is characterized by its simplicity and straightforward implementation. At the same time, its formulation makes it highly parallelizable compared to other approaches. In this method, spatial derivatives are replaced with finite difference approximations, transforming the original PDE-based problem into an algebraic one. These difference-based approximations can be derived from interpolation or Taylor series expansions. Several schemes are commonly used, such as central, forward, and backward differences, each associated with a characteristic error. For example, the central difference scheme for the approximation of the first and second derivatives provides second-order accuracy [99, 101, 117]:

$$\frac{\partial V}{\partial x} = \frac{V_{i+1} - V_{i-1}}{2\Delta x} \tag{1.30}$$

$$\frac{\partial^2 V}{\partial x} = \frac{V_{i+1} - 2V_i + V_{i-1}}{\Delta x^2} \tag{1.31}$$

where V_i is the value of the unknown variable at the i^{th} node. The domain of integration is typically discretized using a uniform (regularly spaced) grid with spacing Δx. However, the restriction to structured grids makes it difficult to accurately represent curved or irregular domains (see Figure 1.27a, left).

As a simple case, consider the monodomain model in a one-dimensional (1D) domain discretized into N nodes along the x-axis and with length L. By setting $V_m = V$, $\sigma_m = \sigma$, and $I_s = 0$, the monodomain model (Equations 1.13-1.15) reduces to:

$$\frac{dV}{dt} = \frac{\sigma}{\beta C_m}\frac{\partial^2 V}{\partial x^2} - \frac{1}{C_m} I_{ion}(V), \quad \text{when} \quad 0 < x < L, t > 0 \tag{1.32}$$

$$V(x, 0) = f(x), \quad \text{when} \quad 0 < x < L, t = 0 \tag{1.33}$$

$$\frac{\partial V}{\partial x} = 0, \quad \text{when} \quad x = 0, x = L, t \geqslant 0 \tag{1.34}$$

where σ is a scalar representing the conductivity along the fiber, and f specifies the initial condition for V, often chosen as the uniform resting potential of the cellular model.

Discretizing in time using an explicit scheme and in space using central differences at an interior node i gives:

$$\frac{V_i^{t+\Delta t} - V_i^t}{\Delta t} = \frac{\sigma}{\beta C_m}\frac{V_{i+1}^t - 2V_i^t + V_{i-1}^t}{\Delta x^2} - \frac{1}{C_m} I_{ion}(V_i^t), \tag{1.35}$$

Alternatively, defining the spatial derivative in terms of the future values using an implicit scheme leads to:

$$\frac{V_i^{t+\Delta t} - V_i^t}{\Delta t} = \frac{\sigma}{\beta C_m} \frac{V_{i+1}^{t+\Delta t} - 2V_i^{t+\Delta t} + V_{i-1}^{t+\Delta t}}{\Delta x^2} - \frac{1}{C_m} I_{ion}(V_i^t), \tag{1.36}$$

Equation 1.35 can be solved independently for each node ($V_i^{t+\Delta t}$ is the only unknown), making it highly parallel. In contrast, Equation 1.36 introduces coupling between neighboring nodes (3 unknowns), requiring the assembly and solution of a global algebraic system of N equations with N unknowns.

The treatment of Neumann boundary conditions is less straightforward in FDM. For example, at $x = 0$:

$$\frac{\partial V}{\partial x} = \frac{V_{i+1} - V_{i-1}}{2\Delta x} = 0 \Rightarrow V_{i+1} = V_{i-1} \tag{1.37}$$

Substituting this relation modifies the explicit nodal Equation 1.35 at $x = 0$ to:

$$\frac{V_i^{t+\Delta t} - V_i^t}{\Delta t} = \frac{\sigma}{\beta C_m} \frac{2V_{i+1}^t - 2V_i^t}{\Delta x^2} - \frac{1}{C_m} I_{ion}(V_i^t), \tag{1.38}$$

This can be interpreted as introducing a ghost node outside the domain, with its value set equal to that of the adjacent interior node. While effective in simple 1D isotropic cases, this treatment becomes cumbersome in multidimensional domains with anisotropy, as often encountered in cardiac electrophysiology [101, 117].

FEM: It addresses several limitations of the FDM. It allows accurate representation of complex geometries (see Figure 1.27a, right) and incorporates boundary conditions naturally into the formulation. This comes, however, at the expense of a more complex implementation and a denser algebraic system.

In this approach, the solution domain is divided into smaller elements: lines in 1D, triangles in 2D, and tetrahedra or hexahedra in 3D (see Figure 1.27b). Within each element, the unknown variable is approximated by an interpolation function, typically polynomial. These local solutions are assembled into a global solution, ensuring continuity across the boundaries between elements.

For the 1D case, the approximation is assumed to be linear:

$$V(x) = a + bx \tag{1.39}$$

with coefficients determined by the nodal values V_{x_1} and V_{x_2} at the element endpoints:

$$V(x_1) = V_{x_1} = a + bx_1 \tag{1.40}$$

$$V(x_2) = V_{x_2} = a + bx_2 \tag{1.41}$$

which is a system of 2 equations with 2 unknowns. Solving to calculate the values of a and b gives:

$$a = \frac{V_{x_1}x_2 - V_{x_2}x_1}{x_2 - x_1} \tag{1.42}$$

$$b = \frac{V_{x_2} - V_{x_1}}{x_2 - x_1} \tag{1.43}$$

Replacing a and b in the initial Equation 1.39 leads to:

$$V(x) = N_1(x)V_{x_1} + N_2(x)V_{x_2}, \tag{1.44}$$

$$N_1(x) = \frac{x_2 - x}{x_2 - x_1}, \tag{1.45}$$

$$N_2(x) = \frac{x - x_1}{x_2 - x_1}, \tag{1.46}$$

where N_1 and N_2 are interpolation functions [117]. They satisfy the partition of unity and ensure that the approximation matches the nodal values exactly [101].

Substituting the approximate solution $V(x) = V^*$ into the monodomain equation 1.32 yields a residual R equal to:

$$\frac{dV^*}{dt} - \frac{\sigma}{\beta C_m}\frac{\partial^2 V^*}{\partial x^2} + \frac{1}{C_m}I_{ion}(V) = R \tag{1.47}$$

In the Galerkin formulation, weighting functions are used, and the residual is minimized by enforcing:

$$\int_{\Omega^e} R w_i^e dx = 0, \quad i = 1, ..., n^e \tag{1.48}$$

where Ω^e is the domain of the element, w_i^e is the weighting function for node i in element e, and n^e is the total number of nodes per element. In the 1D case, this equation can be written for a line element as:

$$\int_{\Omega^e} w_i^e \left(\frac{dV^*}{dt} - \frac{\sigma}{\beta C_m}\frac{\partial^2 V^*}{\partial x^2} + \frac{1}{C_m}I_{ion}(V) \right) dx = 0, \quad i = 1, 2 \tag{1.49}$$

The nodal weighting functions are often selected to be equal to the interpolation function. Replacing these functions and reordering yields:

$$\frac{\sigma}{\beta C_m}\int_{\Omega^e} N_i^e \frac{\partial^2 V^*}{\partial x^2} dx = \int_{\Omega^e} N_i^e \left(\frac{dV^*}{dt} + \frac{I_{ion}(V)}{C_m}\right) dx \quad i = 1, 2 \tag{1.50}$$

Integrating by parts, the integral on the left-hand side results in:

$$\int_{\Omega^e} N_i^e \frac{\partial^2 V^*}{\partial x^2} dx = N_i^e \left.\frac{\partial V^*}{\partial x}\right|_{x_1}^{x_2} - \int_{x_1}^{x_2} \frac{\partial V^*}{\partial x}\frac{\partial N_i^e}{\partial x} dx \quad i = 1, 2 \tag{1.51}$$

Replacing the above expressions into Equation 1.50 results in the weak form formulation, which reduces the order of the derivatives and automatically introduces boundary terms. Defining $f(x,t) = \frac{dV^*}{dt} + \frac{I_{ion}(V)}{C_m}$ and reordering, the equation for node 1 becomes:

$$-\frac{\sigma}{\beta C_m}\int_{x_1}^{x_2} \frac{\partial V^*}{\partial x}\frac{\partial N_1^e}{\partial x} dx = \frac{\sigma}{\beta C_m}\frac{\partial V^*(x_1)}{\partial x} + \int_{x_1}^{x_2} N_1^e f(x,t) dx, \quad i = 1 \tag{1.52}$$

Here, the left-hand side describes diffusion within the element, while the right-hand side includes two components: the first accounts for a boundary condition specific to the element, while the second reflects the forcing function of the system, involving the variation of the potential in time and the density of the ionic current [117]. For an element in the boundary, the first term of the right-hand side can be trivially made zero for the zero-flux Neumann boundary condition to be satisfied [117]. The corresponding equation for $i = 2$ can be derived in an analogous manner.

Defining $D = \frac{\sigma}{\beta}$ and multiplying both sides of Equation 1.52 by C_m gives:

$$\int_{x_1}^{x_2} N_1^e \left(C_m \frac{dV^*}{dt} + I_{ion}(V)\right) dx + \int_{x_1}^{x_2} D\frac{\partial V^*}{\partial x}\frac{\partial N_1^e}{\partial x} dx + D\frac{\partial V^*(x_1)}{\partial x} = 0, \quad i = 1 \tag{1.53}$$

Expanding the approximation as $V^*(x,t) = \sum_{i=1}^{n^e} N_i^e(x) V_i^e(t)$ allows the integrals to be discretized, yielding the elemental system in matrix form for element e:

$$\boldsymbol{M}^e \dot{\boldsymbol{V}}^e + \boldsymbol{K}^e \boldsymbol{V}^e = \boldsymbol{Q}^e \tag{1.54}$$

where:

$$\boldsymbol{M}^e, \quad \text{with } M_{ij}^e = \int_{\Omega^e} C_m \, N_i^e \, N_j^e \, dx, \tag{1.55}$$

$$\boldsymbol{K}^e, \quad \text{with } K_{ij}^e = \int_{\Omega^e} D \frac{\partial N_i^e}{\partial x} \frac{\partial N_j^e}{\partial x} dx, \tag{1.56}$$

$$\boldsymbol{Q}^e, \quad \text{with } Q_i^e = \int_{\Omega^e} N_i^e I_{ion} \, dx. \tag{1.57}$$

Assembling the elemental systems produces the global system:

$$\boldsymbol{M}\dot{\boldsymbol{V}} + \boldsymbol{K}\boldsymbol{V} = \boldsymbol{Q} \tag{1.58}$$

Interior boundary terms cancel during assembly, while Neumann boundary conditions are enforced automatically by not including into the discretization the elemental boundary condition term of Equation 1.53 [101, 117]. This natural treatment of boundary conditions, combined with the ability to represent curved or irregular domains, is a major advantage of FEM. However, compared with the algebraic systems generated by FDM, those from FEM typically have larger bandwidth and poorer conditioning, leading to higher computational cost for the same number of degrees of freedom [101].

1.6.3.4 Direct and iterative solution strategies

After the discretization of the monodomain model, using either FDM or FEM, the result is typically a system of N equations with N unknowns, where N denotes the total number of nodes in the domain. At each time step, this linear system, expressed as $\boldsymbol{A}\{\boldsymbol{x}\} = \{\boldsymbol{b}\}$, must be solved. The coefficient matrix $\boldsymbol{A}$ is usually sparse and has dimensions $N \times N$ [99]. To address this problem, two main categories of solvers are employed: direct and iterative methods.

Direct solvers: They explicitly manipulate the system matrix to compute the exact solution [99]. Their logic can be illustrated with a simple system of two equations in two unknowns: one equation is rearranged to isolate a variable, which is then substituted into the other equation to eliminate one unknown. This produces a single equation with one unknown that can be solved directly, after which the result is back substituted to obtain the remaining variable. Direct solvers extend this principle to large and complex systems [117].

The most common direct method is Gaussian Elimination, which sequentially eliminates unknowns and then applies back substitution to recover the full solution. Other popular approaches include Lower-Upper, or LU, and Cholesky decompositions. LU factorization expresses the matrix as a product

of a lower and an upper triangular matrices and is applicable to both symmetric and asymmetric systems, while Cholesky decomposition is optimized for symmetric positive-definite matrices.

The main advantage of direct methods lies in their efficiency [99]. Although the matrix factorization step is computationally demanding, it is performed only once and reused across the many thousands of time steps in a typical simulation. However, their chief limitation is memory consumption, since storing the matrix, even in sparse form, can become prohibitive. Memory requirements depend heavily on the matrix bandwidth, which in turn is influenced by node connectivity. Reordering algorithms that renumber the nodes, such as the Reverse Cuthill-McKee method [99, 117], are therefore often applied to reduce bandwidth. With modern high-resolution meshes and complex ionic models involving many state variables, however, memory demands remain a major bottleneck [101, 117].

Iterative solvers: They begin with an initial guess and use algorithms to refine it step by step until the error falls below a prescribed tolerance [117]. These methods are typically more memory-efficient than direct solvers, but are not guaranteed to converge. When they converge, performance can deteriorate if the system matrix is ill-conditioned [101], that is, when small changes in the coefficients cause large variations in the solution.

A classical example of an iterative method is the Gauss-Seidel method, which starts with an initial guess (often zero) and updates each unknown sequentially using the latest updated values as soon as they are computed. This process is repeated until the difference between successive approximations falls below a set tolerance [117]. Another widely used approach is the conjugate gradient method, which reformulates the linear system of equations as an optimization problem. Its performance is often enhanced through preconditioning, which transforms the system into one with a more favorable structure, effectively making the optimization search space closer to a paraboloid, thereby accelerating convergence [99, 117].

In practice, the choice of the solver has a strong influence on both computational cost and memory usage. Owing to their reduced memory footprint and scalability, iterative solvers are currently more common in cardiac electrophysiology simulations.

1.6.3.5 Structural and functional considerations at the organ scale

A number of challenges arise when modeling cardiac electrophysiology at the organ level. These include defining the orientation of the CMs, reconstructing the CS, and establishing transmural and apico-basal segmentations to capture spatial heterogeneities. [47, 118, 119].

Modeling CM orientation: As introduced in Section 1.2.2, the myocardium consists of fibers organized in a highly anisotropic structure, in association with connexin distribution, with the greatest conductivity found along the longitudinal direction of the fibers. Correctly representing this anisotropy is essential for accurately simulating wave propagation [120]. Most cardiac models therefore employ an orthotropic conductivity tensor with transverse isotropy [10,15], defined locally and often expressed as:

$$\boldsymbol{\sigma}_f = \sigma_0 \begin{pmatrix} 1 & 0 & 0 \\ 0 & r & 0 \\ 0 & 0 & r \end{pmatrix} \tag{1.59}$$

where σ_0 is the conductivity along the fiber direction and $r \in [0, 1]$ is the transverse-to-longitudinal conductivity ratio. In Cartesian coordinates, the conductivity tensor ($\boldsymbol{\sigma_m} = \boldsymbol{\sigma}$) in the monodomain model (see Equation 1.13) at a given point of the domain becomes:

$$\boldsymbol{\sigma} = \sigma_0[(1-r)\boldsymbol{f} \otimes \boldsymbol{f} + r\boldsymbol{I}] \tag{1.60}$$

with $\boldsymbol{f} = [f_x, f_y, f_z]$ the fiber direction vector, $\boldsymbol{I}$ the second-order identity tensor, and $\otimes$ the tensor product. This expression can be written as:

$$\boldsymbol{\sigma} = \sigma_0(1-r) \begin{pmatrix} f_x f_x & f_x f_y & f_x f_z \\ f_y f_x & f_y f_y & f_y f_z \\ f_z f_x & f_z f_y & f_z f_z \end{pmatrix} + \sigma_0 r \begin{pmatrix} 1 & 0 & 0 \\ 0 & 1 & 0 \\ 0 & 0 & 1 \end{pmatrix} \tag{1.61}$$

To compute this tensor $\boldsymbol{\sigma}$ across the myocardium, a fiber orientation vector must be assigned to each node of the domain. The macroscopic structure of the myocardium as formed by layers containing CM fibers of different lengths that transmurally change direction was described in Section 1.2.2. Experimentally, LeGrice et al. [121] showed that ventricular tissue is arranged in laminar sheets of CMs with three main symmetry axes: longitudinal (parallel to the long axis of CMs), transverse (within the sheet plane but perpendicular to the longitudinal axis), and sheet-normal (normal to the sheet plane) [28, 122]. As

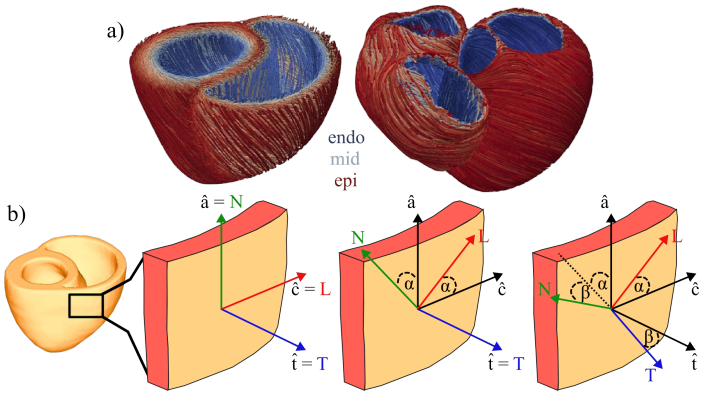


Figure 1.28: RBM-based CM fiber field. a- *In silico* RBM-based CM fiber field depicting the longitudinal to the CM fiber direction with (left) and without (right) outflow tracts. b- Local coordinate system and sequential rotation (from left-to-right) of the orthonormal vector system by following the α and β angles for defining the CM fiber field. â: apico-basal versor, ĉ: circumferential versor, t̂: transmural versor, L: longitudinal to the CM fiber versor, T: transverse versor, and N: sheet normal versor. Image created from images in [122] and [28].

presented in Section 1.3.1.2, these can be obtained with DW-CMR although *in vivo* acquisitions are noisy and require long acquisition times, while *ex vivo* scans are affected by tissue deformation [47].

A practical alternative is the use of rule-based models (RBMs), such as those proposed by Bayer et al. [122] and extended by Doste et al. [28] to include the outflow tracts (see Figure 1.28a). RBM approaches apply experimentally derived constraints and rules, expressed mathematically, to assign region-specific CM orientations within the myocardium. RBMs define the local coordinate system (circumferential, apico-basal, and transmural directions), depicted in Figure 1.28b, and prescribe fiber orientation via angle rules. The α angle describes rotation with respect to the clockwise circumferential direction computed for the heart seen in the apico-basal direction, while the β angle describes rotation of the outward transmural direction (Figure 1.28b). Both angles are defined in the RV, LV and septal endocardium and epicardium. According to well-established observations, the α angle rotates transmurally from $+60^{\circ}$ at the endocardium to -60° at the epicardium [47]. Most RBMs assume a transmural linear variation of the α angle, but others describe this variation as necessarily nonlinear [123]. These rules provide a straightforward way to assign consistent fiber fields to any BiV geometry.

CS: It orchestrates ventricular activation, driving coordinated mechanical contraction. Some studies bypass explicit CS modeling, instead applying stimuli at early-activated sites observed experimentally and assigning higher endocardial conductivity to mimic physiological activation [98, 101, 124]. While such simplifications can reproduce the morphology of the QRS complex, they are inadequate to simulate CS-mediated arrhythmias or conduction disorders, where an explicit CS representation is essential.

Histological studies beginning with Tawara over a century ago [125] provide the anatomical foundation for CS models. Building on this knowledge, different computational architectures have been proposed, most of them based on reported histological images or designed to reproduce physiological and pathological ventricular excitation, ECG patterns, retrograde conduction, and life-threatening arrhythmias [126–130].

A widely used strategy relies on manually identifying key anatomical landmarks, as outlined in Section 1.2.3.2. Once the His bundle is reconstructed, Purkinje fibers are typically generated throughout the myocardium using fractal or iterative growth algorithms. These algorithms expand the network step by step, introducing Y-like, L-system-based bifurcations from terminal branches to create tree-like structures (see Figure 1.29) [118, 129, 131]. In this thesis, the fractal algorithm developed by Sahli-Costabal et al. [118] was employed to generate a 2D fractal Purkinje network. As illustrated in Figure 1.29, the algorithm begins with an initial node and direction of growth. From the terminal point of this first branch, two new branches are created, and the process is repeated iteratively. Each branch is represented as a polyline of segments connected by nodes, where mutual repulsion between nodes induces curvature in the branches [118, 131].

The orientation of each new segment is determined by the direction of the preceding segment combined with the gradient of the distance to all existing nodes, as shown in Figure 1.29. Once this projection direction is calculated, the segment is extended with a length defined by dividing the total branch length by the number of branch segments. This mechanism produces naturally curved branches. User-defined parameters, such as branch length and repulsion strength, control the final shape of the network: higher repulsion values yield stronger curvature. Collisions are handled by checking whether a newly projected node falls close to an existing branch. In such cases, the algorithm either forms a loop or terminates the branch by dismissing the colliding node [118, 131]. If the network is first generated in a plane rather than directly in situ, the resulting structure can be projected onto the endocardial surface [118, 129, 131].

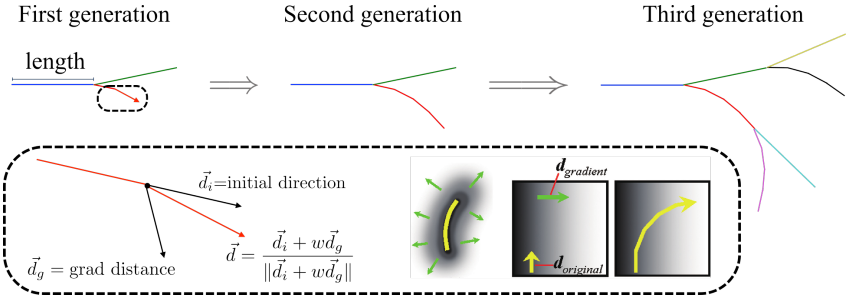


Figure 1.29: Fractal algorithm for Purkinje tree generation. Here, d is the direction of extension of the growing branch and w is an user-defined scalar value, termed repulsion, which defines the degree of curvature of the branch. Image created from images in [118] and [131].

Another critical aspect of CS modeling is reproducing realistic PMJ behavior, which plays a key role in retrograde activation and can give rise to bundle branch reentrant VTs [36, 128, 132]. To address the conductivity mismatch between the rapidly conducting Purkinje fibers and the slower myocardium (see Section 1.2.3.2), an intermediate adaptation region can be introduced, as in [128]. In this region, located along the Purkinje endbranches, conductivity is gradually reduced using a sigmoid-based function:

$$\sigma_{eb}(x) = \sigma_{CM} + \frac{\sigma_P - \sigma_{CM}}{1 + e^{k(x-\bar{x})}} \tag{1.62}$$

where x is the distance of a node in the endbranch to the end of the endbranch, $\bar{x}$ is the distance between the center of the endbranch to the end of the endbranch, k is a parameter defining the smoothness of the sigmoid function, σ_{eb} is the longitudinal conductivity of the endbranch, and σ_{CM} and σ_P are the longitudinal conductivities of the CM and the Purkinje fibers, respectively. This formulation ensures a smooth transition from high conductivity at the proximal end of the Purkinje endbranch to low conductivity at the distal end, thereby modeling the PMJ while avoiding abrupt changes in conduction.

Transmural and apico-basal segmentation: Heterogeneities across the ventricular wall have been extensively described in myocardial tissue, especially in humans, particularly between the endocardium, mid-myocardium, and epicardium. These transmural differences underlie key electrophysiological features, such as the spatial variation of the APD, which in turn shapes T-wave morphology in the ECG, a marker routinely used in the diagnosis of multiple cardiac conditions [119, 133].

To reproduce these features *in silico*, transmural and apico-basal segmentations can be defined using a Laplace-based diffusion analysis [119]. For the transmural case, a diffusion problem is solved between the endocardial and epicardial surfaces, since ventricular thickness is non-uniform. Specifically, a Laplace equation is integrated over the BiV domain Ω with Dirichlet boundary conditions at the endocardial (Γ_{endo}) and epicardial (Γ_{epi}) surfaces, and a zero-flux Neumann condition at the base (Γ_{base}). This diffusion equation is then solved in three configurations:

$$
\begin{aligned}
\phi_1(\boldsymbol{x}) = \phi(\boldsymbol{x}) \quad \text{such that} \quad & \begin{cases} \nabla^2\phi = 0 & \text{in } \Omega, \\ \boldsymbol{n}\cdot\nabla\phi = 0 & \text{on } \Gamma_{\text{base}}, \\ \phi = \phi_0 & \text{on } \Gamma_{\text{endo}}, \\ \phi = \phi_1 & \text{on } \Gamma_{\text{epi}}, \end{cases} \\
\phi_2(\boldsymbol{x}) = \phi(\boldsymbol{x}) \quad \text{such that} \quad & \begin{cases} \nabla^2\phi = 0 & \text{in } \Omega, \\ \boldsymbol{n}\cdot\nabla\phi = 0 & \text{on } \Gamma_{\text{base}}, \\ \phi = \phi_0 & \text{on } \Gamma_{\text{endo RV}}, \\ \phi = \phi_1 & \text{on } \Gamma_{\text{epi}} \cup \Gamma_{\text{endo LV}}, \end{cases} \\
\phi_3(\boldsymbol{x}) = \phi(\boldsymbol{x}) \quad \text{such that} \quad & \begin{cases} \nabla^2\phi = 0 & \text{in } \Omega, \\ \boldsymbol{n}\cdot\nabla\phi = 0 & \text{on } \Gamma_{\text{base}}, \\ \phi = \phi_0 & \text{on } \Gamma_{\text{endo LV}}, \\ \phi = \phi_1 & \text{on } \Gamma_{\text{epi}} \cup \Gamma_{\text{endo RV}}, \end{cases}
\end{aligned}
\tag{1.63}
$$

where ϕ_0 and ϕ_1 are the boundary conditions. Figure 1.30a shows the corresponding solutions for the three diffusion problems. Next, two threshold values representing the mid-endo ($\phi_$) and mid-epi (ϕ_+) diffusion limits are set to define three discrete regions, Ω^-, Ω^+, and $\Omega^{-/+}$, for each diffusion case ϕ_1, ϕ_2, and ϕ_3:

$$
\begin{aligned}
\Omega_i^- &= \{\boldsymbol{x} \in \Omega \mid \phi_i(\boldsymbol{x}) < \phi_\}, \\
\Omega_i^+ &= \{\boldsymbol{x} \in \Omega \mid \phi_i(\boldsymbol{x}) > \phi_+\}, \quad \text{with} \quad i = 1,2,3 \\
\Omega_i^{-/+} &= \{\boldsymbol{x} \in \Omega \mid \phi_ < \phi_i(\boldsymbol{x}) < \phi_+\},
\end{aligned}
\tag{1.64}
$$

Figure 1.30b, illustrates the resulting three-region partition for each diffusion case. The endocardial, mid-myocardial, and epicardial regions are then

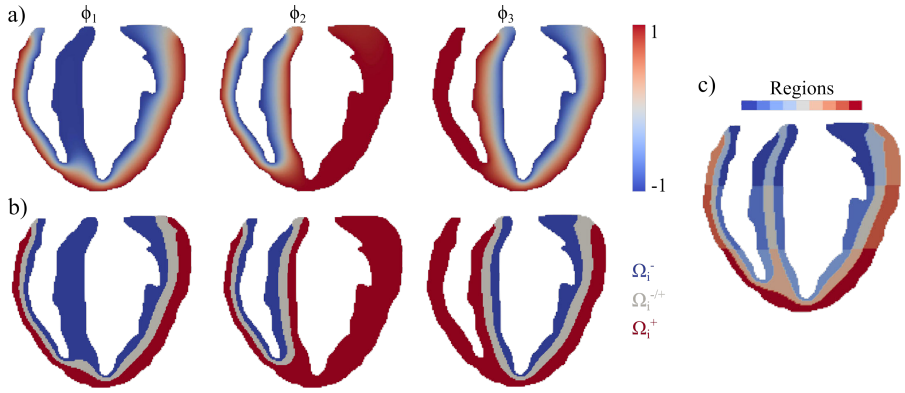


Figure 1.30: Transmural and apico-basal segmentation. a- Solution of the Laplace equation solved with three different Dirichlet boundary conditions. b- Discrete regions obtained for each diffusion solution when mid-endo and mid-epi thresholds were used. c- Final transmural and apico-basal segmentation obtained for the BiV model. Image created from images in [119].

derived via set operations:

$$\begin{aligned} \Omega_{\text{epi}} &:= \Omega_1^+, \\ \Omega_{\text{mid}} &:= (\Omega_1^- \cup \Omega_1^{-/+}) \cap (\Omega_2^+ \cup \Omega_2^{-/+}) \cap (\Omega_3^+ \cup \Omega_3^{-/+}), \\ \Omega_{\text{endo}} &:= (\Omega_1^- \cup \Omega_1^{-/+}) \cap (\Omega_2^- \cup \Omega_3^-), \end{aligned} \tag{1.65}$$

Similarly, apico-basal segmentation can be obtained by solving a Laplace equation with Dirichlet boundary conditions applied at Γ_{base} and the LV epicardial apex. Thresholding the resulting diffusion field then divides the BiV model into typically three apico-basal sections [119]. Figure 1.30c shows the combined (transmural and apico-basal) segmentation results.

1.6.3.6 *ELECTRA*: simulation framework

All simulations in this thesis were carried out using the solver *ELECTRA*, which enables the simulation of cardiac electrophysiology by integrating real anatomical data, thus providing accurate and clinically meaningful simulations for evaluating arrhythmias and other CVD-related electrical disorders. It has been developed by the Biomedical Signal Interpretation and Computational Simulation (BSICoS) research group at the University of Zaragoza.

The software is primarily implemented in C++ using an object-oriented paradigm, supporting simulations at both the cellular level (ElectraCell) and the tissue level (ElectraSim) [115]. To improve computational efficiency, it leverages concurrency through multi-threading in shared-memory systems.

At the cellular scale, gating variable equations are integrated using the Rush-Larsen method, while concentration-related ODEs are explicitly solved with the forward Euler scheme (see Section 1.6.3.2). Intercellular propagation is described by the monodomain model, for which *ELECTRA* applies operator splitting to the associated parabolic PDE. The diffusion term is integrated explicitly in time, whereas the reaction term is advanced using an adaptive explicit method [115]. Spatial discretization of the diffusion term is carried out with the FEM, which naturally accommodates zero-flux Neumann boundary conditions and accurately represents smooth anatomical surfaces (see Section 1.6.3.3) [115].

The source code of *ELECTRA* is openly available at `https://github.com/lino202/ELECTRA`. A language-independent JSON (JavaScript Object Notation) file is read by the ElectraSim executable program to configure simulations at the tissue level. At the cellular level, simulation settings are manually specified as arguments to the ElectraCell program. The following paragraphs provide a brief description of the JSON input file and its parameters as implemented in version 0.6.3 of ElectraSim:

- *application*: the document header includes information about the software version, e.g., "ElectraSim v0.6.3".
- *simulation*: defines the *name* and *scale* of the simulation. At present, the only supported simulation scale is "tissue". Furthermore, the *load cells state* allows the user to specify a previously saved simulation checkpoint to resume computations.
- *reference units*: specifies the units employed for *time*, *capacitance*, and *current*.
- *tissue*: defines the attributes of the *geometry* for the simulated tissue, including *units*, mesh *dimensions*, number of *cell vertices*, and the *file* path to the geometry used in the simulation. The input mesh file must be provided in **.inp* format. The *dimensions* parameter enables the user to select among 1D, 2D, or 3D simulations. The number of vertices corresponds to the element type, as detailed below:
  - 1D: linear elements with two vertices.
  - 2D: triangular or quadrilateral elements with three or four vertices, respectively.
  - 3D: tetrahedral or hexahedral elements with four or eight vertices, respectively.

- *material*: defines the electrical properties of the simulated tissue.
  - *type*: currently, only transverse anisotropy is supported.
  - *diffusivity unit*: typically expressed in cm^2/ms.
  - *transmembrane diffusivity*: accepts either a single value or an array of values to define global or region-specific diffusion coefficients.
  - *transverse ratio*: specifies the ratio of diffusivity applied perpendicular to the CM fiber orientation. For instance, a value of 0.25 indicates that transverse diffusivity is one-quarter of the longitudinal diffusivity. This parameter may be defined as a single value or as an array corresponding to multiple nodesets.
  - *fibers*: the fiber orientation can be defined directly within the JSON file, either as a single vector or as a multidimensional array of vectors. Alternatively, a file path to an external JSON file may be provided. The number of vector components must match the simulation dimensionality.
- *stimuli*: defines the characteristics of the applied electrical stimuli.
  - *number of stimuli*: specifies the total number of stimuli in the simulation.
    - *id*: stimulus identifier.
    - *nodeset*: group of nodes where the stimulus is applied.
    - *start*: onset time of the stimulus, typically expressed in ms.
    - *duration*: duration of the applied stimulus, typically expressed in ms.
    - *cycle length*: defines the periodicity of the stimulus, typically expressed in ms.
    - *amplitude*: specifies the current amplitude of the stimulus. The units depend on the implementation of the underlying cellular model, particularly on the definition of the cell membrane capacitance. In this thesis, the stimulation amplitudes for the O'Hara et al. [51], Paci et al. [110, 113], Gaur et al. [16] and Stewart et al. [108] cellular models are given in µA, nA, $\mu A/cm^2$ and $\mu A/cm^2$, respectively.
- *electrophysiology*: specifies the AP cellular models used in the simulation.
  - *models number*: defines the total number of electrophysiological regions.

  - *model-1*: defines the *model type* (e.g., paci2020v), *cell type* (endo|mid|epi|ventricular|purkinje|atrial), the associated *nodeset*, and optionally a *manual init file* that specifies a prepaced steady state for the selected cellular model.

- *conduction system*: when defined, this section describes the cardiac CS configuration and includes the following parameters:

  - *geometry*: specifies the path to the **.inp* file containing the CS *geometry*, as well as the distance *unit* and the *PMJ radius*.
  - *nodesets*: defines the nodesets corresponding to the AVN and Purkinje endpoints (*terminal nodes*).
  - *diffusivity*: specifies the CS *tree diffusivity* and the *PMJ diffusivity* for the endpoints forming the PMJs. The *sigmoid kappa* parameter modulates the sigmoid function (see k parameter in Equation 1.62), controlling the smoothness of the diffusivity transition from the CS to the myocardium. Typically, a value of -1 is used.
  - *electrophysiology*: defines the cellular model for the CS, following the same structures as for the tissue definition. A nested *stimuli* subsection may also be defined within this *conduction system* section.

- *numerical approximation*: specifies the numerical integration method. At present, only the FEM is supported.

- *physics*: configures the reaction-diffusion system.

  - *type*: monodomain.
  - *solver*: supports various numerical schemes, including forward Euler, semi-implicit, and dual adaptive explicit time integration methods [115].
  - *dt unit*: defines the time step unit.
  - *dt*: specifies the main time step value.
  - *dt min*: defines the minimum time step for the adaptive time integration of the reaction term when the dual adaptive explicit method is selected.
  - *simulation time*: total duration of the simulation.
  - *simulation time unit*: unit of the total simulation duration.

  - *output interval*: specifies the frequency at which simulation results are saved, expressed as a function of *dt*.

- *output*: all simulation results are stored in the binary Ensight gold format. Paths must be provided for *geometry*, *states* and *animation* files corresponding to both the myocardium and the CS. Additionally, a file path may be specified for saving the *cells state* at the end of the simulation, enabling simulation checkpointing for future continuation.

Concrete examples of these input files, together with corresponding meshes and prepaced cellular initializations for various scenarios, are available in the referenced repository.

For simulations at the cellular level, the bash-based ElectraCell executable is invoked with the following arguments:

- argument 1: file path for saving the simulation results.
- argument 2: cellular model name, corresponding to the model type in tissue-level simulations.
- argument 3: cell type (endo|mid|epi|ventricular|purkinje|atrial).
- argument 4: total simulation duration in ms.
- argument 5: stimulation onset time in ms.
- argument 6: stimulation duration in ms.
- argument 7: stimulation cycle length in ms.
- argument 8: stimulation amplitude, with units dependent on the selected cellular model implementation, as discussed previously for tissue-level simulations.
- argument 9: optional file path specifying input constants and state variable initializations for the selected cellular model.

The results generated by ElectraCell include cellular initialization files that can be used to prepace a cellular model prior to its integration within ElectraSim. Additionally, the resulting V_m is provided as a text file with a temporal resolution of 0.01 ms.

1.7 Objectives and research questions

This thesis investigates the *in silico* assessment of arrhythmogenic electrophysiological alterations in chronic post-MI hearts, and how these changes evolve following EHT-based engraftment. The ultimate goal is to provide new insights into both the risks and opportunities of post-MI remuscularization. To achieve this, a large body of experimental data is used to guide and validate computational models and simulations representing a range of *in vitro* and *in vivo* EHT designs, multi-substrate MI conditions, and diverse engraftment scenarios. Additional contributions include evaluating synthetically augmented, anatomically consistent segmentation of cardiac images for improved patient-specific modeling, as well as developing strategies for rapid simulation using optimized software on high-performance hardware to handle large digital twin cohorts.

The research is structured around the following objectives:

1. Perform *in silico* electrophysiological analysis of *in vitro* EHTs to optimize their design based on experimental electrical characterization.
2. Develop a semi-automatic pipeline to reconstruct personalized healthy and diseased BiV heart models.
3. Validate and refine healthy and diseased swine heart models using experimental data, and analyze electrophysiological alterations in chronic MI.
4. Assess, through *in silico* experiments, the electrophysiological consequences of EHT-mediated remuscularization in post-MI BiV hearts, with particular focus on arrhythmia inducibility.

The research carried out in this thesis to achieve each of the described objectives is described below.

Objective 1: The electrical activity of several bioprinted EHT designs is analyzed using high spatiotemporal resolution OM recordings of calcium transients and V_m signals collected from EHTs. Post-processing enables the quantification of activation patterns, which, together with hiPSC-CMs organization data, are used to calibrate computational models. Various EHT configurations, differing in pore size and geometry, cell-to-cell coupling, and cell orientation, are simulated, including attachment to infarcted tissue, to identify the most biomimetic design.

Objective 2: Multi-sequence CMRs from healthy and MI swines are processed using DL algorithms to enable semi-automatic segmentation for numerical modeling. Publicly available, multi-center, multi-vendor, multi-class, and multi-contrast datasets are analyzed. Moreover, a complete pipeline for fast construction of digital twining is proposed, which defines fiber orientation (via diffusion CMRs), transmural and apico-basal heterogeneities (via multi-Laplace problem resolution), and highly detailed CS (via anatomical landmark identification and fractal algorithms) for healthy and MI BiV models. The MI substrate is derived from contrast-enhanced CMRs.

Objective 3: Fluorescent OM recordings of V_m captured from healthy and infarcted swine hearts, combined with imaging and electrocardiography, are used to validate and refine the models. Post-MI changes in CV, AT, depolarization patterns, and APD are simulated to shed light on electrical alterations associated with chronic MI remodeling. Particular attention is given to rotor dynamics and their role in triggering transient or sustained arrhythmias.

Objective 4: The electrophysiological impact of different EHT implantation strategies is evaluated in a patient-specific model, including variations in location, degree of ventricular attachment, electrical maturation, and hiPSC-CM orientation. Results show that both the degree of electrical coupling in the EHT and its implantation location in relation to the MI substrate are critical determinants of arrhythmogenicity. To generalize these findings, a pool of nine multi-site MI personalized porcine models is analyzed. An *in silico* arrhythmia inducibility protocol (AIP) is applied to each digital twin in both MI and remuscularized states under varying cell-to-cell coupling and implantation location. The obtained insights aim to identify strategies that minimize arrhythmic risk and support the safe and effective clinical translation of EHTs-based remuscularization therapies.

1.8 Structure of the thesis

This section provides an overview of the organization of the thesis, highlighting the alignment between the defined objectives, the corresponding chapters, and the scientific publications derived from the work. The thesis is structured into eight chapters, all focused on electrophysiological simulation and cardiac imaging segmentation for the evaluation of post-MI remuscularization therapy.

The first part establishes the theoretical and experimental foundations of the research, including the state of the art and background knowledge. The second part presents our experimentally guided modeling and simulation ap-

proach for assessing remuscularization therapies. Results are reported from *in vitro* investigations, tissue slab analyses, and BiV simulations, supported by systematic grouping of simulation experiments labeled "CXGY", where X indicates the chapter and Y the simulation group. The methodological framework is complemented by contributions in digital twinning, automated medical image segmentation, and optimized software-hardware implementations. Finally, the thesis closes with concluding remarks and perspectives for future research.

- **Chapter 1:** This chapter introduced the necessary background concepts to ensure a clear understanding of the work. It has begun with a motivation for the thesis (Section 1.1), followed by a review of cardiac anatomy and electrophysiology in healthy and diseased hearts, including differences and similarities between humans and swine (Section 1.2). Section 1.3 detailed the experimental techniques used in this work: CMRs, OM, EAM, and electrocardiography. hiPSC-CMs were introduced in Section 1.4, with emphasis on their therapeutic potential and electrophysiological differences from adult CMs. Section 1.5 presented DL-based approaches for automated CMRs segmentation, including CNNs, GAN-based data generation and topological constraints via PH. Finally, Section 1.6 reviewed the principles of *in silico* cardiac electrophysiological modeling and simulation.
- **Chapter 2:** This chapter reviews the state of the art in three areas relevant to this thesis: (i) anatomically consistent segmentation of CMRs using DL methods (Section 2.1); (ii) post-MI remuscularization in preclinical and clinical settings (Section 2.2); and (iii) prior *in silico* studies in this domain (Section 2.3). Finally, Section 2.4 reviews current electrophysiological solvers, with emphasis on their implementation and parallelization strategies.
- **Chapter 3:** This chapter investigates different *in vitro* EHT designs to identify configurations that best reproduce physiological electrical activity while minimizing arrhytmic risk. Acquisition and processing of experimental recordings are combined with computational modeling and simulation to evaluate scaffold architectures (pore size, shape, thickness) and cell orientations, both before and after engraftment onto infarcted tissue. Scaffolds made of small, elongated hexagons lead to faster EHT activation and better mimic the cardiac anisotropy. EHT engraftment on MI tissue shows that a biomimetic EHT conductivity is paramount for bidirectional EHT-myocardium electrical propagation and minimizing the likelihood for arrhythmias after EHT transplantation.

The following publications were derived from the work in this chapter:

- **R. M. Rosales**, K. A. Mountris, M. Doblaré, M. M. Mazo, and E. Pueyo, "In Silico Electrophysiological Evaluation of Scaffold Geometries for Cardiac Tissue Engineering", in 2021 Computing in Cardiology (CinC), vol. 48, (Brno, Czech Republic), pp. 1–4, 2021.
- **R. M. Rosales**, K. Mountris, M. Doblaré, M. Mazo, and E. Pueyo, "Evaluación Computacional de la Arquitectura de la Matriz de Cultivo en la Electrofisiología Cardíaca", Jornada de Jóvenes Investigadores del I3A, vol. 9, 2021.
- **R. M. Rosales**, K. A. Mountris, A. Oliván-Viguera, M. Pérez-Zabalza, G. Cedillo-Servin, O. Iglesias-García, A. Hrynevich, M. Castilho, J. Malda, F. Prósper, M. Doblaré, M. M. Mazo, and E. Pueyo, "Experimentally-Guided In Silico Design of Engineered Heart Tissues to Improve Cardiac Electrical Function After Myocardial Infarction", Computers in Biology and Medicine, vol. 171, p. 108044, 2024.

- **Chapter 4:** This chapter explores the use of SA and TC for 3D CMR segmentation across challenging multi-vendor, multi-center, multi-class and multi-contrast datasets. Results show improved overlap with GTLs and enhanced topological consistency, particularly in infarct segmentation and when topologically consistent data are available for training.

  The following manuscript was derived from this chapter:

  - **R. M. Rosales**, M. Doblaré, and E. Pueyo, "3D Segmentation of Multi-Contrast Cardiac Magnetic Resonances With Topological Correction and Synthetic Data Augmentation", Annals of Biomedical Engineering, vol. -, pp. -, 2026.

  In addition, the chapter also reports our participation in the MYOSAIQ challenge [96] under the user name *rrosales*, with the corresponding results included in the following publications:

  - B. Olivier, W. A. Romero R., C. Bouton, C. Goujat, H. Jung Ling, P.-M. Jodoin, F. Guo, C. Sheagren, G. Wright, A. Qayyum, M. Mazher, S. A. Niederer, H. Wang, X. Wu, F. Thaler, G. Plank, M. Urschler, **R. M. Rosales**, E. Pueyo, N. Duchateau, F. Cervenansky, P. Clarysse, L. Belle, N. Mewton, T. Bochaton, M. Viallon,

and P. Croisille, "The MYOSAIQ Challenge: Myocardial Segmentation with Automated Infarct Quantification", Submitted - Under Review.

– **R. M. Rosales**, and E. Pueyo, "GAN-Based Data Augmentation and Uncertainty Estimation for Improved Automatic Myocardial Infarction Segmentation", 2025, url: `https://humanheart-project.creatis.insa-lyon.fr/myosaiqResources/2025_proceedings_myosaiq_rosales.pdf`.

- **Chapter 5:** This chapter develops swine-specific digital twins by integrating extensive multimodal experimental data into electrophysiological models of healthy and infarcted hearts. The role of CS, spatial repolarization heterogeneity, and CM orientations is investigated in healthy models, while infarct-related remodeling is characterized in MI models. Simulated ECGs are compared with experimental recordings to identify location-specific electrocardiographic signatures. Personalized CM orientation minimally affects electrophysiology, while accurate CS and repolarization heterogeneities reproduce depolarization and repolarization patterns. Incorporating experimentally guided MI-induced alterations enabled replication of MI electrophysiological features, yielding realistic T-wave morphologies, and revealed ECG patterns specific to vessel-dependent occlusions.

  The results of this chapter led to the following manuscripts:

  – **R. M. Rosales**, K. A. Mountris, M. Doblaré, M. M. Mazo, and E. Pueyo, "Ventricular Conduction System Modeling for Electrophysiological Simulation of the Porcine Heart", in 2022 Computing in Cardiology (CinC), vol. 49, (Tampere, Finland), pp. 1–4, 2022.

  – **R. M. Rosales**, M. Wu, P. Claus, S. Janssens, G. R. Ríos-Muñoz, M. E. Fernández-Santos, P. Martínez-Legazpi, J. Bermejo, A. Flanagan, M. Doblaré, A. Mincholé, and E. Pueyo, "Integrated Multi-Modal Data Analysis for Computational Modeling of Healthy and Location-Dependent Myocardial Infarction Conditions in Porcine Hearts", PLOS Computational Biology, vol. 22, pp. 1-38, 2026.

- **Chapter 6:** This chapter investigates the arrhythmogenic potential of infarcted ventricles before and after remuscularization. A combination of experimentally validated porcine BiV models and a mechanistic hiPSC-CM cellular model is used to assess the impact of EHT implantation parameters (attachment, cell organization, and conductivity) on

arrhythmia inducibility. Multi-site MI models are analyzed under programmed stimulation to quantify arrhythmic burden. Post-remuscularization VT burden increases in pigs with highly transmural dense scars, albeit this effect is mitigated when the EHT is implanted laterally rather than directly over the MI. In pigs with poorly transmural dense scars, VT burden is strongly dependent on the EHT implantation site. Moreover, biomimetic cell-to-cell coupling within the EHT consistently reduces post-engraftment arrhythmicity.

The work carried out in this chapter led to the following publications:

- **R. M. Rosales**, K. Mountris, M. Doblaré, M. Mazo, and E. Pueyo, "In Silico Assessment of Arrhythmic Risk in Infarcted Ventricles Engrafted with Engineered Heart Tissues", in 2023 Computing in Cardiology (CinC), vol. 50, (Atlanta, USA), pp. 1–4, 2023.
- **R. M. Rosales**, M. Doblaré, M. M. Mazo Vega, and E. Pueyo, "Design of Engineered Heart Tissues to Minimize Arrhythmic Risk After Implantation in Infarcted Hearts", in 2024 Computing in Cardiology (CinC), vol. 51, (Karlsruhe, Germany), pp. 1–4, 2024.
- **R. M. Rosales**, G. R. Ríos-Muñoz, A. M. Sánchez de la Nava, M. E. Fernández-Santos, J. Bermejo, M. Doblaré, A. Mincholé, and E. Pueyo, "*In Silico* Assessment of Arrhythmic Risk Following the Implantation of Engineered Heart Tissues in Porcine Hearts with Varying Infarct Locations", PLOS Computational Biology, vol. 22, pp. 1-32, 2026.

- **Chapter 7:** This chapter focuses on methodological translation by describing extensions to the electrophysiological solver used throughout this thesis and by developing *Cocoro*, a GPU-based solver designed for efficient electrophysiological simulation and rendering. Comparative benchmarks with gold-standard solvers and experimental validation show its accuracy and efficiency.

  A publication related to the development and outcomes of *Cocoro* is listed:

  - **R. M. Rosales**, A. Mincholé, and E. Pueyo, "Cocoro: Fast Simulation of Cardiac Electrophysiology with WebGPU", in 2025 Computing in Cardiology (CinC), vol. 52, (São Paulo, Brazil), pp. 1–4, 2025.

- **Chapter 8:** This chapter summarizes the main outcomes and conclusions of the thesis, discusses limitations, and outlines future research directions.

CHAPTER 2

STATE OF THE ART

2.1 Segmentation of cardiac magnetic resonances
- 2.1.1 Convolutional neural networks
- 2.1.2 Synthetic data augmentation
- 2.1.3 Anatomical consistency
- 2.1.4 Uncertainty estimation

2.2 Post-MI remuscularization therapy
- 2.2.1 Preclinical evidence of EHT therapy
- 2.2.2 Early clinical translation
- 2.2.3 Cell survival and paracrine mechanisms
- 2.2.4 Immature phenotype and arrhythmogenic risk
- 2.2.5 Outstanding challenges and future directions

2.3 Modeling and simulation of chronic and remuscularized MI
- 2.3.1 Personalization
- 2.3.2 Arrhythmic risk
- 2.3.3 Remuscularization
- 2.3.4 Future directions for digital twin–guided regeneration

2.4 Parallel computation of *in silico* electrophysiology

2.5 Chapter summary

In this chapter, the most recent advances in the areas relevant to this thesis are reviewed. First, the current state-of-the-art in CNN-based biomedical image segmentation is introduced, with particular attention to approaches

incorporating SA, TC, and uncertainty quantification. Subsequently, developments in EHT-mediated post-MI remuscularization are summarized, including both preclinical and early clinical evidence, as well as mechanistic insights obtained from modeling and simulation. Finally, recent advances in specialized software that leverages parallel computing to accelerate large-scale *in silico* electrophysiological simulations are discussed.

2.1 Segmentation of cardiac magnetic resonances

2.1.1 Convolutional neural networks

Manual segmentation of CMRs images was historically performed by clinical experts, a process that is both time- and resource-intensive. Recent advances in DL, particularly CNNs, have demonstrated segmentation performance comparable to human experts in multiple biomedical imaging contexts [79, 80].

Since the introduction of the UNet architecture in 2015 [81], many variants have been proposed, achieving state-of-the-art performance in diverse segmentation tasks [80]. Azad et al. [134] recently reviewed these developments, presenting a taxonomy of UNet extensions [134]:

- Transformers: These extensions involve the combination of the UNet with natural language processing models, called transformers. Hybrid UNet-transformer models improve geometric and topological robustness in image semantic segmentation by capturing long-range inter-pixel dependencies that standard CNNs struggle to represent due to limited receptive fields of their convolutions.

- Probabilistic designs: These extensions, including Bayesian skip connections, Markov random fields, and other related methods, incorporate uncertainty modeling into segmentation pipelines.

- Rich representation enhancement: Multi-modal and multi-scale extensions (e.g., cascade UNets) improve segmentation by fusing complementary information from diverse image modalities.

- Bottleneck enhancement: These extensions act on the low-dimensional encoded features present in the latent space of the UNet to improve feature abstraction and robustness.

- Skip connection enhancement: Alternative skip-connection schemes, such as bidirectional information flow (also passing information from the decoder to the encoder) or multi-scale feature aggregation, enhance structural consistency.
- Backbone design enhancement: Variations in convolution, normalization, pooling, or activation layers, such as residual connections or 3D convolutions, adapt UNet to biomedical applications.

Among these approaches, nnUNet has emerged as one of the most effective frameworks for biomedical image segmentation [79]. Unlike fixed architectures, nnUNet automatically configures the segmentation algorithm based on previously identified fixed and robust schemes and rule-based parameters defined from the given dataset. The nnUNet automatically explores different dimensionalities (2D and 3D) and image resolutions, and ensembles the resulting models when this improves performance, as determined through 5-fold cross-validation. It includes data preprocessing steps such as normalization, cropping, and padding, as well as postprocessing operations, including the suppression of all but the largest connected component [79].

The UNet architecture has thus become the standard backbone for cardiac and biomedical image segmentation, combining modularity, simplicity, and robustness [80, 134]. This has led the UNet to consistently achieve top-ranking results in international segmentation challenges, such as M&Ms [82] and M&Ms-2 [83] challenges for segmenting cine CMRs and MYOSAIQ [96] challenge for segmenting LGE CMRs.

2.1.2 Synthetic data augmentation

Data scarcity remains a significant challenge in biomedical segmentation. GANs have been increasingly adopted as a DA strategy, generating synthetic images that expand limited training datasets [135]. Early studies demonstrated that augmenting training sets with GAN-generated data improved segmentation accuracy in computed tomography and magnetic resonance imaging. For example, Bowles et al. [136] demonstrated the feasibility of GAN-based DA, showing that combining synthetic data with conventional DA enhanced segmentation of cerebrospinal fluid in computed tomography and white matter hyperintensity in magnetic resonance imaging. Similarly, Frid-Adar et al. [137] improved liver lesion classification in computed tomography, while Sandfort et al. [138] reported a substantial reduction in multi-organ volume prediction errors on non-contrast computed tomography using GAN-based DA.

For CMR segmentation, Al Khalil et al. [139] proposed a synthesis framework combining variational autoencoders and a GAN. The trained autoencoders enabled consistent label deformation, which was then used as an input to a label-conditional GAN to generate synthetic SAx and LAx images. By applying this SA, the authors improved baseline nnUNet performance, achieving enhanced contour agreement and overlap with GTLs when trained and tested on the M&Ms-2 dataset [83], as well as improved generalization on the out-of-distribution M&Ms dataset [82]. Similarly, Lustermans et al. [140] proved that incorporating GAN-generated LGE SAx images improved MI segmentation. Their sequential cascaded approach first segmented the LV blood pool and myocardium, followed by MI scar segmentation. Two 2D nnUNet models were trained and tested on the Emidec dataset [141], excluding the MVO class. Using SA improved scar segmentation overlap with GTLs by 6% with the cascaded nnUNets and 3% with a single nnUNet.

Most implementations are based on pix-2-pix [86] and cycleGAN [87] architectures for paired and unpaired image-to-image translation (see Section 1.5.3). In these frameworks, UNets are commonly employed as Gs and PatchGANs Ds. Both networks are typically constructed from convolutional, batch normalization, and activation layers. The loss function for G is generally formulated as the sum of the conditional GAN objective (L_{cGAN}) and an L_1 reconstruction loss:

$$L_{cGAN}(\mathrm{G},\mathrm{D}) = \mathbb{E}_{\boldsymbol{x},\boldsymbol{y}}[\log \mathrm{D}(\boldsymbol{x},\boldsymbol{y})] + \mathbb{E}_{\boldsymbol{x}}[1 - \log \mathrm{D}(\boldsymbol{x},\mathrm{G}(\boldsymbol{x}))] \tag{2.1}$$

$$L_1(\mathrm{G}) = \mathbb{E}_{\boldsymbol{x},\boldsymbol{y}}[||\boldsymbol{y} - \mathrm{G}(\boldsymbol{x})||_1] \tag{2.2}$$

$$G_{loss} = \arg \min_{\mathrm{G}} \max_{\mathrm{D}} L_{cGAN}(\mathrm{G},\mathrm{D}) + \lambda L_1(\mathrm{G}) \tag{2.3}$$

where G maps an input image $\boldsymbol{x}$ to an output image, and λ acts as a regularization parameter controlling the similarity of the synthetic output to the real target. The discriminator D produces a lower-resolution binary output in which each pixel indicates whether a local image patch is real or generated. It is well established that the L_1 loss encourages reconstructions that preserve low-frequency information but result in blurry images. To counter this, the design of D focuses on capturing high-frequency details that sharpen the synthetic images. Isola et al. [86] demonstrated that using smaller patch sizes in D yields sharper images with reduced tiling artifacts, whereas larger patches lead to blurrier outputs.

More recently, spatially adaptive (de)normalization (SPADE) GAN [142] has been introduced for semantic-to-real image translation and applied to CMR-related SA in [139, 140]. Unlike conventional normalization, SPADE

modulates normalization layers with two learnable parameters, γ and β, that vary in space and depend on the semantic input. This mechanism preserves semantic information that would otherwise be lost in standard normalization layers.

2.1.3 Anatomical consistency

CNNs are typically optimized using pixel-wise loss functions, which often limits their ability to capture anatomically coherent structures [80]. To address this issue, several segmentation strategies have been proposed to enforce anatomical consistency. Oktay et al. [143] introduced convolutional autoencoders to generate low-dimensional representations (shape codes) from both predictions and GTLs of cardiac computed tomography images, enabling the incorporation of a shape-based regularization term into the loss function. Similarly, Zheng et al. [18] constrained cine-CMR slice segmentations by leveraging anatomical information from adjacent slices, combining the contextual and current latent spaces derived from 2D slices of the same 3D volume. These approaches rely on the assumption that anatomical definitions can be implicitly captured within latent representations. However, the fuzzy nature of such representations complicates both interpretability and supervision during segmentation [19]. Furthermore, these methods rarely exploit the well-defined 3D topology of the heart, which remains relatively stable across a wide range of pathologies.

An alternative line of work leverages topological priors. Brüel-Gabrielsson et al. [93] demonstrated that the differentiable properties of PH, combined with prior topological knowledge of cubical complexes, can guide DL models toward topologically consistent outputs. Along these lines, Clough et al. [92] showed that incorporating a topological loss improved both noisy handwritten digit classification and 2D CMR segmentation of the LV myocardium. More recently, Byrne et al. [19] reported improvements in multi-class segmentation for both 2D medial SAx slices and 3D whole-heart images.

2.1.4 Uncertainty estimation

Since 2015, the three most widely adopted strategies for quantifying uncertainty in DL have been Monte Carlo dropout, ensemble methods, and softmax-based approaches [88]. In essence, Monte Carlo dropout performs multiple stochastic forward passes with dropout layers activated (see Section 1.5.2.2), generating a distribution of predictions from which uncertainty can be estimated. Ensemble methods train multiple CNNs with varying initialization pa-

rameters or subsets of the training data. For example, a 5-fold cross-validation produces five models whose predictions for the same input form a distribution. The softmax-based approach instead interprets the network outputs as true probabilities, thereby yielding a prediction distribution. However, as discussed in Section 1.5.5, modern CNNs are often poorly calibrated. Thus, calibration techniques such as temperature scaling are typically applied to adjust the softmax outputs so that they more faithfully reflect true probabilities [88, 95].

Modern recent approaches for uncertainty quantification either build upon these foundations or employ less conventional techniques. One direction involves Bayesian neural networks, in which each weight is modeled as a distribution rather than a deterministic scalar. Another relies on directly learning uncertainty from the data during training [88]. For instance, Corbière et al. [144] introduced ConfidNet, a CNN that learns pixel-wise confidence scores alongside segmentation. Similarly, Judge et al. [145] proposed CRISP, which learns a joint latent space by encoding image-GTL pairs during training. At test time, the M GTL-based latent vectors closest to the latent representation of the input image are selected to generate M predictions. The final uncertainty map is computed as the average pixel-wise difference between the latest prediction and these M latent-derived predictions. Despite their novelty, both ConfidNet and CRISP exhibit limitations. State-of-the-art methods frequently overestimate uncertainty at segmentation boundaries, which becomes problematic when large segmentation errors occur, as in cases where predictions diverge significantly from the GTL. Furthermore, CRISP demands extensive and representative training datasets. Otherwise, the resulting uncertainty maps are unreliable [145].

A growing body of work focuses on structural uncertainty estimation, which aggregates pixel- or voxel-level uncertainty into clinically interpretable measurements at the instance (organ or lesion) or case (whole image) level [88]. Simple aggregation operators such as averaging or log-sum have been proposed for fusing voxel-wise confidence into instance-level estimates. Additionally, ensemble, Monte Carlo dropout, and related strategies can be combined to produce multiple predictions, with their level of agreement serving as a surrogate for confidence [88].

This thesis addresses the scaling of voxel-wise to instance-level uncertainty. This is particularly important because cardiac volume-wise CDF must be estimated to compute the CRPS confidence metric in the MYOSAIQ challenge [96]. A common approach for this task involves modeling the segmented volume value and its instance-level confidence as the mean and standard deviation of a Gaussian probability density function (PDF), from which the CDF

is derived. More advanced strategies can avoid assuming Gaussianity and instead approximate the distribution directly for CRPS computation. In Chapter 4, we describe our proposed methodology to reliably estimate the CDF from voxel-level uncertainty values.

2.2 Post-MI remuscularization therapy

Over the past decades, implantation of EHT following MI has yielded encouraging results in restoring ejection fraction, with most evidence from preclinical studies involving small and large non-human mammals [6, 7, 69, 146].

2.2.1 Preclinical evidence of EHT therapy

EHT therapies have been extensively tested in animal models, providing foundational proof-of-concept for their potential in myocardial repair. For instance, Iglesias-García et al. [6] demonstrated that epicardial implantation of EHTs containing hiPSC-CMs improved post-MI ejection fraction in athymic rats subjected to LAD occlusion. Although direct connexin-mediated electrical coupling between host myocardium and EHT was not assessed, the authors reported infiltration of host cells into the graft, accompanied by vascular ingrowth from host to implant. In a large-animal study, Ye et al. [146] showed that cellularized EHTs enhanced ejection fraction and contractility while reducing infarct size in MI pigs. Similarly, Jebran et al. [7] found that EHT implantation in infarcted macaques improved contractile function and ejection fraction, with evidence of hiPSC-CMs retention and functional vascularization.

Encouraged by these results in both small and large animals, investigators have begun to explore the feasibility of EHT implantation in humans.

2.2.2 Early clinical translation

Initial clinical studies have demonstrated that EHT implantation is technically feasible and appears safe, with early signs of structural benefit in post-MI patients. Ensminger et al. [24] assessed 13 patients with MI-induced HF who received epicardial implantation of varying doses of EHTs (2-10 million cells per kilogram). The study confirmed the feasibility of implantation across all dose levels and reported no related adverse events, including arrhythmias. In one patient who subsequently underwent successful heart transplantation, histological analysis revealed the presence of vascularized muscle tissue. Furthermore,

a dose-dependent increase in myocardial wall thickness at the infarct site was observed [24].

Despite this progress, important challenges remain that may limit the efficacy of EHT therapy in the long term.

2.2.3 Cell survival and paracrine mechanisms

One major barrier is the poor survival of transplanted cells, with only a fraction persisting after engraftment. Follow-ups of up to four months consistently show that only a small fraction of hiPSC-derived stromal and parenchymal cardiac cells (around 10%) persist within the myocardium-EHT complex after implantation [3, 68, 146].

This limited viability raises questions about how functional recovery is achieved, pointing toward paracrine signaling as a likely mechanism. A widely discussed hypothesis is that secreted factors from surviving hiPSC-derived cells promote repair during the early stages of engraftment [3, 71, 146]. Supporting this, Ye et al. [146] identified 21 factors, expressed in hiPSC-derived cells, implicated in promoting cell migration or homing, proliferation, and anti-apoptotic pathways, all of which may contribute to functional recovery following EHT implantation.

Alongside poor persistence, another challenge is the immature phenotype of transplanted hiPSC-CMs, which carries its own set of risks.

2.2.4 Immature phenotype and arrhythmogenic risk

The hiPSC-CMs retain a fetal-like phenotype, with electrophysiological immaturity that predisposes them to arrhythmias. Features such as prolonged APD, reduced CV, and spontaneous beating predispose these cells to arrhythmic behavior [3, 38, 147].

In cell injection studies, Romagnuolo et al. [38] reported severe VTs between days 10 and 28 post-transplantation in MI pigs treated with human embryonic stem cell-derived CMs. Unlike the reentry-driven VTs typically observed in low-conduction post-MI tissue [148], electrophysiological mapping suggested a focal ectopic mechanism, as no reentry circuits were identified with EAM, and pacing the RV failed to reset or entrain the tachycardia. Similarly, Marchiano et al. [147] described “engraftment arrhythmia”, defined as sustained polymorphic VT arising from focal ectopic activity, typically within a week of hiPSC-CMs transplantation and persisting for about a month. Their findings

were reinforced by reduced arrhythmia incidence in pigs transplanted with genetically modified hiPSC-CMs engineered to suppress automaticity through downregulation of depolarization currents and upregulation of hyperpolarizing mechanisms.

In contrast, most studies involving EHT-based therapy report little to no arrhythmic activity [7, 24, 68, 71, 146]. However, these studies frequently show poor long-term cell survival and, in many cases, no confirmed electrical coupling between graft and host tissue [6, 7, 71, 146]. For example, Ye et al. [146] reported survival rates of only 4.2% and 8.9% for stromal and parenchymal cells, respectively, at four weeks post-implantation in pigs receiving either cell suspensions or EHTs. Electrical integration was absent in the study by Iglesias-García et al. [6] and not demonstrated in the studies by Jebran et al. [7] or Cui et al. [71].

Taken together, these limitations highlight the need for further refinement of EHT therapies before they can be broadly adopted in clinical practice.

2.2.5 Outstanding challenges and future directions

Achieving durable engraftment, promoting functional maturation, and ensuring safety will be critical for the success of post-MI remuscularization. Ongoing advances in bioengineering, cell reprogramming, and clinical trial design offer promising avenues toward safe and effective myocardial regeneration.

2.3 Modeling and simulation of chronic and remuscularized MI

Recent research efforts in computational cardiology are largely oriented toward the development of cardiac digital twins, which are increasingly used for arrhythmic risk stratification in various cardiomyopathies as well as for assessing remuscularization therapies [11, 13, 76–78].

2.3.1 Personalization

Building cardiac digital twins requires the calibration of multiscale electrophysiological and anatomical models using extensive experimental datasets. Since this thesis is framed within preclinical studies, the following overview highlights recent work on porcine electrophysiological modeling and simulation. At the single-cell level, Gaur et al. [16] introduced a mechanistic model of porcine CMs

capable of faithfully reproducing species-specific AP dynamics, thereby providing mechanistic insight into arrhythmia generation in healthy swine. Details on this cellular model were already presented in Section 1.6.2.3.

At the tissue scale, nearly contemporaneous with the development of this porcine cellular model, Mendonca-Costa et al. [15] investigated the influence of modeling parameters on post-MI conduction and arrhythmogenesis in pigs. They systematically tested different CMR resolutions and compared both generic and individualized tissue conductivities and ionic conductances. The CV and APD of the simulated tissue were adjusted to experimental recordings, primarily from ECG-derived QRS complexes and QT intervals. To represent porcine ventricular electrophysiology, the Ten Tusscher et al. [52] human model was adapted.

Using six porcine post-MI BiV models, Mendonca-Costa et al. [15] concluded that both electrophysiological tuning and infarct resolution strongly affect VT inducibility, but are not strictly necessary to reproduce biomimetic paced activation. For instance, BiV models constructed from low-resolution infarct imaging preserved paced activation, but underestimated VT incidence, likely due to loss of fine low-conductivity isthmuses, known to sustain reentry. Furthermore, the inclusion of the RV in LAD infarct models drastically altered VT incidence and dynamics. Interestingly, personalized CV, but not APD, derived from non-invasive ECG improved agreement with experimentally observed arrhythmias. Despite highlighting the critical role of infarct resolution and personalized conduction properties, this work lacked direct comparison between simulated and experimental VT morphologies and did not include realistic ventricular repolarization heterogeneities or realistic CS distributions.

2.3.2 Arrhythmic risk

To date, two major AIP have been developed for *in silico* evaluation of VT inducibility. In 2016, Arevalo et al. [10] proposed the Virtual Heart Arrhythmic Risk Predictor (VARP), a clinically inspired protocol in which BiV models undergo programmed stimulation (S1-S2-S3-S4) at 19 pacing sites. Seventeen of these are distributed across the central endocardium of the 17 standardized LV segments defined by the American Heart Association [149], while two are placed in the RV outflow tract and apex. Each site is paced with eight S1-stimuli at a 600 ms cycle length, followed by decremental S2-stimuli starting at 300 ms and stepwise reduced by 10 ms until reentry occurs or refractoriness prevents capture. If S2 fails, additional S3 and S4 are applied. In a retrospective analysis of 41 post-MI patients (21 with clinical arrhythmic events), this

approach outperformed conventional predictors such as LV ejection fraction, BZ size, LV mass, and scar volume. Since then, the VARP protocol has become the benchmark for evaluating VT susceptibility [15, 150] and guiding ablation strategies [151].

While effective, VARP is computationally demanding, particularly when coupled with mechanistic cell models and high-resolution BiV geometries. Its implementation is therefore impractical without access to supercomputers or large clusters. To overcome this limitation, Campos et al. [150] introduce the Virtual Induction and Treatment of Arrhythmias (VITA) protocol in 2022. This approach identifies critical post-MI isthmuses, proposed as substrates required for unidirectional block and reentry [10, 15, 33, 148]. By generating distant fields from multiple pacing sites (e.g. the VARP pacing sites), potential isthmuses and their exit sites are delineated. Simulated unidirectional block is imposed in these regions, and electrical wave propagation from exit sites is simulated using the efficient eikonal equation. If round-trip propagation from and back to the exit site exceeds a threshold, a plausible VT substrate is assumed. Subsequent comparison of simulated ECGs or AT maps enables the identification of unique VT morphologies. Virtual ablation can also be assessed by disconnecting exit sites associated with long round-trip times [150]. Although computationally efficient and fully automated, VITA cannot reproduce conduction block from repolarization heterogeneity and omits the CS, which may provide alternative conduction pathways.

2.3.3 Remuscularization

Computational modeling and simulation of remuscularization therapies using hiPSC-CMs have only recently emerged, primarily to explore the focal versus reentrant mechanisms of arrhythmogenesis after cell injection or EHT implantation.

2.3.3.1 HiPSC-CMs injection

A pioneering study by Yu et al. [152] defined key modeling considerations to simulate this therapy. Their multi-scale framework, informed by experimental findings, revealed that local injection of high-dose hiPSC-CMs near the infarct can trigger ectopic beats. This is consistent with the findings described by Riebel et al. [153], who reported greater arrhythmogenicity with higher densities of hiPSC-CMs injected near the infarct, although in their case no spontaneous activity was observed and higher arrhythmic risk was measured as a

widened vulnerability window for reentry when ectopic stimulation was applied near the remuscularized infarct [153]. Discrepancies between the two studies likely arise from differences in SZ representation or in the cellular models used to describe hiPSC-CMs dynamics [152, 153].

In another study, Gibbs et al. [77] modeled slices of infarcted BiV tissue with hiPSC-CM grafts, treating the SZ either as passive tissue or as an insulator. Without applying external pacing, the authors observed that, when the SZ was modeled as an insulator, ectopic activity from the hiPSC-CM graft to the host myocardium increased from a null ectopy in the uncoupled configuration to its maximum at partial, relatively low (10-13%) graft-host coupling. Importantly, they highlighted the role of source–sink mismatch in suppressing ectopic activity, noting that higher graft–myocardium coupling abolished ectopy. This suppression was more pronounced when the SZ was modeled as passive tissue rather than as an electrical insulator, since the passive SZ acted as an electrical sink that absorbed spontaneously generated current from the graft, thereby reducing the graft's ability to elicit an ectopic beat. Moreover, the authors reported a lower incidence of graft-induced ectopy with increasing intercellular coupling among hiPSC-CMs within the graft.

More recently, Riebel et al. [78] computationally demonstrated that ectopic activity in a BiV model of LAD MI following cell therapy occurred only when highly heterogeneous hiPSC-CMs (ventricular, atrial, and nodal subtypes) were engrafted within the infarcted region. The incidence of ectopic activity was higher when the MI was chronic, with the infarction modeled as passive tissue. Furthermore, the authors found that the development of sustained VT required not only cellular heterogeneity but also the occurrence of an additional bradycardic beat and suppression of retrograde conduction through the CS. Interestingly, the same study computationally showed that rapid host-driven pacing of hiPSC-CM grafts could reduce automaticity by lowering Ca^{2+} levels at the sarcoplasmic reticulum, an effect the authors observed after rapid pacing of the Paci2020 hiPSC-CM model [78, 113].

2.3.3.2 Epicardial EHT implantation

In the context of epicardial EHT therapy, Fassina et al. [154] analyzed key parameters governing electrophysiology in slabs of infarcted tissue following EHT-mediated remuscularization. The authors used bidomain simulations to feed machine learning algorithms relating propagation characteristics with variations in parameters such as inter slab-EHT bath thickness, EHT conductivity, EHT thickness, conductive polymer thickness and conductivity as well as

scar size, conductivity and transmurality. They identified SZ definition as the dominant factor influencing conduction. Importantly, when the SZ was transmural and non-conductive, the conductivity of the EHT was the most critical determinant of propagation delay. They also proposed upregulation of I_{Na} and I_{K1} conductances in hiPSC-CMs to restore physiological ATs and reduce repolarization time gradients (RTGs) without inducing ectopic beats.

Yu et al. [152] were among the first to simulate EHT implantation over infarcted ventricles. They observed higher arrhythmogenicity when the grafts were placed directly over the infarct compared to lateral implantation. Graft anisotropy and hiPSC-CMs orientation were found to strongly affect outcomes when the EHT was distant from the infarct. Notably, no spontaneous ectopy arose from the EHT. In an extension, Yu et al. [11] studied the effects of graft location, size, orientation, and maturation on VT inducibility after MI remuscularization using two BiV models (large anterior versus moderate posterior infarct). Applying the VARP protocol with the Paci2013 [110] hiPSC-CM model, they showed reentrant VT as the dominant mechanism over focal ectopy after EHT implantation, and patient-specific post-MI substrate as a critical determinant of VT susceptibility. The source current from the EHT was insufficient for depolarizing the bulky myocardium acting as a huge electrotonic sink, thereby preventing ectopic beats, as outlined by Gibbs et al. [77]. Complete EHT engraftment allowed conduction to follow the host myocardium, while thicker or partially engrafted EHTs reduced CV increasing the arrhythmic risk. For complete engraftment, EHT location largely determined the success of remuscularization therapy.

More recently, Fassina et al. [76] extended their analysis to whole-LV models with either large, highly transmural infarcts or smaller infarcts with epicardial isthmuses. By applying a S1-S2 AIP on the LV apex, they showed that hiPSC-CMs with reduced APD and more mature electrical coupling lowered VT burden in the latter model, while in the former, the cell-to-cell coupling of hiPSC-CMs was the critical factor to prevent reentrant activity. Interestingly, even minimal, heterogeneous or homogeneous EHT-myocardium coupling sufficed for host-driven graft repolarization and depolarization, consistent with Yu's findings [11, 152]. Additionally, the authors reported a reduced likelihood of ischemia-mediated ectopicity, attributing this to an increased electrotonic sink due to graft presence. This interpretation aligns with Gibbs et al. [77] and Yu et al. [11], who emphasized source-sink mismatch as the mechanism suppressing graft-originated ectopy.

Overall, these works indicate that graft placement and infarct-related substrate heterogeneity are the principal determinants of VT inducibility, while

increased electrical maturity of grafted hiPSC-CMs appears key to reducing arrhythmic burden. Orientation and anisotropy of the graft play a secondary, but non-negligible, role in reentry generation [11, 76, 152, 154].

2.3.4 Future directions for digital twin–guided regeneration

Together, these advances show that computational modeling provides unique mechanistic insights into how chronic MI substrates and remuscularization therapies interact. Future efforts should aim to integrate more realistic scar heterogeneity, graft maturation dynamics, and electrophysiological characteristics, paving the way for predictive digital twin–based virtual trials of regenerative therapies.

2.4 Parallel computation of *in silico* electrophysiology

With the growing need to investigate broader ranges of physiological and pathological conditions, combined with experimental advances, cardiac simulations have reached a level of complexity where answering key scientific questions demands expensive high-performance clusters operating for extended periods [13]. To ensure feasibility, simulation environments must therefore rely on efficient solvers carefully optimized for modern hardware architectures.

A considerable number of software solutions exist today for solving the bidomain and monodomain formulations in cardiac electrophysiology. Commercial multiphysics solvers are widely available and capable of tackling electrophysiological problems. However, most of these platforms were not originally tailored to simulate cardiac excitation phenomena, and consequently lack the highly specialized memory and computational optimizations that large-scale electrophysiology now requires [10, 23, 98].

An exception is the framework *Alya* introduced by Vázquez et al. [20]. Implemented in C++, *Alya* is a multiphysics solver based on the FEM for spatial integration and supports both explicit and implicit schemes for time integration. It was designed to handle extremely large-scale problems, particularly fluid dynamics and electromechanics governed by coupled PDEs and ODEs, and optimized for massively parallel execution. Parallelization is achieved through workload division into multiple cores using mesh partitioning and message passing interface, making it suitable for memory-distributed architectures, such as central processing unit-based high-performance clusters. In

addition, the developers created customized solvers for the extremely large linear systems of equations arising from these models, aligned with the parallel architecture [20].

Given the rising complexity of simulation studies and the importance of exploiting novel hardware architectures to accelerate calculations, the field has seen extensive development of in-house software tailored specifically to cardiac electrophysiology [23]. Many of these solvers have been made open-source, such as our own platform *ELECTRA* (see Section 1.6.3.6). Over time, some projects have been discontinued due to low adoption or limited maintenance, while others have been merged into larger initiatives. In the following, we highlight currently active open-source solvers specifically developed for cardiac applications and capable of solving at least the monodomain equation, all of which are of interest for this thesis.

One of the most widely adopted open-source electrophysiological solvers is *openCARP* [23]. Written in C++, *openCARP* shares several design philosophies with *Alya*, including parallelization based on mesh partitioning and message passing interface. Spatial and temporal integration are performed with the FEM and θ-schemes, respectively, while operator splitting enables fully explicit or semi-implicit solver schemes, with the reaction term always computed explicitly. Other open-source libraries are used to solve the sparse system of linear equations and the ODEs related to the reaction term. Typically, *openCARP* is run within the Python-based environment *carputils*, which provides a rapid and reproducible workflow for configuring simulations at the tissue and cellular level. Recent updates have added a browser-based interface for running and visualizing simulations, as well as GPU-based implementations, mainly targeting the reaction term of the reaction-diffusion system.

Another open-source solver is *MonoAlg3D*, presented by Sachetto-Oliveira et al. [155] and more recently extended by Berg et al. [156]. Implemented in C++, it focuses on the monodomain equation and leverages GPU-based parallelization. For temporal integration, it employs an adaptive Euler method, similar to that implemented in *ELECTRA*, which can be executed either on the central processing unit or the GPU. Stability is ensured by comparing the Euler explicit solution with a second-order Runge-Kutta method and adaptively reducing the time step until the specified error tolerance is satisfied [155]. Unlike *Alya*, *openCARP*, and *ELECTRA*, *MonoAlg3D* employs the finite volume method on hexahedral meshes for spatial integration. In this context, it implements a graph-based dynamic mesh refinement and derefinement strategy, referred to as the autonomous leaves graph, to enhance computational efficiency while preserving accuracy. Simulations have primarily been performed

on non-distributed memory architectures [155,156]. The software supports parallelization via the open multi-processing application programming interface for multi-core execution on the central processing unit or through NVIDIA CUDA for GPU–accelerated implementation of the conjugate gradient method used to solve the diffusion term [156]. Reported limitations include computational overhead from central processing unit–GPU communication in hybrid hardware configurations and workload imbalance across GPU threads caused by variable adaptive time steps [155, 156]. More recently, a web-based interface has been released [22], enabling interactive configuration and visualization of simulations.

Finally, Kaboudian et al. [21] introduced *Abubu.js*, a JavaScript library designed for GPU-based simulation and rendering of electrophysiological problems. This library abstracts WebGL functionality, simplifying development while enabling GPU-accelerated computing in web-native environments. The monodomain model is solved, with the forward Euler method used for temporal integration and the FDM for spatial discretization of the diffusion term [157]. The selected numerical methods produce nodal equations that can be independently solved in parallel GPU threads. Boundary conditions are handled with ghost nodes (node mirroring). Published cardiac electrophysiological simulations seem to have assumed isotropic conduction, likely to simplify the resolution of the diffusion term [21, 157]. To approximate $\nabla^2 V_m$, the authors implemented a 19-point second-order central FDM scheme, including cross-diagonal terms to improve accuracy in thin anatomical structures such as papillary muscles. Since WebGL was originally intended for efficient GPU-based rendering on the web rather than numerical computing, the authors had to overcome limitations of its render-oriented data structures to efficiently represent, store, and transfer 3D grid data between the central processing unit and the GPU [157].

2.5 Chapter summary

This chapter has reviewed recent advances in four interconnected areas of relevance to this thesis. First, CNN-based approaches for CMR segmentation were discussed, with emphasis on strategies to address data scarcity, enforce anatomical consistency, and quantify predictive uncertainty. Next, developments in EHT-based cardiac remuscularization were summarized, highlighting both preclinical and clinical progress, as well as its current challenges. The chapter then explored key breakthroughs in preclinical digital twinning at both cellular and tissue scales, with a particular focus on arrhythmicity analysis in

the context of cellular- and EHT-based remuscularization, followed by a review of specialized software and parallel-computing frameworks developed to accelerate *in silico* simulations.

Together, these advances underscore a convergence of biomedical imaging, regenerative therapy, and computational modeling. However, challenges remain in ensuring anatomical consistency in multi-modal real-world image segmentation, in efficiently simulating patient-specific electrophysiology at clinically relevant scales, and in predicting the safety and efficacy of novel therapeutic approaches with the aid of *in silico* methods. Addressing these gaps motivates the methodological developments and applications presented in the following chapters of this thesis.

CHAPTER 3

EXPERIMENTALLY-GUIDED IN SILICO DESIGN OF ENGINEERED HEART TISSUES TO IMPROVE CARDIAC ELECTRICAL FUNCTION AFTER INFARCTION

3.1 Methodology
- 3.1.1 Experimental analysis of *in vitro* EHTs
- 3.1.2 *In silico* analysis of EHTs

3.2 Results
- 3.2.1 EHT models *in vitro*-based calibration
- 3.2.2 *In silico* assessment of EHT designs
- 3.2.3 *In silico* analysis of the EHT-MI interaction

3.3 Discussion
- 3.3.1 *In silico* replication of *in vitro* electrophysiology
- 3.3.2 Small elongated pores accelerate EHT activation
- 3.3.3 EHT thickness role *in vitro*
- 3.3.4 EHT design determines activation of MI-coupled EHTs
- 3.3.5 Higher EHT conductivity lowers arrhythmic risk in MI-coupled EHTs

3.4 Limitations

3.5 Conclusion

Building on the advances reviewed in the previous chapter, this chapter develops computational methods for the study of EHTs. While recent progress has highlighted the promise of EHTs for cardiac remuscularization, many open

questions remain regarding how scaffold properties influence electrophysiological behavior, integration with host myocardium, and arrhythmogenic risk. To address these challenges, this chapter combines experimental data acquisition and processing with *in silico* modeling and simulation to systematically investigate the relationships between scaffold structure, electrical conductivity, and tissue-level electrophysiological function. A major aim is to ascertain the scaffold characteristics that enable EHTs to reproduce the electrophysiology of healthy myocardium.

The study begins with a calibration step based on the acquisition and processing of *in vitro* OM recordings from EHTs manufactured via melt electrowriting and loaded with hiPSC-CMs. From these data, we establish a linear relation between electrical conductivity, expressed as the longitudinal diffusion coefficient (LDC), and cellular alignment (CA) in the *in silico* EHT models. Once this conductivity-alignment relationship is defined, we perform a systematic evaluation of depolarization and repolarization dynamics across scaffolds with varying thicknesses and pore shapes and sizes. Finally, *in silico* EHTs are engrafted onto 3D slabs representing infarcted myocardium, where ATs, CVs and RTGs are quantified to assess conduction patterns and arrhythmic risk in the coupled EHT-host tissue system.

3.1 Methodology

Figure 3.1 depicts the four main tasks conducted in this work, one experimental task described in Section 3.1.1 and three *in silico* tasks described in Sections 3.1.2.2, 3.1.2.3 and 3.1.2.4. First, we acquired and analyzed electrophysiological data obtained from *in vitro* EHTs (Figure 3.1a). Next, we *in silico* replicated this experimental data (Figure 3.1b) by adjusting the model parameters. Subsequently, we *in silico* assessed the electrophysiological behavior of distinct EHT designs both before and after being implanted on a slab of MI tissue (Figure 3.1c and 3.1d, respectively).

3.1.1 Experimental electrophysiological analysis of *in vitro* EHT

3.1.1.1 Experimental data acquisition

Electrophysiological recordings from a 2D scaffold-free culture and four 3D scaffold-based EHTs were acquired and processed. Three different recordings were collected for each of the EHTs and one recording was collected for the

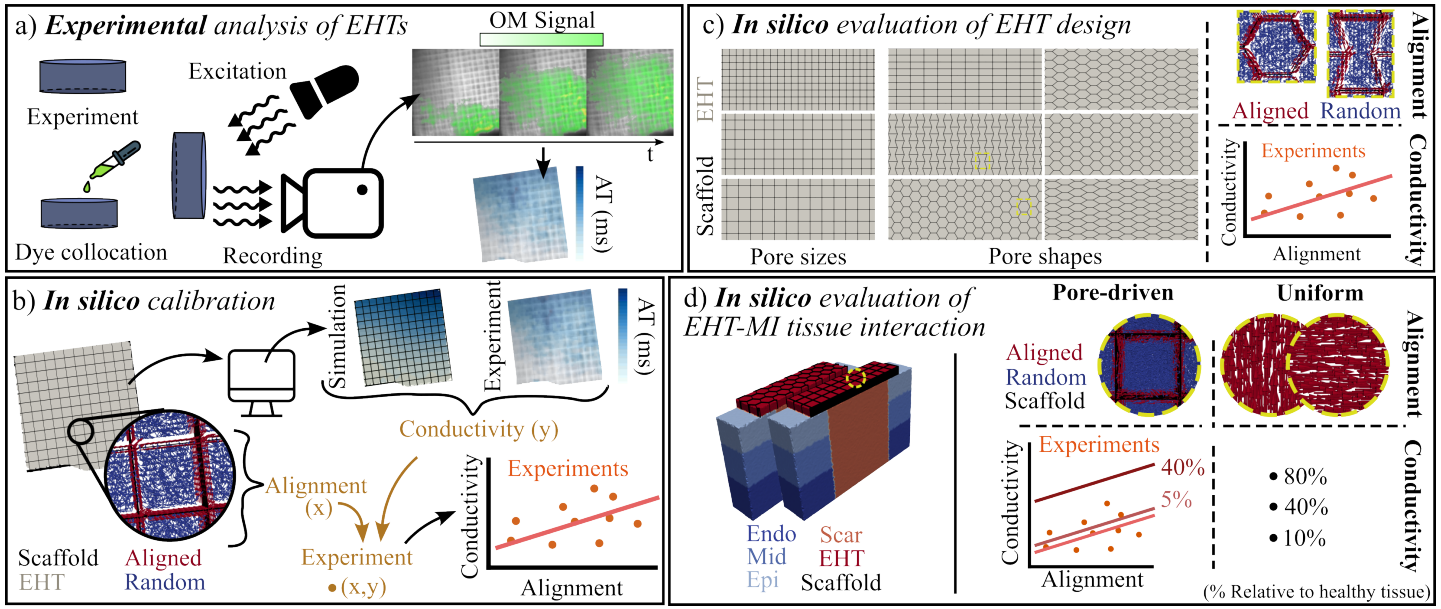


Figure 3.1: Experimental and *in silico* assessment of the EHT design. a- Experimental data acquisition by OM and resulting AT map for a square-pore EHT. b- *In silico* calibration of EHT models, with illustration of the comparison between experimental and simulated ATs and the derived CA-conductivity relation. c- *In silico* evaluation of EHT designs by electrophysiological analysis of different scaffold's pore sizes and shapes (left panel) and its definition of CA and conductivity (right panel). d- *In silico* evaluation of EHTs engrafted on a slab of MI tissue (left panel) and the pore-driven and uniform approaches used for defining CA and electrical conductivity in the engrafted EHT (right panel).

2D control culture, which rendered 13 electrical recordings for analysis. The results of the electrical propagation analysis served as a basis to evaluate the impact of the scaffold used to culture hiPSC-CMs. In particular, the alignment and maturation of hiPSC-CMs, which have been reported to be lower for 2D scaffold-free cultures than 3D EHTs [74], were considered as a function of the scaffold characteristics.

For EHTs, fiber scaffolds were printed in medical grade poly-ε-caprolactone (mPCL, Purasorb PC 12, Corbion) using a purpose-built melt-electrowriting device (QUT, Queensland, Australia). Of the 4 EHTs, 3 had square pores and 1 had regular hexagonal pores. All 2D and 3D experiments had a surface area of 5 x 5 mm^2 and, in the 3D cases, a thickness of 0.2 mm. The pore area was 0.04 and 0.42 mm^2 for square and hexagonal geometries, respectively. hiPSC-derived cells were produced in-house as described in [74] and embedded in growth factor reduced matrigel and fibrin for the square and hexagonal pore-shaped EHTs, respectively. Both hydrogels were expected to provide only a transient support and to quickly degrade, thus not interfering with cellular communication. The hexagonal pore EHT was made available from an ongoing investigation assessing culturing hydrogels and it contained 10% of human induced pluripotent stem cell-derived cardiac fibroblasts (hiPSC-CFs). The hydrogel-cells complexes were cast on the printed scaffolds, with similar cellular densities for all EHTs, and were cultured for 28 days. For the 2D culture, cells were plated on slide chambers (Ibidi).

High temporal and spatial resolution videos of Ca^{2+} transient activity in the EHTs were acquired by OM employing a MiCAM O5-Ultima CMOS camera (SciMedia, Costa Mesa, CA). Samples were stained by immersion in culture medium supplemented with Rhod-2 AM (Ca^{2+} sensitive dye, Invitrogen, Eugene, OR) at 5 µM for 30 min under incubation conditions (37°C, 5% CO_2). Blebbistatin (10 µM, Tocris Bioscience, St. Louis, MO) incubation during 30 min prevented motion artifacts. Ca^{2+} transients were acquired due to the increased recorded fluorescence amplitude associated with Ca^{2+} dyes compared to voltage dyes. After dye incubation, the EHTs were placed in a heated chamber (RC-27NE in a PM-6 heated platform, Warner Instruments) at 36.5°C with 1 mL pre-oxygenated Tyrode solution (supplemented with 30 mM 2,3-butanedione monoxime to prevent motion artifacts) and Ca^{2+} concentration was mapped. EHTs were excited using a high intensity LED illumination system through an excitation filter of 530 nm (LEX2-LZ4, SciMedia, Costa Mesa, CA, USA). Emitted fluorescence was collected through a THT-macroscope (SciMedia) and detected with a camera equipped with a 575/15 nm band-pass filter. A sampling frequency of 500 Hz and a spatial resolution of 100 x 100 pix-

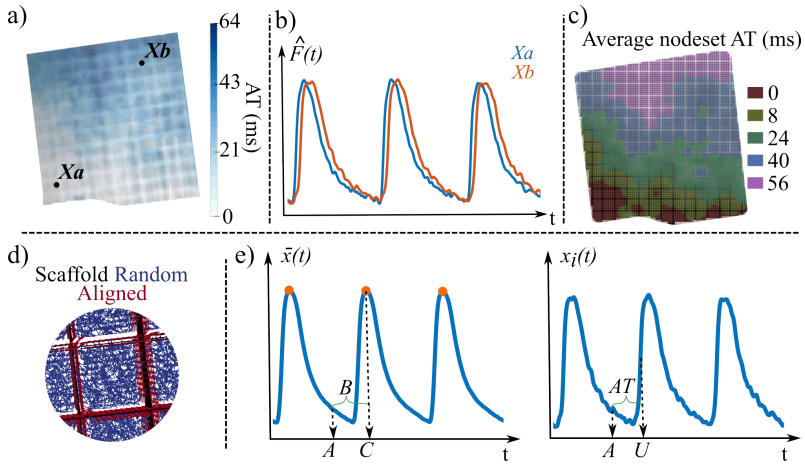


Figure 3.2: OM processing of *in vitro* EHTs. a- Experimental AT map. b- Normalized OM signals for points X_a and X_b. c- *In silico* mesh generation and node set definition. d- Tissue node alignment, with red and blue arrows representing aligned and random orientations, respectively. e- AT calculation for an individual AP. A is the time reference computed from the time of peak C of the average EHT AP, $\overline{x}(t)$, minus a predefined distance B. The time U corresponds to the maximum derivative of the AP upstroke for the individual signal $x_i(t)$. AT is the time difference between A and U.

els per frame, with a field of view of 3.1 mm, were used. The EHTs were field-stimulated with two platinum electrodes at 1 and 2 Hz [158], using an A385 stimulator (World Precision Instruments, Sarasota, FL) to apply monopolar pulses of 70 mA amplitude and 3 ms duration. After a short stimulation period to allow the EHTs to adjust to the pacing rate, 20-second recordings were acquired.

3.1.1.2 Experimental data processing

OM signals were analyzed using custom-written software [159]. A region of interest was manually defined for each mapped EHT. Baseline drift in the signals was attenuated by high-pass filtering with a cut-off frequency of 0.4 Hz. High-frequency noise was removed by using an adaptive spatio-temporal Gaussian filter with automatic selection of its parameter values as a function of the recording characteristics [159, 160]. Figure 3.2b presents the Ca^{2+} signals corresponding to the points X_a and X_b marked in the EHT of Figure 3.2a, which were obtained after the application of the described processing and subsequent normalization. From the individual signals, denoted by $x_i(t)$, $i = 1, ..., N$, with N the total number of pixels in the region of interest, a mean Ca^{2+} signal,

$\overline{x}(t)$, was calculated by first aligning the signals and subsequently averaging them. Cross-correlation between each individual signal $x_i(t)$ and the mean signal $\overline{x}(t)$ was computed, and only those individual signals with maximum correlation above 0.86 were used for subsequent analysis. Next, local ATs were calculated for each $x_i(t)$, $i = 1, ..., N$, as exemplified in Figure 3.2e. Specifically, the AT value for $x_i(t)$ and a given beat was computed as the time elapsed between a fixed time reference, denoted by A, and the time associated with the maximum derivative of $x_i(t)$ in that beat, denoted by U. The reference A was defined from the mean signal $\overline{x}(t)$ in the given beat by subtracting a constant B from the time C associated with the maximum $\overline{x}(t)$ value. Thus, a unique reference A was set for AT calculation in all pixels. A final AT value was computed for each pixel as the median of the ATs of all beats.

As depicted in Figure 3.2a, an AT map was obtained from the ATs of all pixels. Image processing techniques, including opening, closing, and median filtering operations, were applied to remove isolated clusters of cells. The AT values from all pixels were clustered with a dendrogram based on the Euclidean distance among cluster centroids, as illustrated in Figure 3.2c. This served to visually assess depolarization propagation and to define the stimulation region when using *in silico* models (see Section 3.1.2.5).

3.1.2 *In silico* electrophysiological analysis of EHTs

3.1.2.1 Cellular alignment and conductivity of *in silico* models

Three sets of computational simulations were conducted, as shown in Figure 3.1b-d. Both pore-driven and uniform approaches were used to define the CA and conductivity values in the *in silico* analysis. The CA was defined as:

- **Pore-driven:** hiPSC-CMs located in the center of the scaffold pore were set to be randomly aligned, while the hiPSC-CMs near the pore walls were oriented following the pore wall direction, as observed experimentally [74].
- **Uniform:** all hiPSC-CMs in the EHT were oriented either randomly or following a unique direction.

The conductivity was defined as:

- **Pore-driven:** the LDC was defined based on the percentage of CA associated with the scaffold architecture. Specifically, each *in vitro* EHT

Table 3.1: CA and conductivity values used in each set of *in silico* simulations. The offset percentage applies to the linear CA-conductivity relation and it is relative to the conductivity in the healthy myocardium.

Case	CA	Conductivity
Experimental replication	pore-driven	determined
Not engrafted EHT designs	pore-driven	pore-driven
Engrafted EHT designs	pore-driven	pore-driven (5% offset)
	pore-driven	pore-driven (40% offset)
	uniform	uniform

experiment was represented by an *in silico* model and the percentage of pore-driven CA was paired to the *in silico* LDC required to replicate the maximum AT in the experiment. All the CA-LDC pairs were fitted using a linear function, which allowed setting the EHT conductivity for any EHT design.

- **Uniform:** the conductivity in the EHT was set to a constant value, which was made relative to the conductivity in the healthy myocardium.

Table 3.1 presents a summary of CA and conductivity definitions for each of the three sets of *in silico* simulations. The following sections describe the modeling and simulation in each of the three sets and present the methods used to run the simulations and compute the electrophysiological markers derived from those simulations.

3.1.2.2 *In vitro*-based construction of *in silico* EHT models

In silico scaffold-free and scaffold-based models were built. For calibration purposes, we generated *in silico* scaffold meshes that allowed reproducing the experimental results described in Section 3.1.1.2. Square pore-shaped scaffold meshes were automatically constructed from the corresponding experimental images. For the hexagonal pore-shaped scaffold, experimental images showed substantial deformation associated with contraction-relaxation cycles prior to its inhibition with blebbistatin. This deformation was significantly more accentuated in the hexagonal pore-shaped scaffolds due to their lower stiffness compared to square pore-shaped scaffolds [70]. Therefore, a semiautomatic approach was developed to generate the *in silico* meshes. This included threshold and manual segmentation in combination with skeletonization to determine the scaffold profile from microscopical images. The *in silico* meshes were defined

from the skeleton's binary images. The scaffold wall directions were subsequently identified.

The *in silico* EHT models were built by assembling the *in silico* scaffold meshes with coupled hiPSC-CMs. The spatial resolution of these models was fixed at 31 µm, which agrees with the pixel resolution of the OM experiments. The spatial discretization was implemented using quadrilateral and hexahedral elements for 2D and 3D models, respectively. For the 2D scaffold-free model, CA for every node of the tissue was assigned from a uniform statistical distribution spanning 0-180 degrees in plane. For 3D scaffold-based EHT models, tissue nodes within a distance of 27 µm to the scaffold were assigned a CA according to the direction of the pore walls, as depicted in Figure 3.2d. This distance threshold was chosen in agreement with experimental measures reported in the literature [70, 74]. The CA assigned to every other node far from the scaffold was extracted from a uniform random distribution, as in the 2D scaffold-free case. The CA along the thickness was kept constant due to the lack of accurate experimental information.

Conductivity was considered to be orthotropic with transverse isotropy, i.e. with equal transverse and sheet-normal conductivities (see Section 1.6.3.5). A transverse-to-longitudinal conductivity ratio of 0.25 was used, which led to CV anisotropy in agreement with that reported for cardiac tissue [120]. As mentioned, the LDC was adjusted so that the maximum AT values in the simulations of square and hexagonal pore-shaped EHTs matched the corresponding experimental AT values calculated as described in Section 3.1.1.2.

To extrapolate the LDC values to EHT designs other than those used for model calibration, the data representing the relationship between conductivity and CA for all experimentally based simulations were fitted with a linear polynomial using a least-squares criterion. The percentage of CA was calculated by dividing the number of tissue nodes aligned to the scaffold fibers by the total number of nodes.

3.1.2.3 *In silico* testing of scaffold designs for EHTs

Once model conductivity values were set based on the calibration described in Section 3.1.2.2, additional EHTs models were built to assess the impact of variations in scaffold pore geometry and size, and in scaffold thickness.

Scaffold pore shapes included square, rectangle, hexagons with half angles of 60°, 50°, 40° and 30°, and auxetic architectures perpendicular and parallel to the depolarizing direction. The 3D EHTs with all these pore geometries

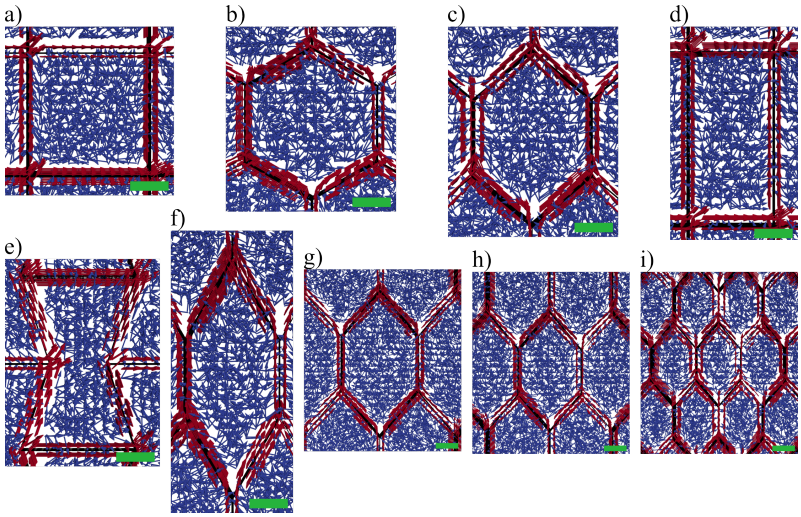


Figure 3.3: EHT pore architectures and fiber alignments: a- square, d- rectangle, e- auxetic, b-, c- and f- hexagonal with 60°, 50° and 30° half angles and 0.4 mm^2 area; g-, h- and i-: 40° half-angle hexagons with 0.6, 0.4 and 0.2 mm^2 area. Red and blue arrows represent aligned and random orientations, respectively, while black lines depict the scaffold's pore walls. The length of the green scale bars is 0.2 mm.

were tested for 0.2, 0.4 and 0.6 mm^2 pore areas, as shown in Figures 3.3g-3.3i for the 40° elongated hexagon. Only the 0.4 mm^2 pore area was studied for 2D scaffold-based EHTs.

Rectangular tissue meshes of 4 x 10 mm^2 were generated for 2D EHTs. For 3D EHTs, tissue meshes of the same surface size with a thickness of 0.2 mm were built. This thickness enhanced cell viability compared to larger thicknesses [161]. The tissue model was discretized with 50 µm-side square and hexahedral elements for 2D and 3D cases, respectively [115].

Scaffold meshes were built covering the corresponding tissue. The scaffold and tissue centroid positions were matched. CA was defined according to the scaffold wall directions, as described in Section 3.1.2.2. To emphasize the effect of the scaffold's pore structure, a higher distance threshold of 55 µm was used to define tissue nodes CA (Figure 3.3).

The LDC was computed as a function of the CA percentage according to the linear relationship established in Section 3.1.2.2. To further describe the effect of the scaffold's characteristics on electrical activation while taking into account that the scaffold walls may orient cells transversely to the propagating wavefront, we additionally calculated a longitudinal cellular alignment (LCA)

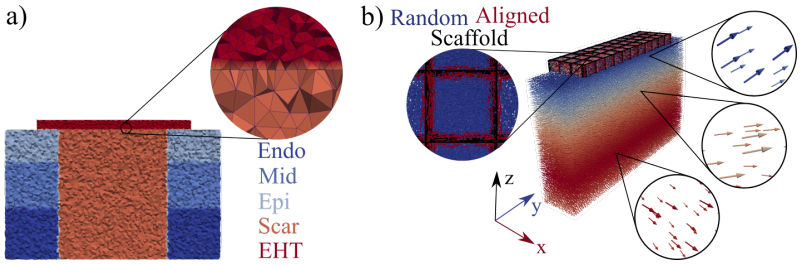


Figure 3.4: *In silico* model of an EHT engrafted on a slab of infarcted myocardial tissue. a- Myocardial tissue and EHT mesh. b- The CA of the myocardial tissue and the EHT cultured in a square pore-shaped scaffold.

metric different from the CA metric. The LCA metric was defined as the percentage of tissue nodes oriented within $\pm$ 45° from the overall depolarization direction.

Next, we modeled variations in the EHT thickness by varying it from 0.2 to 0.6 mm, with the surface area of the tissue set at 3 x 6 mm^2. The spatial resolution was equal to 50 µm in the three dimensions, as in the above described tests. The scaffold size matched the tissue size, with a 0.2 mm-side square pore. The CA was set using a distance threshold of 27 µm and the LDC was obtained from the linear relationship established in Section 3.1.2.2.

3.1.2.4 *In silico* models coupling EHTs and infarcted tissues

The EHT models of previous sections were coupled to a slab of myocardial tissue. Figure 3.4 shows an example of an *in silico* transmural tissue slab of healthy and infarcted tissue with a size of 2 x 10 x 6 mm^3 on which a 2 x 7 x 0.5 mm^3 EHT was engrafted. The myocardial thickness was chosen based on the human ventricular wall size [154]. The EHT thickness was representative of modern scaffolds based on melt electrowriting [70]. The integrated EHT-myocardium mesh was discretized with 702 486 irregular tetrahedrons interconnecting 125 202 nodes. The mean edge length of the mesh was 120 and 50 µm for the myocardial and EHT regions, respectively. Transmural heterogeneities were represented by assigning 40%, 35% and 25% of the nodes with endocardial, mid-myocardial and epicardial cell properties. A scar of 2 x 5 x 6 mm^3 was positioned in the center of the tissue slab to model a chronic transmural MI.

Orthotropic conductivity with transverse isotropy was considered for the myocardial tissue and the EHT. The LDC in the myocardium was set to 0.0013

cm^2/ms (equivalent to 0.13 S/m for a membrane surface-to-volume ratio of 1000 cm^{-1} and capacitance per unit area of 1 $\mu F/cm^2$) and the scar was defined as a non-conducting region. The LDC and CA in the EHT were set as pore-driven or uniform, as described in Section 3.1.2.1. In the pore-driven approach, a distance threshold of 55 µm for the cells with respect to the scaffold walls was used for computing the CA metric. If the calculated EHT LDC was below 1% of that in the healthy myocardium, a 5% offset was added to avoid conduction block at the EHT. For both the myocardial tissue and the EHT, the transverse-to-longitudinal conductivity ratio was set to 0.25.

The CA in the myocardium was linearly varied in a 120° range from epi- to endocardium. The EHT was oriented in three different ways, representing the EHT being parallel and perpendicular to the epicardial CMs and parallel to the LAx of the LV. This was equivalent to the epicardial cells being oriented with angles of 0°, 90° and 30° from the longitudinal direction of the EHT. Since similar electrophysiological outcomes were obtained for different pore shapes with a common area of 0.4 mm^2 when the three different EHT alignments were tested, the following analyses were only performed with the overall EHT architecture being aligned parallel to the epicardial CMs.

As shown in Table 3.1, three groups of numerical simulations were conducted to evaluate electrophysiological changes when the EHT was engrafted on the infarcted tissue slab. In the first group (C3G1), we tested different scaffold pore shapes and sizes with pore-driven EHT CA and using the minimum value of EHT conductivity that allowed electrical wave propagation in the entire EHT-myocardial tissue. In the second group (C3G2), we tested different pore shapes with an equivalent area of 0.4 mm^2, but this time the EHT conductivity was increased by adding an offset of 40% of that in healthy tissue. In the third group (C3G3), we tested completely random, parallel and perpendicular CA in the EHT with respect to the epicardial CMs and we also varied the conductivity to be 10, 40 and 80% of that in the healthy tissue.

3.1.2.5 Electrophysiological simulations

The AP models of Paci et al. [110], from 2013, and the O'Hara et al. [51] were used to computationally describe the cellular electrophysiology of ventricular-like hiPSC-CMs and human adult ventricular CMs, respectively. Electrical impulse propagation was described by solving the monodomain model (see Section 1.6.1) with the in-house developed software *ELECTRA* (see Section 1.6.3.6). All simulations were performed on a personal computer equipped with an Intel® Core® i7-9700K microprocessor clocked at 3.6 GHz and with

32 GB of RAM.

After initializing the models to steady-state, each simulation consisted of three 1 Hz-paced cycles, with the last cycle used for electrophysiological evaluation. The I_f in the Paci model was inhibited in the simulations of *in vitro*-based EHT models so that the APs in the EHT were elicited by the applied external stimulation, which has been observed to occur more likely than self-driven EHT depolarization in OM experiments and once the EHT has been engrafted on the myocardial tissue [11]. In simulations of EHTs not coupled to myocardial tissue, stimuli of 5-nA magnitude and 2-ms duration were applied to depolarize the EHT. In simulations of coupled EHT-myocardial tissue, stimuli of 80-µA magnitude and 1-ms duration were applied to the healthy myocardium.

For *in silico* EHTs reproducing *in vitro* results of square and hexagonal pore-shaped EHTs, node sets were defined following the experimental AT-based classification, as described in Section 3.1.1.2 and depicted in Figure 3.2c. The stimulus current was applied onto the node set initiating the depolarization (i.e. with the shortest AT), shown in red in the figure. In all other simulations with *in silico* EHTs not based on *in vitro* results, the stimulus was applied onto a half millimeter side of the EHT or EHT-myocardial model covering their entire cross sections.

3.1.2.6 Computation of electrophysiological markers

Numerically computed V_m was saved with a time step resolution of 1 ms. AT, action potential duration at 90% repolarization (APD_{90}), repolarization time, and RTG were computed for each node in the EHT or coupled EHT-myocardium meshes. Mean CV was computed on the overall EHT.

In brief, AT was calculated as the difference between a fixed time reference and the time instant when the AP upstroke crossed 0 mV, i.e. changed from negative to positive values. APD_{90} was defined as the time elapsed from the time instant of maximum voltage derivative in the AP upstroke to the time when repolarization from AP peak to diastolic V_m reached 90%. The repolarization time was measured as the sum of AT and APD_{90}. To compute RTG, the RTG vector between two nodes was first defined as the ratio of the difference between the two repolarization times and their Euclidean distance. Next, RTG was calculated for a given node as the mean of the RTG vectors between this node and its neighboring nodes within a radius of 210 µm. This radius value was taken to be the maximum edge length of the coupled EHT-myocardial mesh so that at least one neighboring node was included in all node-wise RTG computations, while avoiding an RTG smoothing effect due

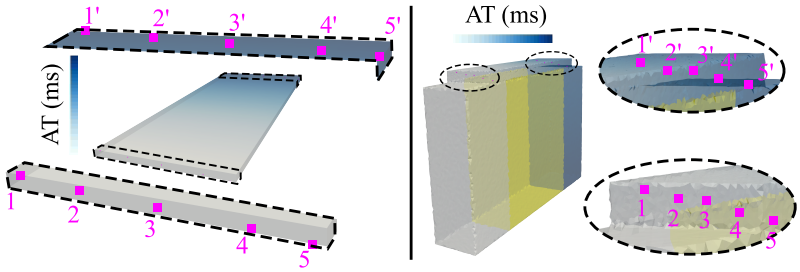


Figure 3.5: The five linear paths used for computing the mean EHT CV are depicted for the individual (left) and on MI slab-engrafted (right) EHT. Each path is the line between X and X' with $X = 1, 2, 3, 4, 5$.

to averaging if higher radius values were used. We evaluated RTG only for coupled EHT-myocardial tissue, in which larger repolarization heterogeneities can be expected. In particular, the mean RTG magnitude at the EHT region was analyzed.

For mean CV calculation, we manually selected five nodes in both extremes of the EHT covering the whole thickness as observed in Figure 3.5. We calculated the distances and AT differences for the five corresponding linear paths and we computed the ratio between distance and time for defining the path-wise CV values. The mean EHT CV was defined as the mean of these five individual CV values. In Section 3.2, relative EHT CVs are shown. The reference CV was set to the CV of the EHT with the largest square pore shape, when CA and conductivity were pore-driven, and to the EHT with hiPSC-CMs perpendicularly aligned and with 10% relative conductivity, when CA and conductivity were uniform.

3.2 Results

3.2.1 *In vitro*-based calibration of *in silico* EHT models

Model calibration of experimentally-based EHTs identified LDCs leading to simulated activation patterns and maximum AT values closely reproducing the corresponding experimental ones. The experimental AT maps served as a basis to generate *in silico* EHT models that reproduced such maps. The CA in the *in silico* models was defined based on the experimental observations and, next, the LDC value was set so that simulated and experimental maximum ATs matched.

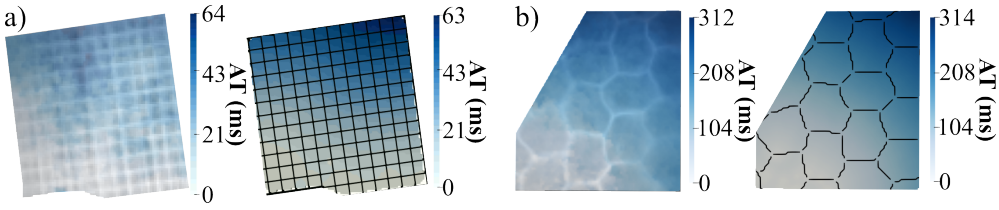


Figure 3.6: Experimental (left) and simulated (right) AT maps for square (a) and hexagon (b) pore-shaped scaffolds.

Table 3.2: Pore shape, CA and LDC values for different experimentally-based *in silico* EHT models to reproduce *in vitro* AT values. S: Square, H: Hexagon and (-): 2D scaffold-free.

Pore shape	-	S	S	S	S	S	S	S	S	S	H	H	H
CA (%)	0	39.3	39.9	46.9	39.5	38.4	40	39.3	40.3	40	8.1	8.3	7.9
LDC (10^{-5} cm^2/ms)	0.35	1	1	1	3.5	2.5	3.5	0.43	1	0.75	0.13	0.2	0.1

Specifically, LDC values ranging from 1.35×10^{-6} to 3.5×10^{-5} cm^2/ms led to simulated and experimental maximum ATs differing by less than 2 ms in all tested cases. Figure 3.6 depicts examples of experimental and simulated AT maps for square and regular hexagonal pore-shaped scaffolds. Experimentally measured maximum ATs were, on average, 94 ms for square and 256 ms for hexagonal pore-shaped EHTs, as illustrated in Figure 3.6. The delayed activation of the hexagonal architecture was in correspondence to the lower CA (mean 8.11%) of this pore shape and size compared to the square architecture (mean 40.4%). The identified LDC values were, on average, 1.56×10^{-6} cm^2/ms for hexagons and 1.63×10^{-5} cm^2/ms for squares. Table 3.2 shows the CAs and LDCs used on the *in silico* experimentally-based EHTs for achieving a maximum simulated AT similar to the experimental case. The fitted linear relationship between CA and LDC was $y = 3.8x + 4.8$, where x is the percentage of CA and y is the LDC in 10^{-7} cm^2/ms.

To sum up, the simulated EHTs replicated the *in vitro* observations and allowed inferring EHT conductivity values, represented as the LDC, in function of the CA.

3.2.2 *In silico* assessment of EHT designs

We compared electrical activation for 2D versus 3D scaffold-based EHTs. For this comparison, the 3D EHTs had the same pore geometry and size as the 2D EHTs and presented equal characteristics for all layers along the EHT thickness. Numerical simulations showed that the maximum AT was very

similar for the 2D and 3D EHTs. The mean difference in maximum AT over all tested pore geometries was equal to 1.75 ms. In view of these results, subsequent analysis was performed for 3D EHTs only.

Next, we assessed CA for scaffolds with different pore geometries and sizes. Square and rectangle-pore shaped scaffolds presented higher CA than 60° half-angle hexagon pore-shaped scaffolds. The CA increased with hexagon's elongation. Auxetic pore-shaped scaffolds led to the highest CA percentages among all studied designs. Regarding the relationship between CA and pore size, we found a clear inverse relation between them. Figure 3.7b summarizes the CA percentages calculated for different pore shapes and sizes.

The maximum ATs and relative CVs for each of the EHTs modeled by varying the pore geometry and size are shown in Figures 3.7a and 3.7d, respectively. The LDC was calculated in each case as a function of the CA percentage presented in Figure 3.7b. As can be observed, faster EHT activation was found as the pore size was reduced. Mean maximum AT was 402, 367.2, and 313.5 ms for the 0.6, 0.4, and 0.2 mm^2 pore size scaffolds over all pore geometries. Similarly, the mean relative CV over all pore shapes increased by 8.32% and 27.3% in the 0.4 and 0.2 mm^2 pore size scaffolds, respectively, when compared with the 0.6 mm^2 pores. Square and rectangle pore-shape scaffolds rendered only slightly different electrical propagation patterns, which were always faster than those for regular hexagons. As hexagons became more elongated, CA increased, which translated into higher conductivity, leading to lower ATs and higher CVs than for square and rectangle pores. Even though auxetic pores were associated with higher CA, and thus higher LDC, than 30° elongated hexagons, faster propagation of the electrical excitation was observed for the most elongated hexagonal pores. The reason for this is the fact that more fibers were oriented parallel to the depolarizing direction for this pore shape than for auxetic, square, and rectangular pore shapes. Figure 3.7c shows that the LCA was more than 18% larger for the 30° elongated hexagons than for all other pore geometries. Furthermore, as pore size was reduced, the number of fibers oriented parallel to the propagation wavefront markedly rose for all hexagonal geometries, thus contributing to explain the corresponding increment in CV (Figure 3.7d) and reduction in maximum AT (Figure 3.7a).

Also, we evaluated the effects of varying the scaffold thickness. Thicknesses of 0.2, 0.4, and 0.6 mm rendered equal activation patterns and a maximum AT of 191 ms as well as an equal mean CV of 3 cm/s.

In conclusion, the fastest activation was found for the EHTs with the smallest and most elongated hexagons, which better reproduced cardiac anisotropy.

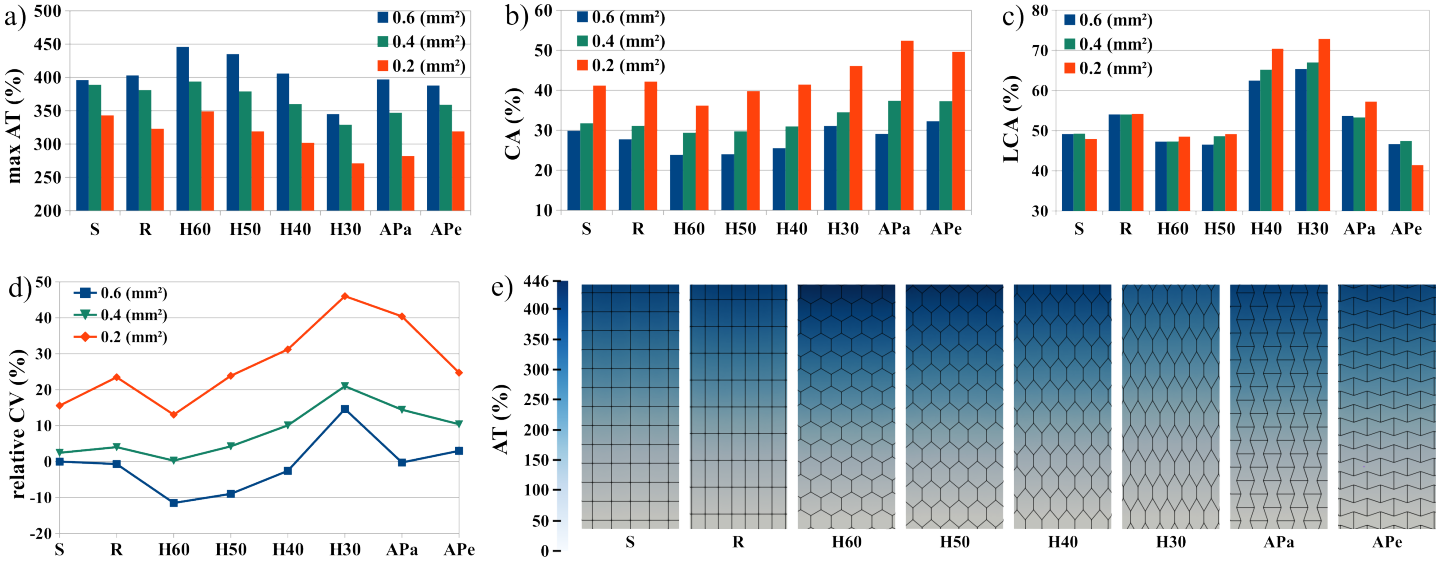


Figure 3.7: Maximum ATs, overall CA and LCA and relative CV percentages are shown in panels a, b, c and d, respectively, for 3D EHTs with different scaffold pore shapes and sizes. e- AT maps for pore geometries with an equivalent pore area of 0.6 mm^2. S: square, R: rectangular, APa: parallel-oriented auxetic, APe: perpendicular-oriented auxetic and HX: hexagonal with half angle of X degrees.

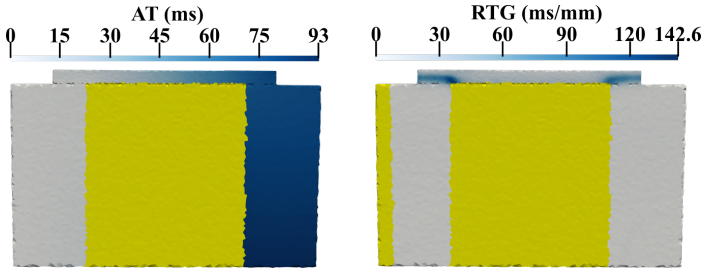


Figure 3.8: AT map (left) and RTG map (right) for the most elongated hexagonal pore shape with a pore size of 0.4 mm^2 (C3G1 group of simulations). Yellow areas depict tissue regions where the variable of interest was not computed (infarction scar and stimulation region).

The EHT thickness played a secondary role.

3.2.3 *In silico* analysis of the interaction between EHT and infarcted tissue

3.2.3.1 Role of scaffold pore shape and size in the EHT-myocardium interaction

The EHT models obtained by varying the scaffold's pore shape and size were engrafted on a tissue slab containing healthy and infarcted tissue. To avoid conduction block, we added an offset equivalent to 5% of the healthy myocardial electrical conductivity to the EHT conductivity obtained from the CA-conductivity relationship computed in Section 3.2.1 (C3G1 group of simulations). Maps depicting AT and RTG for an EHT with a 30° hexagon pore of 0.4 mm^2 engrafted on a tissue slab are shown in Figure 3.8. The maximum AT, relative CV and mean RTG for the simulations using different EHT designs can be seen in Figure 3.9.

Rectangular pores led to faster conduction than square pores in the coupled EHT-myocardium, with the relative CV being 5.8% higher for the rectangular than the square pore geometry for 0.2 mm^2 pores. In addition, lower ATs and higher CVs were obtained when the auxetic pore was oriented parallel rather than perpendicular to the depolarization direction. The largest relative CV difference of 8.27% between these two pore orientations was found for the smallest pore size. An increment in CV, and consequently a decrease in AT, was measured with hexagonal elongation. The mean over all pore sizes of the relative CV in the EHT-myocardium increased from 2.7% to 12% for the regular and 30° elongated hexagons, respectively. The most elongated

hexagons yielded faster conduction than all the other pore geometries, reaching the highest relative CV of 14.8% and the lowest maximum AT of 89 ms for 0.2 mm^2 pores.

Overall, the ATs for the EHT-myocardium were higher for 0.6 than for 0.2 mm^2 pores for all pore geometries. Slight mean increments in the relative CV of 1.53% and 3.7% were measured when the pore size was reduced from 0.6 to 0.4 and from 0.4 to 0.2 mm^2. Higher variability in the relative CV and maximum AT values was found for the coupled EHT-myocardium when smaller pore sizes were assessed. Maximum relative CV differences of 14.3%, 10.9%, and 6.9% were found for 0.2, 0.4, and 0.6 mm^2 pore sizes, respectively, when different pore shapes were tested. This suggested that scaffold pore shapes had a larger impact on CV, and consequently on depolarization times, when the pore size was smaller.

Different pore shapes did not lead to significantly different repolarization duration in the EHT-myocardium or RTG in the EHT. Differences in the mean RTG over different pore geometries were as low as 1.12, 1.15 and 0.88 ms/mm for 0.2, 0.4 and 0.6 mm^2 pore sizes, respectively. Thus, the scaffold pore shape played an insignificant role on RTG. The lowest mean RTGs were associated with the auxetic shape aligned with the depolarization direction (see Figure 3.9c).

The mean RTGs in the EHT were lower for decreasing pore sizes, with the mean RTG over all pore shapes decreasing by 0.58 ms/mm for 0.4 with respect to 0.6 mm^2 pores and by 1.02 ms/mm for 0.2 with respect to 0.4 mm^2 pores.

3.2.3.2 Role of EHT conductivity and CA in the EHT-myocardium interaction

Additional groups of simulations (C3G2 and C3G3) were conducted to assess the impact of both EHT conductivity and CA on the coupled EHT-myocardium electrophysiology, as described in Section 3.1.2.4.

For simulations with EHTs having 0.4 mm^2 pore size and the EHT conductivity being incremented by an offset equivalent to 40% of the healthy myocardium conductivity (C3G2), the maximum CV increment in the EHT was found for the 30° half-angle hexagonal pore shape (7.6%), as shown in Figure 3.10b. As a consequence, the maximum AT in the EHT-myocardium attained the lowest value of 46 ms for the same pore architecture (see Figure 3.10a). Similarly to the results reported for *in silico* representations of not engrafted EHTs, the CV in the EHT raised with hexagonal pore elongation (around 2%

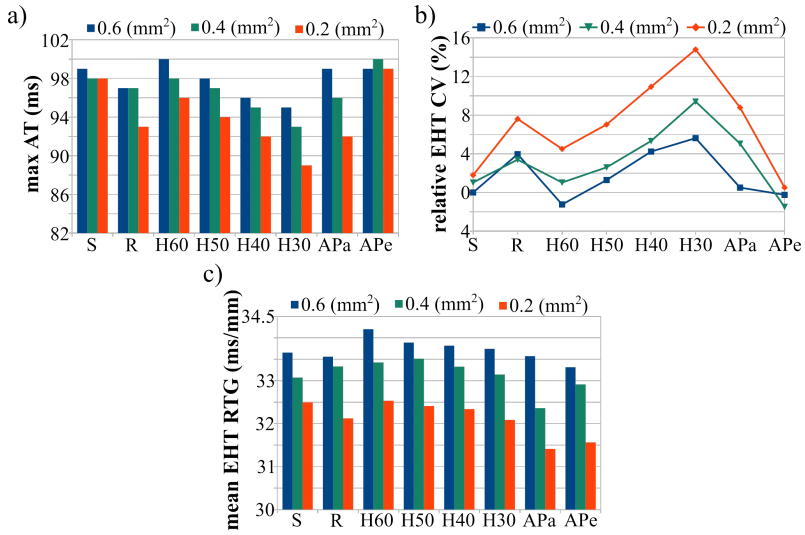


Figure 3.9: Maximum AT (a), relative EHT CV (b) and mean EHT RTG (c) for different scaffold pore shapes and sizes (C3G1 group of simulations). S: square, R: rectangular, APa: parallel-oriented auxetic, APe: perpendicular-oriented auxetic and HX: hexagonal with half angle of X degrees.

for elongation step as depicted in Figure 3.10b).

When the EHT conductivity and CA were uniform (C3G3), we observed large variations in the relative CV and maximum AT on the EHT and on the whole EHT-myocardium, respectively. As depicted in Figure 3.11a, the perpendicular CA of the hiPSC-CMs led to total ATs of 109, 62, and 50 ms for 10%, 40% and 80% of EHT conductivity relative to healthy myocardium. For parallel alignment, the total ATs were the lowest, with values of 66, 42, and 36 ms (93.6%, 191.4% and 281% relative CV increments, respectively) for increasingly higher EHT conductivity. Generally, the largest AT reductions and CV increments were found when the relative EHT conductivity increased from 10% to 40%, while the increase from 40% to 80% led to smaller AT reductions and CV increments, respectively. The differences in maximum AT over the three analyzed alignments were 43, 20, and 14 ms for 10%, 40% and 80% relative EHT conductivity, respectively. Differences in relative CV over the studied alignments were 93%, 191% and 281% for the three EHT conductivity cases. Increasing the EHT conductivity stressed CV variations in the EHT while it attenuated discrepancies in the depolarization times in the whole EHT-myocardium due to different CA.

In terms of mean RTG in the EHT after being coupled to the myocardium,

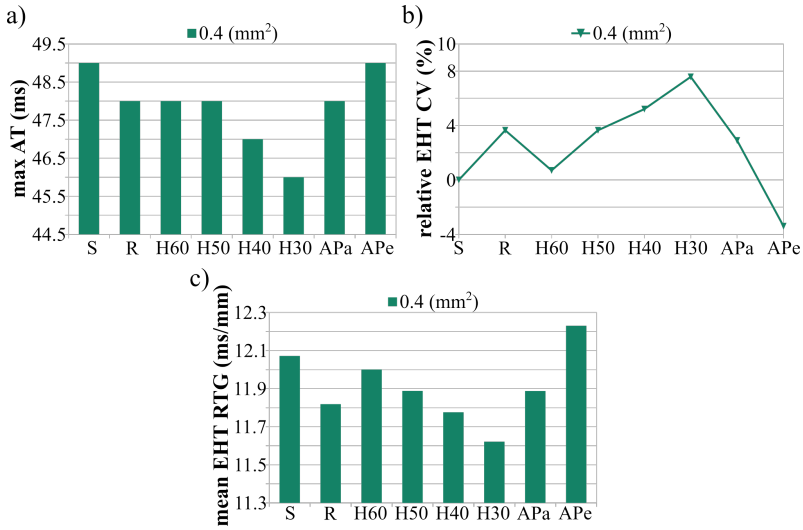


Figure 3.10: Maximum AT (a), relative EHT CV (b) and mean EHT RTG (c) for the C3G2 group of simulations. EHTs had pore-driven CA and conductivity, 0.4 mm^2 pore size scaffolds were used and the conductivity was incremented by an offset equal to 40% of that in healthy myocardium. S: square, R: rectangular, APa: parallel-oriented auxetic, APe: perpendicular-oriented auxetic and HX: hexagonal with half angle of X degrees.

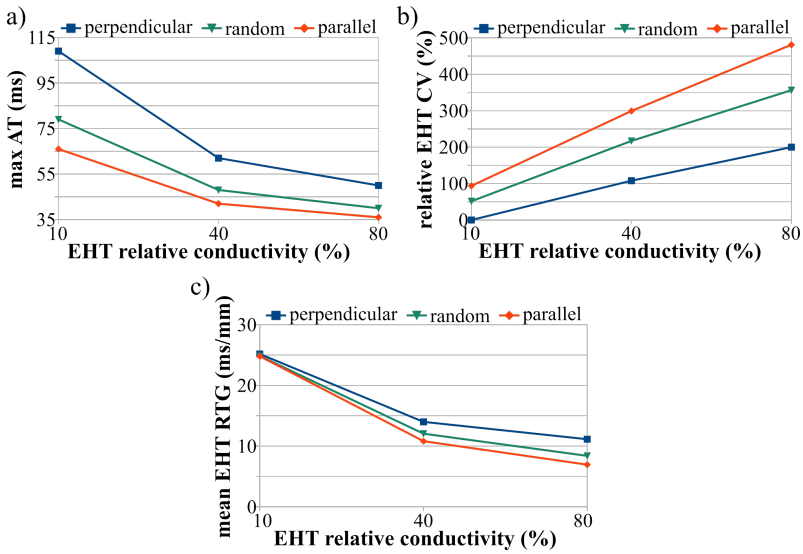


Figure 3.11: Maximum AT (a), relative EHT CV (b) and mean EHT RTG (c) for the C3G3 group of simulations where EHTs had uniform CA and conductivity. EHTs with conductivity of 10%, 40% and 80% of that in healthy myocardium were evaluated with random, parallel or perpendicular CA with respect to the epicardial cells.

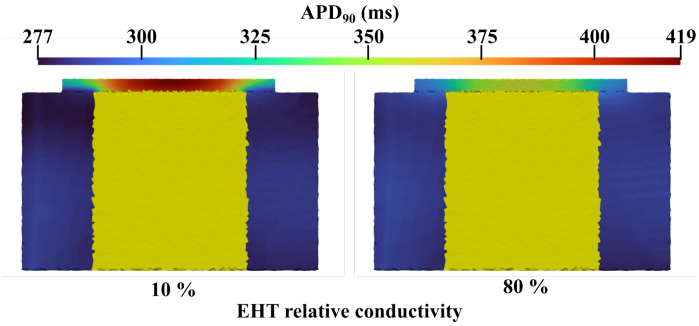


Figure 3.12: APD_{90} in the coupled EHT-myocardium is shown for variations in the EHT conductivity when EHT cells were aligned parallel to the epicardial CMs (C3G3 group of simulations).

we found practically no differences in the values obtained for different pore shapes (differences of 0.61 ms/mm) when the relative EHT conductivity was set to 40% (C3G2) of that in the healthy myocardium (see Figure 3.10c). The minimum mean RTG was obtained for the most elongated hexagon, with the value being 11.62 ms/mm, while this slightly increased to 12 ms/mm for regular hexagons.

When the uniform relative EHT conductivity increased (C3G3), the EHT-myocardial coupling was enhanced in the non-infarcted contact regions and this had an impact on APD_{90}. In particular, APD_{90} was increased in the myocardium and was reduced in the EHT within the engraftment region. Figure 3.12 illustrates how the repolarization heterogeneities partially vanished with the increment in EHT conductivity. The lowest values of mean EHT RTG were found for the highest EHT conductivity and the parallel orientation of the EHT cells (Figure 3.11c). We computed mean EHT RTGs of around 25 ms/mm for all EHT alignments when the relative EHT conductivity was 10%. When the relative EHT conductivity was 80%, mean EHT RTGs of 11.13, 8.39 and 6.94 ms/mm were calculated for the perpendicular, random and parallel alignment. The reduction in the mean RTG was more marked when the relative EHT conductivity varied from 10 to 40% than when it varied from 40 to 80%.

In summary, after the EHT being engrafted on the infarcted tissue, EHT conductivities higher than those inferred from *in vitro* experiments were required to enable bi-directional electrical propagation. The hiPSC-CMs conductivity and CA in the EHT, which increased along with cellular maturation, played a major role in increasing CV while reducing RTG, thus contributing

to mitigating the arrhythmic risk.

3.3 Discussion

3.3.1 Calibrated *in silico* EHT models reproduce *in vitro* EHT electrophysiology

We acquired and processed OM data from *in vitro* EHTs generated using scaffolds of square and hexagonal pores, and we used them to build and calibrate *in silico* EHT models. We aligned the hiPSC-CMs in the models according to their distance to the scaffold walls based on experimental evidence [70, 71, 74]. Specifically, we followed [74], which reported that hiPSC-CMs located near the pore walls had higher connexin 43 expression levels than hiPSC-CMs in the pore center and were oriented following the scaffold walls. Here, we represented such CA in the models, and we subsequently adjusted the electrical conductivity so that the maximum AT agreed between simulations and experiments.

From the *in vitro* EHT measurements, we observed faster activation and lower scaffold deformation for square pores than for regular hexagonal pores. This might be due to the smaller pore size used in square pore-shaped scaffolds, which incremented the amount of scaffold fibers per unit area, leading to higher CA and reduced pore deformation due to the raised overall stiffness. As a consequence, cellular coupling was enhanced for square pore-shaped scaffolds with respect to regular hexagonal ones, and the electrical propagation was faster, as confirmed by our simulations with the constructed *in silico* EHT models.

In the *in vitro* EHTs used in this study, only the one with hexagonal pore-shape scaffold included 10% hiPSC-CFs cocultured with hiPSC-CMs. Several studies have recently assessed the coculturing of 90% hiPSC-CMs with 10% hiPSC-CFs. Napiwocki et al. [162] observed no significant variation in CV when hiPSC-CFs were added to pre-cultured hiPSC-CMs. Lou et al. [163] demonstrated that the addition of hiPSC-CFs on cultures of hiPSC-CMs, endothelial and smooth muscle cells significantly rose CV. On the other hand, Zhang et al. [164] obtained twice slower electrical conduction when hiPSC-CFs were added to hiPSC-CMs cultures. These contradictory results highlight the uncertainty in the electrophysiological effects of adding hiPSC-CFs. Taking this as a basis, we postulate that the slower electrical activation of our hexagonal pore-shaped EHT could to a large extent be attributed to the pore architecture and size rather than being a reflection of the influence of hiPSC-CFs.

From the experimentally adjusted relation between LDCs and CA percentage of the analyzed EHTs, we fitted a linear polynomial that enabled extrapolation of the LDC to any other *in silico* EHT built from any scaffold pore shape and size. This was further employed to assess the electrical activity for EHTs with varied scaffold pore shapes and sizes, both before and after being engrafted on a transmural slab of infarcted tissue.

3.3.2 EHTs with scaffolds of small elongated hexagonal pores activate faster than with other scaffold designs

In silico simulations using EHT models showed that, as the scaffold pore size was reduced, a higher number of hiPSC-CMs were in contact with the scaffold walls and this led to higher CA and faster depolarization. Thus, the shortest global AT and highest CV in the EHT was found for the smallest scaffold pore size of 0.2 mm^2. On the basis of these results, the selection of the 3D printing technique is essential to attain sufficiently small scaffold pores that guarantee rapid electrical propagation in the EHT. The additive manufacturing field is rapidly evolving and more precise structures are expected to be delivered in the coming years.

Regarding scaffold pore shapes, our study emphasized the importance of the CA in the EHT and how this CA varied for different scaffold pore shapes. In cardiac applications, it is vital that the EHT replicates the anisotropy of the native tissue and it renders electrical CV similar to that of healthy myocardial tissue. We observed that auxetic configurations aligned a higher percentage of hiPSC-CMs than other scaffold pore shapes, although the highest CA was not necessarily correspondent with the highest LCA due to the different directions of the scaffold fibers. The scaffolds built with the most elongated (30°) hexagonal pores led to the highest LCA and were the ones best mimicking the cardiac anisotropy of the native tissue and delivering the fastest electrical conduction. Although some works have investigated the performance of scaffolds with pore shapes like auxetic [161, 165], rectangular [69], square, and hexagonal [70] geometries, to the best of our knowledge, this is the first study investigating a large set of scaffold pore geometries and sizes and identifying their suitability in terms of electrophysiological behavior.

Considering our results, EHTs presenting a preferential conduction direction can be best suited for cardiac tissue engineering. Such preferential conduction direction should be taken into account when engrafting the EHT on the infarcted heart. Besides, future computational studies could be conducted to assess the possibility of implanting multiple single-direction conducting EHTs

rather than a single EHT depending on the characteristics of the infarction substrates.

3.3.3 EHT thickness has a negligible electrophysiological role when *in vitro*

We assessed the role of EHT thickness on electrical activation. Adding printed layers to the scaffold led to EHTs presenting the same electrophysiological behavior, with AT maps sharing similar characteristics for all layers along the different tested thicknesses. This outcome on the very minor role of EHT thickness in electrical terms is in line with results reported in other experimental [161] and computational [154] studies. In [161], similar Ca^{2+} transient signals were experimentally measured from auxetic pore-shaped EHTs with different thicknesses. In [154], the EHT thickness was not a determining factor for electrical activation when the *in silico* EHTs were engrafted on models of partial or transmural infarcted myocardium.

Nevertheless, in an *in silico* study using BiV infarcted models with engrafted EHTs [11], CV was found to decrease and the arrhythmogenic risk to increase with EHT thickness. In addition, it is paramount to highlight that cellular differentiation improves in 3D constructs but cellular viability decreases with EHT thickness [4, 74, 161]. Therefore, a trade-off in the amount of EHT thickness should be attained to promote *in vitro* cellular differentiation and maturation when in culture while favoring cell viability and integration with the native tissue once the EHT is engrafted on the infarcted cardiac tissue.

3.3.4 EHT design determines the activation properties of coupled EHT-infarcted myocardium

When the *in silico* EHTs were engrafted on slabs of infarcted tissue, the depolarization wave successfully traveled from the myocardium to the EHT but there was a conduction block when traveling from the EHT to the myocardium. The EHTs showed considerably long ATs with respect to healthy myocardial tissue, in association with conductivity values that were low enough to impair excitation from the EHT to the myocardium due to the presence of a source-sink mismatch [166]. When a conductivity offset equal to 5% of myocardial conductivity was added to the EHT (C3G1 group of simulations), no conduction block in the coupled EHT-myocardium was observed. This suggests that the current experimental methods to culture hiPSCs in 3D scaffolds should be improved to guarantee that the electrical conductivity in the EHTs

is high enough that, when the EHT is engrafted on the infarcted myocardium, propagation occurs between the EHT and the surrounding native tissue.

By designing scaffolds with different pore shapes and sizes, variations in the maximum AT of the coupled EHT-myocardium and in the mean RTG and CV of the EHT were measured. In particular, we observed a reduction in ATs and RTGs and an increment in CV when the pore size was diminished to 0.2 mm^2 for all tested pore shapes, which is in agreement with the faster conduction we measured experimentally for smaller pore sizes. Similarly to the results reported for the not engrafted EHTs, the most elongated hexagons favored the anisotropic alignment of the hiPSC-CMs in the EHT, thus producing faster conduction in the coupled EHT-myocardium than other scaffold pore shapes. Additionally, the analysis of arrhythmic risk evaluated by the RTG metric showed that the higher the elongation of the hexagons, the lower the likelihood of arrhythmic activity. Specifically for RTG, we observed that the parallel-oriented auxetic pore shape led to the lowest RTG values, which were somewhat below those of the elongated hexagons. Nevertheless, the variations in RTG over all tested pore shapes were minor.

To complete the characterization of the scaffold design, we set the pore size to 0.4 mm^2 and we increased the EHT conductivity by adding an offset equal to 40% the healthy tissue conductivity to investigate the impact of the EHT engraftment on the myocardial tissue provided the culturing methods allowed to increase the EHT conductivity (C3G2 group of simulations). Under those conditions, the maximum AT and the mean RTG were found to attain the lowest values for the 30° half-angle hexagonal pores. Nonetheless, similarly to the outcomes obtained for the C3G1 group of simulations, the RTG, maximum AT and CV differences for distinct pore shapes were practically negligible.

3.3.5 Increased EHT conductivity reduces arrhythmic risk in coupled EHT-infarcted myocardium

We further tested variations in the EHT conductivity and alignment of its hiPSC-CMs to assess the impact on the depolarization and repolarization of the coupled EHT-myocardium (C3G3 group of simulations). We tested EHT conductivity values of 10%, 40% and 80% of that in the healthy myocardium, considering that improved EHT manufacturing and culturing could at some point allow reaching such values. We found that the largest conductivity in the EHT led to drastic exponential-like declines in both AT and RTG while it raised CV linearly. Also, we tested random, parallel, and perpendicular hiPSC-CMs alignments with respect to the epicardial cells in the tissue slab,

and we found that the parallel and perpendicular alignments always produced the lowest and highest AT and RTG, respectively. Taken together, the impact of hiPSC-CMs orientation on EHT-myocardium depolarization was more noticeable for low EHT conductivities, whereas the impact on repolarization heterogeneities and CV was larger for high EHT conductivities. Thus, hiPSC-CMs alignment can be concluded to play a relevant role in mitigating arrhythmic risk throughout the whole maturation process, with the impact on depolarization and repolarization occurring over the whole range of EHT conductivities. These results should be considered when designing scaffolds for regenerative medicine to maximize the benefits on the electrophysiology of the coupled EHT-myocardium.

Our findings on the need for the EHT to present conductivity and CA characteristics that avoid conduction delays are consistent with previous studies [154]. Yu et al. [11] reported that EHT AT and CV were driven by the electrotonic interaction with the healthy myocardium when the EHT engraftment on an *in silico* BiV model of infarction remuscularization was complete. In a study using two geometries of infarcted LV, Fassina et al. [76] showed how the healthy myocardium drove the EHT activation in the EHT-tissue interacting regions, suggesting that, once the EHT was implanted, the myocardium accelerated the EHT depolarization. Importantly, these results applied to cases where the EHT was electrically coupled to healthy myocardium, whereas, if coupled to the infarct scar, the engrafted EHT preserved its electrophysiological characteristics. Thus, as slow conducting regions favor reentrant arrhythmias [11, 76, 148, 154], achieving EHT depolarization times and CV values similar to those in healthy tissue should reduce the arrhythmic risk (see Chapter 6) [167]. Our study provides a characterization of how EHT properties, including electrical conductivity and CA modulated by the scaffold shape and size, could help in building EHTs that better mimic the characteristics of healthy myocardial tissue.

With regards to repolarization heterogeneity and proarrhythmic risk, our results describe how the RTG metric is remarkably influenced by the EHT properties. High RTG values are observed when the EHT electrical conductivity is low and/or the hiPSC-CMs in the EHT are not oriented parallel to the epicardial cells of the host myocardial tissue. Laurita et al. [168] experimentally showed that unidirectional blocks developed with repolarization gradients as low as 3.7 ms/mm when an isthmus was present in the cardiac tissue. They predicted that even in the absence of isthmuses, unidirectional blocks can occur when repolarization gradients are large. Fassina et al. [154] conducted an *in silico* analysis and reported mean RTGs higher than the threshold set by

Laurita et al. [168] for cases in which the conductivities in the EHT and the myocardium were highly distinct. Also, Riebel et al. [153] *in silico* demonstrated that an increase in repolarization heterogeneities due to the injection of a high number of hiPSC-CMs in the infarcted region can lead to enhanced arrhythmic vulnerability. In line with these results, here we found that the major reduction in RTG towards values found in healthy myocardium was attained when the relative EHT conductivity was increased to almost 100%. The addition of electrically conductive elements, as suggested in some studies, could be used to increase the EHT conductivity [165, 169]. Furthermore, in accordance with the computational and experimental results in [154, 170], we measured higher APD_{90} values in the healthy myocardium near the engraftment and lower APD_{90} values in the EHT when the conductivity in the EHT was augmented, which confirms better integration of the EHT in the native tissue. It should be noted that in our study the highest RTG values were measured in the EHT, as conductivities lower than the one in the healthy myocardium were always considered. In agreement with this, Fassina et al. [154] reported that, when the EHT conductivity was increased over the one in the healthy myocardium, the electrotonic load applied onto the myocardium by the EHT rose, originating the highest RTGs in the host tissue near the engraftment.

Even if to a lesser extent, the contribution of the completely parallel CA in the EHT aided in reducing RTG and increasing CV and, thus, diminishing the arrhythmic risk. These effects could be better appreciated when the EHT conductivity was high enough. The smallest, most elongated hexagonal scaffold pores would facilitate such alignment and would contribute to reducing proarrhythmia in the coupled EHT-myocardium.

3.4 Limitations

Using computational modeling and simulation based on experimental data, we investigated the impact that the EHT design has on cardiac electrophysiology, both before and after implantation on a slab of infarcted ventricular tissue. Our main objective was to assess the effect that the different EHT design features have on electrical activity, including CV and repolarization heterogeneity. Even though our *in silico* representations were carefully based on experimental results, there are areas for improvement that we address in the following.

In terms of CA modeling, we based our *in silico* modeling and simulation study on available experimental data, including acquired and processed OM recordings and published microscopic data of the EHT [70, 71, 74]. If newer

and more precise experimental data became available, e.g. supporting that hiPSC-CMs may orient parallel to the pore direction with less stiffness to facilitate contraction, these could be easily incorporated into the *in silico* models by defining such alignment of the hiPSC-CMs in the EHT. Furthermore, in our *in silico* EHTs, two different distance thresholds were used for the alignment of the cells depending on their distance to the scaffold walls. The first one, 27 µm, was grounded on experimental data [70,74]. A second distance threshold of 55 µm was used to further compare the EHT electrical activity for different pore geometries. The value of this second threshold was chosen to be slightly higher than the 50 µm mean edge length of the EHT meshes, which is lower than currently used mesh resolutions in cardiac simulations [11,76,154]. The value of such second threshold lies between the distance of 27 µm reported in [70,74] and the approximated 100 µm graphically reported by Cui et al. [71] for the orientation of hiPSC-CMs following the scaffold fibers when located within such distance. New studies could refine and extend the results presented here by using finer EHT meshes and testing different threshold distances for the definition of CA.

As derived from our results, the EHT electrical conductivity is a major factor determining the proarrhythmicity of this tissue engineering therapy. Currently, new manufacturing techniques are continuously being tested for improving EHT conductivity, such as the addition of electrically conductive elements to scaffolds or hydrogels [165,169]. Here, we set a unique electrical conductivity in the whole EHT which was proportional to the CA found for each particular design, as aligned cells near the pore walls showed a more mature electrical phenotype [74]. Even though this CA-conductivity relation was adjusted from experimental outcomes as described, enhanced EHT models can be attained with a more realistic representation that locally incorporates the spatial distribution of the added electrically conductive elements and/or precisely replicates the local areas of more mature/immature hiPSC-CMs on the EHT.

Concerning cellular population modeling, the *in silico* evaluations of this study consider EHTs containing only one cell type, i.e. hiPSC-CMs. These were based on the available experiments, which contained hiPSC-CMs only, except for the hexagonal pore-shaped EHT that contained 10% hiPSC-CFs. Further studies could use more extensive *in vitro* data containing hiPSC-CFs and other cell types, like endothelial and smooth muscle cells, to enable more detailed *in silico* modeling representative of the electrical interactions between cell types. The simulation of these interactions could serve to further adjust the scaffold design and deliver even deeper improvements on the EHT fabrication

procedure.

We tested the engraftment of the EHT on a 3D tissue slab containing an infarct scar. Also, we considered complete attachment of the EHT on the myocardial tissue while it is likely that poor attachment occurs due to several factors, such as poor gluing or shear stresses due to contraction-relaxation cycles, as described in Section 1.4.5. Simulation studies have examined the effect of EHT–myocardium engraftment on remuscularization results, reporting different observations depending on whether the EHT-mediated epicardial engraftment is homogeneously or heterogeneously detached from the host myocardium (see Section 2.3.3). Building on this, Chapter 6 extends the results presented in this chapter by incorporating realistic BiV-EHT models into the analysis and evaluating the impact of partial heterogeneous interactions at the EHT–heart interface.

To close the gap, the *in silico* predictions on the outcomes of EHT-grafted infarcted hearts should be contrasted with *in vivo* electrophysiological data. Based on this, subsequent extensive *in silico* evaluations of the EHT-heart activity could be conducted to aid in the development of improved cardiac assist devices, which could accelerate their therapeutic implementation while avoiding costly and time-consuming experiments aimed at optimizing the scaffold design.

3.5 Conclusion

We simulated an extensive set of EHT models with varied scaffold pore shapes and sizes. Scaffolds made of small, elongated hexagonal pores led to the fastest conduction, as they conveyed the highest number of cells oriented parallel to the depolarization wavefront. *In silico* engraftment of the EHT on infarcted tissue showed that the EHT conductivity is the most critical parameter to avoid conduction block due to EHT-myocardium source-sink mismatch and to increase CV and reduce depolarization delays and repolarization heterogeneity, all of which contribute to diminishing pro-arrhythmic risk. Also, by aligning the EHT cells parallel to the epicardium of the tissue slab, the arrhythmic risk following EHT engraftment was further reduced.

CHAPTER 4

3D SEGMENTATION OF MULTI-CONTRAST CARDIAC MAGNETIC RESONANCES WITH TOPOLOGICAL CORRECTION AND SYNTHETIC DATA AUGMENTATION

4.1 Methodology
- 4.1.1 Data description and processing
- 4.1.2 Baseline training
- 4.1.3 GAN-based data augmentation
- 4.1.4 Topological correction and priors definition
- 4.1.5 Inference and postprocessing

4.2 Results
- 4.2.1 *Ex vivo* dataset
- 4.2.2 Cine dataset
- 4.2.3 LGE dataset

4.3 Discussion

4.4 MYOSAIQ challenge
- 4.4.1 Preprocessing, synthetic augmentation, segmentation and confidence estimation
- 4.4.2 Results

4.5 Conclusion

This chapter investigates the performance of advanced GAN-based approaches for SA and TC in the context of 3D segmentation of complex, real-world CMR datasets. Specifically, we address the challenges posed by modern multi-vendor, multi-center, and multi-class CMRs, focusing on both cine and LGE images, while also employing a manually segmented *ex vivo* dataset to enable evaluation under more topology-controlled conditions. To this end, CNNs

and GANs are trained on 3D data for segmentation and SA, respectively, with a topological loss incorporated to promote anatomically consistent segmentation. A central contribution of this work is the selective application of TC, informed by prior topological assessment of GTLs, thereby reducing the risk of prediction errors associated with dataset-specific topological inconsistencies. In addition, we present our contribution to the MYOSAIQ challenge [96], which provides a comprehensive multi-center, multi-vendor dataset covering multi-stage and multi-type MI imaging, derived from LGE-CMR scans. Within this framework, our SA strategy is employed to improve the generalization capabilities of the state-of-the-art nnUNet model. Finally, we propose a novel methodology to estimate instance-level uncertainty from voxel-level segmentation outputs, offering a more reliable quantification of prediction confidence.

4.1 Methodology

The segmentation pipeline consisted of preprocessing, GAN-based DA, topological evaluation, training, inference, and postprocessing (Figure 4.1). Each component is described in detail below.

4.1.1 Data description and processing

Cardiac microstructure, ventricular geometry at end-diastole, and MI identification are key features for clinical diagnosis and computational modeling. Therefore, publicly available datasets representing these data types were selected and preprocessed (Figure 4.2).

4.1.1.1 Cine-CMR

The open access M&Ms challenge dataset contained 345 human cine CMRs acquired in 3 different Spanish and German healthcare centers with 4 different scanner manufacturers. Data comprised images of healthy volunteers and patients with hypertrophic and dilated cardiomyopathy [82]. The labeled data included contours for the LV myocardium (labeled as MYO), the LV cavity (labeled as LV) and RV cavity (labeled as RV), as can be seen in Figure 4.2. Unlabeled data were not included in the analysis.

For preprocessing, little spurious islands were cleaned from the GTLs in a label-wise manner. As different spacings were found throughout the samples,

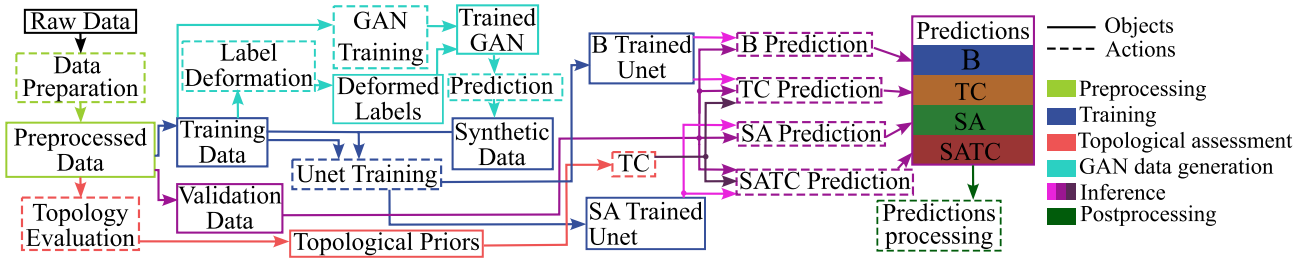


Figure 4.1: Segmentation pipeline applied independently to each of the three CMR datasets. B: Baseline, TC: Topologically Corrected, SA: Synthetically Augmented and SATC: Synthetically Augmented and Topologically Corrected.

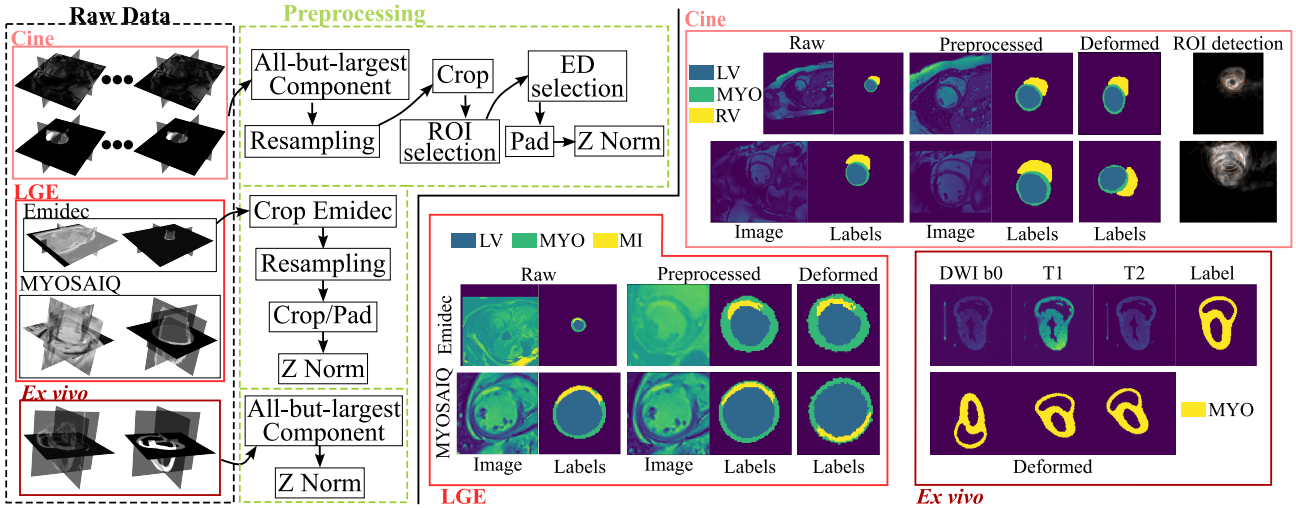


Figure 4.2: Left: CMR datasets and their preprocessing. Right: 2D slices illustrating preprocessing results and applied GTL deformations as part of SA. Cine CMR panel includes SAx images of the LAx-averaged first-harmonic components with its fitted Gaussian distribution in orange, obtained during detection of the region of interest.

a resampling was performed to homogenize the amount of region in the physical space that a voxel depicts in every sample. In the high-resolution SAx plane, images and GTLs were resampled to the median spacing computed for all samples with linear and nearest-neighbor interpolation, respectively. In the low-resolution LAx plane, a resampling to the 10^{th} percentile spacing found along all samples was performed in images and labels using nearest-neighbor interpolation. This out-of-plane resampling avoided the generation of spurious middle SAx images and loss of information due to the large out-of-plane resolution variance, as reported in previous works [79, 139].

As illustrated in Figure 4.2, the SAx cine CMR images depict several structures in addition to the heart, making the detection of a region of interest necessary. In cine CMR, the time evolution of the cardiac cycle and the fundamental spatial frequency generated by cardiac beating can be used in a Fourier-based technique to determine a region of interest [171, 172]. First, a centered crop equivalent to 80% of each SAx plane dimension was applied, that is, an image of $100\times100\times10$ voxel space resulted in an image of $80\times80\times10$ voxel space with equivalent center. The resulting SAx borders were observed to have relevant first-harmonic components in some samples, which disturbed the Fourier-based determination of the region of interest. Thus, we performed a per-slice 2D Fourier transform, and only its first harmonic was used to calculate the inverse transformation. The 3D array was cleaned by median filtering, normalization, and deletion of all values below 5% of the maximum intensity threshold. Subsequently, a 2D image with the combination of per-slice first harmonic motion information was obtained by summing the stack in the LAx direction, as shown in the images for the detection of the region of interest in Figure 4.2. Iteratively, a Gaussian distribution (in orange in Figure 4.2) was fitted to this motion image and the boundaries corresponding to less than 5% of its height were removed until the center of the Gaussian distribution changed position by less than one pixel.

Once homogeneous spacing was obtained and the end-diastole samples were SAx-cropped to their determined region of interest, zero-padding was applied to achieve a common target voxel space along the samples. This target voxel space was constrained in its lower limit by the minimum per-dimension voxel resolution found in the preprocessed dataset, whilst its increment led to a higher memory load with the addition of irrelevant information. Moreover, fixing a target voxel space that can be repeatedly divisible by 2 eases the definition of a convolutional layer in network architecture. Therefore, the final preprocessed end-diastole cine dataset consisted of 320 samples with common $1.25\times1.25\times8.8$ mm^3 spacing and $160\times160\times20$ voxel space.

4.1.1.2 LGE-CMR

The Emidec [141] and MYOSAIQ [96] datasets containing human LGE-CMRs were combined here. The Emidec dataset originally consisted of 150 samples. However, the 50 test samples were not considered as GTLs were not available. For simplicity, only MI cases without MVO from both datasets were used. In addition, a sample of the MYOSAIQ data with an extremely large LV was discarded. This selection resulted in a multi-vendor, multi-center, and multi-class LGE dataset comprising 288 samples from MYOSAIQ and 27 from Emidec, with labels for the LV cavity (labeled as LV), LV myocardium (labeled as MYO), and MI region (labeled as MI), as presented in Figure 4.2.

The MYOSAIQ samples were already cropped and LV-centered, as shown in Figure 4.2. As the Emidec SAx plane was centered in the LV, we cropped the voxels equivalent to 60 mm in each of the 4-sided SAx images. Due to their anisotropic resolution, high in the SAx plane and low out-of-plane, the images and GTLs of both datasets were resampled as previously described (Section 4.1.1.1). In addition, the target voxel space was selected with the same criteria presented for cine CMRs and achieved through zero-padding or cropping. The preprocessed dataset comprised 315 samples with common $1.56 \times 1.56 \times 5$ mm^3 spacing and $64 \times 64 \times 24$ voxel space.

4.1.1.3 *Ex vivo*-CMR

A publicly available dataset from the Stanford Cardiac MRI Research Group containing 7 *ex vivo* porcine DW-CMRs was used [173]. The T1- and T2-weighted sequences and baseline zero gradient (b0) images from the DW-CMR were included in the analyzed dataset, which comprised 21 samples (no diffusion data were used). The manual segmentation of the ventricular myocardium (labeled as MYO) for generating topologically consistent GTLs (Figure 4.2) was enabled by the high resolution and motion-free nature of the data.

This dataset was already consistent in terms of spacing and voxel space. It was the one out of the three with the lowest variability in its properties because it was acquired from a single-vendor, single-center study. Here, we only checked that myocardial GTLs were composed of a single connected component without any resampling, cropping, or padding. As the data were acquired *ex vivo*, isotropic voxel space and high resolution were possible on all axes, which differs from the previously described datasets. The final preprocessed dataset included 21 samples with common $1 \times 1 \times 1$ mm^3 spacing and $128 \times 128 \times 128$ voxel space.

At the end of the preprocessing and for all datasets, an image intensity adjustment was performed with a Z-Score normalization per sample. The raw and preprocessed data for all datasets can be seen on the right side of Figure 4.2.

4.1.2 Baseline training

The cine CMR and LGE-CMR datasets were split to perform a 5-fold cross-validation. For the *ex vivo* CMR dataset, a 7-fold cross-validation was applied by setting the three image-GTL pairs belonging to the same subject (T1, T2, and DWI b0) for validation in every fold. Thus, the training/validation sets consisted of 256/64, 252/63, and 18/3 samples in every fold for the cine, LGE, and *ex vivo* datasets, respectively.

The 3D UNet architecture [81] shown in Figure 4.3a, and described in Section 1.5.2.2, was used for the segmentation of all datasets. Following [79], the outermost 3D convolutions treated the input 3D array as a 2D stack for the highly anisotropic datasets. Namely, when the feature map downsampling in the SAx plane resembled the out-of-plane voxel resolution, the 3D convolutions were applied on the entire 3D feature map as a whole, i.e., the kernel size became isotropic (see Figure 4.3a, 4.3c and 4.3d).

The CNN was always trained for 250 epochs, and the batch size was chosen to have the same maximum amount of samples per batch while avoiding memory overload. The batch size was set to 3 samples for the *ex vivo* dataset and 4 samples for the cine and LGE datasets. Furthermore, the Adam method was used for stochastic optimization with momentum parameters of 0.5 (β_1) and 0.999 (β_2). The learning rate was steady at 0.0002 during the first 125 epochs and linearly decreased to 0 in the second half of the training. A cross-entropy loss was selected as the objective function for the optimization problem, and both training and validation losses were monitored during training. On-the-fly random standard DA consisted of rotation around LAx ($p^i = 0.4$), array flip on the SAx plane (p = 0.5), blurring (p = 0.4), Gaussian noise (p = 0.4), bias field (p = 0.4) and one of motion, spike, and ghost artifacts (p = 0.5). Intensity alterations were applied only to the image, whilst spatial alterations were applied to the image-GTL pair. Then, the array intensity of all samples was normalized to the [-1,1] range and, only for the samples in the training set, they were shuffled on the fly before being input to the CNN.

[i] p: probability

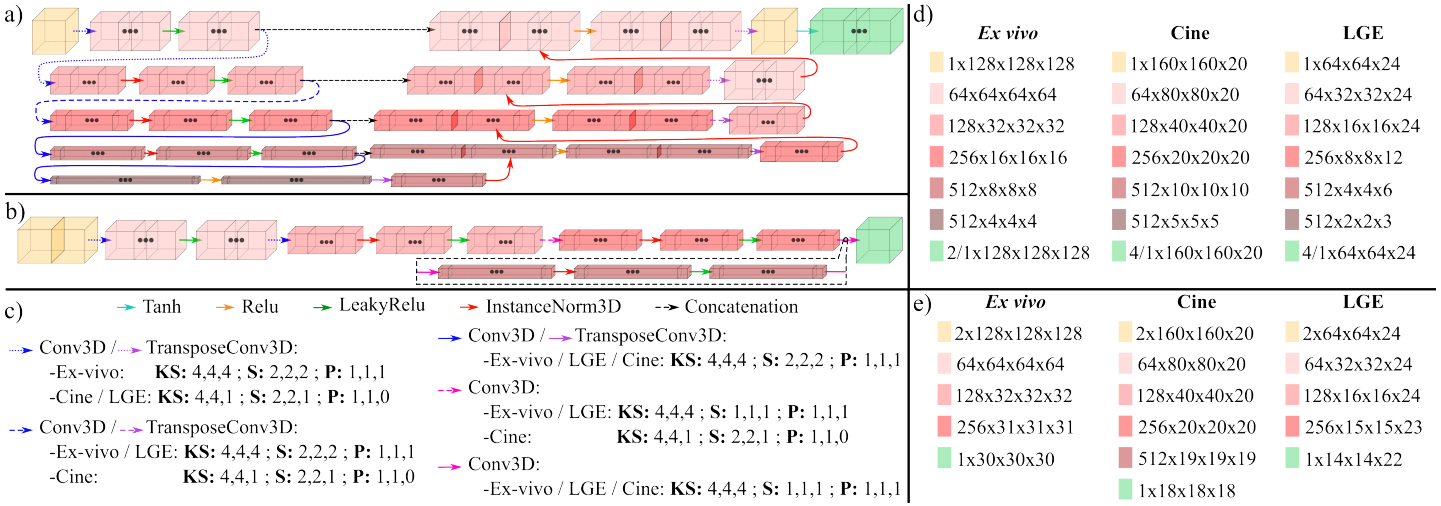


Figure 4.3: UNet/G (a) and D (b) graphical architectures. c- CNN details and convolutional layers configuration across datasets. KS: Kernel Size, P: Padding and S: Stride. Tensor shapes mapped to the color-based graphical images of UNet/G (d) and D (e). In (d), the output classes are different in the UNet/G cases.

4.1.3 GAN-based data augmentation

This step involved the implementation of a conditional GAN to generate synthetic images from modified GTLs. The UNet architecture described in Section 4.1.2 was also used here as G. As a mapping from GTL to the image domain was learned, the output array differed in the number of classes with respect to the UNet defined in Section 4.1.2 (see the voxel space of the output array in Figure 4.3d). For example, the UNet output in the cine case was 4×160×160×20, since 4 classes were segmented, while when used as G the output array was of 1×160×160×20 for the same data, since a grayscale image was obtained.

The adversarial training of G was achieved with the help of a patch level D (Figure 4.3b), as proposed in [86]. Here, D encoded patch-wise information of the real or synthetic image with its GTL. As for the UNet in Section 4.1.2, an initial 2D encoding was performed in the SAx plane until the feature map became nearly isotropic. Then, convolutions started to involve inter-slice information. The global evaluation of the latent space defined whether an image was fake or real. As reported in [86], increasing the receptive field of D led to improved representation of high-frequency features on synthetic images. Authors showed that for an isotropic 286-pixel image, it was sufficient to use a 70×70 (24.4% relative) receptive field to capture sharp image details and avoid tiling artifacts (see Section 2.1.2). As can be deduced from Figure 4.3, here the sizes of the receptive fields were 34×34×34, 70×70×7 and 34×34×7 for the *ex vivo*, cine and LGE CMRs, respectively. Thus, the smallest receptive field versus input shape relation obtained here (26.6%) was superior to the one defined in [86], considered to be sufficiently accurate.

The same training samples, epochs, batch sizes, optimizer, and learning rate schedule described in Section 4.1.2 were used to train the GANs. As the input consisted of GTLs instead of images, only the random spatial on-the-fly standard DA was applied to the shuffled training samples. In addition, the intensity on image-GTL pairs was normalized to the [-1,1] range. The D and G losses were obtained as follows (see Section 2.1.2) [86]:

$$G_{loss} = \text{MSE}(\text{D}(\text{GTL}, S_i), R) + \lambda\ \text{L1}(S_i, R_i) \tag{4.1}$$

$$D_{loss} = 0.5\ [\text{MSE}(\text{D}(\text{GTL}, S_i), S) + \text{MSE}(\text{D}(\text{GTL}, R_i), R)] \tag{4.2}$$

where MSE stands for mean squared error, L1 measures the mean absolute error, R_i and S_i are real and synthetic images, and R and S are binary arrays that represent completely real and synthetic predictions, respectively. The regularization term λ was set to 100. From these definitions, it follows that when G performs well, the D_{loss} increases while the G_{loss} decreases, and when

D performs well, the D_{loss} decreases while the G_{loss} increases, defining this, the adversarial learning.

Once the GAN was trained, the GTLs of the training samples were deformed for synthetic image generation, as shown on the right side of Figures 4.2 and 4.4. For cine and *ex vivo* data, the deformation involved random scaling in the ±20% range, random rotation along LAx, and random translation in the SAx plane in the ±10 mm range. For LGE data, the random scaling and translation ranges were reduced to half. In addition, non-rigid deformation was applied in the SAx plane with a random elastic deformation with a maximum displacement equivalent to 10% of the LV end-diastolic diameter. Finally, the new synthetic data were combined with the training set to define the SA approach.

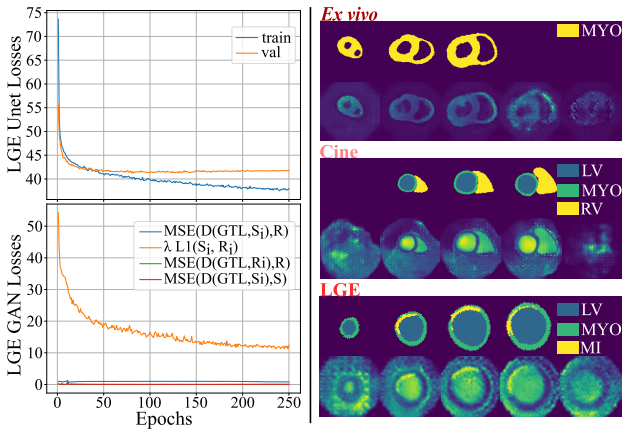


Figure 4.4: Left side shows loss functions and loss function terms during the UNet (top) and GAN (bottom) training of one fold of the LGE-data, respectively. Right side depicts deformed GTLs and their GAN-generated images for all datasets.

4.1.4 Topological correction and priors definition

Once the UNet has been trained, a sample-wise PH-based TC can be enforced by retraining the network to minimize a topological loss without substantially changing the original prediction, as reported by Byrne et al. [19]. The baseline training settings were reused for this post-training with the exception of the now steady 1×10^{-5} learning rate. Post-training optimization was performed on each validation sample for 100 iterations.

The set of class-wise logits obtained for an input $\mathbf{X}$ with GTL $\mathbf{Y}$ was denoted as $\hat{\mathbf{Y}}^c$ with $c = 1, 2, ..., C$, where C corresponds to the number of

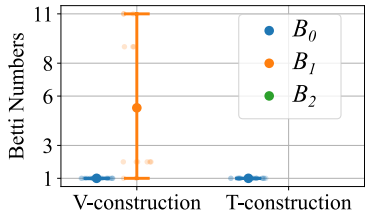


Figure 4.5: Betti numbers obtained from the preprocessed *ex vivo* GTLs with V- and T-constructions.

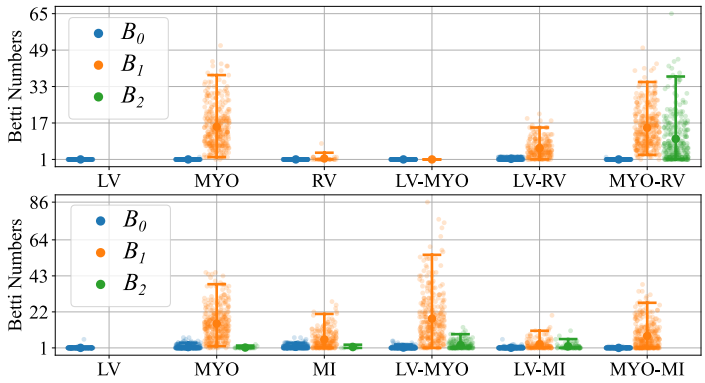


Figure 4.6: Betti numbers for the preprocessed cine (top) and LGE (bottom) CMR datasets along different topological classes.

foreground classes in the dataset. Here, the topological evaluation was applied to the topological classes that corresponded not only to the single foreground classes but also to their combination, as a previous work reported that an improved TC was achieved in that way [19]. $\hat{\mathbf{Y}}^n$ was defined as the logits of the n^{th} plausible topological class obtained from a single or combined $\hat{\mathbf{Y}}^c$. In addition, the lifetime of the l^{th} topological structure with dimension d found on $\hat{\mathbf{Y}}^n$ was denoted as $\Delta p_{l,d}(\hat{\mathbf{Y}}^n)$. If $\Delta p_d(\hat{\mathbf{Y}}^n) = \{\Delta p_{0,d}(\hat{\mathbf{Y}}^n), ..., \Delta p_{L,d}(\hat{\mathbf{Y}}^n)\}$ where $\Delta p_{0,d}(\hat{\mathbf{Y}}^n) > ... > \Delta p_{L,d}(\hat{\mathbf{Y}}^n)$, with L the total amount of d-dimensional topological structures found in $\hat{\mathbf{Y}}^n$, the topological loss was defined as follows:

$$L_{topo} = \sum_{d,n} B_d^n - A_d^n + Z_d^n \tag{4.3}$$

$$A_d^n = \sum_{l=1}^{B_d^n} \Delta p_{l,d}(\hat{\mathbf{Y}}^n) \qquad Z_d^n = \sum_{l=B_d^n+1}^{L} \Delta p_{l,d}(\hat{\mathbf{Y}}^n) \tag{4.4}$$

where B_d^n, A_d^n, and Z_d^n are the topological prior and the added lifetimes of the correct and incorrect topological structures, respectively, on dimension d for the

Table 4.1: Preprocessed cine topological priors (B_0, B_1, B_2). E: Expected, M: Measured and F: Final priors.

	LV	MYO	RV	LV-MYO	LV-RV	MYO-RV
E	(1,0,0)	(1,1,0)	(1,0,0)	(1,0,0)	(2,0,0)	(1,1,0)
M	(1,0,0)	(1,7,0)	(1,0,0)	(1,0,0)	(1,0,0)	(1,7,0)
F	**(1,0,0)**	**(1,-1,0)**	**(1,0,0)**	**(1,0,0)**	**(2,0,0)**	**(1,-1,0)**

Table 4.2: Preprocessed LGE topological priors (B_0, B_1, B_2). E: Expected, M: Measured and F: Final priors.

	LV	MYO	MI	LV-MYO	LV-MI	MYO-MI
E	(1,0,0)	(1,1,0)	(1,0,0)	(1,0,0)	(1,0,0)	(1,1,0)
M	(1,0,0)	(1,7,0)	(1,0,0)	(1,7,0)	(1,0,0)	(1,1,0)
F	**(1,0,0)**	**(1,-1,0)**	**(1,0,0)**	**(1,-1,0)**	**(1,0,0)**	**(1,1,0)**

n^{th} topological class. The final sample-wise retraining loss was obtained as the sum of this L_{topo} and the MSE between the original and the new topologically corrected predictions multiplied by a regularization value of 1000.

This loss definition shows the importance of selecting topological priors that match the GTL topology. Here, two sources of variation were found in the calculation of Betti numbers: one inherent to the topological construction used for the filtration (Figure 4.5); and the other, inherent to the intrinsic topological discrepancy between samples of the same dataset (Figure 4.6). Specifically, Figure 4.5 shows how the V-construction did not lead to null B_1 for the topologically checked *ex vivo* GTLs, contrary to the T-construction. This occurred because the thin RV apex impaired the V-construction 6-neighbor connectivity to detect the RV as a one-sided closed cylinder instead of a tunnel. Thus, all topological calculations for this study were performed with the T-construction. Moreover, we defined the final B_d^n (F) for a dataset by comparing the expected B_d^n (E) with the mode of the Betti numbers measured (M) in the preprocessed data (see Tables 4.1 and 4.2). If E and M were equal, F was set as this value, while if E was different from M, F was set as -1, which means that L_{topo} will not be affected by this prior. The only exception was made for B_0 in the LV-RV topological class, for which F was set at 2.

4.1.5 Inference and postprocessing

After calculating the predictions, we brought all samples to their original physical space, with original spacing and voxel space, by reversing the preprocessing steps of cropping, padding, and resampling. Next, every segmentation approach was evaluated by calculating overlapping and topological similarity

metrics. Prediction and GTL class-wise spatial overlap and contour distance were assessed with the widely known per-class dice similarity score (DSC) and Hausdorff distance (HD) metrics. Complementary and as defined by Byrne et al. [19], the topological correctness between prediction and GTL was assessed by computing the absolute difference between Betti numbers, named Betti error (BE), per class.

The complete source code for this work is available at `https://github.com/lino202/3Dseg`. Mainly, Python (3.8.16) code was used, where main dependencies were PyTorch (1.12) [174] for DL, TorchIO (0.18.90) [175] for data input, output and processing and Monai (1.2.0) [176] for metrics computation among others. The TC and evaluation is a slightly modified version of code in [19]. All DL code was executed in an NVIDIA Titan RTX GPU with CUDA version 11.4 for the cine and *ex vivo* datasets while an NVIDIA Titan V GPU with CUDA 12.6 was used for the LGE dataset. Moreover, pre- and post-processing was run in an Intel® Core® i7-13700K central processing unit clocked at 3.4 GHz with 64 GB of RAM.

4.2 Results

Figure 4.4 shows the loss optimization for the UNet and GAN during training on a fold of the LGE dataset. After training, predictions were generated, with GAN outputs displayed in the right panel. Final results for the four proposed approaches across all datasets are presented below.

4.2.1 *Ex vivo* dataset

The results of the analysis for the *ex vivo* dataset are depicted in Figure 4.7. In terms of median DSC, both TC and SA produced slightly higher values of 87.4% and 87.2%, respectively, compared to 87% for the baseline case. The addition of synthetic images not only improved the median DSC but also reduced its dispersion by almost 11%. The combined SATC approach maintained the improvements achieved with SA while increasing the maximum DSC from 90.8% to 91%. In terms of HD, TC reduced dispersion by 22.3% compared to SA and SATC. Moreover, similar median values of around 10.7 mm were measured for the baseline, TC and SA cases, while SATC reduced the median HD to 9.2 mm.

In terms of BE, the largest error was found for connected components and tunnels. The median BE values were 11, 1, 8 and 0 in B_0, and 9, 2, 7 and 2

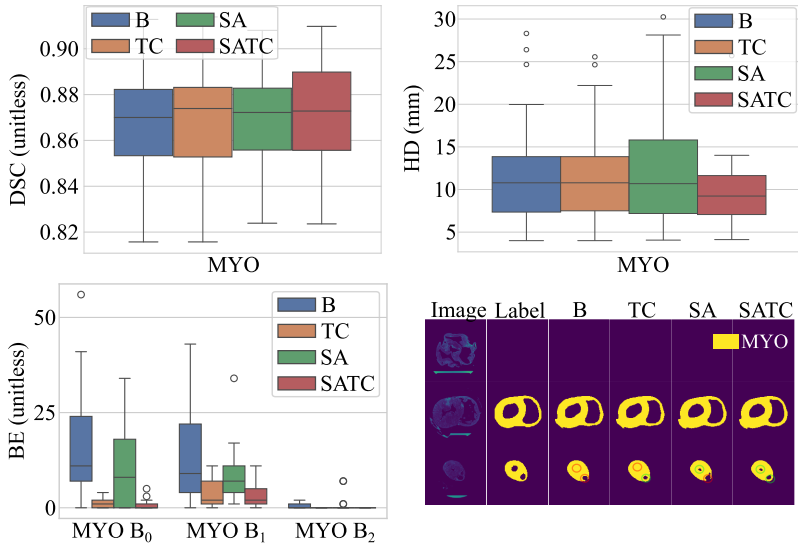


Figure 4.7: Segmentation results for the *ex vivo* dataset. Red and green circles indicate regions of poor and improved segmentation, respectively. B: baseline.

in B_1 for baseline, TC, SA and SATC approaches, respectively. These results showed not only a major BE reduction when topological-aware segmentation was performed but also a decrease in topological error when the synthetic GAN-based data were incorporated into the training. In addition, 2 and 4 samples were segmented with exact topology when using TC and SATC, respectively.

The bottom right panel of Figure 4.7 qualitatively depicts how SA and TC can aid in segmentation. TC segmentation correctly closed the RV at the apex to avoid generating a tunnel, and SA avoided premature closing of the LV blood pool. Specifically, regarding RV closing, which is a cumbersome task in automatic segmentation due to its extremely thin thickness, it can be observed from Figure 4.8 how baseline logits were corrected by the TC, which eliminated all spurious non-persistent topological entities (top left graph), leaving a consistent global topology of one connected component (top right graph).

4.2.2 Cine dataset

Figure 4.9 presents the results for the cine dataset, which showed minimal variations in the multi-class DSC and HD values for all approaches. DSC reductions of up to 0.4% compared to the baseline approach were observed for all classes when TC-based approaches were used. Slight increments in DSC

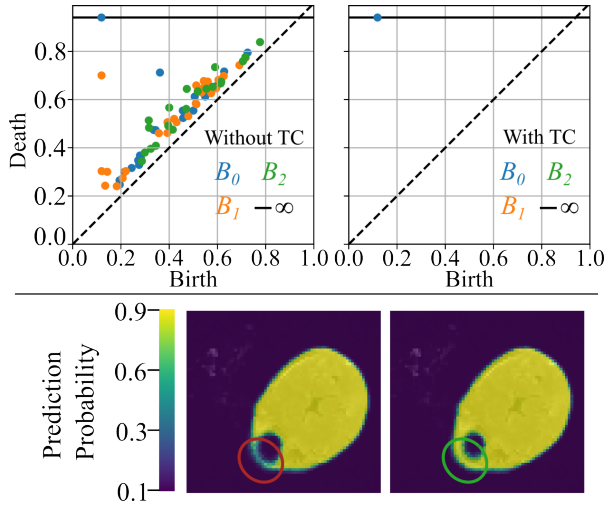


Figure 4.8: Lifetime plots (top) and near RV-apex logits (bottom) for baseline (left) and TC (right) when applied to the segmentation of an *ex vivo* CMR. Red and green circles indicate regions of poor and improved segmentation, respectively.

were found for SA with respect to the baseline. The median HD remained stable when the different approaches were used for the evaluation of the LV. For the MYO and RV classes, the median HD was minimally reduced by 1.78% and 0.09%, respectively, for TC with respect to the baseline. SATC led to additional median decreases in HD with respect to baseline for the same MYO (2.7%) and RV (2.3%) classes.

As for the *ex vivo* dataset, the highest BE values were found for the Betti numbers B_0 and B_1 (top panel of Figure 4.11). In the MYO class, the lowest B_0-related BE values were found when TC and SA were applied. The maximum values of B_0-related BE in the MYO class were 37, 18, 25 and 7 for the segmentation obtained using baseline, TC, SA and SATC. Furthermore, the median B_1-related BE decreased by 1 in this class for all other approaches with respect to baseline. In the RV class, when the Betti numbers B_0 and B_1 were analyzed, the maximum BE values of 23 and 10 obtained for the baseline approach decreased to 7 for SATC. The B_0- and B_1-related BE dispersion followed the same trend for the approaches tested. In the combined LV-RV topological class, the 75^{th} percentile for B_0- and B_1-related BE took the highest value when the SA approach was used. The maximum BE values found for baseline (27) and SA (14) were reduced for TC (14) and SATC (7), when B_0 was assessed in the MYO-RV topological class. In the same topological class but for B_1, the median BE decreased from baseline to TC by 2 and from SA

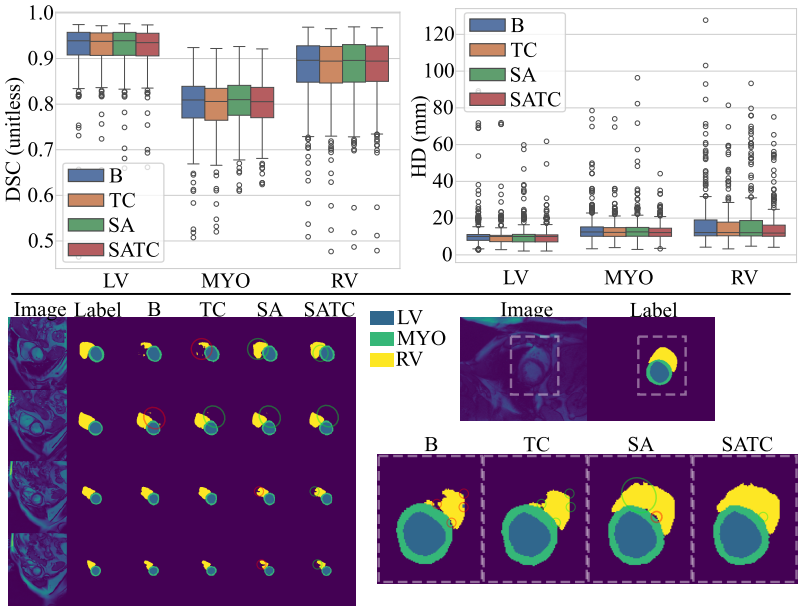


Figure 4.9: Segmentation results for the cine dataset. Red and green circles indicate regions of poor and improved segmentation, respectively. B: baseline.

to SATC by 1. The highest BE values were found for the MYO and MYO-RV topological classes in B_1.

The lower panels of Figure 4.9 illustrate the corrections made in the baseline predictions by TC, SA, and SATC in two cardiac CMRs. The addition of synthetic images improved the RV segmentation while TC erased spurious connected components of all classes and closed the erroneous space between the MYO and RV classes.

4.2.3 LGE dataset

As shown in Figure 4.10, TC minimally reduced the median DSC values with respect to baseline in the LV (0.1%) and MYO (0.7%) classes. SA slightly increased the median DSC with respect to baseline by 0.64% and 0.86% for the LV and MYO classes, respectively. SATC minimally reduced the increase in median DSC induced by SA for LV and MYO. In the MI class, the median DSC increased steadily by 1.1%, 1.7% and 2.8% when TC, SA and SATC were employed. The panel in the upper right of Figure 4.10 shows how the median HD changed minimally from 8 mm for baseline to 8.3 mm for SATC in LV segmentation. In the MYO class, TC unexpectedly increased the median HD

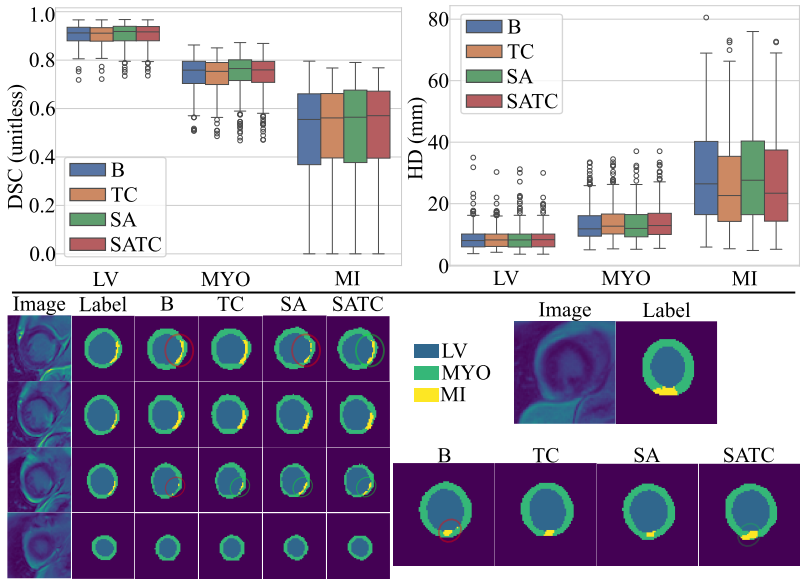


Figure 4.10: Segmentation results for the LGE dataset. Red and green circles indicate regions of poor and improved segmentation, respectively. B: baseline.

found in baseline by 7.4% for TC and 9% for SATC. The opposite behavior was observed in MI segmentation, where a decrease in baseline of 14.4% and 11.5% in the median HD was calculated when TC and SATC were used.

Here, as in the cine data, the highest BE values were found for the topologies B_0 and B_1, especially in the MYO and MI classes, as can be seen in the lower panel of Figure 4.11. For MI, the maximum BE for the topology B_0 was reduced by 10 (median BE decreased by 3) and 13 (median BE decreased by 3) when TC and SATC were used compared to baseline and SA, respectively. The maximum BE for the topology B_1 was increased by 14 (median 2) and 15 (median 1) with respect to baseline and SA when TC and SATC were used for MI segmentation. Moreover, regarding the generation of spurious tunnels in the MYO class, it can be observed that TC increased BE, with relative median increments of 4 and 2 for the baseline-TC and SA-SATC pairs, respectively. When comparing the LV-MYO class against the MYO class, the median number of spurious tunnels was lower in all four approaches for the LV-MYO class (reduction of baseline: 4, TC: 6, SA: 6 and SATC: 5 from MYO to LV-MYO). However, the trend of a higher number of erroneous tunnels on TC and SATC compared to baseline and SA remained. When the MYO class was combined with the MI class, TC did not increase the median BE with respect

to baseline for the topology B_1. SA presented a median number of erroneous tunnels that was higher by 1 than all other approaches.

As qualitatively presented in the lower part of Figure 4.10 and quantitatively illustrated by the measures of DSC and HD, TC and SA contributed to improved precision in the segmentation of the MI class.

4.3 Discussion

Data scarcity and data variability are common problems in CMR segmentation that hamper the performance of DL algorithms. Here, we assessed the use of GAN-based DA and TC in several CMR datasets presenting these drawbacks. Lately, GAN-based DA and PH have shown some ability to assist in various segmentation tasks individually. To the best of our knowledge, this is the first time that their combination has been tested on several complex multi-contrast CMR datasets.

Most modern CMR datasets do not have strict 3D topological consistency, as can be observed from the huge dispersion in some of the Betti numbers presented in Figure 4.6. The main reasons for this have been the lack of knowledge about PH and the unavailability of algorithms for its efficient calculation until a few years ago [89]. More importantly, the out-of-plane slice misalignment that occurred in the *in vivo* anisotropic cine and LGE data strongly contributed to topological distortion, with experts mainly focusing on the precise segmentation of the individual slices while overlooking the topological coherence across segmented slices. This led to a huge dispersion in the Betti numbers of thin, non-bulky labels, such as the MYO class for anisotropic datasets and the MI class for LGE data. This segmentation error propagates to other related topological classes, such as LV-RV in the cine data. Hence, we built a 3D *ex vivo* dataset with isotropic spacing and voxel space and controlled 3D topology to present the results when TC was applied to a CNN trained with topologically consistent data.

In the work presented by Byrne et al. [19], the authors showed that, in terms of DSC, TC greatly deteriorated the 3D segmentation of the whole heart, while, in terms of HD, the segmentation of all classes improved with respect to the baseline. Here, TC led to small (lower than 0.7%) reductions or increments in DSC in all 3D datasets. The differences in the results obtained here compared to reports by Byrne et al. [19] might be caused by our slightly enhanced topological loss computation, in which we avoided the inclusion of topological features that were found to be extremely inconsistent throughout the CMRs in

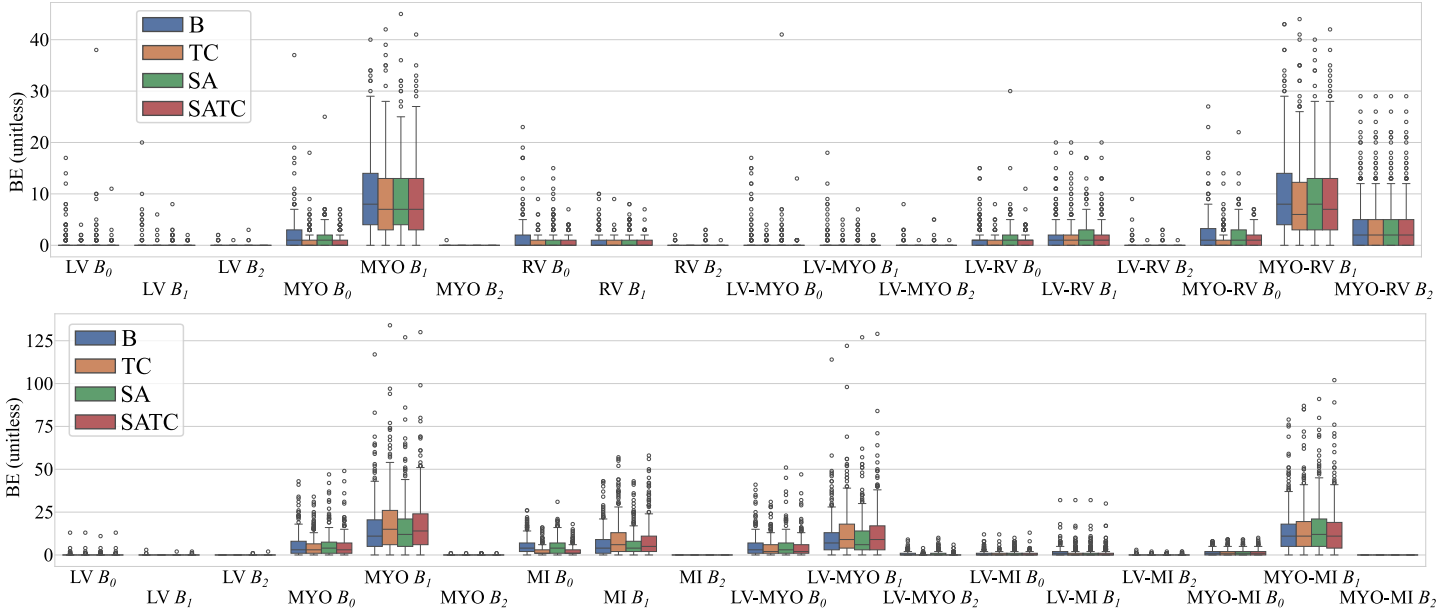


Figure 4.11: Computed BE for all topological classes in the cine (top) and LGE (bottom) datasets. B: baseline.

the dataset (see Section 4.1.4). Regarding HD, we found that it was generally reduced in all cases where TC was incorporated. The major HD reduction with TC happened in the MI class of the LGE data, showing that the use of a single-value topological prior can lead to an overall improved HD, in spite of the high inter-sample topological heterogeneity found in this class. On the other hand, we obtained an unexpected increase in the median HD for the MYO class when TC was used for segmentation of the LGE data. We hypothesized that this occurred because of the extra topological variability added by the different MI substrates in these data, since such an increase was not reproduced for the MYO class in the cine data. This is supported by the higher dispersion in the Betti numbers for the MYO and MYO-related topological classes in the LGE dataset than in the cine dataset (Figure 4.6). Also, as shown in Figure 4.11, BE increased when TC was used in the LGE data but not in the cine data for the MYO single and combined classes with topology B_1. This strengthens our hypothesis that the higher LGE topological heterogeneity in the MYO class owing to different MI substrates was the cause of the poorer than expected performance of TC in terms of HD and BE. Except for this particular situation, TC generally led to contained decreases in DSC and increases in HD and BE in topologically inconsistent datasets. Furthermore, the analysis of *ex vivo* CMRs showcased the importance of having topologically consistent CMRs in the entire dataset to maximize improvements not only in topological correctness, but also in spatial overlap between prediction and GTL. The suppression of all but the largest connected components is a common practice applied to the results obtained by modern segmentation pipelines. In this work, we decided to avoid its use, as Byrne et al. [19] have already shown that TC can achieve improved segmentation compared to this technique in terms of topological correctness. Altogether, these results highlight the need for clinicians to take into account 3D topological consistency when building new datasets.

The anisotropic datasets were composed of a large amount of samples with high variability in contrast to the isotropic *ex vivo* dataset, which has a low number of samples with low variability. This low variability in the *ex vivo* dataset made learning feasible with such a small amount of data. Also, this dataset served to accurately assess the effects of TC, as its high out-of-plane spatial resolution and inter-slice alignment avoided the generation of topological inconsistencies in GTLs. However, applying TC and BE to anisotropic, topologically heterogeneous samples with a fixed set of Betti numbers per dataset is a limitation of this work. Nevertheless, we showed that the results did not deteriorate, and in some cases, considerable improvements were achieved when TC was applied to these data. A continuation of this work

would consist of: first, correction of the misalignment in the LGE and cine datasets; second, assessment of whether more homogeneous topological definitions are reached; and third, evaluation of how the new aligned data might influence segmentation outcomes for the pipeline proposed here.

Generally, GAN-based DA slightly improved BE, HD, and DSC in all datasets. Although the overall enhancement was minor, some important improvements were achieved. In the *ex vivo* dataset, SA consistently contributed to the reduction of BE. In the LGE dataset, the use of SA increased DSC in all classes. In the work of Al Khalil et al. [139], a 2D segmentation pipeline was presented involving GAN-based DA and applied in an out-of-domain context to the same cine dataset used here. The improvement achieved by their proposed method with respect to the baseline was reported to be more relevant in terms of DSC and HD metrics than ours. However, the DSC values after SA in that paper [139] (LV: 0.925, MYO: 0.821, RV: 0.901) were very similar to the DSC values obtained here for both baseline and SA (LV: 0.939, MYO: 0.81, RV: 0.896). Furthermore, our improvements in terms of DSC when GAN-based DA was used in the LGE case were in agreement with the results in [140], where the authors found an increase in DSC from baseline 2D nnUNet to GAN-based DA of 3% for the MI class. Thus, good agreement was found between our results, when SA was applied to cine and LGE datasets, and state-of-the-art DL approaches [139, 140], even though different data, preprocessing, CNNs, and more importantly, GAN architectures were used. In this context, these recent studies involving CMR segmentation have suggested that the SA approach proposed here could have achieved better results if a spatially adaptive (de)normalization-GAN architecture had been used, as it mitigates the loss of semantic information typically caused by modern normalization techniques (Section 2.1.2) [139, 140, 142]. However, even if suboptimal and taking into account that our baseline results were in the range of cutting-edge algorithms, our GAN-based DA led to small but significant improvements in some of the performance metrics for all datasets tested. This stressed the capacity of GAN-based DA to improve predictions in different CMR datasets. In this line, future studies could be conducted to provide a proper quantitative assessment of how other GAN-based architectures could improve segmentation results.

The combination of SA with TC showed the ability to improve segmentation results. For example, for MI segmentation in LGE data, SATC had the best DSC and HD scores, as SA increased DSC and TC corrected the HD error generated by SA while maintaining the DSC values. Furthermore, in the *ex vivo* dataset, there was a reduction in HD and BE, as well as an increase in

DSC for the TC approach after SA was applied compared to the metrics for the case where neither TC nor SA were used. In this dataset, the combination of SA and TC resulted in a greater BE reduction than either SA or TC achieved individually. Moreover, improvement in prediction overlap with the GTL was observed predominantly when the approaches were employed together, rather than separately, in the *ex vivo* dataset.

4.4 MYOSAIQ challenge

4.4.1 Preprocessing, synthetic augmentation, segmentation and confidence estimation

In the second round of the MYOSAIQ challenge, the training set comprised 358 samples acquired at three time points following MI: 8 days (D8), 1 month (M1), and 12 months (M12). Four images corresponding to patients without MI were identified and excluded. Preprocessing followed the same pipeline used for the anisotropic datasets (Section 4.1.1), including resampling, padding, cropping, and intensity normalization. The final dataset consisted of 354 samples (D8: 97, M1: 153, M12: 104), resampled to a uniform spacing of $1.66 \times 1.66 \times 5$ mm^3 and voxel dimensions of $64 \times 64 \times 24$.

The preprocessed data were used to train two conditional GANs for SA: one targeting D8 LGE images and the other for MX (M1 and M12) LGE images, thus accounting for the potential presence of MVOs in acute D8 scans. The GANs architectures are depicted in Figure 4.12. Both GANs were trained for 1000 epochs with a batch size of 4. The learning rate was 0.0002 for the first 500 epochs and decreased linearly to 0 in the second half of the training. On-the-fly, only-spatial random standard DA, applied to the training samples, consisted of rotation around LAx ($p^{ii} = 0.4$), scaling within $\pm 10\%$ ($p = 0.4$), and array flip along the SAx plane ($p = 0.5$). Optimization and loss functions were defined as in Section 4.1.3.

Once the GANs were trained, the GTLs of the training samples were modified with random scaling, random rotation along LAx, random translation in the SAx plane in the ± 5 mm range, and non-rigid deformation in the SAx plane, as in Section 4.1.3. Synthetic, G-created GTL-image pairs, preserving their original voxel size and spacing, were added to the MYOSAIQ training set to form the augmented dataset.

[ii] p: probability

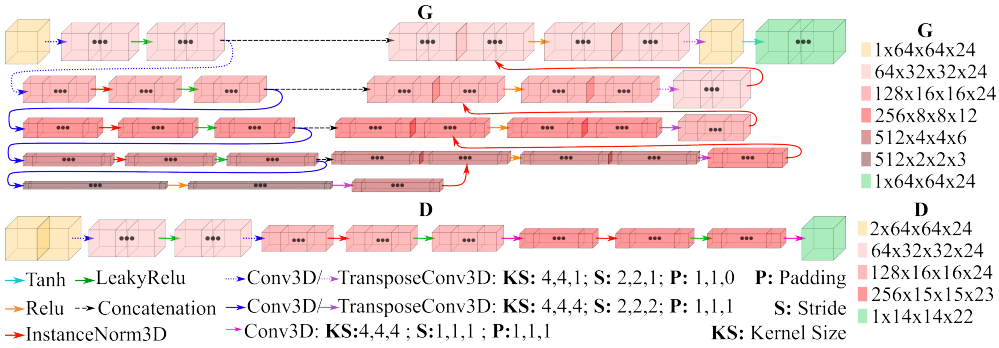


Figure 4.12: Detailed GAN illustration depicting G and D architectures used for SA in the context of the MYOSAIQ challenge.

For core segmentation, two 3D full-resolution nnUNets were trained separately on the augmented D8 (194 samples) and MX (504 samples) datasets. Each model was trained for 1000 epochs using the default nnUNet configuration, including preprocessing, on-the-fly DA, optimization, and loss function [79]. Five-fold cross-validation was employed. The pseudo-DSC and ECE were evaluated on the validation set at the final epoch and the best-performing epoch (epoch with the highest average pseudo-DSC). Based on this comparison, the final checkpoint was used for D8 inference, while the best checkpoint was selected for MX inference.

Uncertainty in volume estimation was quantified using the CRPS, computed for each class defined in the LGE images (see Section 1.5.5). This required estimation of the class-wise PDF and CDF of the random variable volume (V) for each patient (P). Logits were calibrated via temperature scaling to obtain per-voxel probabilities, as described by Guo et al. [95]. As can be observed in Figure 4.13a, calibration substantially reduced the ECE of the MX-trained nnUNet (see Section 1.5.5).

The estimation of the PDF of V in a patient P was performed by sampling calibrated logits, which represent per-voxel probabilities, generating multiple realizations of the volume distribution. For a certain V in a patient P, the following steps were taken:

- Voxels with Shannon entropy values below 0.4689 were considered sufficiently certain to belong to the class indicated by their probability (p) (either V or background). Next, samples of V were generated by grouping voxels with p between 0.1 and 0.9, which represent the most uncertain regions in the segmentation, as seen in the right panel of Figure 4.13b.

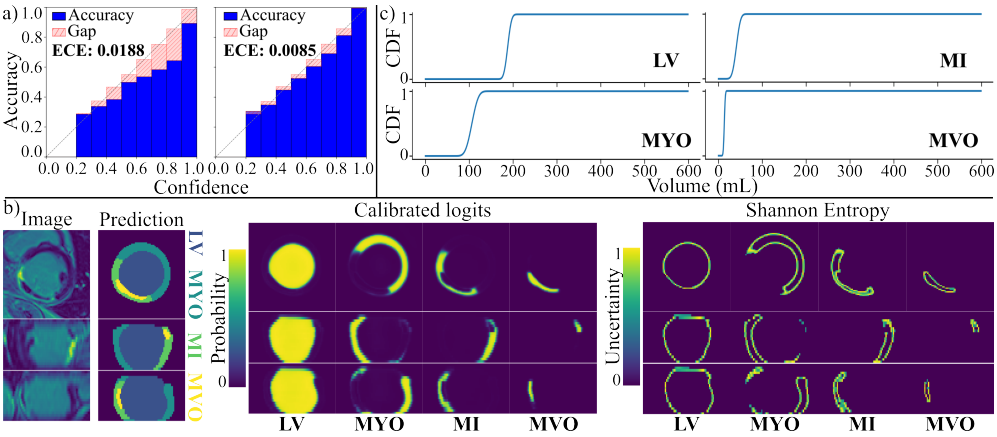


Figure 4.13: Instance-level uncertainty estimation results. a- Reliability diagrams before (left) and after (right) calibration of the nnUNet-obtained logits after training MX samples on the fold 1. b- Different views (rows) of the image and predicted segmentation, calibrated logits and uncertainty ($p > 0.9$ or $p < 0.1$ depicted as completely certain) obtained for the test sample 031_D8. c- Volume CDFs for the test sample 031_D8.

This thresholding strategy was adopted to reduce the number of voxels included in the sampling process, thus mitigating computational and memory demands.

- The 0.1-0.9 range of p was divided into N equally spaced bins, and the voxels were grouped into N voxel groups based on their values of p. Voxels with $p > 0.9$ were considered to form the minimum volume V_{min}. The rationale for this approach is that these voxel groups could be included or excluded from V_{min}, allowing us to generate 2^N samples of the random variable V. A high value of N reduces the constraints on the sampling of V, allowing a more accurate but expensive approximation of the PDF where each uncertain voxel is treated individually and not grouped. To balance computational efficiency and estimation accuracy, we empirically set N to 20.
- For the i^{th} of the 2^{20} possible combinations, we selected the voxel groups included in the configuration and calculated the resulting sample V_i, along with an associated pseudo-probability p_i. Each combination was represented as a 20-digit binary number, where a digit value of 1 indicates the inclusion of the corresponding voxel group. For instance, the binary combination 00000000000000000111 includes the voxel groups 0, 1, and 2. Next, V_i was calculated as V_{min} plus the volumes of the voxel groups that were included. Its p_i was estimated as the mean of the probabilities

of the voxels within V_i, comprising the voxels from V_{min} and the selected voxel groups. Note that the same V_i can appear M times in different realizations of V, each with potentially distinct p_i. In addition, the values of p_i do not represent real probability measures, since $\sum_{i=1}^{2^{20}} p_i \neq 1$. However, p_i serves as an indicator of how likely a specific V_i is, based on the underlying voxel-wise probabilities, hence the term pseudo-probability.

- Lastly, we defined the unique volumes V_u with $u = 1, ..., U$ and U the total number of unique volumes V_i. We computed the unique probability p_u for each V_u as $p_u = \sum_{m=1}^{M} p_i^m$ and normalized it as $p_u = p_u / \sum_{u=1}^{U} p_u$. In this way, we defined a PDF, composed of V_u and its correspondent p_u. Note that $\sum_{u=1}^{U} p_u = 1$, and that the value p_u depends on the M number of times the unique volume value V_u was present in the 2^{20} realizations of V_i and on the voxel-wise probabilities through p_i. From this distribution, the CDF was calculated as $p(V_u <= v)$ with $v = 0, 1, \ldots,$ 599 mL (see Figure 4.13c).

The main scripts used for preprocessing, postprocessing and CDF estimation are available at `https://github.com/lino202/myosaiq_scripts/tree/main`. The 3D GAN source code is provided at `https://github.com/lino202/3Dseg/tree/minimal_modifications_for_myosaiq_challenge`. The modified nnUNet with logit calibration can be found at `https://github.com/lino202/nnUNet/tree/master`.

4.4.2 Results

Geometrical scores: Table 4.3 reports geometrical scores for all participants of the MYOSAIQ challenge [96], including class-wise spatial overlap (DSC) and contour distance (Average symmetric surface distance and HD) between the segmentation results and the GTLs. Across participants, segmentation accuracy was higher for the LV and MYO classes compared to MI and MVO classes. Our implementation achieved mean DSC scores of 0.928, 0.84, 0.669 and 0.537 for LV, MYO, MI and MVO classes, respectively. For the LV and MYO classes, our implementation achieved the fourth and second highest mean DSC value. When evaluating HD, our results were either the best (MYO) or not statistically significantly different from the best result (LV). For MI segmentation, we obtained the third-highest mean DSC and the sixth HD, while MVO results were less competitive, with DSC using our method being the lowest, but mean HD not being statistically significantly different from the best result. Nevertheless, our method achieved similar results compared to

other participants and, importantly, led to fully accurate detection of the presence or absence of MVO in all images of the test set. The lower performance observed for the MI and MVO classes was anticipated, given their higher morphological complexity and variability, along with their under-representation in the dataset relative to the LV and MYO classes. Figure 4.13b illustrates an example segmentation for the test sample 031_D8.

Clinical scores: To evaluate class-wise volume estimation, clinical scores including correlation coefficients, mean absolute error, and limits of agreement (defined as 1.96 times the standard deviation) between predictions and GTLs were computed. Uncertainty in volume estimation was quantified using the CRPS, calculated from the estimated CDFs (Section 4.4.1). As reported in Table 4.4, our volume estimates showed strong agreement with ground truth, with mean absolute errors and limits of agreement remaining small relative to typical class volumes. Correlation values were high across all classes: 0.969, 0.967, 0.882, and 0.972 for LV, MYO, MI, and MVO classes. Particularly for MYO, our predicted volumes had the highest agreement among all participants across all clinical metrics. These results confirm the ability of our method to accurately estimate clinically relevant volumes from LGE-CMRs while eliminating the need for time-consuming manual annotations.

Improvement strategies: Segmentation performance could be further enhanced by adopting cascade structures. As shown by Lustermans et al. [140], a two-stage pipeline where a first CNN segments LV and MYO classes and a second CNN segments MI within the MYO region, could yield improved MI segmentation results. Indeed, three out of the six MYOSAIQ participants used cascade-type segmentation, including the top-performing team in terms of geometrical scores [96]. This suggests that our approach, already competitive, could benefit from similar strategies, with separate networks for LV/MYO and MI/MVO sequential segmentation. Furthermore, incorporating spatially adaptive (de)normalization-GAN architecture for improved SA and applying topological priors to enforce anatomical consistency represent promising future directions, as discussed in Section 4.3.

Uncertainty estimation: Regarding uncertainty quantification, our method achieved the lowest CRPS values across all classes (Table 4.4). Our probabilistic framework, based on temperature scaling, produced CRPS values 3 to 7 times lower than those of ensemble-based approaches (see Section 2.1.4). These gains persisted even for LV and MYO, where uncertainty boundaries are larger and typically increase CRPS. Overall, this demonstrates the capacity of our method to provide instance-level uncertainty quantification from voxel-level predictions.

Table 4.3: Results of geometrical scores for the MYOSAIQ challenge. Bold numbers are the best results for each column and blue numbers indicate results that are not significantly different from the best result in each column (paired t-test, >0.05). ASSD: average symmetric surface distance (mm), HD measured in mm, TP: number of times an MVO was present in an image and correctly detected, TN: number of times a method correctly identified that no MVO is present in an image. The data on this table was obtained from data in [96] and in [84].

Method	LV			MYO			MI			MVO				
	DSC	ASSD	HD	DSC	ASSD	HD	DSC	ASSD	HD	DSC	ASSD	HD	TP	TN
P1 (ours)	0.928 ±0.031	0.5 ±0.2	7.2 ±2.4	0.840 ±0.036	**0.4 ±0.2**	**9.0 ±2.8**	0.669 ±0.177	**1.0 ±1.7**	19.8 ±14.4	0.537 ±0.190	1.2 ±1.0	19.5 ±14.6	10/10	15/15
P2	**0.933 ±0.029**	**0.4 ±0.2**	6.8 ±2.1	0.840 ±0.038	**0.4 ±0.1**	**9.0 ±3.0**	**0.700 ±0.145**	**1.0 ±1.7**	**16.8 ±13.2**	**0.681 ±0.119**	**0.7 ±0.4**	14.4 ±4.7	9/10	15/15
P3	0.930 ±0.034	0.5 ±0.4	7.7 ±5.8	**0.841 ±0.041**	**0.4 ±0.2**	9.9 ±6.1	0.688 ±0.168	**1.0 ±1.3**	17.3 ±12.4	0.648 ±0.140	0.8 ±0.4	14.1 ±5.0	8/10	15/15
P4	0.926 ±0.031	0.5 ±0.2	7.3 ±2.4	0.827 ±0.043	**0.4 ±0.1**	9.5 ±3.3	0.660 ±0.159	**1.0 ±1.5**	19.5 ±13.5	0.647 ±0.126	**0.7 ±0.3**	**13.5 ±5.0**	8/10	15/15
P5	0.914 ±0.034	0.6 ±0.3	7.9 ±3.2	0.806 ±0.043	**0.4 ±0.2**	10.6 ±3.4	0.628 ±0.170	1.2 ±1.8	23.9 ±14.9	0.552 ±0.186	1.0 ±0.5	16.2 ±3.4	9/10	15/15
P6	0.931 ±0.030	**0.4 ±0.2**	**6.7 ±2.2**	0.839 ±0.038	**0.4 ±0.1**	9.6 ±3.8	0.661 ±0.150	**1.0 ±1.3**	19.7 ±13.2	0.568 ±0.145	1.1 ±0.6	19.6 ±10.3	7/10	15/15

Table 4.4: Results of clinical scores for the MYOSAIQ challenge. Bold numbers are the best results for each column. CC: correlation coefficient, MAE: mean absolute error (mm), LOA: limits of agreement (mm). The data on this table was obtained from data in [96].

Method	LV				MYO				MI				MVO			
	CC	MAE	LOA	CRPS	CC	MAE	LOA	CRPS	CC	MAE	LOA	CRPS	CC	MAE	LOA	CRPS
P1 (ours)	0.969	8.2	23.8	**0.002**	**0.967**	**8.6**	**24.5**	**0.004**	0.882	3.4	12.1	**0.001**	0.972	2.7	6.5	**0.000**
P2	**0.980**	**6.7**	**18.0**	0.011	0.946	11.2	31.1	0.018	0.892	3.4	12.3	0.005	0.989	**1.1**	3.0	0.003
P3	0.978	7.4	19.6	0.012	0.924	13.1	38.1	0.022	0.888	3.2	11.7	0.006	0.990	2.6	4.9	0.006
P4	0.977	7.5	20.4	0.012	0.918	12.3	38.2	0.021	0.868	3.3	12.6	0.006	**0.997**	1.4	**2.9**	0.004
P5	0.976	8.1	19.9	0.014	0.923	17.5	52.5	0.030	0.902	3.5	11.6	0.007	0.970	2.5	5.6	0.006
P6	**0.980**	6.8	18.7	0.011	0.945	12.1	33.9	0.020	**0.909**	**3.1**	**10.0**	0.004	0.919	4.2	10.2	0.004

Summary: Our approach accurately estimated class-wise geometry and volume while providing reliable uncertainty quantification, thereby improving clinical interpretability and trust in automated predictions.

4.5 Conclusion

In this chapter, we evaluated how GAN-based DA and topologically driven corrections can improve 3D CNN-based segmentation of complex multi-vendor, multi-center, multi-class, and multi-contrast CMRs. For the isotropic topologically homogeneous *ex vivo* dataset, SA and TC individually or in combination led to clear and consistent segmentation improvements. For cine and LGE datasets, despite low out-of-plane resolution and inter-slice misalignment, our methods yielded slight but significant segmentation improvements. Notably, infarction segmentation in LGE data benefited substantially from the joint use of SA and TC.

For the MYOSAIQ challenge, our GAN-based DA approach, combined with an nnUNet-based method, achieved state-of-the-art performance, as demonstrated by both geometrical and clinical volume estimation scores. Moreover, the integration of uncertainty quantification provided robust confidence measures, further enhancing clinical reliability. Altogether, these findings underscore the potential of our proposed framework to advance CMR segmentation and support its translation to clinical practice.

CHAPTER 5

INTEGRATED MULTI-MODAL DATA ANALYSIS FOR COMPUTATIONAL MODELING OF HEALTHY AND LOCATION-DEPENDENT MYOCARDIAL INFARCTION CONDITIONS IN PORCINE HEARTS

5.1 Methodology
- 5.1.1 Experiments
- 5.1.2 Structural data
- 5.1.3 Functional data
- 5.1.4 Electrophysiological modeling
- 5.1.5 Numerical simulations

5.2 Results
- 5.2.1 Effective CS-BiV coupling
- 5.2.2 BiV activation and QRS
- 5.2.3 BiV repolarization and T wave
- 5.2.4 Personalized CM orientation
- 5.2.5 Post-MI alterations
- 5.2.6 Post-MI activation and the ECG
- 5.2.7 Location and morphology of MI and the ECG

5.3 Discussion
- 5.3.1 CS-myocardial coupling
- 5.3.2 CS and HERP determine QRS complex
- 5.3.3 Small APDSH shapes repolarization
- 5.3.4 Limited impact of CM orientation
- 5.3.5 Post-MI remodeling
- 5.3.6 Post-MI ECG replication
- 5.3.7 MI-induced ECG changes
- 5.3.8 Limitations

5.4 Conclusion

Although porcine *in silico* models are widely used to support preclinical research, many remain adapted from human data, which restricts their mechanistic accuracy, predictive capacity, and ability to individualize key simulation parameters. To address these limitations, this chapter proposes that porcine cardiac conditions can be more faithfully reproduced by tailoring essential modeling parameters, identified through comprehensive multi-modal porcine data and systematically validated via large-scale simulations.

Specifically, this work pursues three objectives:
1) To guide the development and calibration of BiV electrophysiological models for healthy and MI pig hearts by processing cardiac signals and images from *in vivo* and *ex vivo* pig experiments;
2) To identify the critical parameters necessary to reproduce porcine-specific electrophysiological features under both healthy and MI conditions;
3) To show the clinical relevance of these experimentally informed models by characterizing infarction-induced changes in simulated ECGs across an extensive set of LAD and LCx MI scenarios.

5.1 Methodology

5.1.1 Experiments

5.1.1.1 Animals

The study population consisted of 15 large white domestic pigs, of both sexes, sourced from two centers: Katholieke Universiteit Leuven (KUL), Leuven, Belgium and Servicio Madrileño de Salud (SERMAS), Madrid, Spain. Animals weighing 20-30 kg (KUL) and 55-65 kg (SERMAS) were included. Structural and functional data from both healthy and MI pigs were collected and processed as detailed in Table 5.1. All animal procedures complied with the guidelines from Directive 2010/63/EU of the European Parliament on the protection of animals used for scientific purposes, were approved by local regulatory authorities, and adhered to the animal welfare regulations applicable in each country.

Prior to each experiment, animals were sedated and anesthetized following site-specific protocols. At KUL, animals were sedated with Telazol (tiletamine 4 mg/kg and zolazepam 4 mg/kg, Zoletil100, Virbac Animal Health, Carros, France) combined with xylazine (2.5 mg/kg, Vexylan, CEVA Sante Animale, Brussels, Belgium). Anesthesia was induced intravenously with propovet (10

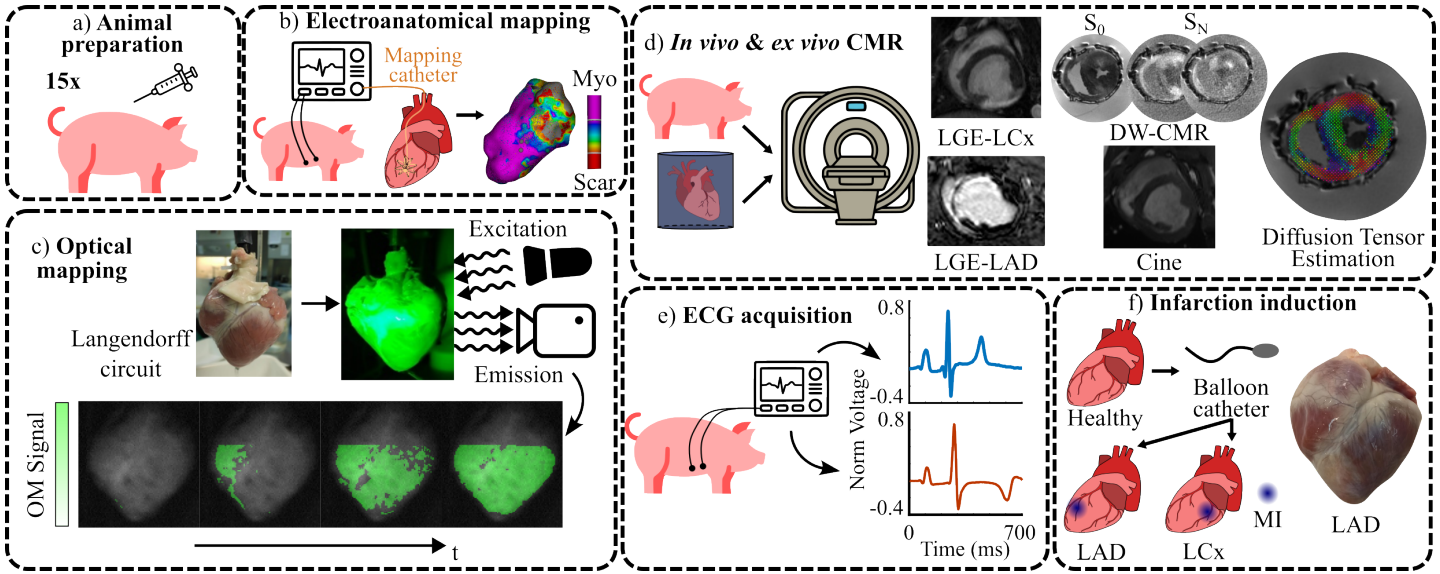


Figure 5.1: Graphical summary of experimental data acquisition. a- Animal preparation was conducted on 15 pigs. b- EAM of pig 6. c- OM scheme with activation of pig 13. d- Different CMR techniques applied. LGE-LCx: pig 7, LGE-LAD: pig 10, cine: pig 3, DW-CMR and diffusion tensor estimation: pig 2. e- ECG acquisition. It shows the ECG signal at lead II for healthy pig 15 (blue) and LCx-MI pig 6 (orange). f- Scheme of MI induction with a picture of the anterior view of an LAD-MI swine heart. Healthy data were acquired prior to MI induction. MI data were acquired 4 weeks after MI (chronic phase).

mg/kg, propofol, Med'Vet, Chatillon, France) followed by continuous infusion of the same anesthetic (10 mg/kg/h) and remifentanil (18 µg/kg/h, Ultiva, GSK, Genval, Belgium). At SERMAS, a standardized anesthesia protocol was applied. Premedication was administered intramuscularly using ketamine (10 mg/kg), midazolam (0.3 mg/kg), and atropine (0.05 mg/kg). Anesthesia was induced intravenously with fentanyl (0.01 mg/kg) and propofol (4 mg/kg). Maintenance of anesthesia was sustained by continuous intravenous administration of fentanyl (0.01 mg/kg) and propofol (14 mg/kg).

Table 5.1: Summary of collected and processed experimental data. HE: healthy.

Pig	State	Center	CMR			Signals		
			Cine	LGE	DW	OM	EAM	ECG
1	HE	KUL	X		X			
2	HE	KUL	X		X			
3	HE	KUL	X		X			
4	LCx	KUL		X				
5	LCx	KUL		X				
6	LCx	KUL		X			X	X
7	LCx	KUL		X	X			
8	LAD	SERMAS		X		X		
9	LAD	SERMAS		X		X		
10	LAD	SERMAS		X		X		
11	LAD	SERMAS		X		X		
12	LAD	SERMAS		X		X		
13	HE	SERMAS				X		
14	LAD	SERMAS			X			
15	HE	KUL						X

5.1.1.2 Induction of myocardial infarction

LCx artery MI and LAD artery MI were induced at KUL and SERMAS, respectively (Table 5.1). At KUL, pigs received amiodarone orally for two weeks (400 mg/d during the first week, 200 mg/d during the second week). One day before MI induction, animals were preloaded with acetylsalicylic acid and clopidogrel (300 mg each) via oral gavage. Sedation and anesthesia protocols followed those described in Section 5.1.1.1. Mechanical ventilation with an air-oxygen mixture (1:1) was adjusted to maintain normocapnia and normoxia using a tidal volume of 8-10 mL/kg. Continuous monitoring of blood pressure, ECG, and peripheral oxygen saturation was performed using an intensive cardiac monitor system (Siemens). Following anticoagulation with heparin (10,000 IU) and antiplatelet administration (acetylsalicylic acid, 500 mg), MI was induced by proximal occlusion of the LCx coronary artery. Briefly, a guide wire was advanced through the coronary artery and a dilation balloon catheter, sized according to angiographic measurements, was positioned and inflated for 90

min to occlude the vessel, followed by deflation to allow reperfusion. Coronary artery occlusion and reperfusion were confirmed by angiography. At SERMAS, MI was induced by balloon occlusion of the mid-LAD coronary artery, distal to the first diagonal branch, via femoral access. Occlusion was maintained for 90-150 min to achieve TIMI 0 flow, followed by reperfusion. Lidocaine (1 mg/kg IV) was administered prior to occlusion to prevent arrhythmias. Ventricular tachyarrhythmias were treated according to standard resuscitation protocols. Procedures were conducted under general anesthesia with sevoflurane and mechanical ventilation via orotracheal intubation. After MI, pigs received aspirin (500 mg QD), clopidogrel (300 mg QD), and amiodarone (400 mg QD for 5 days). This reperfusion model has been previously validated and produces a heterogeneous scar that more accurately represents clinical MI cases [177, 178]. MI data were collected 4 weeks after MI induction (chronic stage).

5.1.2 Structural data

The structural data in this study involved cine-CMR, DW-CMR, and LGE-CMR sequences. At KUL, all CMR acquisitions were performed during suspended respiration using electrocardiographic triggering and cardiac-dedicated surface coils on a 3T Siemens system (TRIO-Tim, Siemens, Erlangen). At SERMAS, DW-CMR and LGE-CMR were performed using 1.5T Philips Achieva and Intera magnetic resonators (Philips Healthcare, Best, The Netherlands).

5.1.2.1 Cine-CMR

Cine-CMR was performed to capture the diastole-systole motion of the heart by acquiring images of cardiac slices throughout the cardiac cycle (Section 1.3.1.1). Following sedation and general anesthesia, mechanical ventilation was applied with an air-oxygen mixture (1:1) at a tidal volume of 8-10 mL/kg.

The three collected cine-CMR datasets had an anisotropic voxel resolution of 1.33 x 1.33 x 6 mm^3. End-diastolic volumes were selected for analysis. Preprocessing included cropping, padding, anisotropic resampling, and Z-score intensity normalization. Based on the algorithms presented in Chapter 4, the blood pools of the LV and RV and the LV myocardium were segmented using a semi-automatic DL-based pipeline combining SA and TC.

Table 5.2: DW-CMR characteristics. HE: healthy

Pig	State	Resolution (mm^3)	Gradients	b value
1	HE	1.09 x 1.09 x 1	64	1000
2	HE	1.14 x 1.14 x 1.2	48	1000
3	HE	0.98 x 0.98 x 1.3	36	1000
7	LCx	0.98 x 0.98 x 1.08	36	1000
14	LAD	1.09 x 1.09 x 1.2	15	600

5.1.2.2 LGE-CMR

LGE-CMR was used to delineate MI by exploiting the preferential accumulation of gadolinium in AZ (Section 1.3.1.3). During acquisition, sedation, mechanical ventilation, and continuous vital sign monitoring were performed. At KUL, LGE-CMR was acquired 12 min after intravenous injection of gadolinium 0.2 mM/kg (Dotarem, Guerbet, Roissy, France). At SERMAS, LGE-CMR images were acquired 10 min after injection of gadodiamide 0.2 mM/kg.

LGE-CMR data from SERMAS and KUL had anisotropic voxel resolutions of 1.28 x 1.28 x 2.5 mm^3 and 1.25 x 1.25 x 5.5 mm^3, respectively. Preprocessing and DL-based segmentation followed the same protocol as for cine-CMR data, with additional segmentation of the MI region (Chapter 4).

5.1.2.3 DW-CMR

DW-CMR was used to characterize the 3D microarchitecture of ventricular tissue by quantifying the directional diffusion rate of water molecules under applied electromagnetic gradients (Section 1.3.1.2). At KUL, hearts were arrested in end-diastole, excised with the great vessels, and perfused via the coronary arteries with 1 L of cold cardioplegic solution at a pressure of 100 mmHg, then immersed in the same solution for 1 hour. The great vessels were firmly tied to maintain pressure, and the hearts were placed in a custom 3D-printed container filled with cardioplegic solution. At SERMAS an atrial transseptal puncture was performed to equalize intracavitary volumes. Warm 2% agarose gel solution (≈38 °C) was infused via cannulas in the aorta and pulmonary artery until the ventricular cavities approximated an *in vivo* diastolic state. Hearts were placed in custom-designed *ad hoc* containers to preserve geometry.

Multiple electromagnetic sensitizing gradients (Table 5.2) were applied to estimate myocardial diffusion tensors. Following segmentation, diffusion tensors were computed and their primary eigenvectors were extracted to determine myocardial fiber orientation (see Section 1.3.1.2) [179]. In MI cases, AZ was

manually added to the segmentation, and voxel-wise fractional anisotropy was calculated for the healthy tissue and AZ as a function of the diffusion tensor eigenvalues λ_i, $i = 1, 2, 3$:

$$FA = \sqrt{\frac{1}{2}\left(\frac{(\lambda_1 - \lambda_2)^2 + (\lambda_3 - \lambda_2)^2 + (\lambda_3 - \lambda_1)^2}{\lambda_1^2 + \lambda_2^2 + \lambda_3^2}\right)}$$

5.1.3 Functional data

5.1.3.1 OM

OM was performed to record the electrical activity of explanted hearts, using voltage-sensitive dyes to track changes in V_m with high spatio-temporal resolution (Section 1.3.2.1).

Immediately after explantation, the hearts were immersed in cold (4 °C) cardioplegic solution containing (in mM): 12.6 $NaHCO_3$, 13.44 KCl, 280 D-glucose, 34 mannitol, 140 NaCl, and 10 2,3-butanedione monoxime, pH 7.4, for preservation during transport. On arrival, a cannula was inserted into the aorta to perfuse the heart via a Langendorff circuit with Tyrode's solution at 37 °C. The Tyrode composition was (in mM): 130 NaCl, 24 $NaHCO_3$, 4 KCl, 1 $MgCl_2$, 5.6 D-glucose, 1.2 NaH_2PO_4, and 1.86 $CaCl_2$, pH 7.4. Temperature (37 °C) and oxygenation were maintained via an external heating bath and an oxygenator with a carbogen gas mixture, using bubble traps and filters to ensure stable perfusion.

Electrical activity was monitored from fluorescence changes after infusion of a 100 µL bolus of di-4-ANEPPS (excitation: 482 nm, emission: 686 nm; Biotium, Inc. Hayward, CA, USA) in 4.16 mM DMSO applied for 5 min following electromechanical uncoupling with 10 µM 2,3-butanedione monoxime in Tyrode's solution. For dye excitation, hearts were homogeneously illuminated with a filtered green LED light source (LED: CBT-90-G; peak power output 58 W; peak wavelength 524 nm; Luminus Devices, Billerica, USA) through a planar-convex lens (LA1951; focal length 25.4 mm; Thorlabs, New Jersey, USA) and a green excitation filter (D540/25X; Chroma Technology, Bellows Falls, USA). Fluorescence was recorded using an EMCCD camera (Evolve-128: 128×128 imaging pixels, 24×24-µm pixels, 16 bits; Photometrics, Tucson, AZ, USA) with a custom multiband emission filter (ET585/50-800/200 M; Chroma Technology) and high-speed lens (DO2595; Navitar Inc., Rochester, USA).

OM was performed on five porcine hearts with LAD MI and one healthy

heart, during sinus rhythm or under external stimulation applied from a catheter located in the right atrium, RV, or LV with a pacing cycle length of 1000 ms. Pixel resolution was determined from a conversion factor that was calibrated immediately before the OM experiment and held constant for all recordings (pig 8: 0.081, pig 9: 0.0729, pig 10: 0.0860, pig 11: 0.0885, pig 12: 0.0906, pig 13: 0.105 cm per pixel). The sampling frequency was 500 Hz in all cases. Data were processed using custom software [159]. A region of interest that included both ventricles was manually defined. High-pass filtering (0.4 Hz cut-off frequency) and adaptive spatio-temporal Gaussian filtering were applied to remove baseline drift and high-frequency noise, as performed in Section 3.1.1.2. The AT for each pixel and beat was defined as the time interval from a fixed time reference to the time corresponding to the maximum positive derivative of V_m. APD_{90} was calculated as the difference between the time associated with the maximum derivative of V_m and the time when 90% repolarization from the peak of the AP to the diastolic V_m was reached. Median AT and APD_{90} values across beats were used to generate AT and APD_{90} maps. The CV vector between two pixels was defined as the ratio of the Euclidean distance between them to their AT difference. The mean CV vector for a given pixel was then calculated across its neighboring pixels within a radius of 3 pixels. The radius value was chosen as a trade-off to avoid over-smoothed CVs while preventing extremely large CVs computed from noisy neighbors.

5.1.3.2 ECG

A 12-lead ECG was acquired from healthy pig 15 at KUL at a sampling frequency of 2000 Hz (Figure 5.1e). Lead placement was as described in Section 5.1.3.3. Signals were filtered using high- and low-pass Butterworth filters with cutoff frequencies of 0.5 and 40 Hz, respectively. ECG waves were delineated using a wavelet transform-based delineator [180]. From the detected QRS complexes, the mean RR interval was 769 ms.

To obtain a median beat $\overline{\boldsymbol{b}}_i$ for each lead i, all beats ($\boldsymbol{b}_i^j$, $j = 1, ..., N$, with N the total number of beats in lead i) were aligned after automatically cropping them at 240 and 538 ms before and after the QRS fiducial point, respectively. The most representative beat $\hat{\boldsymbol{b}}_i$ in lead i was selected as the one with the highest sum of correlation coefficients with all other beats in the lead. The median beat $\overline{\boldsymbol{b}}_i$ was then defined as the median of all $\boldsymbol{b}_i^j$ whose correlation with $\hat{\boldsymbol{b}}_i$ was greater than 0.9.

5.1.3.3 EAM

EAM allows real-time reconstruction of cardiac anatomy with superimposed electrogram measures (Section 1.3.2.3). Figure 5.1b illustrates the data obtained from the EAM of pig 6. Sedation was administered as described in Section 5.1.1.1. Aligned LGE and thoracic magnetic resonance images were acquired. For thoracic imaging, visible pins were placed to identify heart-electrodes relative position (HERP) during ECG acquisition (Figure 5.2a). As hind leg electrodes were outside the field of view of the thoracic magnetic resonance, right leg and left leg electrode coordinates were estimated by extending right and left arm coordinates 60 cm in the antero-posterior direction.

LV endocardial mapping was performed using the Rhythmia high-resolution mapping system (Boston Scientific, Cambridge, MA, USA) [60, 61]. A diagnostic catheter was percutaneously inserted in the left femoral vein and advanced into the RV to act as an intracardiac activation reference. The Orion 64-electrode minibasket catheter was inserted into the LV through the aorta using a percutaneous access made in the left carotid artery. Positional reference and impedance electrodes were placed on the right side and right back to avoid spinal interference. The mapping in sinus rhythm yielded 3939 LV endocardial points.

EAM measurements were used to define two EAM-based LV stimulation profiles for numerical simulations: endocardial EAM (e-EAM) and intramyocardial EAM (i-EAM). The aorta and the LV apex from EAM were aligned with the aortic valve and the apical LV from the CMR-based BiV mesh of pig 6, respectively (see Figure 5.2b). In the aligned EAM, electrograms with low bipolar voltage ($\leqslant$ 1 mV) were excluded as SZ (or poor-contact points) [60], since SZ was defined as an insulator *in silico* (Section 5.1.4.3) and therefore its depolarization was irrelevant. Subsequently, outliers in the EAM in terms of bipolar electrogram ATs were removed, resulting in 2630 valid points (Figure 5.2c). Finally, the unique endocardial and intramyocardial points in the LV of the BiV model closest to each EAM site defined e-EAM and i-EAM stimulation sites. Stimulation dynamics were described by interpolating the EAM-based bipolar activation to the e-EAM or i-EAM stimulation points using radial basis functions. Thus, the BiV model was depolarized from the EAM-defined stimulation points on the LV along with the RV CS. In this context, LV depolarization was set to start 5 ms after the first RV endocardial depolarization, consistent with the mainly positive QRS complex for this pig in lead I (Figure 5.10a), which, based on our simulation results, suggests a more RV-to-LV activation (see discussion on the addition of Purkinje fibers to the RV septum in

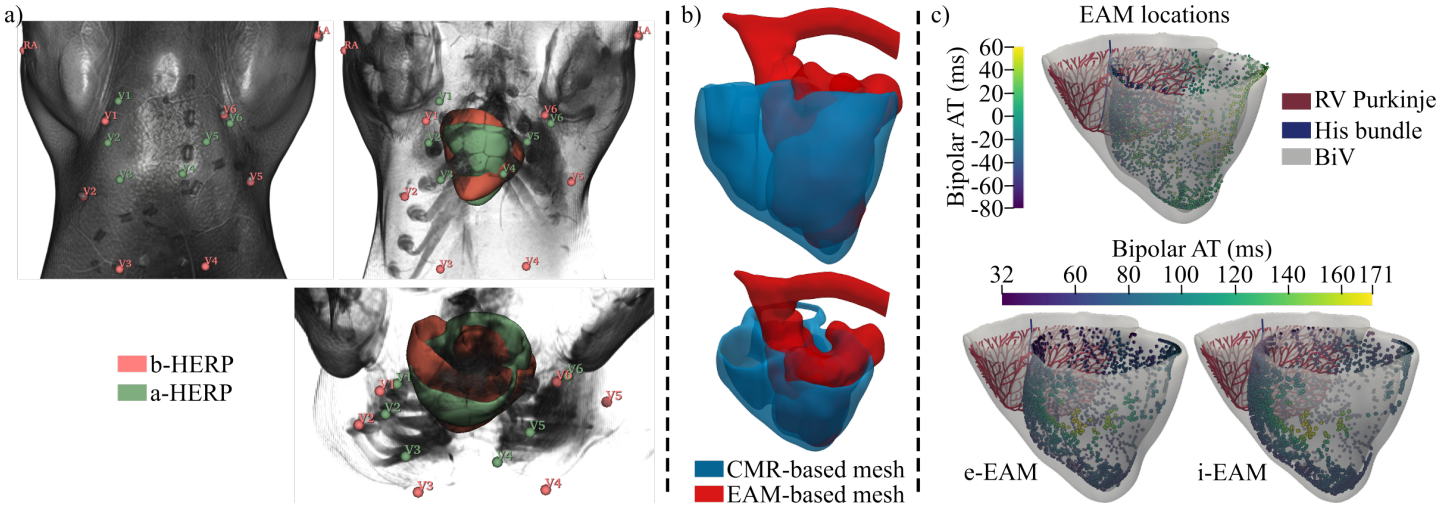


Figure 5.2: HERP of pig 6 and its EAM-based activation. a- Different views of the thoracic magnetic resonance of pig 6 with different opacity, showing the b-HERP (red) and a-HERP (green). RA: right arm, LA: left arm and V1-6: precordial electrodes. Right and left leg electrodes are not shown. b- Alignment of the EAM-based mesh of the LV endocardium with the CMR-based BiV mesh. c- The BiV mesh of pig 6 is shown with the RV Purkinje, the His bundle and the preprocessed LV EAM locations with their bipolar activation (top), as well as the EAM-based endo- (e-EAM) and intramyocardial (i-EAM) bipolar activations (bottom) of the LV.

Section 5.3.2). Bipolar electrograms were used throughout, given their strong agreement with unipolar low voltage areas under high-density mapping with low inter-electrode spacing [59], as implemented here using the Orion catheter (2.5 mm spacing [60]), and their reduced susceptibility to far-field effects compared to unipolar recordings [59].

ECG signals from Rhythmia were preprocessed as described in Section 5.1.3.2. Since these ECG signals were provided as chunks that sometimes did not contain a complete beat, a template, complete ECG beat was selected among all recordings. Beats presenting a correlation coefficient with this template greater than 0.8 in each lead were selected and, based on them, the median ECG beat was calculated (see orange ECG in Figure 5.1e). Finally, the *in silico* ECG reconstructed from the two EAM-based stimulation profiles were compared with those obtained with a CS-based stimulation protocol.

5.1.4 Electrophysiological modeling

5.1.4.1 Anatomy

Using the DL-based segmentations obtained in Section 5.1.2, the RV myocardium was delineated and the final smoothed BiV surface meshes were generated for the healthy and MI cases [181, 182]. Healthy geometries were derived from cine-CMR, and MI geometries were derived from LGE-CMR. As shown in Figure 5.3b, volumetric meshes were generated via tetrahedralization with a mean edge length of 390 µm for all samples [183], consistent with previous studies [10, 15, 50, 184].

In MI cases, AZ and the healthy tissue were manually identified from the automatic DL–based segmentations of LGE images (Section 5.1.2.2), corresponding to high and low voxel intensities, respectively. AZ was subdivided into BZ and SZ using the full-width half-maximum method [49]. Briefly, two thresholds were defined, as shown in Figure 5.3a: S_{BZ+}, corresponding to 50% of the maximum signal intensity in AZ; and S_{BZ-} corresponding to the maximum signal intensity in a remote healthy zone. SZ comprised AZ voxels with signal intensity greater than S_{BZ+}. BZ comprised AZ voxels with signal intensity in the range $[S_{BZ-}, S_{BZ+}]$. The healthy tissue, BZ, and SZ masks were interpolated to the BiV mesh using radial basis functions.

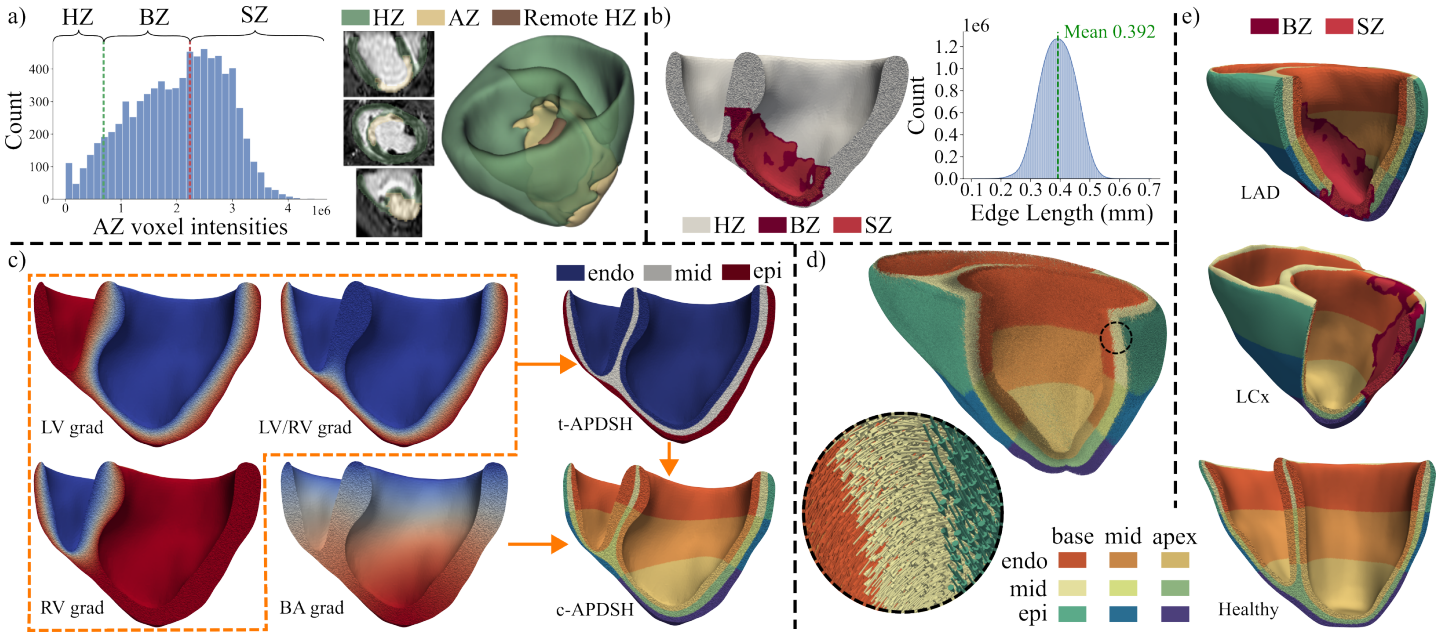


Figure 5.3: *In silico* BiV healthy and MI modeling. a- MI segmentation from LGE-CMR of the pig 10. The histogram of the AZ voxel intensities shows S_{BZ-} (green) and S_{BZ+} (red) thresholds delimitating the BZ. b- BZ and SZ extrapolation onto the tetrahedral mesh (left) and mesh edge length histogram for pig 10. c- BiV APDSH calculation. In the left side, the Laplace solutions representing the diffusion from LV, RV and LV/RV endocardium to epicardium (orange dashed zone) and from base to apex (BA) are shown. In the right side, the final transmural (t-APDSH) and transmural plus apico-basal (c-APDSH) BiV meshes for pig 10 are depicted. d- RBM-based BiV fiber field for pig 10. e- Final BiV meshes for pig 10 (top), pig 6 (middle) and pig 3 (bottom). HZ: healthy zone.

5.1.4.2 Conduction system

Ventricular CS plays a key role in determining the electrical activation sequence that triggers mechanical contraction (Section 1.2.3.2). CS geometry was defined from manually identified anatomical landmarks, geodesic paths, and a fractal tree algorithm (Section 1.6.3.5).

First, the His bundle was generated by connecting landmark points in a 3D space with 1D elements (Figure 5.4a). Briefly, the AVN was placed 5 mm above the septal base toward the anterior RV. The His bundle extended toward the apex, bifurcating into left and right branches, both traversing from the basal to the apical endocardium along geodesic paths. The left branch was divided into the anterior and posterior left branches, while the right branch remained single. Consistent with experimental studies, the LV bundle branches terminated at papillary muscles, whose insertions were identified from cine-CMR [129, 185], while the RV bundle branch terminated in the antero-endocardial face, more basally than the LV bundle branch endpoints and than the analogous structure in humans, in agreement with experimental observations of the septomarginal trabecula (moderator band) in pigs (see Section 5.3.2) [14].

The Purkinje network was generated from the endpoints of the three bundle branches using a fractal tree algorithm [118], resulting in an endocardial CS termed be-CS. However, given experimental evidence that the swine CS lies deeper within the myocardium than in humans [14], an alternative CS termed bi-CS was created. This bi-CS was derived by projecting be-CS into the subendocardium (outer half of the endocardium) (Figure 5.4a) and, for 75% of the CS end branches in the LV and the RV, into the intramyocardial region (middle third of the midmyocardium) [32]. PMJs were distributed throughout both ventricles except for the basal area of the LV and the RV and the septal and posterior regions of the RV, where activation was known to be delayed or initiated by activation of surrounding tissue [118, 186].

To further explore the ventricular CS architecture, four variations of the bi-CS architecture were constructed (Figure 5.4) and the simulation results obtained with each of them were compared with the experimental activation data:

- rvs-CS: departing from bi-CS, a homogeneous distribution of PMJs was added to the RV septum.
- ap-CS: departing from rvs-CS, the end of the anterior and posterior bundle branches of the LV were positioned closer to the LV apex to accentuate the apicobasal LV depolarization.

- ap-e-CS: departing from ap-CS, the entire CS was located on the endocardial surface. This served for *in silico* assessing whether or not swine CS was better represented when projected deeper into the ventricular wall.
- mi-CS: departing from ap-CS, this was modified in the AZ of MI following histological observations for LAD MI [32]. Specifically, PMJs in the AZ were relocated with a proportion of 51:36:13 for the subendocardium, the intramyocardium, and the epicardium, respectively. In addition, the number of PMJs was reduced to 42% of the total amount in each of the three layers (see Figure 5.4c).

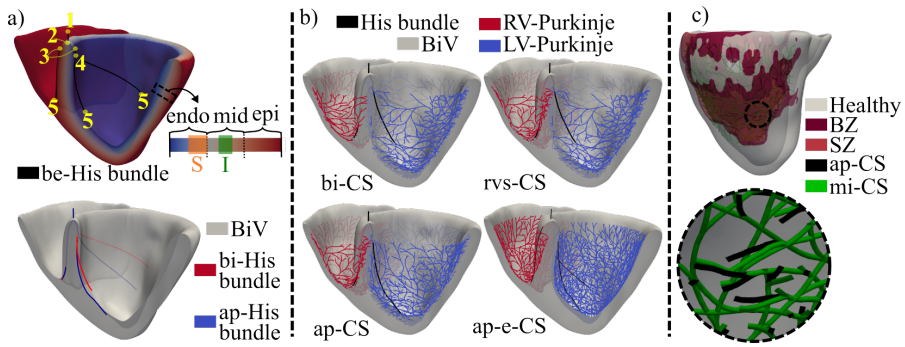


Figure 5.4: Healthy and MI CS distributions for pig 3 and 6, respectively. a- In the top side, manually located landmarks for the creation of the initial be-His bundle and subendocardium (S) and intramyocardium (I) region definitions can be observed. The bottom side depicts the differences between the His bundle in the bi-CS and ap-CS. b- Coronal cut of the pig 3 BiV mesh for depiction of four CS distributions. c- Differences of the ap-CS and mi-CS zoomed in the AZ.

5.1.4.3 Electrophysiology

APs of healthy porcine ventricular myocytes were described using the biophysically detailed model by Gaur et al. [16], while the APs of CS cells were represented with the Stewart et al. [108] model. All ventricular regions were assigned orthotropic conductivity with transverse isotropy. The LDC values were 0.0013 cm^2/ms for the healthy myocardium [100] and 0.013 cm^2/ms for CS (CV $\approx$ 200 cm/s [186]), which were respectively equivalent to 0.13 and 1.3 S/m for a membrane surface-to-volume ratio of 1000 cm^{-1} and capacitance per unit area of 1 $\mu F/cm^2$. These values defined the basal LDC (b-LDC) setting. CS LDC was reduced near its endpoints following a sigmoid curve to

smoothly match the ventricular LDC (Section 1.6.3.5) [128]. The transverse-to-longitudinal diffusion ratio was set to 0.25 for the healthy myocardium, in agreement with the transverse anisotropy reported for cardiac CV [120].

For MI BZ, excitability was reduced by decreasing the conductance of I_{Na} to 38% of the value set for healthy myocardium, following [10, 50, 187]. Conductivity and APD were then adjusted individually for each LAD-MI pig by iteratively modifying LDC and the conductance of I_{K1} (g_{K1}) until the simulated CV and APD_{90} matched OM measurements. These porcine-specific pig-wise values of LDC and g_{K1} defined the mean values that were used in cases where personalization was not possible due to the lack of electrophysiological data.

SZ was modeled as an insulator [10, 50], and thus a zero-flux Neumann condition was imposed at its boundary. Furthermore, from the comparison of the median fractional anisotropy values in the healthy and MI regions of the DW-CMR data, a mean decrease of 38% in anisotropy values was found in the MI region with respect to the healthy region. Specifically, the fractional anisotropy decreased from 0.31 in the healthy myocardium to 0.18 in AZ (41%) in pig 7 and from 0.63 to 0.41 (34%) in pig 14. Consequently, the transverse-to-longitudinal diffusion ratio was increased from 0.25 to 0.345 (38%) in BZ.

5.1.4.4 Fiber orientation

When DW-CMR data are unavailable, RBMs are often used to define the cardiac fiber field in *in silico* ventricular models (Section 1.6.3.5) [122]. Here, DW-CMR data were combined with an RBM to generate porcine-specific BiV fiber fields.

The RBM of Bayer et al. [122] was used, with septal properties matched to the LV and all β angles set to 0° (transverse isotropy). Each sample thus required four parameters: α angles in the endocardium (α_{endo}) and epicardium (α_{epi}) for both LV and RV. A standard fiber field (s-RBM) was defined using α values of +60° and -60° for endocardium and epicardium, respectively.

For the three healthy pigs with DW-CMR data (Table 5.1), RBM-generated fiber fields (with varied α angles) were compared to DW-based fiber fields. Because *ex vivo* DW-based geometries differed from *in vivo* cine-based geometries, making it difficult to extrapolate the fiber field, DW-based RBMs (dw-RBMs) were defined for cine-based anatomical models of pigs 1-3. For this, *ex vivo* BiV tetrahedral meshes were created from the segmentation of the DW-CMR data of each sample, with the meshes having a mean edge length of 1 mm, which matches the voxel resolution of the DW-CMRs (Table 5.2). The DW-based

fiber field was then interpolated using radial basis functions. RBMs were calculated for each *ex vivo* BiV mesh by initially setting the angles α in the LV to the default values of [+60°, -60°] while the RV angles α_{endo} and α_{epi} varied in the range [+90°, -90°) in 10° steps, producing 324 RBM-based fiber fields per mesh. These were compared with the DW-based fiber field to identify the pair of RV angle values [α_{endo}, α_{epi}] minimizing the mean angle $\overline{\Theta}$, defined from the longitudinal fiber directions as [122]:

$$\overline{\Theta} = \frac{1}{M} \sum_{m=0}^{M} cos^{-1} \left(\frac{\boldsymbol{u}_m \cdot \boldsymbol{v}_m}{||\boldsymbol{u}_m|| \, ||\boldsymbol{v}_m||} \right)$$

where M is the total number of nodes and $\boldsymbol{u}_m$ and $\boldsymbol{v}_m$ are the longitudinal fiber directions in node m obtained from RBM and DW-CMR, respectively. RV α angles were further refined by varying them around the identified values, specifically in the range $[\alpha_x - 10, \alpha_x + 10]$ in steps of 1°, with x being *endo* or *epi*. The values of the angles associated with the lowest $\overline{\Theta}$ were selected. To complete the determination of RBM-based fiber fields, the same procedure was repeated by setting the RV α angles to their optimal values and varying the α angles in the LV to identify their optimal values.

5

5.1.4.5 Repolarization heterogeneities

Three action potential duration spatial heterogeneity (APDSH) configurations were defined (Figure 5.3c): b-APDSH, representing homogeneous APD throughout the BiV mesh; t-APDSH, including transmural APD heterogeneities; and c-APDSH, including transmural and apicobasal APD heterogeneities.

To include transmural heterogeneities, a multi-diffusion problem was solved (Section 1.6.3.5) [119] to accurately segment the BiV mesh transmurally (orange dashed region in Figure 5.3c). A proportion of 40:35:25 was defined for the endocardium, midmyocardium, and epicardium, following previous studies [188, 189]. To include apicobasal heterogeneities, a base-to-apex gradient was defined by solving the Laplace equation with constant Dirichlet boundary conditions at the apex and base of the BiV domain. Based on this gradient and to divide the BiV mesh into three apicobasal regions, a proportion of 48:35:17 was empirically established for the base, middle, and apex regions (Figure 5.3c).

The Gaur et al. [16] cellular AP model lacks native repolarization gradients, so experimental porcine data from Meijborg et al. [40] were used to define APD heterogeneities. The APD of the Gaur et al. [16] model was taken to

Table 5.3: Repolarization heterogeneities definition at 650 ms cycle length. The target (T) and simulated (S) APD_{90} values are shown with the g_{K1} (x10) values leading to the corresponding simulated APD_{90}. B: base, M: middle, A: apex, En: endo, Ep: epi.

	B			**M**			**A**		
	T	S	g_{K1}	T	S	g_{K1}	T	S	g_{K1}
En	213.9	213.9	1.49	222.7	222.4	1.39	218.3	218.1	1.44
M	204.8	204.5	1.61	213.2	213.2	1.5	208.9	208.5	1.56
Ep	199.0	199.4	1.68	207.2	207.3	1.57	203.1	203.1	1.63

correspond to the midmyocardium and the middle height between the apex and the base [16, 190]. Since APD in the model is largely determined by the expression of I_{K1}, as reported by the authors, APD in each of the nine different regions (3 transmural per 3 apicobasal) was defined by varying the conductance g_{K1} to match the target APD values within 0.5 ms (Table 5.3). The nine target APD_{90} values were set by varying the default APD_{90} value in the Gaur model, measured at a cycle length of 650 ms, according to the percentage of variations in repolarization reported in [40]. For b-APDSH, the midmyocardial middle-height g_{K1} value was used. For t-APDSH, the endocardial, midmyocardial, and epicardial middle-height g_{K1} values were used.

5.1.5 Numerical simulations

Cellular models were prepaced for at least 2000 beats until the APD_{90} reached steady state (i.e., remained invariant). Tissue propagation was computed by numerically integrating the monodomain model (Equation 1.13) [115]. Each BiV simulation consisted of 3 cardiac cycles, with the last cycle being used for analysis. Stimuli of 80-$\mu A/cm^2$ magnitude and 1 ms duration were applied at the AVN. V_m was saved with a time step of 0.25 ms and the adaptive integration time step Δt was searched in the range [0.01,0.125] ms [115].

Seven simulation groups (C5G1 to C5G7) were defined, each with specific CS, CM orientation, repolarization heterogeneities, tissue conductivities, and HERP configuration (Table 5.4). Data used for validation are shown as well. Generally, CMRs and the EAM were employed for feeding the models while OM and ECGs were used for their validation. The cycle duration for the cell and tissue simulations depended on validation data: 769 ms for comparisons with pig 15 ECG (C5G2-4), 898 ms for comparisons with pig 6 ECG (C5G6), and 1000 ms for comparisons with OM data (C5G4-5) or without comparison with experiments (C5G1 and C5G7).

A total of 74 simulations were performed using the open source software

Table 5.4: Simulation groups and associated configurations. Average LDC ($\overline{\text{LDC}}$) and g_{K1} ($\overline{g_{K1}}$) values were defined as the mean of the OM-adjusted LDC^i and g^i_{K1} values at the BZ of pigs 8-12, therefore, i=8,...,12. **PMJr**: PMJ radius (mm), HZ: healthy zone.

Group	Pig	Activation	PMJr	RBM	APDSH	LDC	HERP	Validation (pig)
C5G1	1	[be-CS, bi-CS]	[0.1-2]	s-	b-	b-	-	-
C5G2	1,2,3	[bi-CS, rvs-CS, ap-CS, ap-e-CS]	0.5	s-	b-	b-	[b-, a-]	ECG (15)
C5G3	1,2,3	ap-CS	0.5	s-	[b-, t-, c-]	b-	a-	ECG (15)
C5G4	1,2,3	ap-CS	0.5	[s-, dw-]	c-	b-	a-	ECG (15) OM (13)
C5G5	8-12	ap-CS	0.5	s-	HZ: c- BZ: g^i_{K1}	HZ: b- BZ: LDC^i	-	OM (8-12)
C5G6	6	[ap-CS, mi-CS e-EAM, i-EAM]	0.5	s-	HZ: c- BZ: $\overline{g_{K1}}$	HZ: b- BZ: $\overline{\text{LDC}}$	b-	ECG (6)
C5G7	4-12	ap-CS	0.5	s-	HZ: c- BZ: $\overline{g_{K1}}$	HZ: b- BZ: $\overline{\text{LDC}}$	b-	-

ELECTRA (Section 1.6.3.6) on the HERMES HPC cluster at the University of Zaragoza.

5

5.1.5.1 Postprocessing

In C5G1 simulations, the CS-myocardium coupling was analyzed by varying the PMJ radius for the two types of CS, i.e., be-CS and bi-CS. Three metrics were calculated: the percentage of PMJs with at least one CS-to-myocardium line element; the mean number of connections from the CS to the myocardium per PMJ; the percentage of PMJs where at least one tissue node had an AT difference with the penultimate CS node for the corresponding PMJ in the range [0, 1.5] ms, which implied PMJ activation from the CS to the myocardium (that is orthodromic / anterograde activation).

In C5G1, C5G4, and C5G5 simulations, AT and APD_{90} were calculated from the numerically obtained V_m as described in Section 3.1.2.6. Moreover, CV was computed for each node of the BiV mesh. The magnitude of the velocity vector between two nodes was calculated as the ratio of the Euclidean distance between them and the difference in their ATs. For each node, the mean CV vector between the given node (considered as the central node) and all its neighboring nodes within a radius of 600 µm was determined. The radius value was chosen to cover the maximum edge length found in all meshes (Figure 5.3b for an example). For C5G4 and C5G5 simulations, the anterior

(and posterior for C5G4) surface of the BiV mesh was cut after retrieving the simulation results and CV and APD_{90} were compared with 2D OM data.

The pseudo-ECGs (pECGs) were defined from extracellular unipolar potentials $\phi(\boldsymbol{e})$, which were approximated by the integral of the dipole source density as in [98]:

$$\phi(\boldsymbol{e}) = \int_{\Omega} \left(-\mathbf{D}\nabla V_m \cdot \left(\nabla \frac{1}{||\boldsymbol{r} - \boldsymbol{e}||} \right) \right) d\boldsymbol{r}$$

where $\boldsymbol{e}$ is the vectorial electrode position, $\mathbf{D}$ is the diffusion tensor, and Ω is the BiV domain. Once the 12-lead pECG was drawn from the calculated $\phi(\boldsymbol{e})$ signals, a low-pass Butterworth filter with a 40 Hz cutoff frequency was applied, as for experimental ECGs in Sections 5.1.3.2 and 5.1.3.3. Then, the pECG and the experimental ECG signals were normalized in each of the leads and their baseline was set to zero [191]. Note that the 12-lead pECG was drawn from the third simulated beat (Section 5.1.5) and the 12-lead experimental ECG corresponded to the median beat obtained as described in Sections 5.1.3.2 and 5.1.3.3.

For comparison of simulations and experiments, we separately aligned the QRS complexes and the T waves by segmenting them. Specifically, four mean peak times were calculated corresponding to the QRS complex and the T wave in the simulated and experimental datasets. Each mean peak time was computed as the average of the peak times on the 12 leads for the wave of interest (QRS complex or T wave). The signals were segmented in each lead by taking [-50,50] ms for the QRS complex and [-100,100] ms for the T wave, centered around the corresponding mean peak time. The Pearson correlation coefficient between the simulated and experimental QRS complexes and T waves was calculated to quantify the wave similarity in each of the leads.

In another group of simulations, the impact on the calculation of pECGs of the heart position and the location of the electrodes in the torso was evaluated. Since pig 6 was the only one in which the exact HERP was known, for subsequent pECG computation, all BiV models of pigs 1-12, except 6, were spatially matched to the BiV mesh of pig 6 using the iterative closest point algorithm, which defined the baseline HERP (b-HERP) for each BiV model. To perform this rigid transformation, reference points were manually located in the anterior, posterior, left, right, and septal regions of the base, as well as in the endocardial and epicardial apex of the LV in all meshes. In C5G2-4 simulations, the experimental ECG used for validation was measured in a different swine (pig 15) with a likely different HERP due to a distinct spatial location

of the heart and/or unequal positioning of the ECG electrodes. Thus, not only were several CS distributions tested with b-HERP, but also rotations of the heart position and variations in the electrode location for precordial lead measurement (so-called adjusted HERP, a-HERP) were evaluated in C5G2. The optimal CS distribution and the optimal a-HERP that in combination minimized the mismatch between the pECGs of pigs 1-3 and the experimental ECG of pig 15 were identified. In C5G3-4 and C5G6-7, a-HERP and b-HERP were used for the calculation of pECG, respectively. In C5G6, b-HERP was the exact HERP, and in C5G7, pECGs for different infarcted porcine ventricles were compared (Table 5.4).

5.2 Results

5.2.1 Optimization of PMJ radius for effective CS-myocardium coupling

In C5G1 simulations, multiple PMJ radius values for both be-CS and bi-CS were tested, and their effects on the numerical activation of the BiV model of pig 1 were evaluated. Table 5.5 and Figure 5.5 summarize the results. At small PMJ radii as 0.1 mm, the percentage of PMJs connected with the myocardium was low (28.5% for be-CS, 10.4% for bi-CS), resulting in a limited number of PMJs with anterograde activation (28% for be-CS, 7% for bi-CS). Increasing the radius to 0.5 mm for be-CS and 0.3 mm for bi-CS ensured complete connection of Purkinje endpoints to the myocardium (100% of PMJs were connected with the myocardium) and markedly increased the number of PMJs with anterograde activation (93.8% for be-CS, 90.3% for bi-CS).

The maximum percentages of PMJs with anterograde activation occurred at a PMJ radius of 0.5 mm for be-CS and 0.6 mm for bi-CS, with 12 and 25 mean number of connections per PMJ, respectively. Further increases in PMJ radius increased the mean number of connections per PMJ but reduced the number of PMJs with anterograde activation. For example, the percentage of PMJs with anterograde activation decreased from approximately 90% to 23% (be-CS, radius 1 to 1.5 mm) and to 37% (bi-CS, radius 0.6 to 0.9 mm). At large radii, the percentage of PMJs with anterograde activation became negligible (1%), with the mean number of connections per PMJ exceeding 200.

Given that all models had the same mesh resolution, a PMJ radius of 0.5 mm was selected for C5G2-7 simulations to avoid conduction block at PMJs.

Table 5.5: Results of C5G1 simulations: CS-myocardium coupling. **PMJr**: PMJ radius, **ncPMJ**: the percentage of PMJs connected with the myocardium, **cpPMJ**: the mean number of connections per PMJ, **aPMJ**: the percentage of PMJs with anterograde activation.

CS	**PMJr** (mm)	**ncPMJ** [%]	**cpPMJ**	**aPMJ** [%]
be-	0.1	28.48	1.00	28.13
be-	0.5	100	11.97	93.78
be-	1.0	100	76.83	90.01
be-	1.5	100	240.51	23.05
be-	2.0	100	550.59	1.05
bi-	0.1	10.43	1.00	6.92
bi-	0.3	100	3.21	90.27
bi-	0.5	100	14.51	93.34
bi-	0.6	100	25.21	93.69
bi-	0.9	100	84.91	37.07
bi-	1.2	100	201.24	1.23

5.2.2 Ventricular activation and QRS morphology shaped by CS distribution and electrode position

In C5G2 simulations, the experimentally recorded QRS of pig 15 was compared with the simulated QRS of pigs 1-3 to evaluate how different CS and electrode positions (defined by HERP configurations) influence ventricular activation.

Effect of CS distribution with fixed HERP configuration: When comparing bi-CS and rvs-CS for both b-HERP and a-HERP, rvs-CS consistently improved agreement with experimental QRS morphology, particularly in leads I, II, aVR, and aVL (Figure 5.6a, pig 3). For b-HERP, these effects were even more pronounced, with mean QRS similarity across the three pigs increasing from -0.51, 0.31, -0.20, and -0.84 for bi-CS to 0.96, 0.91, 0.97, and 0.91 for rvs-CS in leads I, II, aVR, and aVL, respectively.

Effect of HERP configuration with fixed CS distribution: For bi-CS, switching from b-HERP to a-HERP improved QRS similarity in precordial leads V2-V5 from -0.8, -0.61, -0.3, and -0.25 to 0.2, 0.7, 0.8, and 0.84. For rvs-CS, the change from b-HERP to a-HERP yielded improvements from -0.01, -0.96, -0.93, and -0.93 to 0.86, 0.91, 0.73, and 0.48 (Figure 5.6a). However, in leads V1 and V6, a-HERP reduced QRS similarity when used with bi-CS, whereas similarity remained high with rvs-CS. Despite improved precordial replication with rvs-CS combined with a-HERP, limb and augmented lead similarity (especially lead III) decreased, as shown in Figure 5.6a.

Effect of ap-CS: With HERP fixed to a-HERP, ap-CS outperformed bi-CS in all leads except aVF (Figure 5.6c). In particular, QRS similarity in lead III

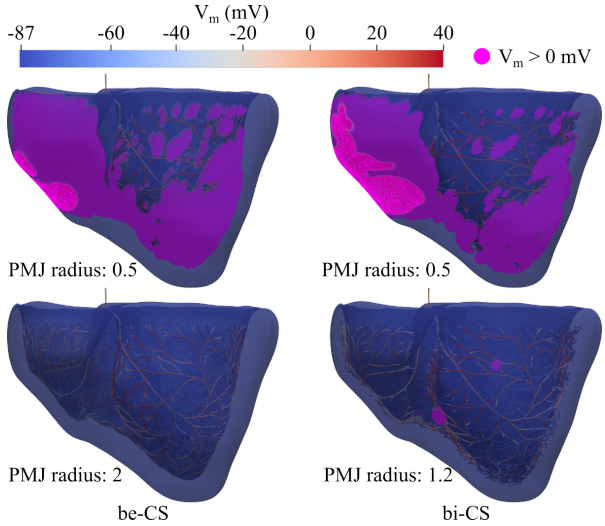


Figure 5.5: Results of C5G1 simulations. Simulated CS-myocardium depolarization for pig 1 when be-CS and bi-CS with different PMJ radius values (mm) were used. Snapshots after 45 ms of AVN stimulation are shown. Myocardial nodes with $V_m \geqslant 0$ mV are represented in purple.

increased to 0.56, while it decreased to -0.15 in lead aVF.

Overall effects: Mean QRS similarity across all samples and leads was -0.3, 0.1, and 0.23 with b-HERP and -0.16, 0.5, and 0.75 with a-HERP for bi-CS, rvs-CS, and ap-CS, respectively. Thus, QRS replication improved progressively with rvs-CS and ap-CS, particularly when combined with a-HERP (Figure 5.6b).

Effect of endocardial vs intramyocardial activation: Comparison of ap-e-CS with ap-CS under a-HERP revealed a reduction in QRS similarity in all leads when activation was restricted to the endocardium (Figure 5.6d). Mean QRS similarity dropped from 0.75 to 0.35, with the largest decreases in leads III (54.3%), aVL (42.8%), V2 (28%), and V6 (31.4%).

5.2.3 Ventricular repolarization heterogeneities and T-wave variations

In C5G3 simulations, the influence of transmural and apicobasal APD heterogeneities on T-wave reproduction was examined.

The experimental T waves of pig 15 were compared qualitatively (Figure 5.7a) and quantitatively (Figure 5.7b) with simulations for pigs 1-3 using b-

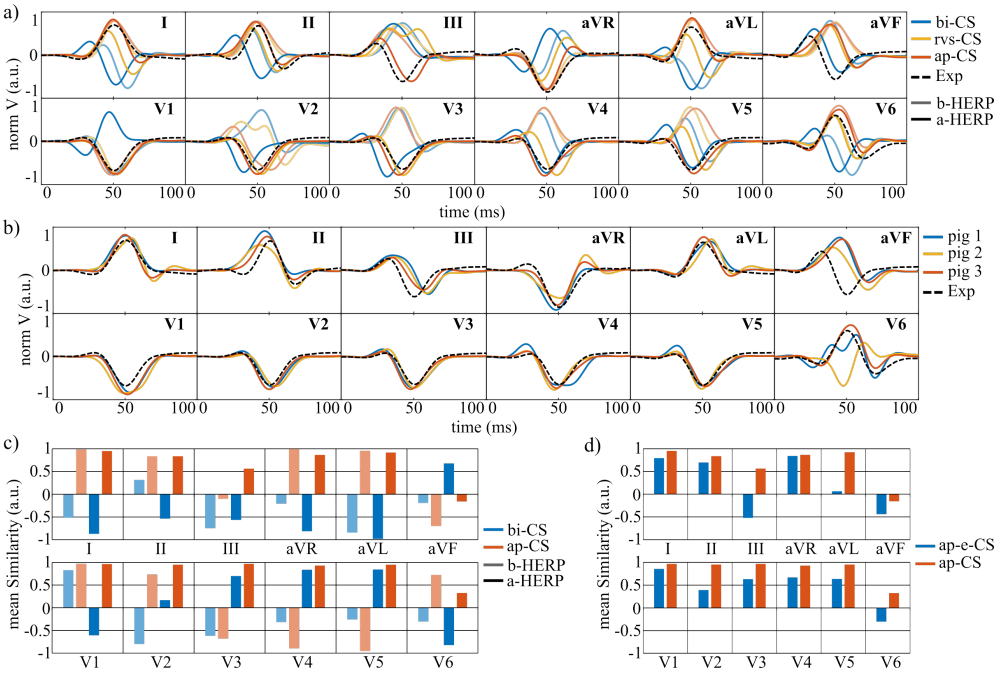


Figure 5.6: Results of C5G2 simulations. a- Simulated QRS for pig 3 when different HERP and CS distributions were used. b- Simulated QRS obtained with a-HERP and ap-CS for pigs 1-3. c- Simulated versus experimental mean QRS similarity obtained for pigs 1-3 when different HERP and CS distributions were employed. d- Mean QRS similarity for pigs 1-3 for simulations with ap-e-CS and ap-CS distributions. Exp: the experimental QRS complex from pig 15 is depicted as a black dashed line.

APDSH, t-APDSH, and c-APDSH. Both t-APDSH and c-APDSH improved T-wave similarity in all leads except I and aVR. The greatest improvements occurred in leads II, III, aVL, and aVF, where mean similarity rose from 0.1, -0.25, 0.62, and -0.57 (b-APDSH) to 0.8, 0.91, 0.89, and 0.92 (c-APDSH). In leads I and aVR, mean similarity decreased by 17% and 29%, although for pig 1, c-APDSH still produced visually similar T waves to the experiment in these leads (Figure 5.7a). Overall, incorporating heterogeneous APDs (t-APDSH or c-APDSH) yielded more biomimetic T waves for all pigs and precordial leads, although similarity in lead V6 was consistently low.

In terms of QRS complex, APD heterogeneities had negligible effect, with mean similarity values of 0.756, 0.753, and 0.756 for b-APDSH, t-APDSH, and c-APDSH, respectively. In contrast, T-wave similarity increased markedly, from 0.49 (b-APDSH) to 0.75 (t-APDSH) and 0.74 (c-APDSH).

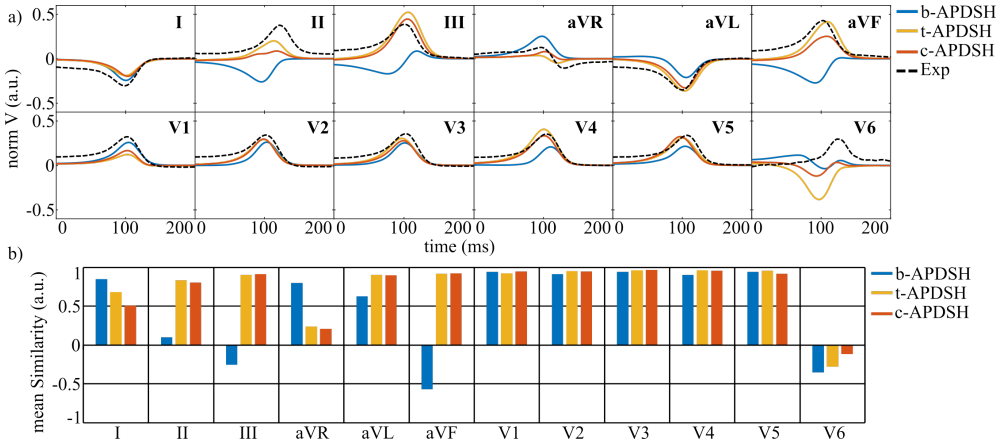


Figure 5.7: Results of C5G3 simulations. a- Simulated T waves for pig 1 when different APDSH were used. b- T-wave mean similarity for simulations of pigs 1-3 for b-APDSH, t-APDSH, and c-APDSH. Exp: the experimental T wave from pig 15 is depicted as a black dashed line.

5.2.4 Electrophysiological effect of personalizing myocardial fiber orientation

In C5G4 simulations, myocardial fiber orientations obtained by individually adjusting the RBM to each pig's DW-CMR data (pigs 1-3, Section 5.1.4.4) were compared with those generated by s-RBM. The greatest deviation from s-RBM was observed for pig 1. After DW-CMR-based adjustment, LV α angles were -100° (endocardium) and -91° (epicardium), while RV α angles were 86° and 73°, respectively. The smallest difference occurred in pig 2, whose DW-RBM produced LV α angles of 53° and -62° and RV α angles of 64° and -51°, closely matching s-RBM.

At the macroscopic level, pECGs were largely unaffected by replacing s-RBM with dw-RBM. Figure 5.8a compares pECGs for pigs 1 and 2, representing the lowest and highest similarity between s-RBM and dw-RBM, respectively. Across all simulations, the mean QRS similarity between the experimental and simulated signals decreased slightly from 0.76 to 0.73, while T-wave similarity increased from 0.74 to 0.76 when using dw-RBM.

At the tissue level, activation patterns were nearly identical between RBMs (Figure 5.8b, right, for pig 1). Almost all differences in maximum AT were below 1 ms. Only a discrepancy of 8.5 ms in maximum AT was observed in the posterior view of pig 1.

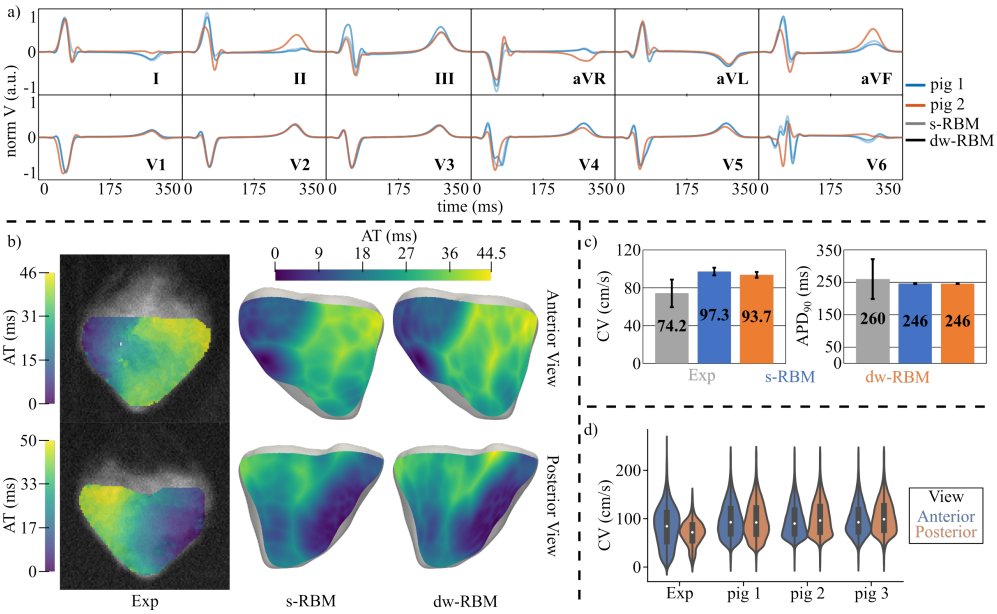


Figure 5.8: Results of C5G4 simulations. a- *In silico* ECGs for pigs 1-2 simulated using s-RBM and dw-RBM. b- Experimental (left) and simulated (right) AT maps for different cardiac views. The experimental maps correspond to pig 13 and the simulated maps to pig 1 using s-RBM and dw-RBM. c- Mean and standard deviation of CV and APD_{90} values for all OM experiments and simulations of pigs 1-3 with s-RBM and dw-RBM. d- CV distribution for the anterior and posterior views of the OM data of pig 13 and the simulations of pigs 1-3 when dw-RBM was used.

Comparisons with the OM-based AT map for pig 13 revealed similar anterior and posterior AT and activation patterns for both RBMs (Figure 5.8b). In both OM and simulations, epicardial activation began in the RV, propagated toward the LV, and concluded at the LV base. Maximum AT values were comparable between OM (46/50 ms for anterior/posterior) and simulations (in pig 1, s-RBM yielded 43/36 ms and dw-RBM 44/44.5 ms).

CV analysis showed a modest 3.6 cm/s reduction in median CV with dw-RBM relative to s-RBM (Figure 5.8c), while median APD_{90} remained identical at 246 ms in both anterior and posterior views. Relative to OM experiments for pig 13 and the healthy zones of MI cases, median APD_{90} differed by 5.4%, whereas simulated median CV exceeded experimental values by 31% (s-RBM) and 26% (dw-RBM). Despite these offsets, CV distributions in the anterior view were similar between dw-RBM simulations and OM (Figure 5.8d). Averaging dw-RBM results for pigs 1-3 showed anterior CVs only 8% above OM

Table 5.6: Results of C5G5 simulations: OM-based CV and APD_{90} tuning for the BZ of MI. E: Experiment, S: Simulation

Pig	CV (cm/s)		LDC	APD_{90} (ms)		g_{K1}
	E	S	(cm^2/ms)	E	S	(%)
8	32.8	31.7	0.001	346	345.3	58
9	27.9	26.9	0.00046	482	476	19
10	38.6	39.0	0.00095	409	406	31
11	31.1	31.8	0.0009	606	557	1
12	43.6	43.7	0.0011	361	354.5	36

values, while posterior CVs remained approximately 30% higher (experimental medians: 84.3 / 71.7 cm/s for anterior / posterior).

5.2.5 Lower cellular coupling and inward rectifier potassium mimic MI electrical dynamics

OM data from the anterior view of MI pigs with LAD occlusion (pigs 8-12) were used to calibrate the *in silico* MI BZ electrophysiology in C5G5 simulations. Table 5.6 lists the LDC and g_{K1} values yielding optimal agreement in CV and APD_{90}. The relative error between experimental and simulated median CV of pigs 8-12 was 3.2%, 3.9%, 1.0%, 2.9%, and 0.2% for LDC values between 0.00046 and 0.0011 cm^2/ms. For APD_{90}, differences for pigs 8-12 were 0.2%, 1.3%, 0.7%, 8%, and 1.8% when g_{K1} was reduced from 1% to 58% of its default value. Based on these calibrations, BZ tissue was modeled with LDC=0.000882 cm^2/ms and g_{K1}=29% of baseline.

Simulated AT maps closely matched OM maps in the anterior BiV view (Figure 5.9), with activation initiating in the anterior RV, propagating to the LV, and terminating near the MI-affected LV apex. Maximum AT differences were 10 ms (pig 9) and 6 ms (pig 10). Experimentally, average CV decreased from 72.4 cm/s in the healthy tissue to 34.8 cm/s in BZ, while average APD_{90} increased from 250 ms to 441 ms. Simulations yielded comparable values: CV=87.3 / 34.6 cm/s in healthy tissue / BZ and APD_{90}=247 / 428 ms in healthy tissue / BZ.

Across pigs 8-12, simulated CVs were 20% lower (healthy tissue) and 0.5% lower (BZ) than experimental values, with APD_{90} differing by only 1% (healthy tissue) and 3% (BZ).

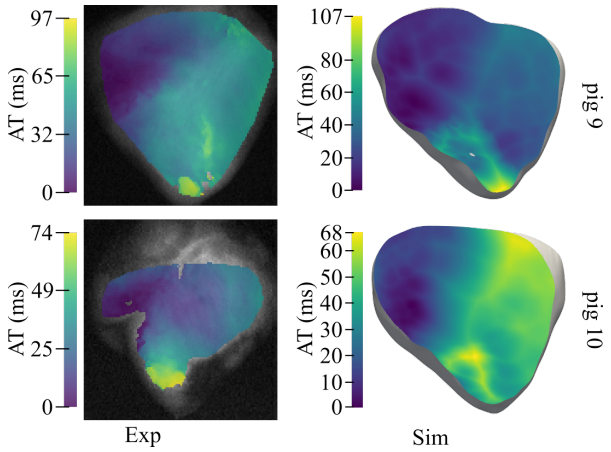


Figure 5.9: Results of C5G5 simulations. Experimental (left) and simulated (right) AT maps of the anterior view for two MI pigs with LAD occlusion.

5.2.6 Post-MI ventricular activation effect on the ECG

In C5G6 simulations, replacing ap-CS with mi-CS produced minimal changes in ventricular depolarization-repolarization dynamics. Figure 5.10a shows identical QRS complexes for both CS distributions across leads. Minor ventricular AT differences were restricted to the MI-affected LV free wall. The T wave remained unchanged, with only localized APD_{90} alterations (data not shown). Mean similarity to experimental ECG for pig 6 was low in both cases (QRS complex / T wave: 0.34 / 0.37 for ap-CS and 0.34 / 0.36 for mi-CS).

Comparison with EAM-based activation (Figure 5.10c) showed that e-EAM and i-EAM substantially improved T-wave similarity, particularly in leads aVF and V4 (Figure 5.10b and Figure 5.10c, right), with mean values increasing from 0.38 (ap-CS) to 0.52 (e-EAM) and 0.63 (i-EAM). However, QRS similarity decreased markedly (Figure 5.10c, left), with mean values of 0.34 (ap-CS), -0.11 (e-EAM) and 0 (i-EAM). Overall, EAM-based activation improved T-wave agreement but worsened QRS matching relative to experimental data.

5.2.7 *In silico* effect of MI morphology and location on the ECG

In C5G7 simulations, qualitative evaluation of ECGs under healthy and MI conditions was performed for pigs 4-12 across seven leads (Figure 5.11a). MI had minimal impact on the QRS complex but substantially altered the T wave.

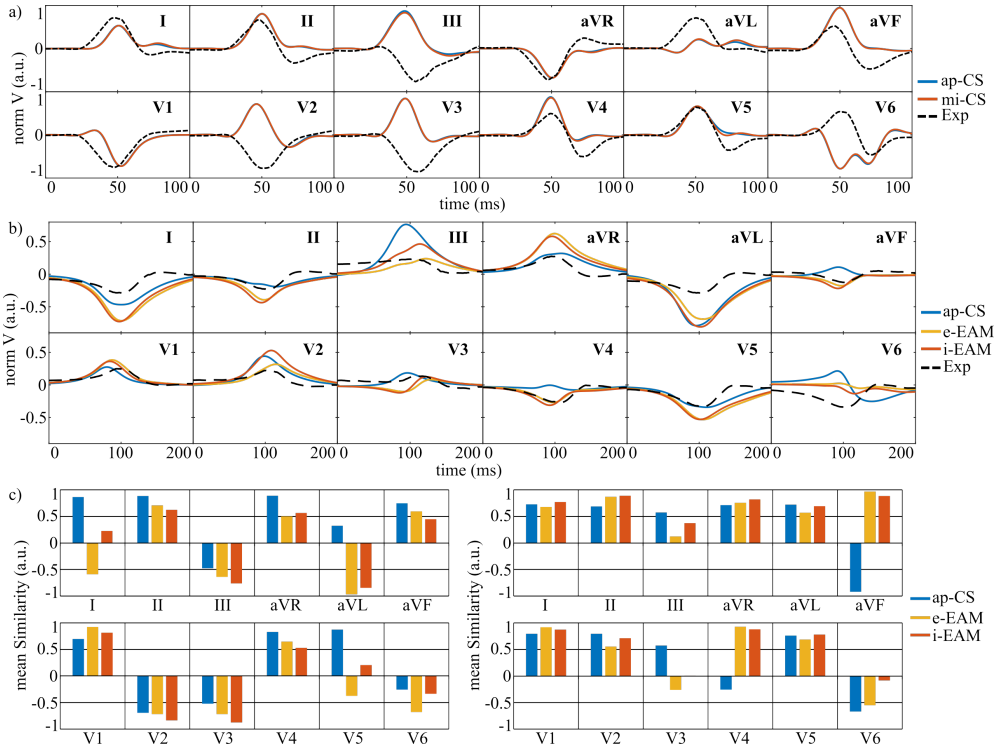


Figure 5.10: Results of C5G6 simulations. a- Experimental and simulated QRS complexes for pig 6 when ap-CS and mi-CS were used. b- Experimental and simulated T waves for pig 6 when the activation was generated by ap-CS and e-EAM and i-EAM stimulations. c- QRS (left) and T-wave (right) mean similarity for different activation approaches.

For LCx MI, T-wave amplitude and duration increased in leads I, II, III, V2, and V5, with the largest changes in pigs 6-7, which had greater proportions of BZ within MI than pigs 4-5: 20%, 21%, 32%, and 45.5% for pigs 4-7, respectively (Figure 5.11b and Appendix Table A.5). In these pigs, the QRS amplitude remained stable across all leads, with slight decreases in leads I and V5.

For LAD MI, the greatest T-wave amplitude increases occurred in leads III, V2, and V3, with T-wave inversion in leads III and V2 for pigs 8-10. The QRS complexes were more disrupted for LAD pigs than for LCx pigs. Leads presenting post-MI T-wave inversion showed a marked QRS distortion compared to the healthy case. Interestingly, a Q wave appeared in lead I for most LAD pigs.

Taken together, enlarged T waves in leads I, II, and V5 may indicate LCx

MI, with greater enlargement suggesting larger MI size. Enlarged T waves in lead V3 or large and inverted T waves in leads III and V2 may indicate LAD MI.

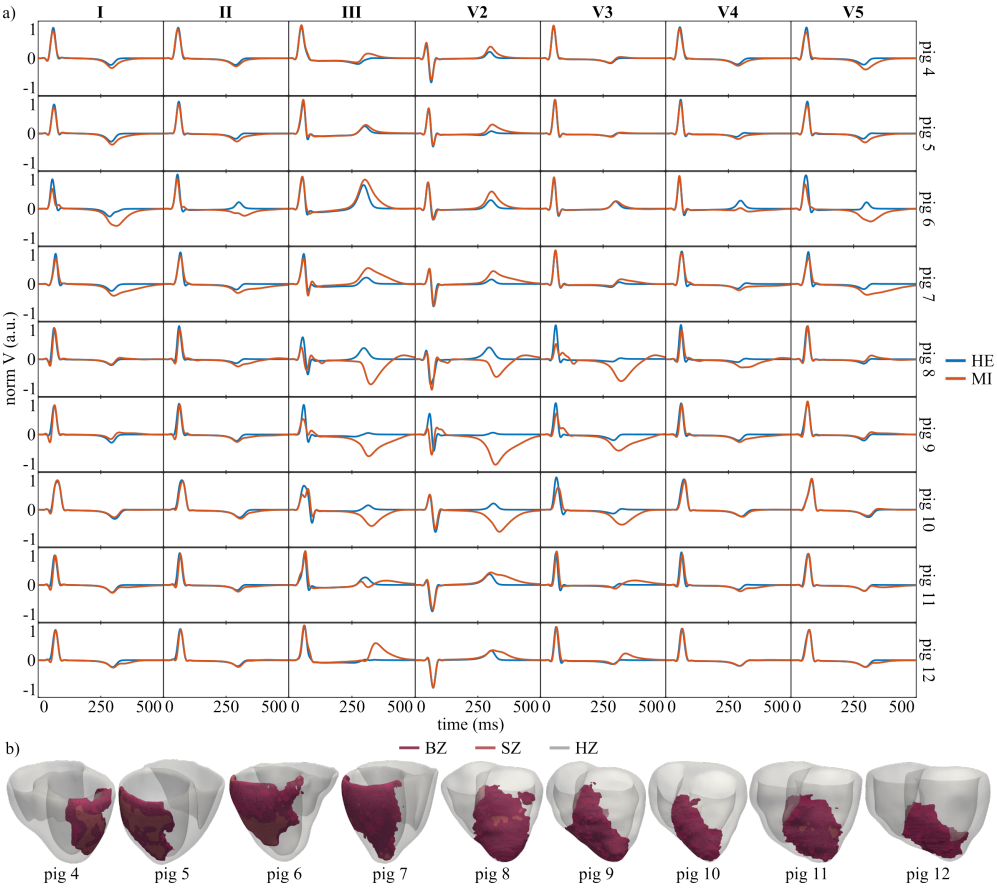


Figure 5.11: Results of C5G7 simulations. a- Healthy and MI pECGs for pigs 4-12. b- MI BiV models for pigs 4-12 depicting the BZ and SZ.

5.3 Discussion

We built swine-specific electrophysiological models that integrate extensive experimental data under both healthy and MI conditions. The main findings indicate that CM orientation exerted only a minor influence on cardiac electrophysiology, whereas CS architecture and APDSH were critical for reproducing normal depolarization and repolarization patterns, respectively. In chronic

MI, incorporating experimentally derived alterations in cell-to-cell coupling and APD into a swine cellular model enabled an accurate reproduction of the MI electrical phenotype. This experimentally guided approach also allowed us to replicate experimental T waves and characterize QRS and T-wave patterns as a function of MI location.

5.3.1 CS-myocardial coupling

A key component of our *in silico* models is the coupling between CS and the ventricular myocardium, which is fundamental to coordinated ventricular activation. Electrical depolarization is governed by the source-sink ratio, defined by the relationship between charge supplied by activated tissue (the source) and the charge required to activate the adjacent tissue (the sink) [166]. When this ratio falls below 1, conduction block occurs because the sink demands more current than the source can deliver. This mismatch is influenced by both structural and electrophysiological properties, including tissue bulk, cell count, intercellular coupling, and excitability [166]. In computational models, such source-sink mismatches have been shown to induce conduction block in diverse settings, from transmurally infarcted tissues remuscularized with engineered minitissue (as observed by us in Chapter 3) to 3D models of SAN-atrial coupling [192].

A relatively unexplored source-sink mismatch arises in PMJ modeling, where thin Purkinje bundles (modeled as line elements) connect to bulkier myocardium (represented with tetrahedral meshes), as in the present study. Conduction block can occur at PMJs despite the higher excitability and stronger intercellular coupling of the CS compared to the BiV myocardium, both defined according to experimental observations. In addition to the larger BiV tissue volume, the high spatial resolution of many simulation meshes can exacerbate this block [10, 50].

Our results revealed an optimal PMJ radius that minimizes activation block when all variables contributing to the source-sink mismatch were fixed. Increasing the PMJ radius generally increased the number of CS-myocardial connections, which initially boosted the number of activated PMJs. However, not all connected PMJs contributed to forward activation, as some were retrogradely activated from the myocardium (Table 5.5). The maximum number of myocardial activations from CS occurred once the PMJ radius allowed connection to a few dozen myocardial nodes, which is in line with a previous computational work where 50 connections per PMJ were employed for CS-myocardium coupling when a hexahedral BiV mesh with 0.5 mm edge length

was used to represent the ventricular myocardium [128]. Beyond this, excessive PMJ-myocardium connections worsened the source-sink mismatch, reducing the number of PMJs with anterograde activation. These findings held for both endocardial and intramyocardial CS distributions, with intramyocardial CS showing the expected drop in the number of PMJs with anterograde activation at slightly smaller PMJ radii due to the greater number of connected myocardial nodes.

5.3.2 Porcine CS architecture and electrode positioning as the determinants of the QRS complex

The ventricular depolarization pattern initiated by CS is reflected in the QRS complex of the ECG. In this work, we simulated pECG signals to evaluate how QRS morphology is influenced by CS architecture in combination with HERP.

Three modifications to a baseline CS configuration were found to improve agreement between simulated and experimental QRS complexes in pig 15:

- **Addition of Purkinje fibers to the RV septum**. The baseline bi-CS configuration failed to reproduce the predominantly positive QRS complexes in leads I and II. Adding Purkinje fibers to the RV septum promoted right-to-left septal depolarization, producing more positive QRS morphologies in these leads and their augmented counterparts (aVR and aVL). This suggests that the RV septum is directly activated by the RV Purkinje branch rather than indirectly from LV activation propagating across the septum, consistent with some experimental reports of RV septal activation in human hearts [186].

- **Adjustment of HERP**. Rotation of the heart combined with more central positioning of the precordial electrodes improved the match between simulated and experimental QRS morphologies in precordial leads. In pig 15, leads V1-V5 showed similar morphology and predominantly negative R waves despite being positioned on opposite sides of the anterior thorax. The adjusted a-HERP increased RV exposure to precordial leads, enabling right-to-left depolarization to appear consistently in leads V1-V5 as a negative QRS deflection, matching experimental observations.

- **Apical repositioning of LV bundle branch endpoints**. Shifting the anterior and posterior LV bundle branch endpoints more apically enhanced apex-to-base depolarization, improving agreement in leads I and II and in augmented leads without disturbing precordial lead similarity.

Additionally, this modification in the fast CS resulted in a more negative QRS complex in lead III bringing it closer to the experimental morphology. Nonetheless, residual mismatches remained in leads II, III, and aVF, while lead V6 remained challenging to match due to its sensitivity to small shifts in electrode or heart position.

Beyond these refinements, the depth of CS penetration emerged as a critical factor. Simulations with intramyocardial ap-CS distributions reproduced experimental QRS complexes better than their purely endocardial counterparts. This is consistent with anatomical studies reporting deeper CS location in pigs than in humans [14]. While human models of QRS generation are numerous [118, 119, 128], few have validated simulated QRS morphology against experimental data across all leads for a full BiV model [98] or have used a topologically detailed CS [126, 127]. Here, we provide CS and HERP definitions validated against experimental ECGs for three porcine-specific BiV models.

OM-based epicardial activation measurements also matched simulations. In sinus rhythm, activation started in the RV and ended in the basal LV for anterior and posterior OM views. The first epicardial breakthrough consistently occurred in the RV area pretrabecularis, matching human experimental observations [186,193]. This pattern likely arises from the thin RV wall and RV bundle branch geometry, which travels from the septal base to the anterior wall via the septomarginal trabecula, a structure well documented in mammals [194] and located higher, more basally, in pigs than in humans [14] (Section 1.2.5). Simulated maximum AT and CV closely matched experimental values, though simulations yielded slightly higher median CVs (see Section 5.3.4).

These results underscore the robustness of our modeling framework. Despite stochastic CS variations, the preservation of QRS morphology across pigs 1-3 (same breed, weight, and age) highlights the robustness and reliability of our modeling approach. Overall, with appropriately defined CS architecture, HERP, and electrophysiological parameters, our healthy porcine models accurately replicate experimental QRS complexes and epicardial activation patterns.

5.3.3 Small APD heterogeneity defines porcine ventricular repolarization

The porcine ventricular cell model used here [16] captures the overall swine ventricular phenotype, but does not include location-specific definitions of re-

polarization. As a result, initial simulations were performed without regional APD variation, consistent with our OM experiments and with findings from Kong et al. [195], who reported no significant APD_{90} differences in swine ventricles. In contrast, Meijborg et al. [40] have found statistically significant spatial repolarization differences using regional repolarization (defined as the time when 50% of recording sites repolarize). Based on those findings, we implemented two APDSH configurations, t-APDSH and c-APDSH, for additional simulations.

Incorporation of APDSH improved replication of the experimental T wave in leads II, III, and aVF for all three healthy cases, without altering the QRS complex. Lead V6 remained the most challenging for T-wave matching, likely due to its sensitivity to HERP. With c-APDSH, lower T-wave similarity was observed in leads I and aVR for pigs 2 and 3 but not pig 1, suggesting inter-animal differences, possibly making pig 1 a better surrogate for pig 15.

At the tissue level, simulated median APD_{90} values on the epicardial surface matched OM-derived repolarization times. APDSH was not clearly detectable in OM data, likely due to the 2 ms acquisition resolution, which may be insufficient to capture subtle APD variations in the porcine epicardium. Using APDSH settings based on Meijborg et al. [40], simulations show a maximum epicardial APD_{90} difference of 8 ms (at a 1000 ms cycle length) between the ventricular base and mid-ventricle.

Overall, our findings support the presence of ventricular APDSH in pigs and align with experimental evidence that porcine repolarization begins in the epicardium and ends in the endocardium [40, 196]. The magnitude of transmural and apicobasal APD differences appears smaller in pigs than in human models [51, 52], which are sometimes (inappropriately) used for representing porcine electrophysiology [15]. To our knowledge, this is the first computational reproduction of experimentally observed porcine APDSH, achieved here by modifying g_{K1} in the Gaur et al. [16] model.

5.3.4 Minor role of personalized fiber orientation in porcine ventricular electrophysiology

We evaluated the impact of using DW-based pig-specific fiber orientations versus RBM-based orientations in porcine BiV models. Since *ex vivo* DW-CMR geometries differed substantially from *in vivo* cine-based geometries, the RBM fibers were adjusted using DW-CMR (s-RBM to dw-RBM, Section 5.1.4.4).

Adjusting RBM fibers to match DW data produced no significant changes in

simulated pECGs or tissue-level electrophysiology. A small decrease in median CV was observed with dw-RBM, most notably for pig 1, where s-RBM and dw-RBM differed most. Simulated CVs still slightly exceeded experimental CVs, consistent with earlier observations in both healthy and MI settings (Sections 5.3.2 and 5.2.5). In the anterior epicardial view, experimental CV in pig 13 closely matched simulated CV in pigs 1-3 using dw-RBM, suggesting that discrepancies arose mainly from lower posterior CVs in the experiment.

These findings align with prior studies showing minimal electrophysiological differences between DW- and RBM-derived fiber fields in dogs and rats [122, 197]. While patient- or animal-specific fiber architectures may be relevant in complex scenarios, such as arrhythmia vulnerability, our results suggest that, in healthy porcine ventricles, fiber orientation exerts only a minimal effect on the ECG morphology and on depolarization-repolarization derived electrophysiological parameters.

5.3.5 MI-induced structural and electrophysiological remodeling in pigs

Experimental data revealed significant structural and electrophysiological remodeling in chronic MI, which informed our *in silico* models.

DW-CMR analysis showed reduced fractional anisotropy in AZ compared to the healthy tissue in pigs with LAD (pig 14) or LCx (pig 7) occlusions. This likely reflects MI-induced microstructural alterations, such as collagen deposition, fiber disarray, and myocyte loss, well documented in both acute and chronic MI [47].

OM experiments revealed a 50% reduction in CV and an almost 200 ms prolongation of APD_{90} in AZ versus the healthy myocardium. CV slowing can result from reduced excitability and AP upstroke velocity, linked to decreased I_{Na} as reported in canine BZ patch-clamp studies [187] as well as from structural remodeling such as fibrosis [198], myocyte disarray, and reduced intercellular coupling [199]. The observed APD_{90} prolongation matches reports of reduced K^+ currents in canine BZ [200], which, in human ventricular models, prolong APD [10, 50].

In the Gaur et al. porcine model, reducing I_{Kr} and I_{Ks} conductances, as done in human models, shortened APD rather than lengthening it, due to the model's higher I_{K1} sensitivity. Therefore, APD prolongation was reproduced here by decreasing g_{K1}. Decreases in patch-clamp-based I_{Na} and DW-CMR-based anisotropy captured structural CV changes. LDC was then adjusted to

match the OM data.

The resulting MI models reproduced experimental activation patterns: earliest breakthrough in the RV area pretrabecularis and activation ending in the LV anterior apex. Simulated MI values of AT, CV, and APD_{90} closely matched experiments, with one exception: in pig 11, APD_{90} (606 ms) exceeds the model's maximum attainable value (557 ms, even with g_{K1} reduced to 1%).

5.3.6 Replication of QRS and T-wave characteristics in infarcted porcine hearts

Comparing experimental and simulated pECGs from infarcted pigs highlighted key factors in MI modeling.

BZ modeling: Fibrosis was not incorporated into the BZ in this study. Prior *in silico* work in humans suggests that adding varying degrees of fibrosis produces minimal changes in QRS and T-wave morphology, causing only small ST-segment deviations [50].

SZ modeling: We modeled SZ as an insulator, consistent with previous computational studies [10, 15, 34, 50]. Modeling SZ as passive tissue, as in Connolly et al. [33], can create unrealistically large potential gradients and ST deviations [50]. Also, it requires additional resistance and resting potential parameters, and SZ acts as an electrotonic sink, shortening BZ APD unless counteracted by very large APD increases.

CS modeling in MI: Although applying the ap-CS distribution from pig 15 to pig 6 did not replicate the QRS complex, highlighting the variability of CS geometry across animals, it emphasized the importance of individualized CS modeling. Implementing MI-specific modifications to CS (mi-CS) based on experimental data [32] altered AT and APD_{90} locally. Although these modifications produced minimal visible changes in the QRS complexes, they are likely to have more drastic electrical effects such as affecting unidirectional block formation and arrhythmia inducibility [50,148,201]. Therefore, a CS distribution that matches sinus rhythm ECG morphology may still be insufficient for *in silico* arrhythmic risk evaluation.

EAM-based LV activation: Replacing ap-CS-based LV activation with EAM-derived patterns surprisingly reduced QRS similarity in all leads. We attribute this to a mismatch: the RV was still activated by the ap-CS Purkinje network, while the LV followed EAM timings, as EAM data were only available for the LV. High-accuracy QRS reproduction in prior EAM-based MI simulations [50] required manual annotation refinement and full BiV endocardial and

epicardial mapping. Despite QRS mismatches, EAM-based LV activation improved replication of T-wave morphology in several leads (especially aVF and V4). Intramural EAM activation (i-EAM) slightly outperformed endocardial EAM (e-EAM), reinforcing the importance of representing the intramural CS position observed in pigs. Overall, these results show that RV activation has a strong influence on QRS morphology, while modeling of MI-related T-wave changes may benefit from invasive mapping integration.

5.3.7 Mechanisms underlying MI-induced ECG changes

The MI BiV models developed here provided insight into the mechanisms driving ECG changes in infarcted hearts. The most prominent effects appeared in the T wave, likely reflecting increased repolarization dispersion [40, 119, 196], while QRS morphology was only minimally altered.

Post-MI ventricular activation remained broadly similar to the healthy state. Although BZ excitability was reduced, the high PMJ density in our CS distributions likely limited the impact on global activation. This held true whether the CS distribution was unchanged or modified for MI (Section 5.2.6).

Concerning repolarization, LCx MI produced T-wave enlargement in leads V2, V5, and bipolar limb leads, which are more sensitive to LV-RV voltage gradients than to apicobasal gradients. Pigs 6 and 7, with larger BZ volumes, showed the greatest T-wave changes, consistent with stronger V_m gradients during repolarization.

In LAD MI, T-wave magnification appeared in leads III, V2, and V3, with clear inversion in pigs 8-10, but not in pigs 11 and 12. This variability may be driven by differences in BiV geometry, MI substrate, or CS configuration. Notably, pigs 8-10 showed larger QRS changes in the same leads when T-wave inversion occurred, suggesting that altered activation patterns could modulate repolarization dispersion, which agreed with the improved *in silico* post-MI T-wave replication when experimentally measured LV activation was used (Section 5.3.6).

These results demonstrate the value of *in silico* modeling for dissecting the mechanisms by which MI alters the ECG. In our models, QRS stability in the face of MI is attributable to robust CS-mediated activation, while T-wave changes reflect MI-driven alterations in repolarization gradients and their interaction with lead orientation.

5.3.8 Limitations

OM is a powerful technique to characterize depolarization-repolarization cardiac cycles, but it has inherent limitations. The 2D fluorescence image obtained at each time point represents photons originating not only from the epicardial surface but also from deeper myocardial layers. Due to photon scattering and the 2D nature of OM, multi-view imaging and advanced reconstruction algorithms are required for full 3D recovery of cardiac electrical activity [57]. In this work, OM videos from anterior and posterior heart views were used, restricting comparisons between simulated and experimental data to these surfaces. The temporal resolution was of 2 ms, sufficient to capture most ventricular electrical dynamics. OM datasets were available for sinus rhythm and for pacing from multiple sites, with pacing data informing steady-state CV and APD_{90} estimates, and sinus rhythm data characterizing AT and depolarization patterns for simulation comparison.

Ex vivo and *in vivo* CMR data were analyzed. Even with care to minimize deformation, *ex vivo* CMR showed smaller LV lumen and thicker myocardium compared to *in vivo* cine-CMR at end-diastole. Therefore, BiV simulation geometries were derived from *in vivo* CMR, with fiber fields mapped from *ex vivo* to *in vivo* geometries. Future work could employ improved protocols to further reduce *ex vivo* deformation [46]. The electrophysiological impact of these geometrical shape changes remains unclear. Durrer et al. [186] reported preserved activation patterns but higher CV when canine hearts were mapped *ex vivo* (Langendorff) versus *in situ*. In our study, mean *ex vivo* CV values from OM are lower than those reported for *in situ* porcine OM [53].

We compared a standard RBM (s-RBM) with an RBM informed by DW data (dw-RBM). Direct use of DW-CMR fiber fields was not possible, as anatomical models were based on *in vivo* cine-CMR. The RBM has its own limitations. RBM imposes a linear transmural helix angle (α) variation and constrains fibers to lie parallel to the apico-basal-circumferential plane [122]. While these assumptions have minimal effect on electrophysiological simulations, they may limit the *in silico* reproduction of experimentally observed shear strain in LV mechanics [123].

Fibrosis was not explicitly modeled, although BZ conductivity was reduced. Previous works showed mixed effects. Campos et al. [148] found only non-sustained arrhythmias when fibrosis was combined with reduced I_{Na} and BZ conductivity, suggesting I_{Na} reduction, not fibrosis, as the key proarrhythmic factor. Lopez-Perez et al. [50] reported that fibrosis plus electrophysiological remodeling increased arrhythmic risk, whereas fibrosis alone had little effect on

ECG or activation. Personalizing fibrosis distribution requires invasive mapping, and myofibroblast-CM coupling remains incompletely understood.

Uncertainties in model definition and the use of overly simplistic or inappropriate numerical settings can distort the results of *in silico* studies [10, 15, 202]. Sensitivity analyses of key parameters, such as segmentation delineation, mesh discretization, and conductivity settings, provide a rigorous means of assessing these uncertainties but are computationally demanding and time-consuming. Although such an analysis was beyond the scope of this study, we adhered to established best practices to maximize confidence in our results. For segmentation delineation, mesh generation relied on state-of-the-art algorithms trained on large real-world datasets, with only minor adjustments applied for BiV modeling (see Chapter 4). Mesh discretization followed edge lengths consistent with previous studies [10, 15, 50, 184], which have reliably captured both physiological and arrhythmic dynamics. In particular, Boyle et al. [203] demonstrated that edge lengths below 400 µm can resolve reentrant circuits consistent with experimental observations while avoiding numerical conduction block artifacts. More recently, Bishop et al. [202] highlighted the need for finer discretizations under low-CV conditions to prevent spurious conduction block and variability in arrhythmia outcomes. Although arrhythmicity was not directly assessed in this work, we argue that the discretization adopted here remains suitable for such contexts, consistent with Sung et al. [204]. Furthermore, we implemented Bishop et al.'s recommendations for CV tuning in coarser meshes [202]: CVs in infarcted regions were case-specifically adjusted using OM data when available, while conductivity in healthy zones yielded CVs consistent with experiments, especially when comparing anterior-view measurements in pigs 1–3 to pig 13.

Not all experimental modalities were available here for each animal under both healthy and MI conditions, partly because some methods are incompatible (e.g., *ex vivo* DW-CMR vs OM). As a result, some models were more personalized than others. When data were missing, population-average values were used. This compromise is common in high-fidelity *in silico* studies, given the complexity and cost of full multi-modal datasets. Nevertheless, our work integrates an unusually broad range of experimental data to identify features critical for replicating ventricular electrophysiology in health and after MI.

5.4 Conclusion

We develop and validate *in silico* porcine ventricular models for both healthy and MI conditions, using extensive multi-modal experimental data. In healthy

ventricular models, precise CS architecture and realistic APDSH are essential to match simulated and measured ventricular activation (OM) and ECG morphology. In MI models, incorporating altered tissue properties and K^+ conductances reproduces key MI-induced electrophysiological changes, notably prominent T-wave alterations following LAD and LCx occlusions. Simulation analysis reveals that these T-wave changes arise from MI-induced repolarization gradients, while QRS stability reflects robust CS-mediated activation. This framework provides a reproducible pathway for building and validating personalized porcine electrophysiological models, enabling mechanistic dissection of healthy and pathological ventricular ECG features.

CHAPTER 6

IN SILICO ASSESSMENT OF ARRHYTHMIC RISK FOLLOWING THE IMPLANTATION OF ENGINEERED HEART TISSUES IN PORCINE HEARTS WITH VARYING INFARCT LOCATIONS

6.1 Methodology
- 6.1.1 Arrhythmia inducibility
- 6.1.2 BiV-EHT modeling
- 6.1.3 BiV and EHT electrophysiology
- 6.1.4 Numerical simulations

6.2 Results
- 6.2.1 Cell alignment, conductivity and attachment
- 6.2.2 Real and virtual VT
- 6.2.3 Baseline VT
- 6.2.4 CS and post-MI VT
- 6.2.5 EHT location and VT
- 6.2.6 EHT maturation and VT
- 6.2.7 MI substrate and VT

6.3 Discussion
- 6.3.1 Cell alignment, conductivity and attachment
- 6.3.2 Models replicate arrhythmicity
- 6.3.3 Arrhythmia vulnerability protocol
- 6.3.4 CS modulates arrhythmicity
- 6.3.5 EHT conductivity affects arrhythmicity
- 6.3.6 MI substrate modulates arrhythmicity

6.4 Limitations

6.5 Conclusion

This chapter aims to elucidate the mechanisms driving post-MI arrhythmogenesis and how they are influenced by EHT engraftment. To this end,

we conducted *in silico* studies of chronic post-MI arrhythmogenesis and its progression following EHTs implantation across multiple models with varying infarct locations. We began with an MI BiV model to assess how hiPSC-CMs alignment, EHT electrical maturation, and degree of attachment to the host myocardium affect arrhythmic risk. To extend this analysis, we then applied a comprehensive AIP to our nine highly detailed porcine-specific MI models developed in Chapter 5. First, simulated arrhythmic dynamics were compared with experimentally observed reentrant patterns obtained by OM. Next, we quantified VT burden across different infarct substrates, with and without the inclusion of the ventricular CS, thereby highlighting the impact of these factors on arrhythmogenic potential. Building on initial findings regarding EHT-mediated arrhythmic risk, we further performed a sensitivity analysis to determine how post-MI remuscularization with EHT influences arrhythmia susceptibility, with particular attention to implantation site and electrical maturation. Through this approach, we identified key determinants that can either aggravate or mitigate arrhythmic risk in this therapeutic context.

6.1 Methodology

Figure 6.1 shows the different steps of our proposed analysis. In summary, our nine previously developed MI personalized models (Chapter 5) were used in an evaluation of arrhythmogenesis before and after remuscularization therapy.

6.1.1 Arrhythmia inducibility

6.1.1.1 Experimental Protocol

As can be observed in Figure 6.1d, induced arrhythmias in pigs 8-12 were experimentally measured by OM. The experimental preparation and the OM setup were described in detail in the previous chapter in Section 5.1.3.1. Only one induction event was mapped per pig. To induce VT, a stimulation catheter delivered a train of stimuli consisting of 12 initial pulses at a cycle length of 1000 ms, followed by 5 s of pacing with progressively decreasing cycle lengths from 300 to 150 ms until successful induction was achieved. The stimulation catheter was located in the LV for pig 8, in the left atrium for pigs 9-11, and in the right atrium for pig 12. The OM recordings were processed as previously reported (Section 5.1.3.1)

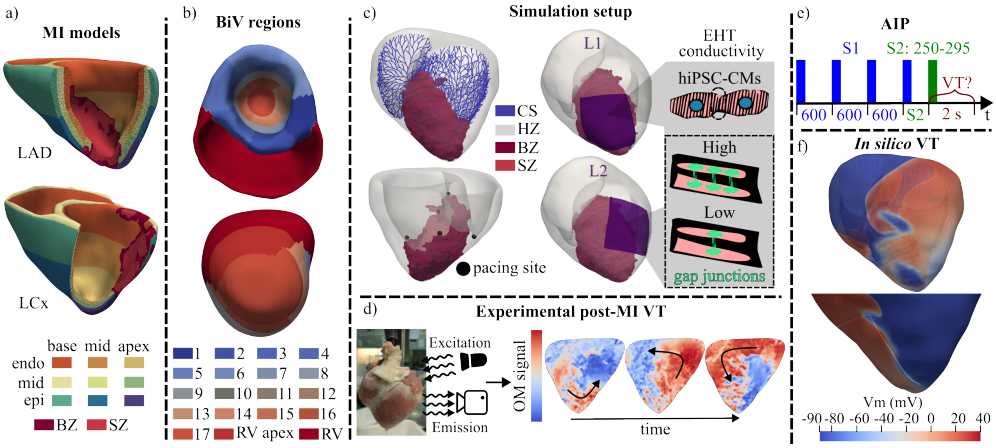


Figure 6.1: Summary of the arrhythmic evaluation performed before and after EHT implantation. a- Examples of BiV models of infarctions with LAD occlusion (top, pig 10) and LCx occlusion (bottom, pig 6). b- LV segments and the RV apex for another BiV model (pig 4). c- Example of a BiV model (pig 10) with its BZ, CS, pacing sites for the AIP and EHT implantation locations and maturation states. d- Experimental OM of the VT induced in pig 8. e- AIP depicting S1-S2 times. f- *In silico* VT induced in pig 10 before (top) and after (bottom) EHT remuscularization. HZ: healthy zone.

6.1.1.2 Computational Protocol

Our implemented AIP was inspired by the work of Arevalo et al. [10]. As shown in Figure 6.1b, each BiV model was automatically divided into 19 regions using LGE-CMR-based segmentation of the LV and RV. The LV was segmented into 17 regions according to the American Heart Association standard [149] and consisted of 6 basal, 6 midventricular, 4 apical segments, and the apex, while the RV was divided into two regions: the apex and the remaining RV (Figure 6.1b). Based on this partition, the centroid of each segment was calculated, and its nearest endocardial node was identified. Pacing sites were defined as the set of nodes located within a 1 mm-radius sphere centered on each of these endocardial nodes. For each pacing site, an S1-S2 protocol was applied. Four S1 stimuli were applied every 600 ms, and one extra stimulus S2 was applied at 250, 265, 280, or 295 ms after the fourth S1 stimulus (Figure 6.1e). All stimuli had an amplitude of 80 $\mu A/cm^2$ and a pulse width of 1 ms [16]. Taking into account the high computational cost of running these simulations for all high-resolution BiV models under different conditions, the number of pacing sites was reduced by manually selecting at least 5 of the 19 pacing sites, with the criterion that they were well distributed around the MI (Figure 6.2). In the LCx and LAD models, the LV apex and RV apex were consistently used

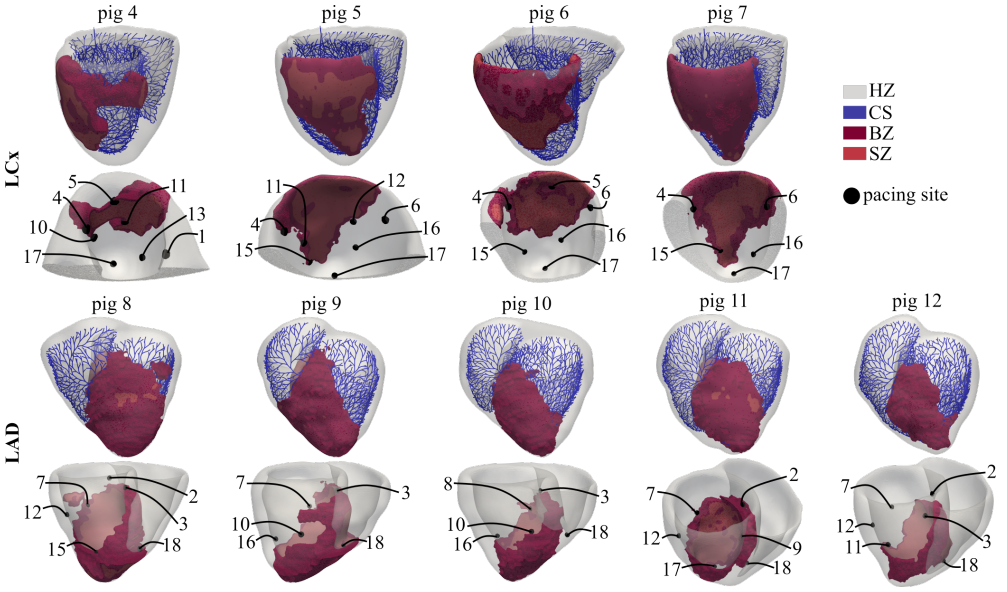


Figure 6.2: Porcine-specific BiV models of MI depicting BZ, SZ and CS together with the manually selected pacing sites used in each pig for application of the AIP. To show the pacing sites in LCx cases, a cut near the LV endocardial septum was performed and a sagittal-like view is presented. HZ: healthy zone.

as one of the selected pacing sites, respectively.

The resulting electrical activity obtained from stimulating every pacing site was labeled as no reentry, non-sustained VT, and sustained VT. No reentry indicates cases where no reentrant activity was observed, while non-sustained and sustained VT indicate that reentry vanished earlier than or was maintained for 2 s after the application of the S2 stimulus, respectively. From this categorization, an inducibility score (IS) was defined as $IS = (\sum_{i=1}^{N} c_i)/(3 \times N)$, where N is the number of simulations used for its calculation, and c_i is 0, 1, or 3 if the i^{th} simulation resulted in no reentry, non-sustained, or sustained VT, respectively. In this way, IS was defined in the range [0,1], with a value of 0 when the N simulations resulted in no reentry, 0.33 when all simulations resulted in non-sustained VT, and 1 when sustained VT occurred in all cases.

6.1.2 BiV-EHT modeling

A pipeline was implemented to build realistic BiV-EHT models (see Figure 6.3). First, the EHT was represented as a 40x40x1 mm^3 squared superficial mesh,

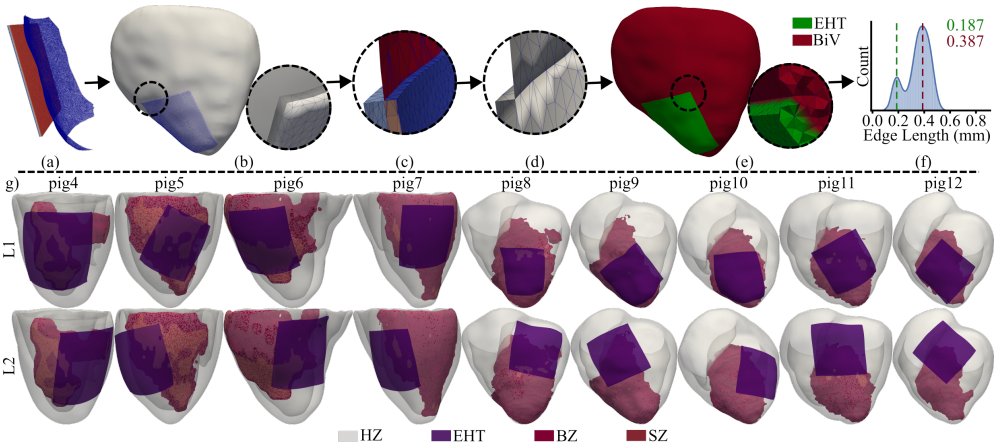


Figure 6.3: BiV-EHT modeling. Pipeline used to generate the BiV-EHT model for pig 10 (a-f) and all BiV-EHT models. a- Aligned EHT and epicardial meshes (EHT contact nodes in red). b- Deformed EHT mesh embedded on the BiV mesh. c- Integrated BiV-EHT mesh with distinct regions and irregular triangles. Light-blue: outer EHT, blue: inner EHT, red: outer BiV, and pink: inner BiV. d- Cleaned BiV-EHT mesh. e- Tetrahedral mesh with BiV (red) and EHT (green) meshes. f- Bimodal edge length distribution in the BiV-EHT model. g- BiV-EHT models for all pigs and the two EHT locations. HZ: healthy zone.

and a rigid transformation was used to bring it closer to the MI region of the BiV mesh (Figure 6.3a). The EHT size was selected based on experimentally achievable dimensions that allow remuscularization of most of the MI region [6,7]. In the high-resolution EHT mesh, contact nodes were defined as those on the face closest to the epicardial surface. These contact nodes were individually projected onto the epicardial surface, with the same displacements applied to the nodes of the non-contacting face. The deformations imposed on the EHT, based on this node-wise contact displacement, resulted in an EHT deformation that followed the epicardial surface of the BiV mesh, as shown in Figure 6.3b. Subsequently, the EHT was embedded in the BiV model by projecting 0.5-0.6 mm of its thickness into the epicardium (see the right circle in Figure 6.3b). The projection direction was set as the inverse of the normal direction of the epicardial node closest to the centroid of the EHT mesh. Once embedded, the EHT and BiV meshes were merged using an *XOR* operation between the two triangular meshes (Figure 6.3c). The part of the EHT located inside the heart (blue region in Figure 6.3c) was removed, and irregular triangles that led to poor quality tetrahedralizations were cleaned with an isotropic explicit remeshing [182] of the BiV-EHT interface (Figure 6.3d).

The BiV-EHT meshes were discretized using Tetgen [183] (Figure 6.3e).

The resulting tetrahedral meshes presented a bimodal edge length distribution, as shown in Figure 6.3f for pig 10. For the initial assessment of the remuscularization's arrhythmic risk, a BiV-EHT model of pig 10, termed l-BiV-EHT, was created with a tetrahedral mean edge length of 995 and 206 µm for the BiV and EHT regions, respectively, which correspond to a model of 2 077 367 tetrahedrons and 349 322 nodes. For the nine high-resolution BiV-EHT models obtained from the MI models in Chapter 5, the low and high modes of their bimodal edge length distributions were calculated. A mean value of 187.2 µm was found for the low mode, which corresponded to the mean edge length in the EHT part. In addition, a mean value of 381.9 µm was found for the high mode, which corresponded to the mean edge length in the BiV part of these models. The mean numbers of tetrahedrons and nodes for the nine high-resolution models were 26 658 338±4 974 043 and 4 512 334±817 799, respectively. These values were reduced to 23 623 451±4 928 526 tetrahedrons and 4 054 310±815 100 nodes after SZ deletion to simulate this region as an insulator. The rationale for this domain discretization was to ensure simulation accuracy, particularly within the thin EHT and its surrounding regions. Due to its small thickness, the EHT required a higher element resolution, while the overall computational burden was kept to a minimum. The electrophysiological characteristics and fiber orientations of the BiV part in the coupled BiV-EHT models were interpolated from the corresponding MI BiV model.

In summary, a total of 10 BiV-EHT models were used: the l-BiV-EHT model, based on pig 10, which has a lower resolution in the BiV region, and 9 high-resolution BiV-EHT models built from the analysis performed in Chapter 5.

6.1.3 BiV and EHT electrophysiology

The biophysically detailed cellular model of Stewart et al. [108] was used to represent the AP of the CS in all 10 models. In the l-BiV-EHT model, the O'Hara et al. [51] model and the first Paci2013 model by Paci et al. [110] were used to represent the cellular-level electrophysiology in the BiV and EHT regions, respectively. In the other 9 high-resolution models, the Gaur et al. [16] model and the updated Paci2020 model by Paci et al. [113] were employed to represent the AP of the CMs and hiPSC-CMs, respectively.

In the l-BiV-EHT model, the BiV healthy region was divided into endocardium, midmyocardium, and epicardium (the same proportion as in Section 5.1.4.5), and the corresponding transmural phenotype of the O'Hara et al. [51] cellular model was associated with each region. In BZ, cellular-level electro-

physiology was defined by modulating some of the ionic current conductances in the O'Hara et al. [51] cellular model. Specifically, the I_{Na} was reduced to 38% of its default value [187], I_{CaL} to 31% [205], and I_{Kr} and I_{Ks} to 30% and 20% [200], respectively. In this manner, the APD was increased, and the upstroke velocity and maximum AP amplitude were decreased in BZ, as in [10,50]. Similar to the high-resolution models, an orthotropic conductivity with transverse isotropy was defined. To reproduce experimental ATs, the LDCs for the healthy zone, BZ, and CS were set to 0.0013, 0.00095, and 0.01 cm^2/ms (equivalent to 0.13, 0.095, and 1 S/m for a membrane surface-to-volume ratio of 1000 cm^{-1} and capacitance per unit area of 1 $\mu F/cm^2$), respectively. The CS LDC was reduced near the CS endpoints to match the ventricular conductivity, and a PMJ radius of 1 mm was used to avoid the CS-myocardium source-sink mismatch present in this BiV-coarser mesh. The SZ was defined as non-conductive, and the transverse-to-longitudinal diffusion ratios were set to 0.25 for the healthy zone and EHT, and to 0.32 for BZ [50, 120].

In the 9 high-resolution CS-BiV-EHT models, the spatial repolarization heterogeneities, conductivities, CS architecture, and CMs alignment were defined as in the C5G7 group of simulations (see Section 5.1.5 and Table 5.4). The EHT conductivity was set to be completely isotropic in these models, owing to the lack of precise information on connexin-43 distribution in hiPSC-CM cultures. In addition, hiPSC-CMs were randomly aligned after proving that this factor plays a secondary role in electrophysiological alterations following remuscularization (see Chapter 3 and Section 6.2.1.1).

6.1.4 Numerical simulations

6.1.4.1 Sinus rhythm simulations

Preliminary, the l-BiV-EHT model was employed to evaluate the electrophysiological alterations that originated when an EHT with different electrical maturation, cellular alignment, and degree of engraftment to the host myocardium was implanted at the apical epicardium, directly over the MI. Higher maturation was represented by a higher cell-to-cell coupling in the EHT.

In the first group of simulations (C6G1), we concomitantly varied the alignment of the hiPSC-CMs and the EHT conductivity. We tested relative EHT conductivities of 10%, 50%, and 90% of that in healthy myocardium, which represent different levels of connexin 43 and are associated with different degrees of maturation. In Chapter 3, we previously observed that minimal variations in the hiPSC-CM alignment had a negligible impact on the arrhythmic

risk associated with the EHT implantation. Therefore, we globally varied the hiPSC-CM orientation on the EHT by setting it to be random, parallel, or perpendicular to the underlying epicardial cells, as depicted on the right side of Figure 6.4. In these simulations, the EHT was fully coupled to the host myocardium.

In a second group of simulations (C6G2), discontinuous meshes were created by duplicating the mesh nodes and edges in the BiV-EHT interface to model 0%, 25%, 50%, and 75% of EHT attachment to the host myocardium, as can be seen on the left of Figure 6.4. The initially defined contiguous BiV-EHT mesh represented 100% EHT engraftment. In these simulations, random cell orientation was assigned to the EHT, and the relative EHT conductivities of 10%, 50%, and 90% of that in healthy myocardium were tested.

In both simulation groups (C6G1-2), all cellular models were prepaced to steady-state by running 1000-second simulations. Stimuli of 80 $\mu A/cm^2$-magnitude and 1 ms-duration were applied at the AVN node. Each organ level simulation consisted of three cardiac cycles at 1 Hz-pacing, with the last cycle being used for the calculation of the AT, APD_{90}, and RTG on the EHT from the numerically obtained V_m. The calculation of these parameters was performed as in Section 3.1.2.6. The mean RTG vector between a central node and its neighboring nodes within a radius of 500 µm was computed, with the radius value chosen to approximately cover the EHT thickness.

6.1.4.2 Arrhythmia inducibility simulations

Simulations were conducted to investigate the contribution of MI characteristics and CS to arrhythmic risk, using the 9 EHT-free high-resolution BiV models from the previous Chapter 5. In a third group of simulations (C6G3), the complete AIP was applied to all BiV models; that is, S1-S2 stimulation was applied 4 times to each pig model in each selected pacing site, corresponding to the four S2 values of 250, 265, 280, and 295 ms. To validate our models, the simulated depolarization patterns calculated for LAD pig models were compared with those obtained from OM experiments for the same pigs when the experimental AIP described in Section 6.1.1.1 was applied. In this set of simulations, proarrhythmicity was evaluated as a function of the S2 delay, as well as the location, shape, and size of the MI.

In a fourth group of simulations (C6G4), proarrhythmicity was evaluated as a function of the inclusion or absence of CS in the models. Specifically, the AIP results after applying an S2 of 295 ms were compared for the LAD and LCx models with the highest and the lowest inducibility, both with and

without CS.

Changes in vulnerability to arrhythmias after post-MI remuscularization with EHTs were investigated using our 9 high-resolution BiV-EHT models. A fifth group of simulations (C6G5) was carried out in which AIP was applied with an S2 of 295 ms before and after the engraftment of EHT in all pigs, and when the EHT was implanted in two different locations. For the central location L1, the EHT was implanted in the center of the MI. In contrast, for the lateral location L2, the EHT was positioned such that half of it overlapped the MI region, while the other half was in contact with healthy tissue (Figure 6.3g). The rationale for selecting these locations was to balance two competing factors: mechanical support is believed to be maximized when the EHT is placed centrally within the MI; on the other hand, the survival of the EHT could be improved when it is in contact with well-vascularized healthy tissue. In all C6G5 simulations, the EHT conductivity was set to 10% of the value found in healthy tissue.

In addition, a sixth group of simulations (C6G6) was performed to assess the effects of the electrical maturation of the EHT on proarrhythmicity. In this simulation group, a pacing site was selected for each pig model based on the results of the C6G3 and C6G5 simulations; subsequently, S1-S2 stimulation was applied. Setting a value for the S2 stimulus of 295 ms at this pacing site, all coupled BiV-EHT models, with L1 and L2 locations for the EHT, were evaluated when the EHT conductivity was set to 90% of that of healthy tissue. The results obtained when the EHT conductivity was set to 10% and 90% relative to the value found in healthy tissue were compared in each of the pigs.

In C6G5-6 simulations, random fiber orientations were assigned to the EHT. As in simulations C6G1-2, all cellular models used for simulations C6G3-6 were prepaced to steady state by applying periodic S1 stimuli (80 µA/cm^2 magnitude, 1 ms duration, 600 ms period). For the Paci2020 model, prepacing was performed according to the stimulation described in [113] (0.55 nA magnitude, 5 ms duration) with a period of 600 ms. Stabilization of all cellular models was confirmed by verifying that APD_{90} remained constant for consecutive beats (CS: 310 ms under spontaneous automaticity, healthy tissue: 196-218 ms, BZ: 384 ms, EHT: 405 ms).

In all simulations, the monodomain reaction-diffusion equation was numerically integrated using *ELECTRA* (see Section 1.6.3.6). High-throughput execution was achieved through batch simulation using HERMES, the high-performance computing unit at the University of Zaragoza. Computed V_m was saved at a time resolution of 1 ms, while the adaptive integration time step was

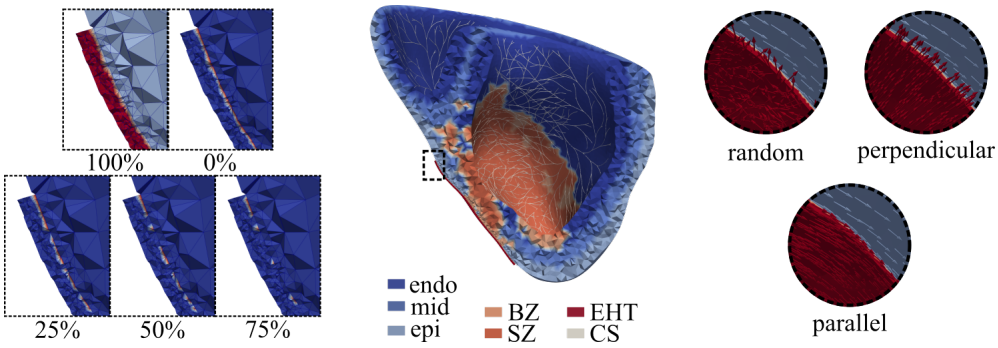


Figure 6.4: BiV-EHT model with varying properties. At the left panel, different BiV-EHT coupling degrees are shown. Unattached regions are shown in red. At the right panel, different hiPSC-CM orientations are depicted.

constrained within the [0.01,0.1] ms range for all *in silico* calculations. In total, 350 simulations were performed. As some pacing sites did not capture any S2 stimulus, this involved the simulation of more than one million milliseconds of electrophysiological activity using high-resolution BiV models. Thus, this constitutes one of the largest and most complex cardiac electrophysiological simulation studies to date [10, 11, 15, 76, 78].

6.2 Results

6.2.1 Effect of EHT cell alignment, conductivity and attachment on BiV-EHT electrophysiology

6.2.1.1 Variation of hiPSC-CM orientation and EHT conductivity

Figures 6.5a and 6.5b show the statistical distributions computed over the EHT and maps computed over the l-BiV-EHT model of AT, APD_{90}, and RTG for the C6G1 simulations.

In C6G1 simulations, we first investigated the impact of the EHT design variables on the depolarization properties of the EHT. We found that the ATs were almost unchanged for the different hiPSC-CM orientations, while they were slightly reduced when the EHT conductivity was increased (left panel, Figure 6.5a). Qualitatively, the depolarization traveled from the lateral corners of the EHT towards its center and continued to the bottom corner for all tested EHT conductivities and hiPSC-CM orientations (top panel, Figure 6.5b). The largest variation in the maximum AT of the EHT was 31 ms when

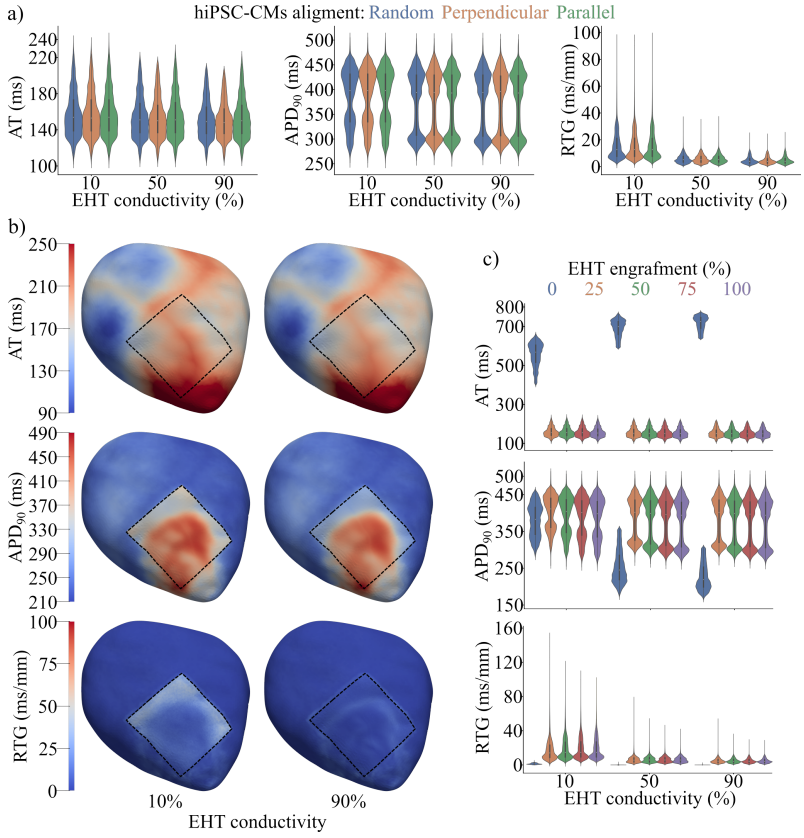


Figure 6.5: a- AT, APD_{90} and RTG distributions in the EHT for different hiPSC-CM orientations and EHT conductivities relative to healthy tissue. b- AT, APD_{90} and RTG maps for 10% and 90% relative EHT conductivity, random hiPSC-CM orientation, and full EHT-myocardium coupling. EHT is highlighted with a dashed black line. c- AT, APD_{90} and RTG distributions in the EHT for different relative EHT conductivities and degrees of attachment.

the EHT conductivity was increased from 10% to 90% of the value found in healthy tissue for the perpendicular hiPSC-CM orientation (left panel, Figure 6.5a). Moreover, only a minimal 11.2% decrement in the maximum AT (in mean over all hiPSC-CM orientations) was observed even after increasing the EHT conductivity 9 times. This small variation in the maximum AT can be explained by the late activation of the EHT bottom corner, as the EHT bottom corner was hidden from the CS by the non-conductive SZ.

Regarding the impact of the EHT design on repolarization, we found that the APD_{90} values in the EHT resembled the values found in the underlying host myocardium. This effect was more accentuated for higher EHT conductivities,

as illustrated in the middle panel of Figure 6.5b. The highest EHT conductivity (90% of that of healthy tissue) allowed for better EHT-myocardium electrical coupling than the lowest EHT conductivity (10% of that of healthy tissue). In this scenario, the APD_{90} in the EHT regions in contact with the healthy tissue and BZ were reduced and maintained, respectively, due to the electrotonic load exerted by the host tissue on the EHT. Moreover, we observed a null influence of hiPSC-CM orientations on the APD_{90} (middle panel, Figure 6.5a).

With respect to the arrhythmic risk marker RTG, its values were nearly constant for all hiPSC-CM orientations (right panel, Figure 6.5a). Importantly, we found EHT conductivity to be a major contributor to RTG. The median RTG in the EHT was reduced with the increasing EHT conductivity. In particular, the median RTGs on the EHT were 12.6, 5.1, and 3.9 ms/mm for the 10%, 50%, and 90% healthy-tissue-relative EHT conductivities, respectively, in mean across all hiPSC-CM orientations. Also, the maximum RTG in the EHT decreased from 97.1 to 24.7 ms/mm for an increment of the EHT conductivity from 10% to 90% of the value found in healthy tissue, in mean across all hiPSC-CM orientations.

6.2.1.2 Variation of EHT attachment and conductivity

Figure 6.5c shows the statistical distributions, computed over the EHT, of AT, APD_{90}, and RTG for the C6G2 simulations.

As can be observed in the top panel of Figure 6.5c, when the EHT was fully unattached from the myocardium, the EHTs retained its automaticity, and high AT values were measured. In this case, the higher the EHT conductivity, the more delayed the AT in absolute terms. With only a minimum EHT attachment, a large decrement in AT and a loss of automaticity in the EHT could be observed. As an example, for the lowest EHT conductivity (10% of that of healthy tissue), the entire EHT depolarization took 262 ms when the EHT was fully unattached, while it took around 140 ms when the EHT was engrafted, even if minimally. For variations in EHT attachment from 25% to 100%, AT barely changed.

For 0% EHT attachment, the median APD_{90} was reduced from 383 to 219 ms when EHT conductivity was set to 10% and 90% of the value found in healthy tissue, respectively. Thus, higher EHT conductivity accelerated hiPSC-CMs repolarization, leading to more adult-like APD_{90}. Also, APD_{90} was slightly reduced with the increasing EHT attachment. Median values of 402, 399, 396, and 394 ms were computed when EHT attachment was 25%, 50%, 75%, and 100%, respectively.

As expected, RTG was almost null for fully unattached EHT. Median RTGs were similar for all EHT attachment values, as RTG was measured in the whole EHT. For the minimum EHT attachment of 25%, the maximum RTG was decreased by 98.8 ms/mm when EHT conductivity increased from 10% to 90% of the value found in healthy tissue. Thus, arrhythmic risk attenuation was found for high EHT conductivity in association with smooth electrophysiological integration. Further arrhythmic risk reduction was found for high EHT attachment, as maximum RTG was reduced by as much as 52.3 ms/mm from minimum to complete EHT attachment when EHT conductivity was set to 10% of that of healthy tissue.

6.2.2 Experimental and simulated arrhythmic patterns on MI-BiV models

The experimental arrhythmic patterns mapped by OM in LAD pigs were compared with the results of the C6G3 simulations for pigs 8, 10, and 11 (Figure 6.6). In pigs 8 and 11, a counterclockwise reentry was observed in the anterior view of the OM recordings. These experimental patterns were reproduced by the *in silico* simulations when AIP was applied with an S2 of 295 ms at pacing site 12 for pig 8 and at pacing site 7 for pig 11. Generally, the depolarization wave traveled in the LV from the apex to the base, crossed to the basal RV, and propagated downward to the apical RV. In pig 10, the experimentally observed clockwise reentry was replicated *in silico* by stimulating pacing site 3 with an S2 of 280 ms. For this pig, the epicardial activation of the anterior view progressed sequentially from the LV apex to the RV base, then to the medial LV, and subsequently, the depolarization reached the laterobasal LV and the LV apex. Simulations also reproduced the counterclockwise reentrant activity observed in LAD pigs 9 and 12, with an S2 of 295 ms applied at pacing sites 16 and 12, respectively.

Experimental VTs were sustained in all infarcted pigs with LAD occlusion, while non-sustained and sustained VTs were numerically observed for pigs 8-10 and 11-12, respectively. As an example, in pig 8, a single reentry was observed because the depolarization wave was stopped when traveling from the basal RV to the apical LV (see the simulated reentry of pig 8 in Figure 6.6). In spite of minor differences, experimental and simulated reentrant dynamics showed good agreement in all cases.

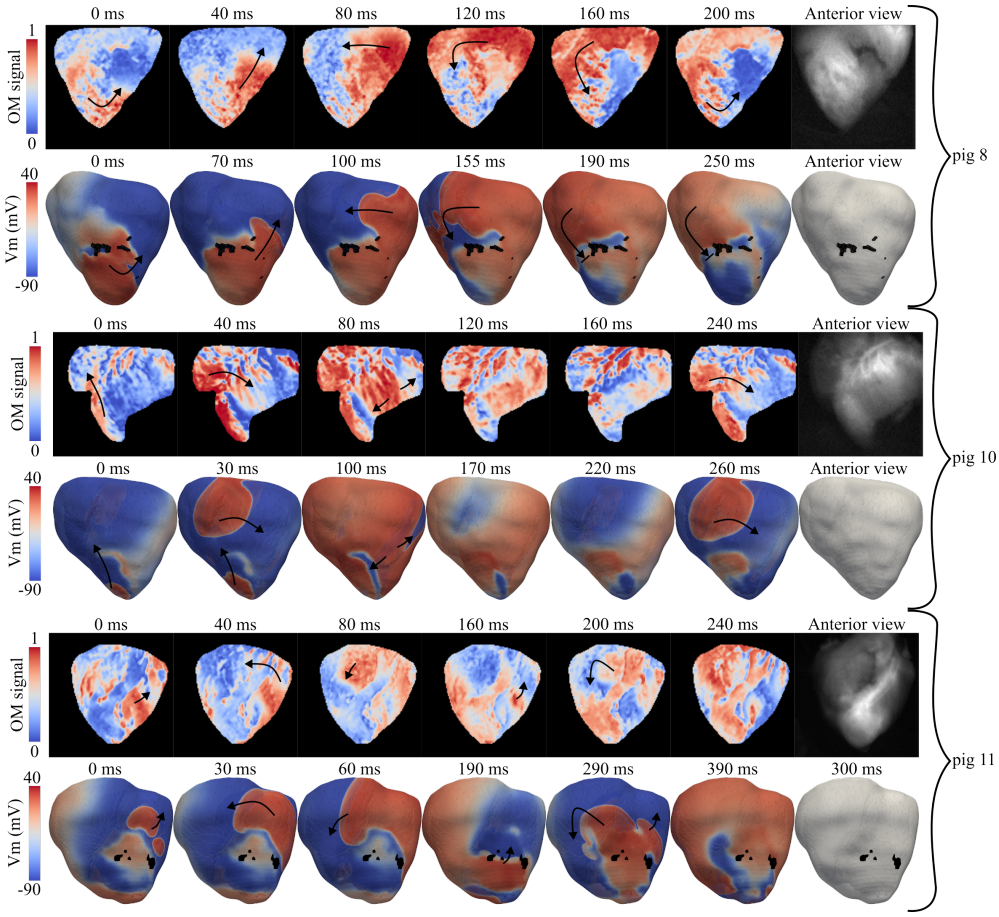


Figure 6.6: Reentrant activity in LAD pigs after application of the experimental (top) and *in silico* (bottom) AIPs.

6.2.3 Quantification of VT inducibility after MI

Figure 6.7 summarizes the results of the C6G3 simulations, while the full set of results is provided in Appendix Table A.1. When AIP was applied, considering all pacing sites and all S2 values, pigs 8, 9, 10, 11, and 12 achieved IS values of 0.30, 0.37, 0.54, 0.7, and 0.1, respectively. Specifically, a single sustained VT was generated for pigs 8, 9, and 12, while 4 and 5 sustained VTs were found for pigs 10 and 11, respectively. Of all pigs with simulated LAD occlusion, pig 11 had the highest inducibility, while pig 12 had the lowest inducibility. In particular, for pig 12, the application of AIP in 84.6% of the paced sites failed to develop a reentry. In addition, LCx pigs were found to be less vulnerable

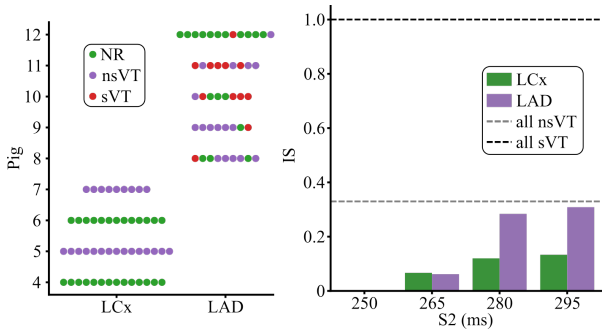


Figure 6.7: VT inducibility results as a function of MI location (left) and IS as a function of S2 values (right) for the 9 high-resolution BiV models when all pacing sites were tested. NR: no reentry, nsVT: non-sustained VT, sVT: sustained VT.

to arrhythmias. Only non-sustained VTs were generated in pigs 5 and 7 (IS: 0.33), and no reentry was observed in any cases in pigs 4 and 6 (IS: 0).

Regarding the S2 stimulus, the stimulated tissue was still refractory when the extra stimulus was applied 250 ms after the last S1 stimulus, preventing capture. Inducibility increased when the S2 delay increased, with contained increments in IS observed in LCx pigs. IS values of 0.06, 0.12, and 0.13 were measured for S2 values of 265, 280, and 295 ms, respectively, in LCx cases. In LAD pigs, IS increased sharply from 0.062 to 0.28 when S2 changed from 265 to 280 ms, and slightly from 0.28 to 0.31 when S2 changed from 280 to 295 ms, respectively. Thus, the S2 delay had a greater effect on inducibility in LAD pigs than in LCx pigs. For both types of MI, an S2 of 295 ms led to the highest inducibility. Therefore, other groups of simulations were conducted using this delay.

6.2.4 CS effect on arrhythmogenesis after MI

In the C6G4 simulations, LCx and LAD pigs with low and high inducibility in C6G3 were considered to evaluate the effect of CS on arrhythmogenesis. The complete set of results for the C6G4 simulations is provided in Appendix Table A.2.

For the group of LCx pigs, pig 6 exemplified a case of low inducibility in which CS played a fundamental role in blocking the reentry. As shown in the upper left panel of Figure 6.8, the application of AIP at the pacing site 6 generated an S2-derived depolarization wave that initially propagated from the anterior to the posterior LV through the apex. Then, a CS-derived epicardial

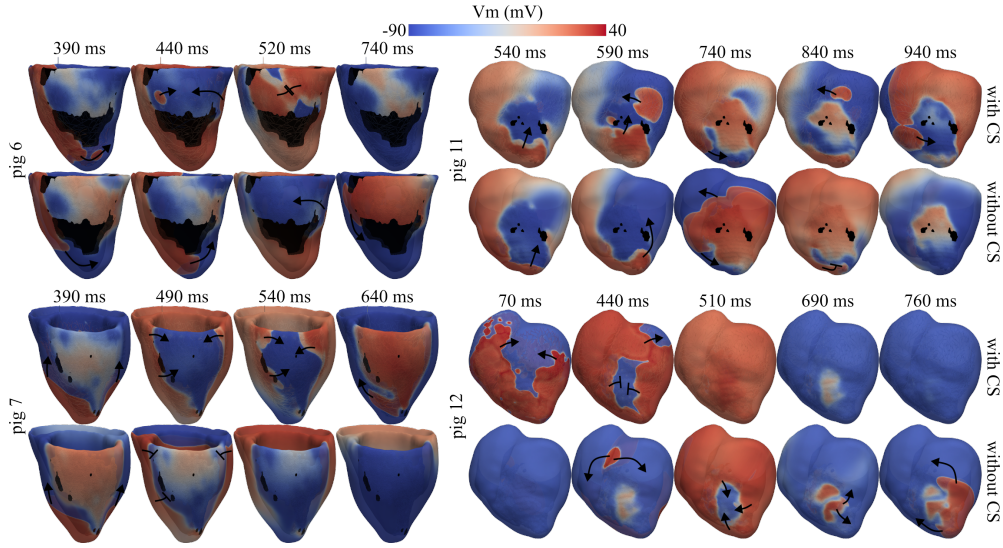


Figure 6.8: Changes in proarrhythmicity associated with CS. Results for pig 6 (LCx with the lowest inducibility) stimulated at the pacing site 6, pig 7 (LCx with the highest inducibility) stimulated at the pacing site 17, pig 12 (LAD with the lowest inducibility) stimulated at the pacing site 3 and pig 11 (LAD with the highest inducibility) stimulated at the pacing site 7 are depicted in the upper left, lower left, lower right and upper right panels, respectively. The timings refer to the time of application of the last S1 stimulus.

breakthrough blocked this S2-derived activation in the laterobasal region, preventing reentry. Without the effect of the CS, the same S2-derived activation was not blocked by the epicardial breakthrough, allowing for a sustained VT. Pig 7 was chosen as an example of a high inducibility case (pig 5 was not chosen, as the non-sustained VT in pig 5 traveled through the low conducting laterobasal isthmus in the LV and could disappear in a simulation of the entire heart, as described in the following Section 6.2.7). The application of AIP at pacing site 17 of pig 7 resulted in a non-sustained VT for a simulation with CS and in no reentry for a simulation without CS. In the first case, CS enabled the MI to function as a capacitor: the faster depolarization and subsequent repolarization of the MI region allowed slow loading of this region with S2-derived activation, followed by the release of the capacitive energy stored in the MI region from its apex back to the healthy tissue once the refractory-based impedance in the healthy zone was low enough to allow the MI to be discharged, producing the reentry. Without CS, S2-derived activation did not penetrate the MI region, as it remained in its refractory period.

Similarly to the LCx cases, the presence or absence of CS determined an

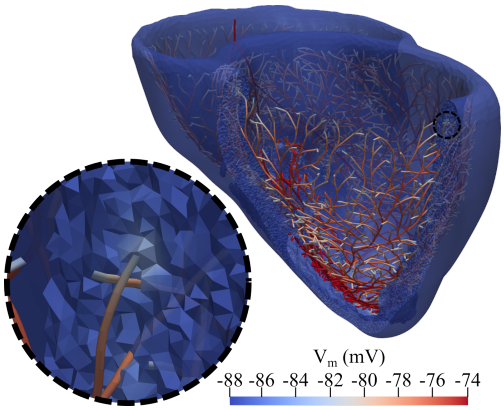


Figure 6.9: Diastolic potential difference between the CS and BiV domain of pig 11, before applying the fourth S1 stimulus at pacing site 7.

inversion in the occurrence of reentry in LAD pigs. In pig 11, associated with the highest inducibility for LAD pigs, CS initiated delayed endocardial activations when pacing at site 7. These activations propagated transmurally, resulting in an epicardial breakthrough at 590 and 840 ms after the last S1 stimulus (see the top side of the upper right panel of Figure 6.8), sustaining VT. Beyond its role as an *electrical bypass*, CS also influenced VT dynamics through another mechanism linked to its intrinsic cellular properties. A nearly stalled and fading depolarization wavefront was reenergized in regions adjacent to PMJs. During the resting phase, CS had a diastolic potential higher than that of the surrounding myocardium, increasing the V_m of the nearby ventricular PMJ nodes, as seen in Figure 6.9. Moreover, because of the longer APD of CS (Section 6.1.4), activated PMJs could further increase V_m in these nodes, especially in the healthy tissue, bringing them closer to the excitation threshold. Together, these mechanisms may have facilitated local depolarization, thus supporting VT sustainability. In contrast, without CS, the re-energizing of fading depolarization wavefronts and, more importantly, the *electrical bypass*-derived epicardial breakthroughs were absent (see the bottom side of the upper right panel of Figure 6.8), and VT became non-sustained, terminating approximately 1 s after the last S1 stimulus. In pig 12 (lowest inducibility for LAD pigs), the presence of CS generated an *electrical bypass* between the septal base and the apex of both ventricles when AIP was applied at the septal base (pacing site 3). This bypass revealed that CS enabled earlier depolarization of the MI region compared to the case without CS (see the lower right panel of Figure 6.8). Consequently, the S2 stimulus arrived at a completely repolarized

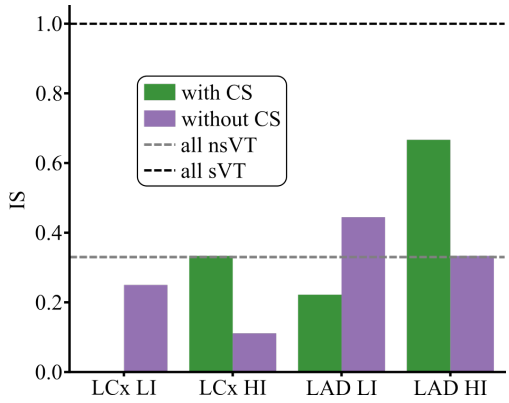


Figure 6.10: IS computed with and without CS for the least (LI) and most inducible (HI) pigs of each MI type (LAD, LCx). LCx LI: pig 6, LCx HI: pig 7, LAD LI: pig 12 and LAD HI: pig 11. nsVT: non-sustained VT, sVT: sustained VT.

MI 440 ms after the last S1 stimulus, resulting in no reentry. Without CS, a *capacitive effect* was observed, similar to that described for pig 7 with CS. The S2-derived depolarization wave partially halted in the MI and slowly penetrated this region. Later, reentry occurred when this MI-stored energy was unleashed back to the healthy tissue as this tissue regained excitability.

In general, the presence or absence of CS drastically influenced arrhythmogenesis. As shown in Figure 6.10, removing CS decreased IS in the cases with the highest inducibility for both MI types (from 0.33 to 0.11 in LCx and from 0.66 to 0.33 in LAD pigs), but increased IS in the cases with the lowest inducibility (from 0 to 0.25 in LCx and from 0.22 to 0.44 in LAD pigs).

6.2.5 Impact of EHT implantation location on arrhythmogenesis after MI

Figure 6.11 shows the effect of EHT engraftment location on arrhythmogenesis. IS values after MI and subsequent EHT implantation highlight a strong dependence of arrhythmogenesis on the occluded artery (see Figure 6.11a). In LCx pigs, EHT at L1 markedly increased IS from 0.16 to 0.49, while implantation at L2 resulted in a smaller rise (IS = 0.35). In LAD pigs, IS was slightly lower after implantation at L1 (IS = 0.33) compared with both pre-implantation and implantation at L2 (IS = 0.38), as can be seen in Figure 6.11a. Appendix Table A.3 collects all the results for the C6G5 simulations.

Analyzing individual LCx pigs, IS remained stable in pigs 5 and 7 after MI

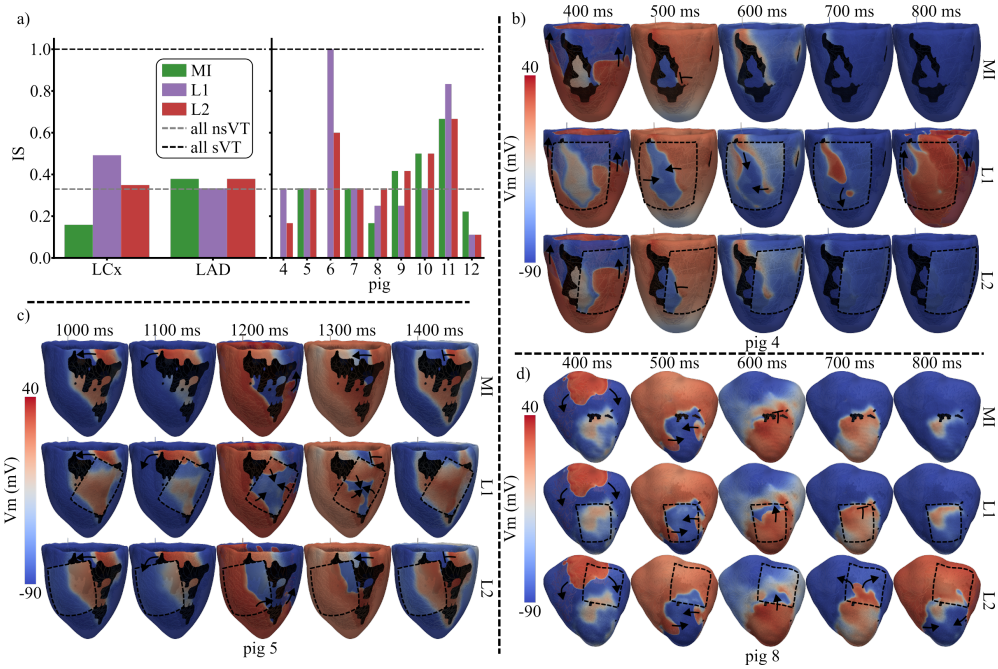


Figure 6.11: Effect of EHT engraftment location on arrhythmogenesis. In a, IS is presented for BiV MI models and for BiV-EHT MI models, with EHT located at L1 and L2. The left panel displays global results for LAD and LCx pigs, while the right panel shows results for each pig. In b, c and d, V_m maps are presented for pigs 4, 5, and 8, with the EHT outlined (dashed black line). The depolarization-repolarization dynamics after AIP application are presented for MI (top), MI with EHT in L1 (middle) and MI with EHT in L2 (bottom). The pacing sites are 17 for pig 4, 6 for pig 5 and 3 for pig 8. The timings of the V_m maps refer to the time of application of the last S1 stimulus. nsVT: non-sustained VT, sVT: sustained VT.

and following EHT implantation at both L1 and L2. In pigs 4 and 6, EHT remuscularization increased IS, and its highest value was always found in the L1 position. For pigs 4, 5, and 6, the EHT covered the SZ extensively in the L1 position, which generated new conductive pathways between the basal and apical regions of the LV free epicardial wall. This phenomenon is illustrated for pig 4 in Figure 6.11b, for pig 5 in Figure 6.11c, and for pig 6 in Figure 6.12a.

Specifically, in pig 4, the S2 stimulus initiated at pacing site 17 propagated first in the apico-basal direction and then reached the central island of BZ, generating reentry when the EHT was located at L1 (middle row Figure 6.11b). In contrast, no reentry was observed for the same pacing site both after MI and

with the EHT at L2, as the S2-derived depolarizing wave at the latero-basal LV was unable to cross to the central BZ due to the lack of EHT-mediated electrical bridging. A similar phenomenon occurred in pig 6. When AIP was applied at pacing site 15, CS blocked reentry after MI, as shown in Section 6.2.4. A new reentrant pathway was generated in the base-to-apex direction when EHT was implanted at locations L1 and L2, as can be observed for L1 in the upper row of Figure 6.12a. This pig exhibited the largest IS increase after EHT engraftment. Across all five pacing sites assigned to this pig, AIP simulations yielded no reentry before remuscularization (MI: 5 no reentries) but resulted in reentry at all sites after remuscularization (EHT-L1: 5 sustained VTs, EHT-L2: 3 non-sustained VTs and 2 sustained VTs). Electrical bridging by the EHT was also observed in pig 5 at the L1 location (see Figure 6.11c), although IS remained unchanged regardless of EHT presence or location (6.11a). This stable IS was probably dependent on the fact that this pig persistently presented a reentry blocking the depolarizing wave traveling from the base to the apex through the electrical bridge associated with the EHT, as illustrated in the middle row of Figure 6.11c.

Unlike LCx pigs, LAD pigs exhibited high variability in proarrhythmic responses following EHT implantation and EHT location (see Figure 6.11a). Interestingly, in LAD pigs, the implantation of the EHT in L1 reduced IS in 3 of the 5 pigs (pigs 8, 9, and 12) and increased it in the other two pigs. When the EHT was implanted in L2, IS was maintained in pigs 9-11, reduced in pig 12, and increased in pig 8. As an example, the depolarization-repolarization dynamics computed when AIP was applied at pacing site 3 in pig 8 are presented in Figure 6.11d. Here, similar electrical activity was observed after MI and after EHT implantation in L1, with S2-derived excitation penetrating the MI region and blocking in the mid-epicardial LV. In contrast, implantation in L2 led to reentry, as S2-derived excitation propagated into the highly excitable EHT and continued through the weakly depolarized wavefront, which had previously acted as a conduction barrier.

6.2.6 Contribution of EHT electrical maturation to arrhythmogenesis after MI

In the C6G6 simulations, EHT electrical maturation was modeled by a variation in its conductivity. As shown in Figure 6.12, increasing the EHT conductivity from 10% to 90% of that of healthy tissue either decreased IS or kept it at the baseline level.

Figure 6.12a illustrates this effect for two different pigs and EHT locations

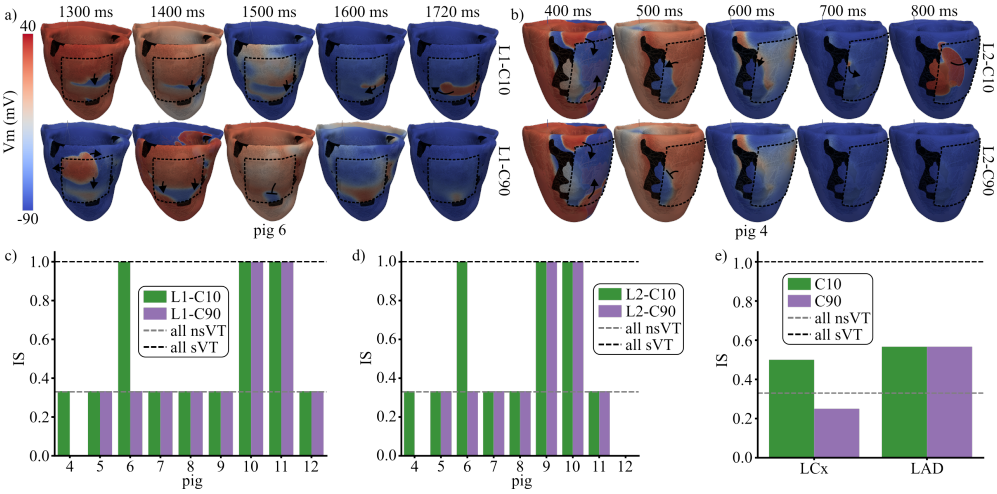


Figure 6.12: Effects of EHT electrical maturation on arrhythmogenesis. AIP-derived electrical activity is shown for pig 6 (a) and pig 4 (b) when low (top) and high (bottom) EHT (dashed black line) conductivities were used. The pacing sites were 15 for pig 6 and 1 for pig 4. The timings refer to the time of application of the last S1 stimulus. IS was obtained per pig using different EHT conductivities and locations L1 (c) and L2 (d). Panel e shows IS for relative EHT conductivities of 10% and 90% in LCx and LAD MI groups. C10/90: EHT with a conductivity equal to the 10/90% of the value found in the healthy adult-like tissue, nsVT: non-sustained VT, sVT: sustained VT.

(pig 6, location L1; pig 4, location L2). In the case of pig 6 and location L1, increasing the EHT conductivity to 90% of that of healthy tissue led to a homogeneous fast depolarization and subsequent repolarization of the EHT area above SZ, which prevented an EHT-mediated slow depolarization wave from maintaining the VT observed for the 10% healthy tissue-relative conductivity of the EHT (Figure 6.12a, 1720 ms after the last S1 stimulus). A similar phenomenon was observed in the case of location L2 for the same pig 6, where the faster activation of the EHT transformed sustained VT into non-sustained VT (see Appendix Table A.4).

For the case of pig 4 and location L2, increasing the EHT conductivity to 90% of that of healthy tissue led to a smoother depolarization wavefront (Figure 6.12b, 600 ms after the last S1 stimulus). For the EHT conductivity set to 10% of that of healthy tissue, a small self-standing activation was detached from the depolarizing wave and arrived at the peninsular BZ area, which maintained the VT, as a new depolarization wavefront was generated and amplified from this region (top Figure 6.12b). Increasing the EHT conductivity to 90% of that of healthy tissue prevented any reentry from occurring in both EHT locations.

For the remaining LCx pigs (5 and 7), as well as for all LAD pigs, increasing EHT conductivity had no effect on IS compared to the low EHT conductivity setup, as can be observed in Figure 6.12c and 6.12d.

When the pigs were divided into LCx and LAD groups, it could be concluded that a higher EHT conductivity reduced the vulnerability to arrhythmias for LCx infarcts and did not change it for LAD infarcts (Figure 6.12e).

6.2.7 Role of MI characteristics on arrhythmogenesis before and after EHT implantation

The overall MI size, encompassing both SZ and BZ, was generally larger for LAD pigs than for LCx pigs, as can be observed in Appendix Table A.5. The ratio between MI and BiV volumes was 8.8%, 8.0%, 10.6%, and 14.0% for LCx pigs 4-7, and 30.2%, 27.1%, 16.6%, 20.8%, and 13.4% for LAD pigs 8-12, respectively.

For LAD pigs 8-11, a positive correlation between the volume of MI occupied by BZ and the value of IS was observed. Both IS (see Section 6.2.3) and the BZ/MI ratio increased progressively from pig 8 to pig 11 (BZ/MI: from 20.7% for pig 8 to 46.5% for pig 11). Pig 12, however, had the lowest IS value of all LAD pigs, despite having an intermediate BZ/MI volume ratio (36.2%). For LCx pigs, pig 7 showed both the highest IS value and the highest BZ/MI volume ratio (45.5%). Pig 5 had the same IS value as pig 7 (the highest among LCx pigs); however, it presented a low BZ/MI volume ratio of 20.8%. This could be explained by the fact that the reentry observed in pig 5 spread along a slow-conducting isthmus located in the latero-basal region of the LV (Figure 6.11c), suggesting that it could disappear in a simulation of the entire heart in which the addition of the outflow tracts and the atrial tissue alters the isthmus.

In the context of MI remuscularization with EHT, we observed that the size of the epicardial SZ correlated with the magnitude of IS induced by EHT implantation. For LCx pigs, the epicardial SZ was higher in pigs 4-6 than in the other pigs (see Figures 6.2 and 6.3g, and Appendix Table A.5). The ratio between the epicardial area of the SZ and the entire MI was 48.6%, 42.9%, 47.4%, and 3.8% for LCx pigs 4-7, respectively. Correspondingly, pigs 4 and 6 experienced the greatest increases in arrhythmia vulnerability after EHT implantation, which were reduced by placing the EHT in location L2 and increasing the conductivity of the EHT in either of the two locations. Pig 5, despite a high epicardial SZ/MI ratio, showed no IS changes. In this case, the EHT created a new reentrant pathway from the base to the apex. However, unlike pigs 4 and 6, this EHT-derived reentry was blocked by the reentry that

occurred before the engraftment of the EHT (Figure 6.11c). In LAD pigs, epicardial SZ/MI ratios were generally low, ranging from 0% (pigs 10 and 12) to 15.1% for pig 8.

6.3 Discussion

6.3.1 Effect of EHT cell alignment, conductivity and attachment on BiV-EHT electrophysiology

The l-BiV-EHT model was employed in C6G1-2 simulations to evaluate the variations in terms of AT, APD_{90}, and RTG when EHTs with varying characteristics were used for remuscularization.

In both simulation groups (C6G1-2), the AT variation of the EHT was null or minimal for different hiPSC-CM orientations, EHT conductivities, and degrees of attachment, provided that minimal attachment occurred (see left panel, Figure 6.5a and top panel, Figure 6.5c). This demonstrates that the host myocardium consistently drives the activation of the engrafted EHT, which agrees with the results reported in [11, 76]. Conversely, Fassina et al. [154] previously showed that the ATs in an EHT engrafted to a transmurally infarcted slab of ventricular tissue were highly influenced by the EHT conductivity value. Similarly, we previously showed that ATs were slightly and greatly dependent on the hiPSC-CMs orientation and EHT conductivity, respectively, when the EHT was implanted in a MI slab of tissue (see Section 3.2.3.2). Taken all together, our results suggest that the driving of the EHT activation by the host myocardium is dependent on the combination of the host myocardium substrate and the EHT implantation location, with this depolarization being driven by the myocardium underneath the EHT when realistic endocardial-to-epicardial wave propagation is simulated employing biomimetic BiV electrophysiological models.

Regarding the impact of the EHT design on repolarization, we found that the APD_{90} values were driven by the underlying host myocardium when the EHT was at least minimally attached in both C6G1-2 simulation groups. In the l-BiV-EHT model used in these simulations, the EHT mostly covered BZ and not the healthy zone. Thus, APD_{90} reduction with EHT conductivity when the EHT was unattached was attenuated for minimal EHT attachment due to the higher BZ-to-EHT exerted electrotonic load. On the other hand, EHT APD_{90} reduction with increasing EHT attachment occurs due to a higher electrotonic load exerted in the EHT by the healthy tissue, which drags APD_{90}

in the EHT to lower values. This electrotonic load between the EHT and the underlying (healthy and BZ) myocardium, primarily modulated by the EHT conductivity, was observed numerically in Section 3.2.3.2, as well as in the literature, in computational [154] and experimental [170] studies.

Concerning the arrhythmic risk, the RTG variations were negligible for different hiPSC-CM orientations, while moderate alterations in maximum values were attained for varying EHT degrees of attachment. In the context of different hiPSC-CM orientations, we have shown an RTG reduction when the hiPSC-CMs were aligned parallel to the myocardial propagation in a transmurally infarcted tissue slab (see Section 3.2.3.2). In this line, a variation in the arrhythmic burden for different hiPSC-CM alignments was observed by Yu et al. [11], when the EHT was attached to two different locations of two BiV models with different MI substrates. Thus, the effect of the alignment of hiPSC-CMs on arrhythmicity seems highly dependent on the MI substrate and the EHT location. Moreover, the maximum RTGs, even for the highest EHT conductivity and EHT attachment (28.5 ms/mm), were remarkably above the RTG thresholds experimentally reported to lead to unidirectional blocks (3.2 ms/mm) [168]. Based on these results, an increase in EHT conductivity, associated with enhanced hiPSC-CM maturation and accompanied by a higher EHT attachment to the host myocardium, could be fundamental to minimizing arrhythmogenicity after EHT engraftment.

6.3.2 *In silico* models reproduce experimental porcine-specific arrhythmic dynamics

Our *in silico* simulations reproduced the experimental dynamics observed in OM recordings of Langendorff-perfused LAD porcine hearts, which consistently exhibited VT induction, predominantly sustained VT. This agreement supports the robustness and reliability of the proposed modeling pipeline. In simulations, non-sustained VTs were observed in pigs 8–10, whereas sustained VTs were reproduced in pigs 11–12, aligning with experimental observations where sustained VT was always induced.

The reduced reentry speed observed in simulations compared to experimental rotors (Figure 6.6) likely reflects the use of an average BZ conductivity across models, which could have attenuated local conduction. This averaged conductivity was calibrated against CVs in the five available LAD pigs and subsequently generalized to all LAD and LCx models. Personalization was not feasible for LCx pigs due to a lack of experimental data (see Table 5.1). Similarly, CS distributions were assigned based on spatial benchmarks but lacked

sufficient experimental validation (see Section 5.3.6). Despite these limitations, the AIP simulations qualitatively captured the experimental arrhythmic dynamics, supporting the robustness of the modeling framework.

6.3.3 An *in silico* protocol for post-MI arrhythmia vulnerability testing

Arrhythmia inducibility was assessed with an *in silico* AIP inspired by prior approaches, such as the VARP (Section 2.3.2) [10], but streamlined with fewer pacing sites, reduced S1 trains, and a single S2 stimulus. Since BZ is the key substrate for reentry [15, 49, 206], pacing sites were placed homogeneously around the MI border, as distant pacing tends to elicit similar reentries. Under deterministic modeling, electrophysiological activity stabilized after a few beats, justifying the shorter pacing protocol. With this strategy, the simulations produced extensive reentry patterns closely resembling the experimental ones (see Section 6.2.2).

S2 intervals ranged from 250 to 300 ms, consistent with earlier studies [10, 15,150,151]. However, due to healthy tissue and BZ refractoriness, as defined by the Gaur et al. [16] cellular model and its experimentally derived MI phenotype, short S2 intervals or near-MI pacing often failed to capture, preventing VT induction. Longer S2 delays increased inducibility, and variability in such inducibility across S2 values highlighted the value of selecting the shortest effective S2 and identifying the S2 delay that produces the highest inducibility for post-MI remuscularization analyses (C6G5 and C6G6 simulations). This establishes a robust framework for assessing inducibility with the Gaur et al. [16] model embedded in BiV simulations.

LAD pigs were consistently more arrhythmogenic than LCx pigs, with each presenting at least one sustained VT. This finding aligns with clinical observations of a greater incidence of arrhythmia in LAD infarction compared to LCx [207], likely reflecting the larger infarct size and remodeling observed in LAD cases [35]. Our simulations further showed that a larger BZ extent within the infarcted region was associated with greater arrhythmia vulnerability, consistent with prior canine and human studies [49, 206]. Exceptions likely arise from BiV modeling constraints, which may introduce artificial low-conduction pathways that sustain reentry (e.g., pig 5) or CS architectures that effectively block reentry (e.g., pig 6).

To our knowledge, this is the first computational study to reproduce the experimentally higher VT burden associated with LAD infarction using biophysically detailed and vessel-specific porcine MI models.

6.3.4 CS as a modulator of post-MI arrhythmia susceptibility

This study identifies the CS as a key determinant of post-MI arrhythmia susceptibility. Although the CS has been recognized as a potential modulator of conduction [32, 127], its specific role in post-MI proarrhythmicity remains unexplored. Using anatomically realistic CS distributions (Section 5.1.4.2) [32], we demonstrate that CS can strongly influence arrhythmic dynamics by creating *electrical bypasses* across ventricular regions. These electrical shortcuts may sustain or terminate reentry or alter MI depolarization timing via the described *capacitive effect*.

Our findings align with clinical evidence reporting CS-induced VTs in ischemia, including reentrant bundle branch VT, involving the entire ventricular CS [132], and Purkinje-based intramyocardial VT, primarily involving the left posterior Purkinje fibers [36, 132]. Regarding the latter, Bogun et al. [36] identified a plausible Purkinje involvement in post-MI sustained monomorphic VT based on relatively narrow QRS complexes with left or right bundle branch block morphology that meet the following criteria: concealed entrainment at sites exhibiting Purkinje potentials; VT cycle length variability following changes in intervals between Purkinje potentials; or reproduction of the VT morphology through pacing at a site showing Purkinje potentials during sinus rhythm. Garcia-Bustos et al. [32] further confirmed the anatomical substrate for post-MI CS-derived VTs by showing that PMJs are capable of surviving reperfusion-related ischemia in chronic MI pigs.

Computationally, Berenfeld et al. [130] showed that reentries through Purkinje fibers can generate endo-epicardial breakthroughs that sustain polymorphic VT in a non-ischemic canine CS-BiV model, in line with our observations here. More recently, Sayers et al. [208] showed that MI-induced downregulation of fast-conducting connexins and alterations in ion channel expression in non-regenerative CS of postnatal mice slowed conduction and increased the incidence of arrhythmias in a BiV human model with LAD MI. Our study extends and complements these insights by testing CS effects across multiple ischemic substrates and pacing sites, showing how CS critically shapes reentry inducibility and dynamics.

Accurate CS modeling is, therefore, essential to prevent underestimation or overestimation of arrhythmic risk and to ensure the reliability of next-generation *in silico* arrhythmia assessments.

6.3.5 EHT conductivity has a major impact on arrhythmia vulnerability after MI remuscularization

Our simulations demonstrate that the conductivity of the EHT is a key determinant of arrhythmia susceptibility following MI remuscularization. Across the nine porcine-specific BiV models and the two implantation sites, greater and more biomimetic intercellular coupling consistently reduced or prevented increases in arrhythmia vulnerability. These results are consistent with previous computational studies [11, 76, 154] and our preliminary simulations (Section 6.3.1 and 3.2.3.2), where higher EHT conductivity decreased both the VT burden in realistic ventricular models and the RTGs (a known proarrhythmic marker) in models of transmural MI slabs.

Specifically, Yu et al. [11] similarly reported a reduced VT burden in BiV-MI models when EHT electrical properties approached those of the host ventricular tissue. Fassina et al. [76] found that sustained VTs disappeared when conductivity reached nearly healthy levels, even in immature repolarization phenotypes. Likewise, Section 6.3.1 showed reduced RTGs with increasing EHT conductivity, irrespective of hiPSC-CM alignment or the degree of graft attachment.

Taken together, these findings highlight that a mature EHT with high conductivity consistently mitigates, or at least contains, remuscularization-induced VT burden across diverse conditions involving cell alignment, degrees of graft attachment, infarct substrates, and implantation sites.

6.3.6 MI substrate strongly modulates arrhythmia risk after EHT implantation

Following post-MI remuscularization, arrhythmia inducibility exhibited marked artery occlusion dependence, varying substantially in LAD pigs but remaining more stable in LCx pigs. In LAD pigs, the average IS after EHT implantation resembled pre-engraftment values across both implantation sites. In contrast, LCx pigs showed a clear increase in average IS after EHT implantation, although lateral placement reduced reentry compared to central placement. These results extend prior observations by Yu et al. [11], who demonstrated location-specific VT incidence in two MI models where infarcts were confined to the endocardium or were highly diffuse in the epicardium, consistent with our findings in LAD pigs.

In pigs with highly transmural SZ, EHTs created novel isthmuses with fetal-like electrophysiology that, in some pigs (e.g., 4-6), enabled base-to-apex

conduction and promoted unidirectional block and reentry. These proarrhythmic effects diminished with increased EHT conductivity, in agreement with previous studies [148]. In some cases, preexisting reentry blocked the EHT conduction path, invalidating any conductivity effects. In pigs where the EHT primarily covered conducting tissue (e.g., 7-12), no additional unidirectional blocks formed, as arrhythmicity was unaffected by conductivity changes. This suggests that inducibility after remuscularization in pigs without transmural SZ depends mainly on EHT-MI spatial relationships and the immature EHT phenotype.

Consistent with Campos et al. [148], we find that low conducting isthmuses are important for the onset of reentry, while reduced conductivity is the main contributor to its sustainability. This mechanism explains why post-remuscularization VT burden in weakly transmural infarcts varies strongly with EHT location at low EHT conductivity but is reduced or contained when EHT conductivity is close to biomimetic values [11]. In contrast, highly transmural infarcts can generate new VTs when covered by the EHT, as shown by Fassina et al. [76] and here. These VTs are suppressed when conductivity is increased.

Overall, our results indicate that the infarct substrate is a primary determinant of VT incidence after remuscularization. For highly transmural SZs, arrhythmicity is reduced when the EHT is implanted laterally to the infarcted region compared to direct implantation over the scar. In contrast, for weakly transmural SZs, VT burden depends on EHT location relative to the infarct, which emphasizes the need for patient-specific digital twins to assess arrhythmic risk and optimize implantation strategies.

6.4 Limitations

Model characteristics: Bishop et al. [202] recently highlighted the need for fine discretizations ($\leqslant$ 200 µm) to avoid spurious conduction blocks in slow-conducting tissue and to ensure the reproducibility of arrhythmia induction. In our models, median edge lengths below this threshold were achieved within the EHT and adjacent BZ, and CVs were tuned to OM data, consistent with these recommendations. Although coarser discretizations have been used successfully in prior studies [184, 203, 204], our approach increases robustness.

Low-resolution CMRs [15] and segmentation uncertainties were mitigated using advanced algorithms and extensive experimental validation (see Chapters 4 and 5). This supports our finding that LCx pigs displayed more transmural SZs than LAD pigs, likely reflecting both differences in MI induction proto-

col (proximal LCx versus mid-LAD balloon inflation) and higher out-of-plane LGE-CMR resolution in LAD cases, which allowed thinner BZ layers to be identified (see Chapter 5).

Accurate CS representation is confirmed to be essential for reducing variability in arrhythmia inducibility. Accurate personalization is still limited, as detailed CS anatomy can only be obtained from *ex vivo* histology. Endocardial mapping and non-invasive extracellular potential matching remain the most viable methods for CS modeling validation [50, 126, 127]. Future work should incorporate post-MI region-specific CS conduction delays, as recently shown to be highly arrhythmogenic by Sayers et al. [208].

Intrinsic heterogeneities of EHTs: Several intrinsic factors [3, 68] may influence outcomes but are simplified here:

- Multicellular composition: Future models could incorporate stromal cardiac cells with fetal-like phenotypes.
- Variability of hiPSC-CMs: Experimental variability in hiPSC-CMs has motivated the development of multiple computational ionic models, resulting in differences in automaticity and susceptibility to arrhythmia [12, 111, 112]. Recently, Riebel et al. [78] computationally demonstrated that the injection of heterogeneous hiPSC-CM (ventricular, atrial, nodal) facilitated the generation of post-treatment ectopic activity in a BiV model of LAD MI. Extending our work to incorporate such variability could reveal pig-specific differences in VT burden.
- Cell alignment: hiPSC-CMs often aggregate in islands or exhibit scaffold-driven orientation [6, 74]. Here, a random distribution was assumed for hiPSC-CMs in the EHT in most of the simulations (C6G2-6 simulations), consistent with prior slab and BiV simulations showing a limited arrhythmic impact of alignment (see Sections 3.2.3.2, 6.2.1.1, and 6.3.1) [11].

Extrinsic factors post-implantation of the EHT: External influences also affect remuscularization outcomes [6, 11, 74, 147].

- Degree of attachment: Incomplete physical engraftment may arise from air bubbles in poorly glued constructs, scar tissue from stitching, immune EHT isolation in xenotransplantation approaches, or shear stress during cardiac contraction-relaxation cycles [6, 11]. Simulations suggest that homogeneous partial engraftment increases the VT risk, whereas the risk

is comparable for partial and complete engraftment when the attachment is heterogeneous [11, 76]. Consistently, our computational study found only slight electrophysiological variations across degrees of heterogeneous engraftment, provided minimal electrical contact existed (Sections 6.2.1.2 and 6.3.1). Therefore, we focused on complete engraftment.

- EHT-induced ectopy: Experimental studies report a high ectopic burden after cellular injection [7, 11, 147]. Computational work indicates that ectopy arises under incomplete engraftment or extreme hiPSC-CM heterogeneity, but not under complete engraftment, and that sustained VT further requires a bradycardic beat and suppression of CS retrograde conduction [77, 78]. Our results throughout this thesis, along with those of others [11, 76, 154], found no ectopic-driven VT, consistent with the high electrotonic load of the host myocardium suppressing spontaneous activity and the intrinsically slower beating rate of the EHT, ensuring that it is paced by the host myocardium (Sections 6.3.1 and 3.2.3.2). Recent EHT-related preclinical and clinical studies [7, 24] reporting no arrhythmogenicity support this; however, confirmation of stable EHT–myocardium coupling and high cell survival is still needed. Future studies could explore bradycardic rhythms and heterogeneous grafts to model conditions more favorable to ectopy.

- Transitional phase: We, like others [11, 76], focused on baseline MI and post-EHT implantation endpoints. However, dynamic processes during graft integration, including changes in EHT-myocardium coupling and cell viability, may strongly influence arrhythmogenicity. Future simulations could incorporate time-varying conductivity and hiPSC-CM electrophysiology to capture this transitional phase.

Outlook: We developed a realistic EHT-myocardium modeling and simulation framework by integrating an updated hiPSC-CM model with a diverse set of infarct geometries. This approach captures key structural and electrophysiological determinants of arrhythmicity and can be extended as new experimental data emerge. Ultimately, it provides a robust platform to guide case-specific risk assessment and the optimization of post-MI remuscularization strategies.

6.5 Conclusion

We developed a novel computational pipeline to generate porcine BiV digital twins of infarcted hearts before and after EHT remuscularization, aimed at analyzing VT incidence following therapy. Using one BiV model, negligible and moderate effects on arrhythmogenicity were observed for hiPSC-CM alignment and EHT attachment, respectively. Simulated arrhythmic patterns closely matched experimental data. On our cohort of nine personalized BiV models, larger LAD infarcts were linked to higher arrhythmogenicity, and CS representation critically influenced post-MI outcomes. Following EHT implantation, VT burden increased in highly transmural scars, particularly when engraftment occurred directly over the infarct; however, it decreased when EHTs were implanted laterally. In less transmural scars, the relationship between VT inducibility and EHT location was highly variable, highlighting digital twins as a tool for personalized risk prediction. Finally, biomimetic EHT conductivity emerged as the key factor in mitigating VT burden after remuscularization therapy.

CHAPTER 7

FAST AND PORTABLE SIMULATION OF CARDIAC ELECTROPHYSIOLOGY

7.1 ***ELECTRA* extension**

7.2 ***Cocoro*: implementation and validation**

7.2.1 Implementation

7.2.2 Accuracy and performance evaluation

7.2.3 Results and discussion

7.3 **Conclusion**

The aim of this chapter is twofold. First, it outlines the extensions incorporated into the *ELECTRA* software during this thesis to support the simulations presented herein. As discussed in Section 2.4, increased model complexity compromises the simplicity and portability of modern solvers aimed at simulating those models, thereby hindering broader usability. To address this, an increasingly popular approach is the development of web-based applications that offer cross-platform compatibility and user-friendly abstraction [22, 23, 157]. Building on this idea, this chapter introduces *Cocoro*, a proof-of-concept WebGPU-based implementation enabling fast, portable, and interactive computation and rendering of cardiac electrophysiological simulations. The following sections describe its implementation and evaluation in terms of accuracy, performance, and clinical applicability.

7.1 *ELECTRA* extension

All the simulations in this thesis were conducted using the *ELECTRA* solver, whose numerical schemes and general functionality were introduced in Section 1.6.3.6. Although originally developed in previous work [115], the software was further validated and enhanced as part of this thesis. The main developments include:

- *Extension and refinement of cellular model implementations*, involving the Paci2020 [113], O'Hara et al. [51], Gaur et al. [16], Ten-Tusscher et al. [52], and Stewart et al. [108] cellular models.
- *Performance and memory-related improvements*, including binary-format output, dynamic data saving during simulations, and efficient management of cellular model variables.
- *Additional features*, such as simulation checkpointing, cellular-level standalone simulations for pre-pacing to be used for tissue simulations, streamlined build processes, Docker-based container generation, and debugging and reporting mechanisms.

As a result, *ELECTRA* has been released as open-source software under the GNU General Public License v3.0 (`https://github.com/lino202/ELECTRA`), facilitating use, reproducibility, and further development by the research community.

7.2 *Cocoro*: implementation and validation

Modern GPUs have demonstrated substantial performance advantages over central processing unit-based solvers for *in silico* cardiac electrophysiology simulations [157, 209], due to their intrinsic parallel processing capabilities. To exploit this, we implemented *Cocoro*, using webGPU, a recently implemented web standard that enables GPU-based computation and rendering, providing high-performance acceleration while facilitating broad adoption through web-based accessibility.

Unlike its predecessor WebGL, WebGPU not only supports GPU-based rendering but also natively allows GPU-based computations. In brief, multiple GPU threads execute parallel workloads organized into workgroups, whose number and size determine the total computational load (amount of threads) invoked by a WebGPU-based application.

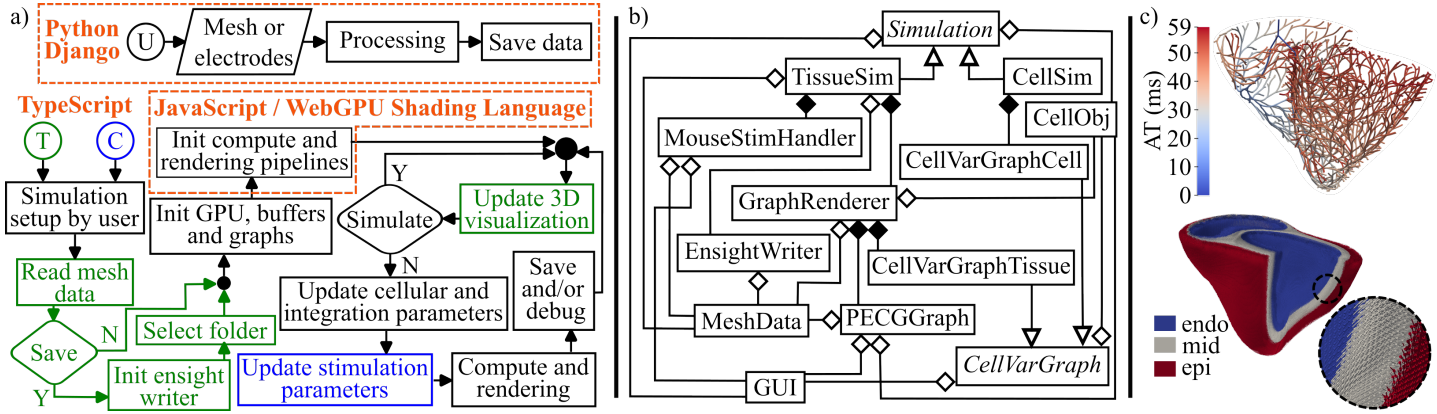


Figure 7.1: *Cocoro* implementation. a- Flux diagram. U: upload, T: tissue and C: cellular web pages b- Conceptual class diagram. c- CS activation (top) and BiV fiber field (bottom).

7.2.1 Implementation

Figure 7.1a outlines the system workflow, and Figure 7.1b illustrates the class relations in our object-oriented design. The implementation minimizes GPU calls and performs both computation and rendering entirely on the GPU. The full source code is available at `https://github.com/lino202/Cocoro`.

A *Django* server hosts three primary interfaces: upload, tissue, and cellular web pages. The upload page allows users to upload meshes defining electrode positions (for pECG computation), simulation domains, stimulation nodes, and fiber orientations. Once saved and processed, these data become available in the tissue simulation interface, where users can select cellular models, whether or not to visualize pECGs and cellular data, apply interactive stimulation, and save or debug results.

Internally, a *TissueSim* object is created and, depending on the user selection, it may instantiate the *MouseStimHandler* class for interactive stimulation and the *EnSightWriter* class for saving results in the EnSight Gold format with the help of web workers. When graph plotting is enabled, a *GraphRenderer* instance handles *PECGGraph* for computation and rendering of pECG and *CellVarGraphTissue* for plotting state variables at a specified location. Cellular-level simulations are handled via the cellular web page, with computation managed by the *CellSim* class and state variable rendering managed by the *CellVarGraphCell* class. In addition, *MeshData* and *CellObj* objects store mesh and cellular information, respectively.

Once a *Simulation* object initiates the GPU, supplementary graph data, and communication buffers, the main simulation loop begins. Each iteration consists of one rendering step and $plot_{interval}/\Delta t$ computation steps, where Δt denotes the time integration step and $plot_{interval}$ represents the user-defined rendering interval. As a result, the simulation update rate is limited by both the computational workload and the display's refresh rate. Time integration is performed using the Rush-Larsen method and an explicit Euler method for gating variables and for all the other state variables, respectively (see Section 1.6.3.2). Diffusion is computed via a central FDM scheme with zero-flux boundary conditions, enforced through ghost nodes at the domain edges (see Section 1.6.3.3), following previous approaches [101, 157].

7.2.1.1 Data races

In parallel computing, concurrent read and write operations can lead to data races unless properly synchronized. WebGPU provides thread-safe atomic op-

erations and synchronization barriers. However, atomic operations are limited to integer operations, and synchronization barriers are thread-safe only within individual workgroups, restricting synchronization when floating-point operations and large meshes are used.

In *Cocoro*, potential data races may occur during computation of spatial derivatives, data shifting for graph updates, pECG calculation, and interactive stimulation. In the first two cases, data races are prevented by using a copy buffer of the array subject to read-write operations. Specifically, the copy is read while the original is written, after which the copy is updated accordingly.

As in [98], the pECG is derived from the extracellular potential: $\phi(\boldsymbol{e}) = \sum_{i=1}^{N} \phi_i(\boldsymbol{e})$, where $\boldsymbol{e}$ is the position of the electrode, $\phi_i(\boldsymbol{e})$ is the node-wise contribution, and N is the number of nodes. Consequently, a thread-safe calculation of $\phi_i(\boldsymbol{e})$ and its subsequent summation is required, since N typically exceeds the maximum synchronizable workgroup size.

To address this, we implemented the reduction algorithm shown in Algorithm 1, where Id_l, Id_{wg} and Id_g correspond to the local, workgroup, and global thread indices, respectively. Briefly, the array $\boldsymbol{a}$ contains N values of $\phi_i(\boldsymbol{e})$. For $Id_{wg} = 0$, a workgroup-level array D_{wg} is loaded with the first workgroup-size elements of $\boldsymbol{a}$. An element-wise sum F is then performed between the first and second halves of $\boldsymbol{a}$, storing the results in the first half. After the reduction, $D_{wg}[0]$ holds the sum of the first workgroup-size elements of $\boldsymbol{a}$, which is written to the element Id_{wg} of the reduced array $\boldsymbol{a}_r$. Thus, $\boldsymbol{a}_r$ contains N_{wg} partial sums, where N_{wg} is the number of dispatched workgroups when the maximum workgroup size is used. Since $N_{wg} << N$, the total sum can be obtained with a simple loop or by applying further reductions until $N_{wg} = 1$.

During interactive stimulation, the same reduction scheme is used, but with F replaced by a minimum operation to compute the shortest distance between mesh elements and a click-defined ray to set the stimulation point.

7.2.2 Accuracy and performance evaluation

To evaluate *Cocoro*, an *ex vivo* DW-CMR of a porcine heart was used to reconstruct the BiV geometry at two resolutions (Figure 7.1c). The high resolution BiV, h-BiV, and the low resolution BiV, l-BiV, hexahedral meshes consisted of 1 334 286 nodes (400 µm edge length) and 387 539 nodes (600 µm edge length), respectively. The standard RBM-defined fiber field and the species-specific CS were generated as in Chapter 5. Electrical propagation was simulated by numerically integrating the monodomain model. BiV nodes within 1 mm of

Algorithm 1 Thread-safe workgroup-wise array reduction

```
1: procedure ReduceArray(a, a_r, workgroupsize)
2:     D_wg[Id_l] ← a[Id_g]
3:     workgroupBarrier()                    ▷ wait all workgroup threads
4:     for (cs ← workgroupsize, cs > 0, cs/2) do
5:         if Id_l < cs then
6:             D_wg[Id_l] ← F(D_wg[Id_l], D_wg[Id_l + cs])
7:         workgroupBarrier()                ▷ wait all workgroup threads
8:     if Id_l == 0 then
9:         a_r[Id_wg] ← D_wg[0]
```

the CS endpoints (PMJs) were stimulated using ATs derived from a CS simulation run with the simulator *openCARP*. Stimuli of 80-µA/cm^2 magnitude, 1-ms duration, and 1000-ms period were applied. The Gaur et al. [16] cellular model was employed in the entire BiV domain, considering both isotropic and anisotropic conductivity profiles. The conductivity along fibers was set at 0.12 S/m and its transverse-to-longitudinal ratio was set at 1 and 0.3 for the isotropic and anisotropic cases, respectively.

First, 3-s simulations were run using the h-BiV model for both isotropic and anisotropic cases. The values of AT and APD_{90} were calculated from the last beat, as in Section 3.1.2.6, and compared with those obtained using *openCARP* [23]. Both solvers used an integration time step of 20 µs and equal anisotropic and isotropic profiles. Second, the execution time was measured for 5-s simulations in *Cocoro* when using both h-BiV and l-BiV. Performance was examined using two NVIDIA GPUs (RTX 2070 Super and Titan V) and enabling or disabling the computation and rendering of additional graphical information. Finally, clinical relevance was explored by comparing simulated pECGs with experimental ECGs after low-pass filtering (55 Hz cutoff frequency), with a focus on QRS complexes. The positions of the electrodes were derived from a thoracic magnetic resonance image acquired in an anatomically similar pig and aligned to our h-BiV through a rigid transformation (see Figure 7.2c). Per-lead normalization and peak-based alignment were performed prior to QRS comparison.

7.2.3 Results and discussion

Cocoro and *openCARP* simulation results showed strong agreement in terms of depolarization-repolarization dynamics. As shown in Figures 7.2a and 7.2b,

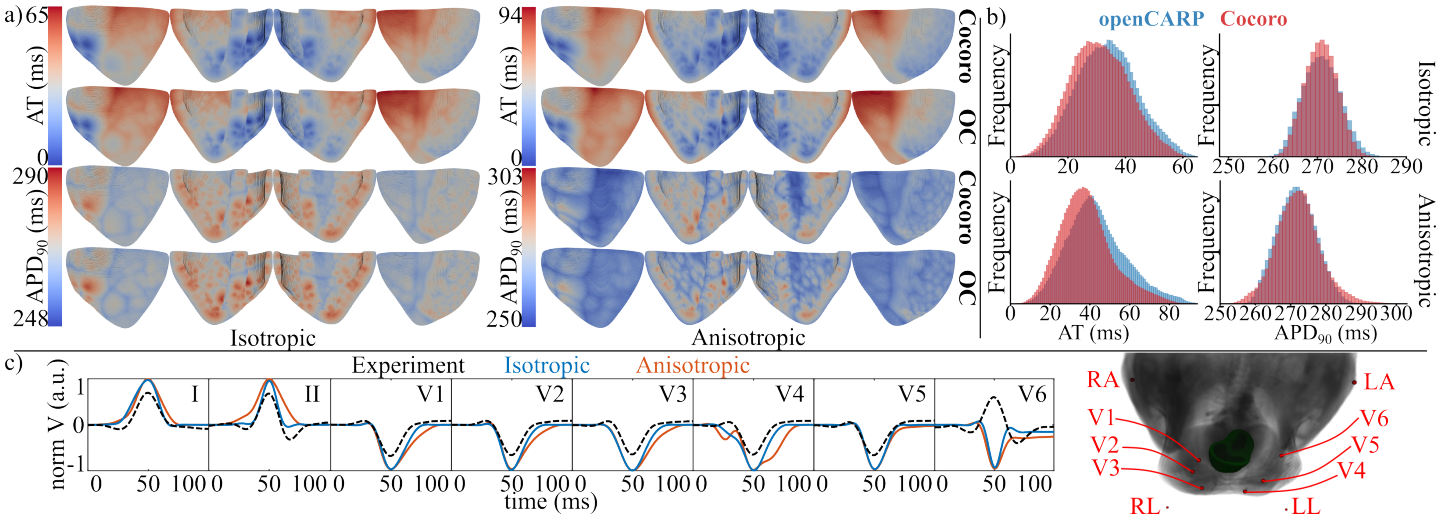


Figure 7.2: Electrophysiological comparison between *Cocoro* and *openCARP* and experimental and simulated QRS complexes. AT and APD_{90} maps (a) and histograms (b) for the isotropic and anisotropic setups. OC: *openCARP*. c- Experimental and simulated QRS complexes (left) and HERP (right).

Cocoro resulted in only slightly faster depolarization and a somewhat more dispersed repolarization pattern, especially for the anisotropic case. Quantitatively, median node-wise AT differences were of 5 ms for the anisotropic case and 2 ms for the isotropic case, with 90^{th} percentiles of 11 and 4 ms. Small deviations likely arise from floating-point precision differences (single and double precision for *Cocoro* and *openCARP*, respectively) and differences in temporal and spatial integration methods, as *openCARP* employed a semi-implicit (forward Euler and Crank-Nicolson) scheme for temporal integration and FEM for spatial integration (Sections 1.6.3.2 and 1.6.3.3). Median APD_{90} differences were negligible, and 90^{th} percentiles were 6 and 2 ms for the anisotropic and isotropic cases, respectively. The slight differences may be due to numerical integration and, specifically, to limitations of the FDM, particularly when imposing zero-flux boundary conditions in the anisotropic cases [101].

In terms of performance, a 5-s simulation on the RTX GPU required 2.92 min for the l-BiV mesh and 9.54 min for the h-BiV mesh, while the Titan GPU required 6.35 and 22.13 min, respectively. These results demonstrate that *Cocoro* efficiently integrates the monodomain model with a biophysically detailed cellular model across different mesh resolutions and hardware architectures.

Execution times remained stable even when computing and rendering additional graphical data, highlighting the efficiency of our approach. This performance gain primarily stems from the reduction algorithm (Section 7.2.1.1), which enabled fast GPU-based pECG calculation while avoiding data races. Comparing solver performance remains inherently difficult due to differences in numerical schemes, software frameworks, target hardware, and development goals. For example, on an MSI Raider GE66 laptop, *openCARP* required 10 hours on 8 central-processing-unit cores for a 3-s simulation with h-BiV, whereas *Cocoro* completed an equivalent 5-s simulation in 9.54 min. Similarly, a recent study [157] reported comparable execution times using a WebGL-based solver. Given the performance advantages of WebGPU over WebGL [210], further optimization opportunities remain in our implementation.

To assess clinical applicability, we compared simulated pECG signals with experimental ECG data. As shown in Figure 7.2c, the *in silico* and experimental QRS complexes aligned closely across most leads, particularly under isotropic conditions. Discrepancies in leads such as V6 likely arise from geometric differences between the simulated and experimental pig data (see Section 7.2.2), consistent with observations in Section 5.3.2. Notably, we obtained biomimetic QRS complexes across most leads without CS personalization, suggesting that individualized tuning could further enhance accuracy. Future work could incorporate cellular-level spatial heterogeneities to enable T-wave com-

putation and detailed ventricular repolarization analysis, as well as extended validation and convergence studies.

Overall, this work enables rapid, accurate cardiac electrophysiology simulations directly in the browser using WebGPU. Unlike existing GPU-based solvers, our implementation provides web-mediated cross-platform usability, fast and clinically relevant pECG calculation, and potential for straightforward integration with WebRTC and WebXR, paving the way for multi-GPU partitioning and immersive applications [22, 157].

7.3 Conclusion

Substantial enhancements were introduced to the *ELECTRA* solver to support high-resolution, long-duration, and complex electrophysiological simulations. Most notably, this chapter presented *Cocoro*, a WebGPU-based platform for fast, portable, and interactive cardiac electrophysiology simulations. Leveraging fully GPU-resident computation and rendering, *Cocoro* achieves high performance and interactivity across diverse GPU architectures. Deployed as a web application, *Cocoro* significantly lowers the technical barriers for conducting advanced simulations without requiring extensive programming expertise, making powerful cardiac modeling tools accessible to a wider research and clinical community.

CHAPTER 8
CONCLUSIONS AND FUTURE WORK

8.1 Main findings
8.2 Major contributions
8.3 Perspectives for future work

This PhD thesis investigated the electrophysiological effects of MI and post-MI epicardial remuscularization therapy using EHTs. A broad range of computational scenarios was analyzed to simulate the influence of EHT scaffold designs both *in vitro* and *in vivo*, either implanted in slabs of transmurally infarcted tissue or epicardially engrafted in personalized swine BiV infarct models. The simulations examined EHTs with varying levels of electrical maturation, hiPSC-CM alignment, implantation sites, and degrees of attachment. To conduct this investigation while circumventing costly and time-consuming clinical trials, a comprehensive framework of porcine digital twins was created from extensive multi-modal datasets, including vessel-specific MI samples.

A novel data-integration pipeline was developed to generate realistic, high-fidelity ventricular models representative of both healthy and MI conditions. To construct these models, structural data derived from CMR were processed using a semiautomatic segmentation pipeline based on DL and topological algorithms, designed to accelerate and improve segmentation accuracy. Moreover, electrophysiological data from OMs, ECGs, and EAM were used to inform and validate the models, particularly regarding the definition of CS architecture, spatial heterogeneities, and MI-induced alterations in cardiac electrical activity. The resulting ventricular models were then coupled with computa-

tional models representing the EHT. Complementing this research, the in-house cardiac solver was expanded and released as open-source software available to the community. In addition, a new fully web-based simulator, *Cocoro*, was introduced. Powered by GPU-resident computation, *Cocoro* enables high-performance, fully interactive electrophysiological simulation and rendering of electrophysiological simulations accessible directly through a web browser. Using all the tools for data processing, computational modeling, and simulation developed in this thesis, a comprehensive and experimentally guided *in silico* analysis was conducted to evaluate whether the therapeutic benefits of EHT are offset by the potential risk of post-implantation arrhythmogenesis.

This chapter summarizes the major findings of the thesis and presents perspectives for future research directions.

8.1 Main findings

Improved 3D CMR segmentation through GAN-based augmentation and topological correction

This work introduced the first comprehensive application of generative adversarial network (GAN)–based synthetic augmentation (SA) and persistent homology (PH)–based topological correction (TC) for 3D CMR segmentation. Applied to multi-vendor, multi-class, and multi-contrast datasets, this approach improved segmentation accuracy and topological consistency, particularly in challenging regions such as the RV apex and infarcted myocardium. In the context of the MYOSAIQ challenge, our segmentation-confidence estimation method achieved top performance, confirming the reliability and interpretability of the proposed DL pipeline.

Porcine ventricular digital twins for electrophysiological simulation

Using a novel porcine cellular model combined with the processing of extensive multimodal experimental data, we generated twelve BiV digital twins, including three healthy hearts and nine vessel-specific post-MI models. Within this framework, we demonstrate that selecting an optimal PMJ radius can effectively mitigate the source-sink mismatch in ventricular activation simulations. We further introduce a method that integrates CS architecture with HERP adjustments, enabling the *in silico* replication of experimentally observed QRS

morphologies. Additionally, by incorporating experimentally derived APD heterogeneities, we reproduced biomimetic T waves and, for the first time, computationally replicated the porcine APDSH by modulating I_{K1} conductance within a swine-based cellular model. Our simulations corroborate experimental findings indicating that the porcine CS lies deeper within the ventricular wall compared to humans and that pigs exhibit smaller APDSH and repolarization gradient in the epicardium-to-endocardium direction.

In post-MI regions, experimental data revealed a twofold reduction in CV, an approximately 40% decrease in anisotropy, and nearly doubled APD. By adjusting the LDC, the transverse-to-longitudinal conductivity ratio, and the I_{K1} conductance accordingly, our simulations successfully reproduced the experimental activation patterns and matched measured AT, CV, and APD_{90} values. While variations in post-MI PMJ location had minimal impact on ECG morphology, MI-induced repolarization alterations were modulated by the activation sequence. Importantly, this experimentally guided approach enabled the replication and detailed characterization of T-wave dynamics as a function of infarct location, underscoring the potential of computational modeling to improve ECG-based clinical evaluation of multi-site MIs.

Scaffold design and arrhythmic risk

We analyzed OM data from *in vitro* EHTs engineered using scaffolds with square and hexagonal pores to build and calibrate corresponding *in silico* EHT models. The experiments revealed faster activation and lower scaffold deformation in square-pore scaffolds compared to hexagonal ones, likely due to the smaller pore size, increased fiber density, enhanced hiPSC-CM alignment, and higher stiffness. From the experimentally derived relation between LDCs and cellular alignment, we formulated a linear polynomial model enabling extrapolation of LDC values for arbitrary pore shapes and sizes. Computational analyses indicated that small, elongated hexagonal pores achieved the fastest conduction and most biomimetic cellular alignment. When implanted into transmurally infarcted tissue, similar trends were observed, although higher conductivity was needed to prevent conduction block and enhance the benefits of improved alignment. Electrophysiological metrics (AT, APD_{90}, and RTG) varied minimally across EHT designs. These findings define key scaffold design criteria for minimizing arrhythmic risk and conduction block following EHT engraftment on infarcted tissue.

Influence of hiPSC-CM alignment and EHT attachment

Using a transmurally infarcted slab model, we show that parallel and homogeneous hiPSC-CM alignment relative to epicardial fibers increases CV and reduces RTGs, lowering arrhythmic susceptibility. These effects are amplified by stronger electrical coupling. In realistic porcine BiV-EHT models, however, hiPSC-CM alignment plays a secondary role, as activation primarily propagates from endocardium to epicardium. Regarding EHT degree of engraftment, minimally attached constructs suppressed spontaneous activity, in line with the low-to-null ectopicity observed in simulations under sinus rhythm. In these cases, activation and repolarization were governed by host myocardium and modulated by EHT conductivity and attachment extent. Notably, higher attachment consistently reduced arrhythmic risk across all maturation levels, underscoring the importance of both structural integration and electrical coupling for safe and effective EHT therapy.

Effect of infarct substrate and EHT placement

Arrhythmia inducibility was systematically assessed using an AIP in nine vessel-specific post-MI BiV swine digital twins. We achieved one-to-one qualitative *in silico* replication of experimentally observed arrhythmogenesis, confirming the predictive capacity of digital twins for individualized risk assessment. Simulations revealed that CS presence strongly influences post-MI arrhythmicity, emphasizing the need for accurate CS representation to avoid misestimation of risk. Following epicardial EHT remuscularization, both monomorphic and polymorphic VTs originated exclusively from reentrant activity rather than ectopic *foci* within the EHTs. Highly transmural, dense infarcts, such as those observed in most of our LCx models, showed elevated arrhythmicity when the graft was implanted directly over the scar, whereas less transmural yet dense infarcts, such as those observed in our LAD models, displayed a highly variable relation between VT inducibility and EHT location. These findings underscore the utility of digital twins for case-specific evaluation of arrhythmic risk and optimization of EHT implantation strategies.

Mature conductivity reduces EHT-derived arrhythmicity

Across arrhythmia inducibility tests, BiV-MI digital twins with highly transmural, dense infarcts exhibited lower VT incidence when implanted EHTs possessed higher, biomimetic conductivity. Arrhythmic risk, quantified by RTGs,

decreased with increasing EHT conductivity across all cellular alignments and attachment levels, for both BiV and tissue slab models. A key outcome of this thesis is that mature EHTs, characterized by elevated intercellular conductivity, consistently mitigate or contain remuscularization-related VT burden across a wide range of conditions, including different hiPSC-CM orientations, attachment levels, infarct substrates, and EHT placement locations, highlighting conductivity as a critical determinant of EHT therapy safety and efficacy.

High-performance web-based simulation

Using a modern web framework, we demonstrated the feasibility of fully interactive cardiac electrophysiology simulations directly in the browser. We introduce *Cocoro*, a WebGPU-based platform performing all computation and rendering on the GPU, enabling high-performance simulations across diverse hardware. By deploying *Cocoro* as a web application, we eliminate the need for specialized programming skills or high-performance computing infrastructure, empowering researchers, clinicians, and students to conduct complex electrophysiological simulations with ease. This work illustrates the potential of web-based technologies to democratize access to advanced computational cardiology tools.

8.2 Major contributions to computational and translational cardiology

This thesis demonstrates the power of integrating tissue engineering, advanced image analysis, personalized digital twin modeling, and high-performance simulation platforms to address key challenges in cardiac research and therapy.

The relevance of the major outcomes of the thesis can be summarized as follows:

- Through extensive simulations of EHTs reproducing *in vitro* conditions and engraftment in tissue slabs, we showed that scaffold microarchitecture and hiPSC-CM alignment critically determine conduction efficiency and arrhythmic vulnerability. Biomimetic conductivity emerged as a key factor for safe electrical integration, providing mechanistic insights into the optimization of EHTs.
- Parallel developments in CMR analysis revealed that GAN-based data augmentation and topology-driven correction substantially improve 3D

DL-based segmentation across heterogeneous, multi-contrast datasets, enabling more robust infarction characterization and reinforcing clinical applicability of automated imaging pipelines.

- At the whole-organ level, we developed and validated *in silico* porcine ventricular models that faithfully reproduce both healthy and post-infarction electrophysiology, including CS-mediated activation and infarct-induced repolarization gradients. This work establishes a reproducible framework for mechanistic ECG interpretation supporting translational investigations of cardiac function and arrhythmogenesis.

- Building upon these foundations, we introduced a pipeline for generating vessel-specific digital twins of MI and EHT remuscularization. These models enable personalized evaluation of VT risk, highlighting the crucial influence of scar transmurality, CS representation, graft placement and mature electrical coupling on arrhythmic outcomes. This frameworks a pathway for individualized therapeutic optimization.

- Finally, with the development of *Cocoro*, a WebGPU-based cardiac electrophysiology simulator, we demonstrated the feasibility of delivering interactive, high-performance, and accessible modeling tools directly through the web. This innovation broadens the reach of computational cardiology, facilitating both research dissemination and clinical translations.

Collectively, these contributions advance the mechanistic understanding of cardiac electrophysiology and arrhythmogenesis, propose actionable strategies for optimizing tissue-engineered therapies, and deliver robust, clinically relevant tools for image analysis and personalized risk assessment. Beyond their immediate applications, these findings underscore the transformative potential of computational and machine learning approaches in cardiology, paving the way for future precision-guided interventions that are safer, more effective, and more widely accessible.

8.3 Perspectives for future work

Enhancing CMR segmentation with GANs and topology correction

The CNN-based segmentation pipeline developed in this work could be further enhanced through the integration of advanced GAN architectures, which

have demonstrated superior capabilities in semantic-to-real image translation tasks. Moreover, anisotropic *in vivo* CMRs could be consistently aligned with the cardiac LAx, while GTLs could be topologically refined to improve structural consistency. These enhancements would support a more rigorous and comprehensive evaluation of the TC methodology.

In addition, combining SA and TC approaches within the nnUNet framework may yield new insights into their complementary effects on state-of-the-art segmentation performance. Regarding uncertainty quantification, the proposed volume-wise estimation of a PDF from voxel-level probabilities warrants further validation across complex CMR datasets to robustly assess its reliability and generalization potential.

Advancing cardiac modeling across scales and conditions

The computational analyses presented here shed light on anatomical and electrophysiological determinants of cardiac electrical function in both healthy and post-infarction conditions. Future work could extend these analyses to larger cohorts and whole-heart simulations enriched with multimodal experimental data, particularly full bicameral and epicardial EAMs and detailed ECGs, to better capture species-specific depolarization patterns across species, including those of the human heart.

An interesting direction would be to investigate the role of the septomarginal trabecula on ventricular depolarization, for instance by examining shifts in the first epicardial breakthrough from the area pretrabecularis of the RV to alternative sites following alterations of this structure. In addition, while CM orientation was shown here to have minimal influence on overall electrophysiology, its potential contribution to post-MI arrhythmicity could be further explored.

Beyond electrophysiological modeling, these frameworks could evolve towards multiphysics simulations, enabling the representation of additional processes such as arrhythmia ablation, defibrillation, blood flow, contractility, and other pathological mechanisms. Such patient-specific digital twins could thus serve as versatile tools for translational research and clinical decision support.

Toward a flexible and scalable simulation ecosystem

Future developments should aim to refine the architecture, broaden the applicability, and optimize the computational efficiency of the proposed modeling

and simulation framework, with emphasis on enhancing flexibility for diverse research and clinical scenarios. In particular, preprocessing and postprocessing workflows could be accelerated through GPU computing or multiprocessing strategies, ideally integrated within an object-oriented design paradigm.

The *Cocoro* platform could be extended to support heterogeneous tissue properties and multiple numerical schemes, including the FEM, adaptive explicit time integration, and implicit solvers, enhancing both accuracy and efficiency while enabling applications on unstructured meshes and multiphysics problems (e.g. cardiac mechanics and fluid dynamics).

Moreover, incorporating modern web protocols could enable multi-GPU work partitioning and immersive applications in augmented or virtual reality environments, facilitating large-scale simulations and interactive exploration. Finally, the development of a standalone version would overcome browser dependencies, improving usability and performance.

Advancing EHT-based cardiac repair: clinical and computational outlooks

We identify several key directions for advancing EHT-based therapies from both clinical and computational standpoints.

From a clinical perspective, the observed reduction in arrhythmic burden following EHT engraftment, compared with direct cell injection therapies, warrants detailed mechanistic investigation. A central challenge lies in establishing the degree of true electrical integration between the EHT and host myocardium, assuming sustained long-term cell graft survival. The predictions formulated in this thesis must therefore be validated through future experimental studies. Any discrepancies that emerge should guide iterative refinement of the computational models.

Notably, both our simulations and the current literature converge on a critical conclusion: electrical maturation, reflected primarily by the conductivity of the EHT, is the dominant factor determining therapeutic success. Strategies aimed at enhancing conductivity, such as upregulating gap junction expression, improving hiPSC-CM structural organization, or employing conductive scaffolds, are thus likely to be pivotal for effective remuscularization.

From a computational perspective, several meaningful extensions can be pursued. The incorporation of hiPSC-derived stromal cell representations or phenotypically diverse hiPSC-CM models would increase the biological realism of EHT representations. Comparative analysis of multiple small-scale EHTs

and a single large EHT, along with the inclusion of a wider range of BiV-MI models, particularly those involving right coronary artery infarctions, could yield novel insights into graft-host interactions. Moreover, whole-heart simulations would enable assessment of how ventricular-scale findings translate to global cardiac dynamics.

Further refinement could involve modeling the transitional implantation phase explicitly, incorporating dynamic modulation of EHT conductivity and cellular electrophysiology to reflect variable coupling and survival over time. In scenarios where experimental data are limited or subject to heterogeneity due to hiPSC-CM variability, stochastic modeling approaches may offer a means to reproduce physiological realistic variability.

Finally, translation to human applications will require integration of emerging human-based datasets and incorporation of uncertainty quantification, thereby strengthening both the interpretability and credibility of model-based predictions, supporting their eventual use in preclinical and clinical decision-making.

APPENDIX

APPENDIX A

MI CHARACTERIZATION AND ARRHYTHMIC RISK IN INFARCTED PORCINE HEARTS BEFORE AND AFTER REMUSCULARIZATION

A.1 Table: arrhythmicity for varying MI locations

A.2 Table: arrhythmicity with and without the conduction system

A.3 Table: arrhythmicity for different EHT locations

A.4 Table: arrhythmicity for different EHT maturation states

A.5 Table: characterization of the MI substrate

A.1 Table: arrhythmicity for varying MI locations

Table A.1: Results of the AIP obtained in the C6G3 simulations, which correspond to the baseline MI-related evaluation. LCx pigs (4-7) are shown at the left table, and LAD pigs (8-12) are shown at the right table. PS: pacing site, NC: no capture, NR: no reentry, nsVT: non-sustained VT, sVT: sustained VT.

Pig	PS	S2 (ms)			
		250	265	280	295
4	4	NC	NR	NR	NR
	5	NC	NC	NC	NR
	1	NC	NR	NR	NR
	11	NC	NC	NC	NC
	10	NC	NC	NR	NR
	13	NC	NC	NR	NR
	17	NC	NR	NR	NR
5	4	NC	NC	nsVT	nsVT
	6	NC	nsVT	nsVT	nsVT
	12	NC	NC	nsVT	nsVT
	11	NC	NC	nsVT	nsVT
	15	NC	NC	NC	NC
	16	NC	nsVT	nsVT	nsVT
	17	NC	nsVT	nsVT	nsVT
6	4	NC	NC	NC	NR
	5	NC	NC	NC	NC
	6	NC	NR	NR	NR
	15	NC	NR	NR	NR
	16	NC	NR	NR	NR
	17	NC	NR	NR	NR
7	4	NC	NC	nsVT	nsVT
	6	NC	NC	NC	nsVT
	15	NC	NC	NC	NC
	16	NC	nsVT	nsVT	nsVT
	17	NC	nsVT	nsVT	nsVT

Pig	PS	S2 (ms)			
		250	265	280	295
8	2	NC	nsVT	nsVT	NR
	3	NC	sVT	NR	NR
	12	NC	NC	nsVT	nsVT
	7	NC	NC	NC	NC
	15	NC	NC	NC	NC
	18	NC	NC	NC	nsVT
9	3	NC	NC	nsVT	NR
	7	NC	NC	nsVT	nsVT
	10	NC	NC	nsVT	sVT
	16	NC	NC	nsVT	nsVT
	18	NC	NC	NC	NC
10	3	NC	NC	nsVT	NR
	8	NC	NC	NC	NC
	10	NC	NC	sVT	sVT
	16	NC	NC	NR	NR
	18	NC	NC	sVT	sVT
11	2	NC	nsVT	nsVT	nsVT
	12	NC	NC	sVT	sVT
	7	NC	NC	sVT	sVT
	9	NC	NC	NC	NC
	17	NC	NC	NC	NC
	18	NC	NC	sVT	nsVT
12	2	NC	NR	NR	NR
	3	NC	NR	NR	NR
	12	NC	NC	NR	sVT
	7	NC	NC	NR	NR
	11	NC	NC	NR	NR
	18	NC	NC	NC	nsVT

A.2 Table: arrhythmicity with and without the conduction system

Table A.2: Results of the AIP obtained in the C6G4 simulations, which correspond to the assessment of the CS presence. LCx pigs (6-7) are shown at the top of the table, and LAD pigs (11-12) are shown at the bottom of the table. PS: pacing site, NC: no capture, NR: no reentry, nsVT: non-sustained VT, sVT: sustained VT. Note that pacing sites which resulted in NC in the C6G3 simulations were excluded (-).

Pig	**PS**	**S2 295** (ms) with CS	**S2 295** (ms) without CS
6	4	NR	NC
	5	NC	-
	6	NR	sVT
	15	NR	NR
	16	NR	NR
	17	NR	NR
7	4	nsVT	nsVT
	6	nsVT	NC
	15	NC	-
	16	nsVT	NR
	17	nsVT	NR
11	2	nsVT	nsVT
	12	sVT	nsVT
	7	sVT	nsVT
	9	NC	-
	17	NC	-
	18	nsVT	nsVT
12	2	NR	nsVT
	3	NR	sVT
	12	sVT	nsVT
	7	NR	nsVT
	11	NR	nsVT
	18	nsVT	nsVT

A.3 Table: arrhythmicity for different EHT locations

Table A.3: Results of the AIP obtained in the C6G5 simulations, which correspond to the evaluation of the EHT location. PS: pacing site, MI: baseline pre-EHT, L1: EHT central, on top of MI, L2: EHT lateral, on top of the MI, NC: no capture, NR: no reentry, nsVT: non-sustained VT, sVT: sustained VT. Note that a low EHT conductivity was used, and pacing sites that resulted in NC in the C6G3 simulations were excluded (-).

Pig	PS	S2 295 (ms) MI	L1	L2
4	4	NR	nsVT	NR
	5	NR	nsVT	nsVT
	1	NR	nsVT	nsVT
	11	NC	-	-
	10	NR	nsVT	nsVT
	13	NR	nsVT	NR
	17	NR	nsVT	NR
5	4	nsVT	nsVT	nsVT
	6	nsVT	nsVT	nsVT
	12	nsVT	nsVT	nsVT
	11	nsVT	nsVT	nsVT
	15	NC	-	-
	16	nsVT	nsVT	nsVT
	17	nsVT	nsVT	nsVT
6	4	NR	sVT	sVT
	5	NC	-	-
	6	NR	sVT	nsVT
	15	NR	sVT	sVT
	16	NR	sVT	nsVT
	17	NR	sVT	nsVT
7	4	nsVT	nsVT	nsVT
	6	nsVT	nsVT	nsVT
	15	NC	-	-
	16	nsVT	nsVT	nsVT
	17	nsVT	nsVT	nsVT
8	2	NR	nsVT	nsVT
	3	NR	NR	nsVT
	12	nsVT	nsVT	nsVT
	7	NC	-	-
	15	NC	-	-
	18	nsVT	nsVT	nsVT
9	3	NR	NR	NR
	7	nsVT	nsVT	nsVT
	10	sVT	nsVT	sVT
	16	nsVT	nsVT	nsVT
	18	NC	-	-
10	3	NR	NR	NR
	8	NC	-	-
	10	sVT	sVT	sVT
	16	NR	NR	NR
	18	sVT	nsVT	sVT
11	2	nsVT	sVT	nsVT
	12	sVT	sVT	sVT
	7	sVT	sVT	sVT
	9	NC	-	-
	17	NC	-	-
	18	nsVT	nsVT	nsVT
12	2	NR	NR	NR
	3	NR	NR	NR
	12	sVT	nsVT	NR
	7	NR	NR	nsVT
	11	NR	NR	NR
	18	nsVT	nsVT	nsVT

A.4 Table: arrhythmicity for different EHT maturation states

Table A.4: Results of the AIP obtained in the C6G6 simulations, which correspond to the assessment of the remuscularization with different EHT maturation states, when the EHT was implanted centrally (L1, left) and laterally (L2, right) on top of the MI. PS: pacing site, NR: no reentry, nsVT: non-sustained VT, sVT: sustained VT, C10/90: EHT with a conductivity equal to the 10/90% of the value found in the healthy tissue.

Pig	PS	S2 295 (ms) C10	S2 295 (ms) C90
4	1	nsVT	NR
5	6	nsVT	nsVT
6	15	sVT	nsVT
7	17	nsVT	nsVT
8	2	nsVT	nsVT
9	10	nsVT	nsVT
10	10	sVT	sVT
11	2	sVT	sVT
12	12	nsVT	nsVT

Pig	PS	S2 295 (ms) C10	S2 295 (ms) C90
4	1	nsVT	NR
5	6	nsVT	nsVT
6	15	sVT	nsVT
7	17	nsVT	nsVT
8	2	nsVT	nsVT
9	10	sVT	sVT
10	10	sVT	sVT
11	2	nsVT	nsVT
12	12	NR	NR

A.5 Table: characterization of the MI substrate

Table A.5: Characterization of the MI substrate. At the left, the volumetric ratios between the MI and the BiV, as well as, between the BZ and the MI are presented. At the right, the epicardial surface ratio of the SZ with whole MI is presented.

Pig	MI/BiV (%)	BZ/MI (%)
4	8.76	19.97
5	8.04	20.8
6	10.55	32.05
7	13.99	45.52
8	30.20	20.7
9	27.14	32.55
10	16.61	41.6
11	20.76	46.55
12	13.42	36.2

Pig	SZ/MI (%)
4	48.64
5	42.93
6	47.3
7	3.85
8	15.14
9	0.53
10	0
11	6.59
12	0

BIBLIOGRAPHY

[1] A. Timmis *et al.*, "European Society of Cardiology: the 2023 Atlas of Cardiovascular Disease Statistics," *European Heart Journal*, vol. 45, pp. 4019–4062, 2024.

[2] S. Frantz, M. J. Hundertmark, J. Schulz-Menger, F. M. Bengel, and J. Bauersachs, "Left Ventricular Remodelling Post-Myocardial Infarction: Pathophysiology, Imaging, and Novel Therapies," *European Heart Journal*, vol. 43, pp. 2549–2561, 2022.

[3] Y. Zhao, N. T. Feric, N. Thavandiran, S. S. Nunes, and M. Radisic, "The Role of Tissue Engineering and Biomaterials in Cardiac Regenerative Medicine," *Canadian Journal of Cardiology*, vol. 30, pp. 1307–1322, 2014.

[4] J. Leor, Y. Amsalem, and S. Cohen, "Cells, Scaffolds, and Molecules for Myocardial Tissue Engineering," *Pharmacology & Therapeutics*, vol. 105, pp. 151–163, 2005.

[5] M. A. Awad, A. Shah, and B. P. Griffith, "Current Status and Outcomes in Heart Transplantation: A Narrative Review," *Reviews in Cardiovascular Medicine*, vol. 23, p. 11, 2022.

[6] O. Iglesias-García *et al.*, "Biologically-Inspired Melt Electrowriting for the Generation of Highly Biomimetic Functional Myocardium," *Advanced Functional Materials*, vol. 35, p. 2420106, 2025.

[7] A.-F. Jebran *et al.*, "Engineered Heart Muscle Allografts for Heart Repair in Primates and Humans," *Nature*, vol. 639, pp. 503–511, 2025.

[8] K. Ronaldson-Bouchard *et al.*, "Advanced Maturation of Human Cardiac Tissue Grown from Pluripotent Stem Cells," *Nature*, vol. 556, pp. 239–243, 2018.

[9] A. Loewe, P. J. Hunter, and P. Kohl, "Computational Modelling of Biological Systems Now and Then: Revisiting Tools and Visions from the Beginning of the Century," *Philosophical Transactions of the Royal Society A: Mathematical, Physical and Engineering Sciences*, vol. 383, p. 20230384, 2025.

[10] H. J. Arevalo *et al.*, "Arrhythmia Risk Stratification of Patients After Myocardial Infarction Using Personalized Heart Models," *Nature Communications*, vol. 7, p. 11437, 2016.

[11] J. K. Yu *et al.*, "Assessment of Arrhythmia Mechanism and Burden of the Infarcted Ventricles Following Remuscularization with Pluripotent Stem Cell-Derived Cardiomyocyte Patches Using Patient-Derived Models," *Cardiovascular Research*, vol. 118, pp. 1247–1261, 2022.

[12] M. Paci *et al.*, "Comparison of the Simulated Response of Three in Silico Human Stem Cell-Derived Cardiomyocytes Models and in Vitro Data Under 15 Drug Actions," *Frontiers in Pharmacology*, vol. 12, 2021.

[13] N. A. Trayanova, A. Lyon, J. Shade, and J. Heijman, "Computational Modeling of Cardiac Electrophysiology and Arrhythmogenesis: Toward Clinical Translation," *Physiological Reviews*, vol. 104, pp. 1265–1333, 2024.

[14] P. P. Lelovas, N. G. Kostomitsopoulos, and T. T. Xanthos, "A Comparative Anatomic and Physiologic Overview of the Porcine Heart," *Journal of the American Association for Laboratory Animal Science*, vol. 53, pp. 432–438, 2014.

[15] C. Mendonca Costa *et al.*, "Determining Anatomical and Electrophysiological Detail Requirements for Computational Ventricular Models of Porcine Myocardial Infarction," *Computers in Biology and Medicine*, vol. 141, p. 105061, 2022.

[16] N. Gaur *et al.*, "A Computational Model of Pig Ventricular Cardiomyocyte Electrophysiology and Calcium Handling: Translation From Pig to Human Electrophysiology," *PLoS Computational Biology*, vol. 17, p. e1009137, 2021.

[17] J. Duan *et al.*, "Automatic 3D Bi-Ventricular Segmentation of Cardiac Images by a Shape-Refined Multi-Task Deep Learning Approach," *IEEE Transactions on Medical Imaging*, vol. 38, pp. 2151–2164, 2019.

[18] Q. Zheng, H. Delingette, N. Duchateau, and N. Ayache, "3-D Consistent and Robust Segmentation of Cardiac Images by Deep Learning with Spatial Propagation," *IEEE Transactions on Medical Imaging*, vol. 37, pp. 2137–2148, 2018.

[19] N. Byrne, J. R. Clough, I. Valverde, G. Montana, and A. P. King, "A Persistent Homology-Based Topological Loss for CNN-Based Multiclass Segmentation of CMR," *IEEE Transactions on Medical Imaging*, vol. 42, pp. 3–14, 2023.

[20] M. Vázquez *et al.*, "Alya: Multiphysics Engineering Simulation Toward Exascale," *Journal of Computational Science*, vol. 14, pp. 15–27, 2016.

[21] A. Kaboudian, E. M. Cherry, and F. H. Fenton, "Real-Time Interactive Simulations of Large-Scale Systems on Personal Computers and Cell Phones: Toward Patient-Specific Heart Modeling and Other Applications," *Science Advances*, vol. 5, p. eaav6019, 2019.

[22] L. Marins Ramalho De Lima *et al.*, "MonoWeb: Cardiac Electrophysiology Web Simulator," in *Computational Science – ICCS 2024*, vol. 14835, pp. 147–154, Springer Nature Switzerland, 2024.

[23] G. Plank *et al.*, "The openCARP Simulation Environment for Cardiac Electrophysiology," *Computer Methods and Programs in Biomedicine*, vol. 208, p. 106223, 2021.

[24] S. Ensminger *et al.*, "Two-Center Surgical Experience from the First-in-Human BioVAT-HF-DZHK20 Clinical Trial," *The Journal of Heart and Lung Transplantation*, vol. 44, pp. S64–S65, 2025.

[25] J. E. Hall, *Guyton and Hall Textbook of Medical Physiology*. Philadelphia: Elsevier, 12 ed., 2011.

[26] A. R. Liard and M. Latarjet, *Anatomía humana*, vol. 2. Buenos Aires: Editorial Médica Panamericana, 5 ed., 2005.

[27] F. H. Netter, *Atlas of Human Anatomy*. Philadelphia: Elsevier, 8 ed., 2021.

[28] R. Doste *et al.*, "A Rule-Based Method to Model Myocardial Fiber Orientation in Cardiac Biventricular Geometries with Outflow Tracts," *International Journal for Numerical Methods in Biomedical Engineering*, vol. 35, p. e3185, 2019.

[29] K. E. Barrett, S. M. Barman, H. L. Brooks, and J. X.-J. Yuan, *Ganong's Review of Medical Physiology.* New York: McGraw-Hill Medical, 23 ed., 2010.

[30] J. F. R. Palomares, *Cambios Dinámicos del Tamaño del Infarto y la Obstrucción de la Microcirculación tras Administración de Contraste Mediante Cardio-Resonancia Magnética y su Valor Pronóstico en el Remodelado Ventricular Izquierdo.* PhD Thesis, Universitat Autònoma de Barcelona, 2015.

[31] K. C. Wu, "CMR of Microvascular Obstruction and Hemorrhage in Myocardial Infarction," *Journal of Cardiovascular Magnetic Resonance*, vol. 14, p. 72, 2012.

[32] V. Garcia-Bustos *et al.*, "Changes in the Spatial Distribution of the Purkinje Network After Acute Myocardial Infarction in the Pig," *PLoS ONE*, vol. 14, p. e0212096, 2019.

[33] A. J. Connolly and M. J. Bishop, "Computational Representations of Myocardial Infarct Scars and Implications for Arrhythmogenesis," *Clinical Medicine Insights: Cardiology*, vol. 10s1, p. CMC.S39708, 2016.

[34] C. Mendonca Costa, G. Plank, C. A. Rinaldi, S. A. Niederer, and M. J. Bishop, "Modeling the Electrophysiological Properties of the Infarct Border Zone," *Frontiers in Physiology*, vol. 9, p. 356, 2018.

[35] K. Ishikawa *et al.*, "Characterizing Preclinical Models of Ischemic Heart Failure: Differences Between LAD and LCx Infarctions," *American Journal of Physiology-Heart and Circulatory Physiology*, vol. 307, pp. H1478–H1486, 2014.

[36] F. Bogun *et al.*, "Role of Purkinje Fibers in Post-Infarction Ventricular Tachycardia," *Journal of the American College of Cardiology*, vol. 48, pp. 2500–2507, 2006.

[37] M. Izquierdo *et al.*, "Endo-Epicardial Versus Only-Endocardial Ablation as a First Line Strategy for the Treatment of Ventricular Tachycardia

in Patients with Ischemic Heart Disease," *Circulation: Arrhythmia and Electrophysiology*, vol. 8, pp. 882–889, 2015.

[38] R. Romagnuolo *et al.*, "Human Embryonic Stem Cell-Derived Cardiomyocytes Regenerate the Infarcted Pig Heart but Induce Ventricular Tachyarrhythmias," *Stem Cell Reports*, vol. 12, pp. 967–981, 2019.

[39] S. J. Crick, M. N. Sheppard, S. Y. Ho, L. Gebstein, and R. H. Anderson, "Anatomy of the Pig Heart: Comparisons with Normal Human Cardiac Structure," *Journal of Anatomy*, vol. 193, pp. 105–119, 1998.

[40] V. M. Meijborg *et al.*, "Electrocardiographic T Wave and its Relation with Ventricular Repolarization Along Major Anatomical Axes," *Circulation: Arrhythmia and Electrophysiology*, vol. 7, pp. 524–531, 2014.

[41] P. S. Rajiah, C. J. François, and T. Leiner, "Cardiac MRI: State of the Art," *Radiology*, vol. 307, p. e223008, 2023.

[42] S. Pagani, L. Dede', A. Manzoni, and A. Quarteroni, "Data Integration for the Numerical Simulation of Cardiac Electrophysiology," *Pacing and Clinical Electrophysiology*, vol. 44, pp. 726–736, 2021.

[43] D. J. Pennell and R. H. Mohiaddin, "Cardiovascular Magnetic Resonance: Past, Present, and Future," *Circulation: Cardiovascular Imaging*, vol. 17, p. e016523, 2024.

[44] A. Banerjee *et al.*, "A Completely Automated Pipeline for 3D Reconstruction of Human Heart From 2D Cine Magnetic Resonance Slices," *Philosophical Transactions of the Royal Society A: Mathematical, Physical and Engineering Sciences*, vol. 379, p. 20200257, 2021.

[45] V. Baliyan, C. J. Das, R. Sharma, and A. K. Gupta, "Diffusion Weighted Imaging: Technique and Applications," *World Journal of Radiology*, vol. 8, pp. 785–798, 2016.

[46] J. Whitaker *et al.*, "Improved Co-Registration of Ex-Vivo and In-Vivo Cardiovascular Magnetic Resonance Images Using Heart-Specific Flexible 3D Printed Acrylic Scaffold Combined with Non-Rigid Registration," *Journal of Cardiovascular Magnetic Resonance*, vol. 21, p. 62, 2019.

[47] S. Nielles-Vallespin *et al.*, "Cardiac Diffusion: Technique and Practical Applications," *Journal of Magnetic Resonance Imaging*, vol. 52, pp. 348–368, 2020.

[48] A. Barmpoutis and B. C. Vemuri, "A Unified Framework for Estimating Diffusion Tensors of Any Order with Symmetric Positive-Definite Constraints," in *2010 IEEE International Symposium on Biomedical Imaging: From Nano to Macro*, pp. 1385–1388, 2010.

[49] A. Schmidt *et al.*, "Infarct Tissue Heterogeneity by Magnetic Resonance Imaging Identifies Enhanced Cardiac Arrhythmia Susceptibility in Patients with Left Ventricular Dysfunction," *Circulation*, vol. 115, pp. 2006–2014, 2007.

[50] A. Lopez-Perez *et al.*, "Personalized Cardiac Computational Models: From Clinical Data to Simulation of Infarct-Related Ventricular Tachycardia," *Frontiers in Physiology*, vol. 10, p. 580, 2019.

[51] T. O'Hara, L. Virág, A. Varró, and Y. Rudy, "Simulation of the Undiseased Human Cardiac Ventricular Action Potential: Model Formulation and Experimental Validation," *PLoS Computational Biology*, vol. 7, p. e1002061, 2011.

[52] K. H. W. J. ten Tusscher and A. V. Panfilov, "Alternans and Spiral Breakup in a Human Ventricular Tissue Model," *American Journal of Physiology-Heart and Circulatory Physiology*, vol. 291, pp. H1088–H1100, 2006.

[53] I. Martišienė *et al.*, "Optical Mapping of the Pig Heart In Situ Under Artificial Blood Circulation," *Scientific Reports*, vol. 10, p. 8548, 2020.

[54] E. Anter, C. M. Tschabrunn, A. E. Buxton, and M. E. Josephson, "High-Resolution Mapping of Postinfarction Reentrant Ventricular Tachycardia: Electrophysiological Characterization of the Circuit," *Circulation*, vol. 134, pp. 314–327, 2016.

[55] M. Attin and W. T. Clusin, "Basic Concepts of Optical Mapping Techniques in Cardiac Electrophysiology," *Biological Research For Nursing*, vol. 11, pp. 195–207, 2009.

[56] J. I. Laughner, F. S. Ng, M. S. Sulkin, R. M. Arthur, and I. R. Efimov, "Processing and Analysis of Cardiac Optical Mapping Data Obtained with Potentiometric Dyes," *American Journal of Physiology-Heart and Circulatory Physiology*, vol. 303, pp. H753–H765, 2012.

[57] T. J. Herron, P. Lee, and J. Jalife, "Optical Imaging of Voltage and Calcium in Cardiac Cells & Tissues," *Circulation Research*, vol. 110, pp. 609–623, 2012.

[58] L. Gepstein and S. J. Evans, "Electroanatomical Mapping of the Heart: Basic Concepts and Implications for the Treatment of Cardiac Arrhythmias," *Pacing and Clinical Electrophysiology*, vol. 21, pp. 1268–1278, 1998.

[59] D. Nairn *et al.*, "Comparison of Unipolar and Bipolar Voltage Mapping for Localization of Left Atrial Arrhythmogenic Substrate in Patients with Atrial Fibrillation," *Frontiers in Physiology*, vol. 11, p. 575846, 2020.

[60] A. Thajudeen *et al.*, "Correlation of Scar in Cardiac MRI and High-Resolution Contact Mapping of Left Ventricle in a Chronic Infarct Model," *Pacing and Clinical Electrophysiology*, vol. 38, pp. 663–674, 2015.

[61] Y. Tanaka *et al.*, "Utility of High-Resolution Electroanatomic Mapping of the Left Ventricle Using a Multispline Basket Catheter in a Swine Model of Chronic Myocardial Infarction," *Heart Rhythm*, vol. 12, pp. 144–154, 2015.

[62] K. Takahashi and S. Yamanaka, "Induction of Pluripotent Stem Cells from Mouse Embryonic and Adult Fibroblast Cultures by Defined Factors," *Cell*, vol. 126, pp. 663–676, 2006.

[63] K. Takahashi *et al.*, "Induction of Pluripotent Stem Cells from Adult Human Fibroblasts by Defined Factors," *Cell*, vol. 131, pp. 861–872, 2007.

[64] Q. D. Vo *et al.*, "Induced Pluripotent Stem Cells in Cardiomyopathy: Advancing Disease Modeling, Therapeutic Development, and Regenerative Therapy," *International Journal of Molecular Sciences*, vol. 26, p. 4984, 2025.

[65] E. Giacomelli *et al.*, "Human-iPSC-Derived Cardiac Stromal Cells Enhance Maturation in 3D Cardiac Microtissues and Reveal Non-cardiomyocyte Contributions to Heart Disease," *Cell Stem Cell*, vol. 26, pp. 862–879.e11, 2020.

[66] J. Ma *et al.*, "High Purity Human-Induced Pluripotent Stem Cell-Derived Cardiomyocytes: Electrophysiological Properties of Action Potentials and Ionic Currents," *American Journal of Physiology-Heart and Circulatory Physiology*, vol. 301, pp. H2006–H2017, 2011.

[67] S. D. Lundy, W.-Z. Zhu, M. Regnier, and M. A. Laflamme, "Structural and Functional Maturation of Cardiomyocytes Derived from Human Pluripotent Stem Cells," *Stem Cells and Development*, vol. 22, pp. 1991–2002, 2013.

[68] K. Raniga *et al.*, "Strengthening Cardiac Therapy Pipelines Using Human Pluripotent Stem Cell-Derived Cardiomyocytes," *Cell Stem Cell*, vol. 31, pp. 292–311, 2024.

[69] L. Gao *et al.*, "Myocardial Tissue Engineering with Cells Derived From Human-Induced Pluripotent Stem Cells and a Native-Like, High-Resolution, 3-Dimensionally Printed Scaffold," *Circulation Research*, vol. 120, pp. 1318–1325, 2017.

[70] M. Castilho *et al.*, "Melt Electrowriting Allows Tailored Microstructural and Mechanical Design of Scaffolds to Advance Functional Human Myocardial Tissue Formation," *Advanced Functional Materials*, vol. 28, p. 1803151, 2018.

[71] H. Cui *et al.*, "4D Physiologically Adaptable Cardiac Patch: A 4-Month in Vivo Study for the Treatment of Myocardial Infarction," *Science Advances*, vol. 6, p. eabb5067, 2020.

[72] N. Silbernagel *et al.*, "Shaping the Heart: Structural and Functional Maturation of iPSC-Cardiomyocytes in 3D-Micro-Scaffolds," *Biomaterials*, vol. 227, p. 119551, 2020.

[73] M. Kristen *et al.*, "Fiber Scaffold Patterning for Mending Hearts: 3D Organization Bringing the Next Step," *Advanced Healthcare Materials*, vol. 9, p. 1900775, 2020.

[74] P. Montero-Calle *et al.*, "Fabrication of Human Myocardium Using Multidimensional Modelling of Engineered Tissues," *Biofabrication*, vol. 14, p. 045017, 2022.

[75] F. Prosper, M. M. Mazo, *et al.*, "BRAVE: A Cardiac Regenerative Medicine European Iniciative," 2020-2025. url: `https://projectbrave.eu/`.

[76] D. Fassina *et al.*, "Assessing the Arrhythmogenic Risk of Engineered Heart Tissue Patches Through In Silico Application on Infarcted Ventricle Models," *Computers in Biology and Medicine*, vol. 154, p. 106550, 2023.

[77] C. E. Gibbs *et al.*, "Graft-Host Coupling Changes Can Lead to Engraftment Arrhythmia: A Computational Study," *The Journal of Physiology*, vol. 601, pp. 2733–2749, 2023.

[78] L. L. Riebel *et al.*, "In Silico Evaluation of Cell Therapy in Acute versus Chronic Infarction: Role of Automaticity, Heterogeneity and Purkinje in Human," *Scientific Reports*, vol. 14, p. 21584, 2024.

[79] F. Isensee, P. F. Jaeger, S. A. A. Kohl, J. Petersen, and K. H. Maier-Hein, "nnU-Net: A Self-Configuring Method for Deep Learning-Based Biomedical Image Segmentation," *Nature Methods*, vol. 18, pp. 203–211, 2021.

[80] C. Chen *et al.*, "Deep Learning for Cardiac Image Segmentation: A Review," *Frontiers in Cardiovascular Medicine*, vol. 7, p. 25, 2020.

[81] O. Ronneberger, P. Fischer, and T. Brox, "U-Net: Convolutional Networks for Biomedical Image Segmentation," in *Medical Image Computing and Computer-Assisted Intervention – MICCAI 2015*, pp. 234–241, Springer International Publishing, 2015.

[82] V. M. Campello *et al.*, "Multi-Centre, Multi-Vendor and Multi-Disease Cardiac Segmentation: The M&Ms Challenge," *IEEE Transactions on Medical Imaging*, vol. 40, pp. 3543–3554, 2021.

[83] C. Martín-Isla *et al.*, "Deep Learning Segmentation of the Right Ventricle in Cardiac MRI: The M&Ms Challenge," *IEEE Journal of Biomedical and Health Informatics*, vol. 27, pp. 3302–3313, 2023.

[84] B. Olivier *et al.*, "The MYOSAIQ Challenge: Myocardial Segmentation with Automated Infarct Quantification," *Under Review*, vol. n/a, p. n/a, n/a.

[85] I. Goodfellow, Y. Bengio, and A. Courville, *Deep Learning*. MIT Press, 2016.

[86] P. Isola, J.-Y. Zhu, T. Zhou, and A. A. Efros, "Image-to-Image Translation with Conditional Adversarial Networks," in *2017 IEEE Conference on Computer Vision and Pattern Recognition (CVPR)*, pp. 5967–5976, IEEE Computer Society, 2017.

[87] J.-Y. Zhu, T. Park, P. Isola, and A. A. Efros, "Unpaired Image-to-Image Translation Using Cycle-Consistent Adversarial Networks," in *Computer Vision (ICCV), 2017 IEEE International Conference on*, 2017.

[88] B. Lambert, F. Forbes, S. Doyle, H. Dehaene, and M. Dojat, "Trustworthy Clinical AI Solutions: A Unified Review of Uncertainty Quantification in Deep Learning Models for Medical Image Analysis," *Artificial Intelligence in Medicine*, vol. 150, p. 102830, 2024.

[89] S. Kaji, T. Sudo, and K. Ahara, "Cubical Ripser: Software for Computing Persistent Homology of Image and Volume Data," 2020.

[90] I. Goodfellow *et al.*, "Generative Adversarial Nets," in *Advances in Neural Information Processing Systems*, vol. 27, 2014.

[91] N. Otter, M. A. Porter, U. Tillmann, P. Grindrod, and H. A. Harrington, "A Roadmap for the Computation of Persistent Homology," *EPJ Data Science*, vol. 6, p. 17, 2017.

[92] J. R. Clough *et al.*, "A Topological Loss Function for Deep-Learning Based Image Segmentation Using Persistent Homology," *IEEE Transactions on Pattern Analysis and Machine Intelligence*, vol. 44, pp. 8766–8778, 2022.

[93] R. B. Gabrielsson, B. J. Nelson, A. Dwaraknath, and P. Skraba, "A Topology Layer for Machine Learning," in *Proceedings of the Twenty Third International Conference on Artificial Intelligence and Statistics*, pp. 1553–1563, Proceedings of Machine Learning Research, 2020.

[94] H. Edelsbrunner, D. Letscher, and A. Zomorodian, "Topological Persistence and Simplification," in *Proceedings 41st Annual Symposium on Foundations of Computer Science*, pp. 454–463, 2000.

[95] C. Guo, G. Pleiss, Y. Sun, and K. Q. Weinberger, "On Calibration of Modern Neural Networks," in *Proceedings of the 34th International Conference on Machine Learning - Volume 70*, p. 1321–1330, 2017.

[96] M. Viallon, P. Croisille, O. Bernard, N. Duchateau, P. Clarysse, F. Cervenansky, W. Romero, and L. Braz, "Myosaiq 2024," 2024. url: `https://codalab.lisn.upsaclay.fr/competitions/19109`, Accessed: 2025-07-05.

[97] B. Rodriguez *et al.*, "Human-Based Approaches to Pharmacology and Cardiology: An Interdisciplinary and Intersectorial Workshop," *Europace*, vol. 18, pp. 1287–1298, 2016.

[98] A. Mincholé, E. Zacur, R. Ariga, V. Grau, and B. Rodriguez, "MRI-Based Computational Torso/Biventricular Multiscale Models to Investigate the Impact of Anatomical Variability on the ECG QRS Complex," *Frontiers in Physiology*, vol. 10, p. 1103, 2019.

[99] E. Vigmond, R. Weber Dos Santos, A. Prassl, M. Deo, and G. Plank, "Solvers for the Cardiac Bidomain Equations," *Progress in Biophysics and Molecular Biology*, vol. 96, pp. 3–18, 2008.

[100] M. Potse, B. Dubé, J. Richer, A. Vinet, and R. M. Gulrajani, "A Comparison of Monodomain and Bidomain Reaction-Diffusion Models for Action Potential Propagation in the Human Heart," *IEEE Transactions on Biomedical Engineering*, vol. 53, p. 11, 2006.

[101] E. A. Heidenreich, *Algoritmos para Ecuaciones de Reacción Difusión Aplicados a Electrofisiología*. PhD Thesis, Universidad de Zaragoza, 2009.

[102] A. L. Hodgkin and A. F. Huxley, "A Quantitative Description of Membrane Current and Its Application to Conduction and Excitation in Nerve," *The Journal of Physiology*, vol. 117, pp. 500–544, 1952.

[103] B. Amuzescu *et al.*, "Evolution of Mathematical Models of Cardiomyocyte Electrophysiology," *Mathematical Biosciences*, vol. 334, p. 108567, 2021.

[104] Zhilin Qu and A. Garfinkel, "An Advanced Algorithm for Solving Partial Differential Equation in Cardiac Conduction," *IEEE Transactions on Biomedical Engineering*, vol. 46, pp. 1166–1168, 1999.

[105] F. Fenton, "Numerical Simulations of Cardiac Dynamics. What Can We Learn from Simple and Complex Models?," in *Computers in Cardiology 2000*, (Cambridge, MA, USA), pp. 251–254, 2000.

[106] V. Iyer, R. Mazhari, and R. L. Winslow, "A Computational Model of the Human Left-Ventricular Epicardial Myocyte," *Biophysical Journal*, vol. 87, pp. 1507–1525, 2004.

[107] K. H. W. J. Ten Tusscher, D. Noble, P. J. Noble, and A. V. Panfilov, "A Model for Human Ventricular Tissue," *American Journal of Physiology-Heart and Circulatory Physiology*, vol. 286, pp. H1573–H1589, 2004.

[108] P. Stewart *et al.*, "Mathematical Models of the Electrical Action Potential of Purkinje Fibre Cells," *Philosophical Transactions of the Royal Society*

A: Mathematical, Physical and Engineering Sciences, vol. 367, pp. 2225–2255, 2009.

[109] C. Trovato *et al.*, "Human Purkinje In Silico Model Enables Mechanistic Investigations into Automaticity and Pro-Arrhythmic Abnormalities," *Journal of Molecular and Cellular Cardiology*, vol. 142, pp. 24–38, 2020.

[110] M. Paci, J. Hyttinen, K. Aalto-Setälä, and S. Severi, "Computational Models of Ventricular- and Atrial-Like Human Induced Pluripotent Stem Cell Derived Cardiomyocytes," *Annals of Biomedical Engineering*, vol. 41, pp. 2334–2348, 2013.

[111] J. T. Koivumäki *et al.*, "Structural Immaturity of Human iPSC-Derived Cardiomyocytes: In Silico Investigation of Effects on Function and Disease Modeling," *Frontiers in Physiology*, vol. 9, 2018.

[112] D. C. Kernik *et al.*, "A Computational Model of Induced Pluripotent Stem-Cell-Derived Cardiomyocytes Incorporating Experimental Variability from Multiple Data Sources," *The Journal of Physiology*, vol. 597, pp. 4533–4564, 2019.

[113] M. Paci *et al.*, "All-Optical Electrophysiology Refines Populations of In Silico Human iPSC-CMs for Drug Evaluation," *Biophysical Journal*, vol. 118, pp. 2596–2611, 2020.

[114] E. A. Heidenreich, J. M. Ferrero, M. Doblaré, and J. F. Rodríguez, "Adaptive Macro Finite Elements for the Numerical Solution of Monodomain Equations in Cardiac Electrophysiology," *Annals of Biomedical Engineering*, vol. 38, pp. 2331–2345, 2010.

[115] K. A. Mountris and E. Pueyo, "A Dual Adaptive Explicit Time Integration Algorithm for Efficiently Solving the Cardiac Monodomain Equation," *International Journal for Numerical Methods in Biomedical Engineering*, vol. 37, p. e3461, 2021.

[116] S. Rush and H. Larsen, "A Practical Algorithm for Solving Dynamic Membrane Equations," *IEEE Transactions on Biomedical Engineering*, vol. BME-25, pp. 389–392, 1978.

[117] S. C. Chapra and R. P. Canale, *Numerical Methods for Engineers*. McGraw-Hill Education, 8 ed., 2020.

[118] F. Sahli Costabal, D. E. Hurtado, and E. Kuhl, "Generating Purkinje Networks in the Human Heart," *Journal of Biomechanics*, vol. 49, pp. 2455–2465, 2016.

[119] L. E. Perotti, S. Krishnamoorthi, N. P. Borgstrom, D. B. Ennis, and W. S. Klug, "Regional Segmentation of Ventricular Models to Achieve Repolarization Dispersion in Cardiac Electrophysiology Modeling: Repolarization Dispersion Through Ventricular Segmentation," *International Journal for Numerical Methods in Biomedical Engineering*, vol. 31, p. e02718, 2015.

[120] M. S. Spach *et al.*, "The Discontinuous Nature of Propagation in Normal Canine Cardiac Muscle. Evidence for Recurrent Discontinuities of Intracellular Resistance that Affect the Membrane Currents.," *Circulation Research*, vol. 48, pp. 39–54, 1981.

[121] I. J. LeGrice *et al.*, "Laminar Structure of the Heart: Ventricular Myocyte Arrangement and Connective Tissue Architecture in the Dog," *American Journal of Physiology-Heart and Circulatory Physiology*, vol. 269, pp. H571–H582, 1995.

[122] J. D. Bayer, R. C. Blake, G. Plank, and N. A. Trayanova, "A Novel Rule-Based Algorithm for Assigning Myocardial Fiber Orientation to Computational Heart Models," *Annals of Biomedical Engineering*, vol. 40, pp. 2243–2254, 2012.

[123] P. H. M. Bovendeerd, W. Kroon, and T. Delhaas, "Determinants of Left Ventricular Shear Strain," *American Journal of Physiology-Heart and Circulatory Physiology*, vol. 297, pp. H1058–H1068, 2009.

[124] L. Cardone-Noott, A. Bueno-Orovio, A. Mincholé, N. Zemzemi, and B. Rodriguez, "Human Ventricular Activation Sequence and the Simulation of the Electrocardiographic QRS Complex and Its Variability in Healthy and Intraventricular Block Conditions," *EP Europace*, vol. 18, pp. iv4–iv15, 2016.

[125] S. Tawara, K. Suma, and M. Shimada, *The Conduction System of the Mammalian Heart: An Anatomico-Histological Study of the Atrioventricular Bundle and the Purkinje Fibers.* Imperial College Press, 1 ed., 1998.

[126] J. Camps *et al.*, "Digital Twinning of the Human Ventricular Activation Sequence to Clinical 12-Lead ECGs and Magnetic Resonance Imaging

using Realistic Purkinje Networks for in Silico Clinical Trials," *Medical Image Analysis*, vol. 94, p. 103108, 2024.

[127] K. Gillette *et al.*, "Automated Framework for the Inclusion of a His–Purkinje System in Cardiac Digital Twins of Ventricular Electrophysiology," *Annals of Biomedical Engineering*, vol. 49, pp. 3143–3153, 2021.

[128] L. Dux-Santoy, R. Sebastian, J. F. Rodriguez, and J. M. Ferrero, "Modeling the Different Sections of the Cardiac Conduction System to Obtain Realistic Electrocardiograms," in *2013 35th Annual International Conference of the IEEE Engineering in Medicine and Biology Society (EMBC)*, pp. 6846–6849, 2013.

[129] R. Sebastian, V. Zimmerman, D. Romero, D. Sanchez-Quintana, and A. F. Frangi, "Characterization and Modeling of the Peripheral Cardiac Conduction System," *IEEE Transactions on Medical Imaging*, vol. 32, p. 11, 2013.

[130] O. Berenfeld and J. Jalife, "Purkinje-Muscle Reentry as a Mechanism of Polymorphic Ventricular Arrhythmias in a 3-Dimensional Model of the Ventricles," *Circulation Research*, vol. 82, pp. 1063–1077, 1998.

[131] T. Ijiri *et al.*, "A Procedural Method for Modeling the Purkinje Fibers of the Heart," *The Journal of Physiological Sciences*, vol. 58, pp. 481–486, 2008.

[132] Z. Blanck and M. Akhtar, "Ventricular Tachycardia due to Sustained Bundle Branch Reentry: Diagnostic and Therapeutic Considerations," *Clinical Cardiology*, vol. 16, pp. 619–622, 1993.

[133] K. Gima and Y. Rudy, "Ionic Current Basis of Electrocardiographic Waveforms: A Model Study," *Circulation Research*, vol. 90, pp. 889–896, 2002.

[134] R. Azad *et al.*, "Medical Image Segmentation Review: The Success of U-Net," *IEEE Transactions on Pattern Analysis and Machine Intelligence*, vol. 46, pp. 10076–10095, 2024.

[135] Y. Sun, P. Yuan, and Y. Sun, "MM-GAN: 3D MRI Data Augmentation for Medical Image Segmentation via Generative Adversarial Networks," in *2020 IEEE International Conference on Knowledge Graph (ICKG)*, pp. 227–234, 2020.

[136] C. Bowles *et al.*, "GAN Augmentation: Augmenting Training Data using Generative Adversarial Networks," 2018.

[137] M. Frid-Adar *et al.*, "GAN-Based Synthetic Medical Image Augmentation for Increased CNN Performance in Liver Lesion Classification," *Neurocomputing*, vol. 321, pp. 321–331, 2018.

[138] V. Sandfort, K. Yan, P. J. Pickhardt, and R. M. Summers, "Data Augmentation Using Generative Adversarial Networks (CycleGAN) to Improve Generalizability in CT Segmentation Tasks," *Scientific Reports*, vol. 9, p. 16884, 2019.

[139] Y. Al Khalil *et al.*, "Reducing Segmentation Failures in Cardiac MRI via Late Feature Fusion and GAN-Based Augmentation," *Computers in Biology and Medicine*, vol. 161, p. 106973, 2023.

[140] D. R. Lustermans, S. Amirrajab, M. Veta, M. Breeuwer, and C. M. Scannell, "Optimized Automated Cardiac MR Scar Quantification with GAN-Based Data Augmentation," *Computer Methods and Programs in Biomedicine*, vol. 226, p. 107116, 2022.

[141] A. Lalande *et al.*, "Emidec: A Database Usable for the Automatic Evaluation of Myocardial Infarction from Delayed-Enhancement Cardiac MRI," *Data*, vol. 5, p. 89, 2020.

[142] T. Park, M.-Y. Liu, T.-C. Wang, and J.-Y. Zhu, "Semantic Image Synthesis with Spatially-Adaptive Normalization," in *2019 IEEE/CVF Conference on Computer Vision and Pattern Recognition (CVPR)*, pp. 2332–2341, 2019.

[143] O. Oktay *et al.*, "Anatomically Constrained Neural Networks (ACNNs): Application to Cardiac Image Enhancement and Segmentation," *IEEE Transactions on Medical Imaging*, vol. 37, pp. 384–395, 2018.

[144] C. Corbière, N. Thome, A. Bar-Hen, M. Cord, and P. Pérez, "Addressing Failure Prediction by Learning Model Confidence," in *Advances in Neural Information Processing Systems*, vol. 32, 2019.

[145] T. Judge *et al.*, "Crisp - Reliable Uncertainty Estimation for Medical Image Segmentation," in *Medical Image Computing and Computer Assisted Intervention - MICCAI 2022*, pp. 492–502, 2022.

[146] L. Ye *et al.*, "Cardiac Repair in a Porcine Model of Acute Myocardial Infarction with Human Induced Pluripotent Stem Cell-Derived Cardiovascular Cells," *Cell Stem Cell*, vol. 15, pp. 750–761, 2014.

[147] S. Marchiano *et al.*, "Gene Editing to Prevent Ventricular Arrhythmias Associated with Cardiomyocyte Cell Therapy," *Cell Stem Cell*, vol. 30, pp. 396–414.e9, 2023.

[148] F. O. Campos *et al.*, "Factors Promoting Conduction Slowing as Substrates for Block and Reentry in Infarcted Hearts," *Biophysical Journal*, vol. 117, pp. 2361–2374, 2019.

[149] M. D. Cerqueira *et al.*, "Standardized Myocardial Segmentation and Nomenclature for Tomographic Imaging of the Heart," *Circulation*, vol. 105, pp. 539–542, 2002.

[150] F. O. Campos *et al.*, "An Automated Near-Real Time Computational Method for Induction and Treatment of Scar-Related Ventricular Tachycardias," *Medical Image Analysis*, vol. 80, p. 102483, 2022.

[151] A. Prakosa *et al.*, "Personalized Virtual-Heart Technology for Guiding the Ablation of Infarct-Related Ventricular Tachycardia," *Nature Biomedical Engineering*, vol. 2, pp. 732–740, 2018.

[152] J. K. Yu *et al.*, "A Comprehensive, Multiscale Framework for Evaluation of Arrhythmias Arising from Cell Therapy in the Whole Post-Myocardial Infarcted Heart," *Scientific Reports*, vol. 9, p. 9238, 2019.

[153] L. L. Riebel *et al.*, "Modelling and Simulation Reveals Density-Dependent Re-Entry Risk in the Infarcted Ventricles After Stem Cell-Derived Cardiomyocyte Delivery," in *2022 Computing in Cardiology (CinC)*, vol. 49, (Tampere, Finland), pp. 1–4, 2022.

[154] D. Fassina *et al.*, "Modelling the Interaction Between Stem Cells Derived Cardiomyocytes Patches and Host Myocardium to Aid Non-Arrhythmic Engineered Heart Tissue Design," *PLoS Computational Biology*, vol. 18, p. e1010030, 2022.

[155] R. Sachetto Oliveira *et al.*, "Performance Evaluation of GPU Parallelization, Space-Time Adaptive Algorithms, and Their Combination for Simulating Cardiac Electrophysiology," *International Journal for Numerical Methods in Biomedical Engineering*, vol. 34, p. e2913, 2018.

[156] L. A. Berg *et al.*, "MonoAlg3D: Enabling Cardiac Electrophysiology Digital Twins with an Efficient Open Source Scalable Solver on GPU Clusters," *bioRxiv*, 2025.

[157] A. Kaboudian, R. A. Gray, I. Uzelac, E. M. Cherry, and F. H. Fenton, "Fast Interactive Simulations of Cardiac Electrical Activity in Anatomically Accurate Heart Structures by Compressing Sparse Uniform Cartesian Grids," *Computer Methods and Programs in Biomedicine*, vol. 257, p. 108456, 2024.

[158] A. Oliván-Viguera *et al.*, "Minimally Invasive System to Reliably Characterize Ventricular Electrophysiology from Living Donors," *Scientific Reports*, vol. 10, p. 19941, 2020.

[159] M. Pérez-Zabalza *et al.*, "Improved Methods for Processing Optical Mapping Signals From Human Left Ventricular Tissues at Baseline and Following Adrenergic Stimulation," in *2020 Computing in Cardiology (CinC)*, vol. 47, (Rimini, Italy), pp. 1–4, 2020.

[160] S. Pollnow *et al.*, "An Adaptive Spatio-Temporal Gaussian Filter for Processing Cardiac Optical Mapping Data," *Computers in Biology and Medicine*, vol. 102, pp. 267–277, 2018.

[161] O. Brazhkina *et al.*, "Designing a 3D Printing Based Auxetic Cardiac Patch with hiPSC-CMs for Heart Repair," *Journal of Cardiovascular Development and Disease*, vol. 8, p. 172, 2021.

[162] B. Napiwocki *et al.*, "Micropattern Platform Promotes Extracellular Matrix Remodeling by Human PSC-derived Cardiac Fibroblasts and Enhances Contractility of Co-Cultured Cardiomyocytes," *Physiological Reports*, vol. 9, p. e15045, 2021.

[163] X. Lou *et al.*, "Cardiac Muscle Patches Containing Four Types of Cardiac Cells Derived From Human Pluripotent Stem Cells Improve Recovery From Cardiac Injury in Mice," *Cardiovascular Research*, vol. 119, pp. 1062–1076, 2023.

[164] J. Zhang *et al.*, "Functional Cardiac Fibroblasts Derived From Human Pluripotent Stem Cells Via Second Heart Field Progenitors," *Nature Communications*, vol. 10, p. 2238, 2019.

[165] D. Olvera, M. Sohrabi Molina, G. Hendy, and M. G. Monaghan, "Electroconductive Melt Electrowritten Patches Matching the Mechanical

Anisotropy of Human Myocardium," *Advanced Functional Materials*, vol. 30, p. 1909880, 2020.

[166] P. Spector, "Principles of Cardiac Electric Propagation and Their Implications for Re-entrant Arrhythmias," *Circulation: Arrhythmia and Electrophysiology*, vol. 6, pp. 655–661, 2013.

[167] S. A. Thompson *et al.*, "Engraftment of Human Embryonic Stem Cell Derived Cardiomyocytes Improves Conduction in an Arrhythmogenic in Vitro Model," *Journal of Molecular and Cellular Cardiology*, vol. 53, pp. 15–23, 2012.

[168] K. R. Laurita and D. S. Rosenbaum, "Interdependence of Modulated Dispersion and Tissue Structure in the Mechanism of Unidirectional Block," *Circulation Research*, vol. 87, pp. 922–928, 2000.

[169] K. Roshanbinfar *et al.*, "Collagen Hydrogel Containing Polyethylenimine-Gold Nanoparticles for Drug Release and Enhanced Beating Properties of Engineered Cardiac Tissues," *Advanced Healthcare Materials*, vol. 12, p. 2202408, 2023.

[170] M. Zaniboni, A. E. Pollard, L. Yang, and K. W. Spitzer, "Beat-To-Beat Repolarization Variability in Ventricular Myocytes and Its Suppression by Electrical Coupling," *American Journal of Physiology-Heart and Circulatory Physiology*, vol. 278, pp. H677–H687, 2000.

[171] X. Lin, B. R. Cowan, and A. A. Young, "Automated Detection of Left Ventricle in 4D MR Images: Experience from a Large Study," in *Medical Image Computing and Computer-Assisted Intervention – MICCAI 2006*, pp. 728–735, Springer Berlin Heidelberg, 2006.

[172] A. Ammar, O. Bouattane, and M. Youssfi, "Automatic Cardiac Cine MRI Segmentation and Heart Disease Classification," *Computerized Medical Imaging and Graphics*, vol. 88, p. 101864, 2021.

[173] Stanford Cardiovascular MRI Group, "Ex vivo Porcine Heart DT MRI Data," 2020. url: `https://med.stanford.edu/cmrgroup/data/ex_vivo_dt_mri.html`, Accessed: 2025-05-22.

[174] A. Paszke *et al.*, "Pytorch: An Imperative Style, High-Performance Deep Learning Library," in *Advances in Neural Information Processing Systems*, vol. 32, Curran Associates, Inc., 2019.

[175] F. Pérez-García, R. Sparks, and S. Ourselin, "Torchio: A Python Library for Efficient Loading, Preprocessing, Augmentation and Patch-Based Sampling of Medical Images in Deep Learning," *Computer Methods and Programs in Biomedicine*, vol. 208, p. 106236, 2021.

[176] M. J. Cardoso *et al.*, "Monai: An Open-Source Framework for Deep Learning in Healthcare," 2022.

[177] A. Carta-Bergaz *et al.*, "Intrapericardial Cardiosphere-Derived Cells Hinder Epicardial Dense Scar Expansion and Promote Electrical Homogeneity in a Porcine Post-Infarction Model," *Frontiers in Physiology*, vol. 13, 2022.

[178] Á. Arenal *et al.*, "Effects of Cardiac Stem Cell on Postinfarction Arrhythmogenic Substrate," *International Journal of Molecular Sciences*, vol. 23, 2022.

[179] F. Zhang *et al.*, "SlicerDMRI: Diffusion MRI and Tractography Research Software for Brain Cancer Surgery Planning and Visualization," *JCO Clinical Cancer Informatics*, vol. 4, pp. 299–309, 2020.

[180] J. Martinez, R. Almeida, S. Olmos, A. Rocha, and P. Laguna, "A Wavelet-Based ECG Delineator: Evaluation on Standard Databases," *IEEE Transactions on Biomedical Engineering*, vol. 51, pp. 570–581, 2004.

[181] R. Kikinis, S. D. Pieper, and K. G. Vosburgh, *3D Slicer: A Platform for Subject-Specific Image Analysis, Visualization, and Clinical Support*, ch. -, pp. 277–289. Springer New York, 2014.

[182] P. Cignoni *et al.*, "Meshlab: an Open-Source Mesh Processing Tool," in *Eurographics Italian Chapter Conference*, The Eurographics Association, 2008.

[183] H. Si, "TetGen, a Delaunay-Based Quality Tetrahedral Mesh Generator," *ACM Transactions on Mathematical Software*, vol. 41, pp. 1–36, 2015.

[184] E. Sung *et al.*, "Fat Infiltration in the Infarcted Heart as a Paradigm for Ventricular Arrhythmias," *Nature Cardiovascular Research*, vol. 1, pp. 933–945, 2022.

[185] D. Sánchez-Quintana and S. Yen Ho, "Anatomía de los Nodos Cardíacos y del Sistema de Conducción Específico Auriculoventricular," *Revista Española de Cardiología*, vol. 56, pp. 1085–1092, 2003.

[186] D. Durrer *et al.*, "Total Excitation of the Isolated Human Heart," *Circulation*, vol. 41, pp. 899–912, 1970.

[187] J. Pu and P. A. Boyden, "Alterations of Na^+ Currents in Myocytes From Epicardial Border Zone of the Infarcted Heart," *Circulation Research*, vol. 81, pp. 110–119, 1997.

[188] E. Drouin, F. Charpentier, C. Gauthier, K. Laurent, and H. Le Marec, "Electrophysiologic Characteristics of Cells Spanning the Left Ventricular Wall of Human Heart: Evidence for Presence of M Cells," *Journal of the American College of Cardiology*, vol. 26, pp. 185–192, 1995.

[189] E. Pueyo *et al.*, "A Multiscale Investigation of Repolarization Variability and Its Role in Cardiac Arrhythmogenesis," *Biophysical Journal*, vol. 101, pp. 2892–2902, 2011.

[190] A. O. Verkerk *et al.*, "Incorporated Sarcolemmal Fish Oil Fatty Acids Shorten Pig Ventricular Action Potentials," *Cardiovascular Research*, vol. 70, pp. 509–520, 2006.

[191] K. Gillette *et al.*, "A Framework for the Generation of Digital Twins of Cardiac Electrophysiology from Clinical 12-Leads ECGs," *Medical Image Analysis*, vol. 71, p. 102080, 2021.

[192] A. Amsaleg, J. Sánchez, R. Mikut, and A. Loewe, "Characterization of the Pace-and-Drive Capacity of the Human Sinoatrial Node: A 3D In Silico Study," *Biophysical Journal*, vol. 121, pp. 4247–4259, 2022.

[193] C. R. Wyndham *et al.*, "Epicardial Activation of the Intact Human Heart Without Conduction Defect," *Circulation*, vol. 59, pp. 161–168, 1979.

[194] S. Y. Ho, K. P. McCarthy, A. Ansari, P. S. Thomas, and D. Sánchez-Quintana, "Anatomy of the Atrioventricular Node and Atrioventricular Conduction System," *International Journal of Bifurcation and Chaos*, vol. 13, pp. 3665–3674, 2003.

[195] W. Kong *et al.*, "Optical Measurements of Intramural Action Potentials in Isolated Porcine Hearts Using Optrodes," *Heart Rhythm*, vol. 4, pp. 1430–1436, 2007.

[196] T. Opthof *et al.*, "Dispersion in Ventricular Repolarization in the Human, Canine and Porcine Heart," *Progress in Biophysics and Molecular Biology*, vol. 120, pp. 222–235, 2016.

[197] M. J. Bishop *et al.*, "Comparison of Rule-Based and DTMRI-Derived Fibre Architecture in a Whole Rat Ventricular Computational Model," in *Functional Imaging and Modeling of the Heart*, pp. 87–96, 2009.

[198] S. de Jong, T. A. B. van Veen, H. V. M. van Rijen, and J. M. T. de Bakker, "Fibrosis and Cardiac Arrhythmias," *Journal of Cardiovascular Pharmacology*, vol. 57, pp. 630–638, 2011.

[199] S. L. Rutherford, M. L. Trew, G. B. Sands, I. J. LeGrice, and B. H. Smaill, "High-Resolution 3-Dimensional Reconstruction of the Infarct Border Zone: Impact of Structural Remodeling on Electrical Activation," *Circulation Research*, vol. 111, pp. 301–311, 2012.

[200] M. Jiang, C. Cabo, J.-A. Yao, P. A. Boyden, and G.-N. Tseng, "Delayed Rectifier K Currents Have Reduced Amplitudes and Altered Kinetics in Myocytes From Infarcted Canine Ventricle," *Cardiovascular Research*, vol. 48, pp. 34–43, 2000.

[201] O. Berenfeld and J. Jalife, "Purkinje-Muscle Reentry as a Mechanism of Polymorphic Ventricular Arrhythmias in a 3-Dimensional Model of the Ventricles," *Circulation Research*, vol. 82, pp. 1063–1077, 1998.

[202] M. J. Bishop and G. Plank, "Stochastic Virtual Heart Model Predictions," *Nature Cardiovascular Research*, vol. 4, pp. 539–542, 2025.

[203] P. M. Boyle, A. R. Ochs, R. L. Ali, N. Paliwal, and N. A. Trayanova, "Characterizing the Arrhythmogenic Substrate in Personalized Models of Atrial Fibrillation: Sensitivity to Mesh Resolution and Pacing Protocol in AF Models," *EP Europace*, vol. 23, pp. i3–i11, 2021.

[204] E. Sung, A. Prakosa, and N. Trayanova, "Reply to: Stochastic Virtual Heart Model Predictions," *Nature Cardiovascular Research*, vol. 4, pp. 543–546, 2025.

[205] W. Dun, S. Baba, T. Yagi, and P. A. Boyden, "Dynamic Remodeling of K^+ and Ca^{2+} Currents in Cells that Survived in the Epicardial Border Zone of Canine Healed Infarcted Heart," *American Journal of Physiology-Heart and Circulatory Physiology*, vol. 287, pp. H1046–H1054, 2004.

[206] H. Arevalo, G. Plank, P. Helm, H. Halperin, and N. Trayanova, "Tachycardia in Post-Infarction Hearts: Insights from 3D Image-Based Ventricular Models," *PLoS ONE*, vol. 8, p. e68872, 2013.

[207] H.-J. Trappe, P. Lichtlen, H. Klein, P. Wenzlaff, and C.-A. Hartwig, "Natural History of Single Vessel Disease. Risk of Sudden Coronary Death in Relation to Coronary Anatomy and Arrhythmia Profile," *European Heart Journal*, vol. 10, pp. 514–524, 1989.

[208] J. R. Sayers *et al.*, "Cardiac Conduction System Regeneration Prevents Arrhythmias after Myocardial Infarction," *Nature Cardiovascular Research*, vol. 4, pp. 163–179, 2025.

[209] A. Neic *et al.*, "Accelerating Cardiac Bidomain Simulations Using Graphics Processing Units," *IEEE Transactions on Biomedical Engineering*, vol. 59, pp. 2281–2290, 2012.

[210] S. Chickerur, S. Balannavar, P. Hongekar, A. Prerna, and S. Jituri, "WebGL vs. WebGPU: A Performance Analysis for Web 3.0," *Procedia Computer Science*, vol. 233, pp. 919–928, 2024.

LIST OF PUBLICATIONS

Journal Publications

- **R. M. Rosales**, K. A. Mountris, A. Oliván-Viguera, M. Pérez-Zabalza, G. Cedillo-Servin, O. Iglesias-García, A. Hrynevich, M. Castilho, J. Malda, F. Prósper, M. Doblaré, M. M. Mazo, and E. Pueyo, "Experimentally-Guided In Silico Design of Engineered Heart Tissues to Improve Cardiac Electrical Function After Myocardial Infarction", Computers in Biology and Medicine, vol. 171, p. 108044, 2024, doi: 10.1016/j.compbiomed.2024.108044.

- **R. M. Rosales**, M. Doblaré, and E. Pueyo, "3D Segmentation of Multi-Contrast Cardiac Magnetic Resonances With Topological Correction and Synthetic Data Augmentation", Annals of Biomedical Engineering, vol. -, pp. -, 2026, doi: 10.1007/s10439-026-04115-8.

- **R. M. Rosales**, M. Wu, P. Claus, S. Janssens, G. R. Ríos-Muñoz, M. E. Fernández-Santos, P. Martínez-Legazpi, J. Bermejo, A. Flanagan, M. Doblaré, A. Mincholé, and E. Pueyo, "Integrated Multi-Modal Data Analysis for Computational Modeling of Healthy and Location-Dependent Myocardial Infarction Conditions in Porcine Hearts", PLOS Computational Biology, vol. 22, pp. 1-38, 2026, doi: 10.1371/journal.pcbi.1013688.

- **R. M. Rosales**, G. R. Ríos-Muñoz, A. M. Sánchez de la Nava, M. E. Fernández-Santos, J. Bermejo, M. Doblaré, A. Mincholé, and E. Pueyo, "*In Silico* Assessment of Arrhythmic Risk Following the Implantation of Engineered Heart Tissues in Porcine Hearts with Varying Infarct Locations", PLOS Computational Biology, vol. 22, pp. 1-32, 2026, doi:

10.1371/journal.pcbi.1013740.

- P. Montero-Calle, M. Flandes-Iparraguirre, K. Mountris, A. S de la Nava, N. Laita, **R. M. Rosales**, O. Iglesias-García, E. M. de Juan-Pardo, F. Atienza, M. E. Fernández-Santos, E. Peña, M. Doblaré, J. J. Gavira, F. Fernández-Avilés, F. Prósper, E. Pueyo, and M. M. Mazo, "Fabrication of Human Myocardium Using Multidimensional Modelling of Engineered Tissues", Biofabrication, vol. 14, p. 045017, 2022, doi: 10.1088/1758-5090/ac8cb3.

- N. Laita, **R. M. Rosales**, M. Wu, P. Claus, S. Janssens, M. Á. Martínez, M. Doblaré, and E. Peña, "On Modeling the In Vivo Ventricular Passive Mechanical Behavior From In Vitro Experimental Properties in Porcine Hearts", Computers & Structures, vol. 292, p. 107241, 2024, doi: 10.1016/j.compstruc.2023.107241.

- O. Iglesias-García, M. Flandes-Iparraguirre, P. Montero-Calle, **R. M. Rosales**, A. Ullate-Agote, A. Sánchez-Bueno, E. Larequi, I. Anaut-Lusar, N. Laita, A. Oliván-Viguera, E. Iglesias, G. Abizanda, P. San Martín-Úriz, P. Aguirre-Ruiz, X. L. Aranguren, M. García de Yébenes, J. J. Gavira, M. Á. Martínez, E. Peña, M. Doblaré, E. M. de Juan-Pardo, E. Pueyo, F. Prosper, and M. M. Mazo Vega, "Biologically-Inspired Melt Electrowriting for the Generation of Highly Biomimetic Functional Myocardium", Advanced Functional Materials, vol. 35, p. 2420106, 2025, doi: 10.1002/adfm.202420106.

Submitted Publications

- B. Olivier, W. A. Romero R., C. Bouton, C. Goujat, H. Jung Ling, P.-M. Jodoin, F. Guo, C. Sheagren, G. Wright, A. Qayyum, M. Mazher, S. A. Niederer, H. Wang, X. Wu, F. Thaler, G. Plank, M. Urschler, **R. M. Rosales**, E. Pueyo, N. Duchateau, F. Cervenansky, P. Clarysse, L. Belle, N. Mewton, T. Bochaton, M. Viallon, and P. Croisille, "The MYOSAIQ Challenge: Myocardial Segmentation with Automated Infarct Quantification", Submitted - Under Review.

Conference Publications

- **R. M. Rosales**, K. A. Mountris, M. Doblaré, M. M. Mazo, and E. Pueyo, "In Silico Electrophysiological Evaluation of Scaffold Geometries for Cardiac Tissue Engineering", in 2021 Computing in Cardiology (CinC), vol. 48, (Brno, Czech Republic), pp. 1–4, 2021.

- **R. M. Rosales**, K. Mountris, M. Doblaré, M. Mazo, and E. Pueyo, "Evaluación Computacional de la Arquitectura de la Matriz de Cultivo en la Electrofisiología Cardíaca", Jornada de Jóvenes Investigadores del I3A, vol. 9, 2021.

- **R. M. Rosales**, and E. Pueyo, "GAN-Based Data Augmentation and Uncertainty Estimation for Improved Automatic Myocardial Infarction Segmentation", 2025, url: `https://humanheart-project.creatis.insa-lyon.fr/myosaiqResources/2025_proceedings_myosaiq_rosales.pdf`.

- **R. M. Rosales**, K. A. Mountris, M. Doblaré, M. M. Mazo, and E. Pueyo, "Ventricular Conduction System Modeling for Electrophysiological Simulation of the Porcine Heart", in 2022 Computing in Cardiology (CinC), vol. 49, (Tampere, Finland), pp. 1–4, 2022.

- **R. M. Rosales**, K. Mountris, M. Doblaré, M. Mazo, and E. Pueyo, "In Silico Assessment of Arrhythmic Risk in Infarcted Ventricles Engrafted with Engineered Heart Tissues", in 2023 Computing in Cardiology (CinC), vol. 50, (Atlanta, USA), pp. 1–4, 2023.

- **R. M. Rosales**, M. Doblaré, M. M. Mazo Vega, and E. Pueyo, "Design of Engineered Heart Tissues to Minimize Arrhythmic Risk After Implantation in Infarcted Hearts", in 2024 Computing in Cardiology (CinC), vol. 51, (Karlsruhe, Germany), pp. 1–4, 2024.

- **R. M. Rosales**, A. Mincholé, and E. Pueyo, "Cocoro: Fast Simulation of Cardiac Electrophysiology with WebGPU", in 2025 Computing in Cardiology (CinC), vol. 52, (São Paulo, Brazil), pp. 1–4, 2025.

- L. García-Mendívil, M. Pérez, **R. M. Rosales**, J. M. Vallejo-Gil, J. Fañanás-Mastral, M. Vázquez-Sancho, J. A. Bellido-Morales, A. S. Vaca-Núñez, C. Ballester-Cuenca, L. Ordovás, and E. Pueyo, "Physiological Variations in CX43 and Fibrosis Deposition Affect Human Ventricular

Electrophysiology Promoting Arrhythmia", in 2023 Computing in Cardiology (CinC), vol. 50, (Atlanta, USA), pp. 1-4, 2023.

- A. Pérez-Martínez, **R. M. Rosales**, C. Pastor, A. Oliván-Viguera, and E. Pueyo, "Cold Storage of Cardiac Slices Better Preserve the Native Characteristics of Cardiac Tissue than Traditional Culture Methods", 47th EWGCCE Annual meeting of the ESC Working Group on Cardiac Cellular Electrophysiology, (Copenhagen, Dennmark), 2023.

- S. González-Lana, A. Oliván-Viguera, **R. M. Rosales**, A. R. Remacha, L. Ordovás, E. Pueyo, R. Monge, C. Sánchez-Somolinos, J. Ciriza, and I. Ochoa, "Structural and Functional Impact of Co-Culturing iPSC-CM and HCAEC Within Microfluidic Devices Exposed to Mechanical and Electrical Stimuli", European organ-on-chip society Annual Meeting, (Berlin, Germany), 2023.

LIST OF FIGURES

1.1 Anterior exposure of the heart without the pericardial sac. 5
1.2 Internal anatomy of the right and left ventricles. 6
1.3 Sternocostal and diaphragmatic faces of the heart showcasing its vascularization. 8
1.4 Illustration and experimental data of the myocardial fibers arrangement in the heart. 9
1.5 Microstructure of the cardiac muscle. 10
1.6 Actin-tropomyosin-troponin complex and tilting and pulling of the myosin heads on the active sites of the actin filament. 10
1.7 Gap junction structure. 11
1.8 AP phases and relation with contraction. 13
1.9 CS of the heart. 15
1.10 Progression of MI. 17
1.11 Mechanisms generating MVO. 18
1.12 Macroscopic view of MI on LAD and LCx and microscopic image of chronic MI. 19
1.13 Different *in vivo* and *ex vivo* CMRs employed. 21
1.14 Simplified scheme of an OM system. 24
1.15 Bipolar and unipolar electrode positioning of the 12-lead ECG. . 26
1.16 The normal ECG waveform. 26

1.17 Example of a mapping catheter and an EAM-derived AT map of the LV during VT. 28
1.18 Schematic pipeline depicting the generation of hiPSC-CMs and their applications. 30
1.19 Characterization of hiPSC-CMs before and after the seeding onto the scaffold. 32
1.20 Macroscopic and microscopic views of preclinical EHT implantation. 34
1.21 CNN and UNet typical network architectures. 36
1.22 Different approaches for GAN-based SA. 37
1.23 Calculation of PH. 38
1.24 Miscalibrated modern CNNs. 41
1.25 Electrical representation of the bidomain model in 2D. 44
1.26 Electrical circuit model for the plasmatic membrane of the cell. 46
1.27 Spatial discretization of the domain of integration. 54
1.28 RBM-based CM fiber field. 62
1.29 Fractal algorithm for Purkinje tree generation. 64
1.30 Transmural and apico-basal segmentation. 66

3.1 Experimental and *in silico* assessment of the EHT design. 99
3.2 OM processing of *in vitro* EHTs. 101
3.3 EHT pore architectures and fiber alignments. 105
3.4 *In silico* model of an EHT engrafted on a slab of infarcted myocardial tissue. 106
3.5 Linear paths used for computing the mean EHT CV for the individual and on MI slab-engrafted EHT 109
3.6 Experimental and simulated AT maps for square and hexagon pore-shaped scaffolds. 110
3.7 Maximum ATs, overall CA, LCA, relative CV percentage values and AT maps for *in vitro* EHTs with different pore shapes and sizes. 112
3.8 AT and RTG maps for the most elongated hexagonal pore shape with a pore size of 0.4 mm^2 (C3G1 group of simulations). 113
3.9 Maximum AT, relative EHT CV and mean EHT RTG for the C3G1 group of simulations. 115

3.10 Maximum AT, relative EHT CV and mean EHT RTG for the C3G2 group of simulations. 116
3.11 Maximum AT, relative EHT CV and mean EHT RTG for the C3G3 group of simulations. 116
3.12 APD_{90} in the coupled EHT-myocardium is shown for variations in the EHT conductivity when EHT cells were aligned parallel to the epicardial CMs (C3G3 group of simulations). 117

4.1 Segmentation pipeline applied independently to each CMR dataset. 129
4.2 CMR datasets and their preprocessing. 129
4.3 UNet/G and D graphical architectures. 133
4.4 Losses of the UNet and GAN during training, together with GAN-generated images. 135
4.5 Betti numbers obtained from the preprocessed *ex vivo* GTLs with V- and T-constructions. 136
4.6 Betti numbers for the preprocessed cine and LGE CMR datasets. 136
4.7 Segmentation results for the *ex vivo* dataset. 139
4.8 Lifetime plots and near RV-apex logits for the baseline and TC when applied to the segmentation of an *ex vivo* CMR. 140
4.9 Segmentation results for the cine dataset. 141
4.10 Segmentation results for the LGE dataset. 142
4.11 Computed BE for all topological classes in the cine and LGE datasets. 144
4.12 G and D architectures used for SA in the MYOSAIQ challenge. 148
4.13 Instance-level uncertainty estimation results. 149

5.1 Graphical summary of experimental data acquisition. 157
5.2 HERP of pig 6 and its EAM-based activation. 164
5.3 *In silico* BiV healthy and MI modeling. 166
5.4 Healthy and MI CS distributions for models of pig 3 and 6, respectively. 168
5.5 Results of C5G1 simulations. 176
5.6 Results of C5G2 simulations. 177
5.7 Results of C5G3 simulations. 178
5.8 Results of C5G4 simulations. 179

5.9 Results of C5G5 simulations. 181
5.10 Results of C5G6 simulations. 182
5.11 Results of C5G7 simulations. 183

6.1 Summary of the arrhythmic evaluation performed before and after EHT implantation. 197
6.2 Porcine-specific BiV models of MI depicting the manually selected pacing sites used in each pig for application of the AIP. . 198
6.3 BiV-EHT modeling 199
6.4 BiV-EHT model with different coupling degrees and hiPSC-CM orientations. 204
6.5 AT, APD_{90} and RTG values obtained from a BiV-EHT model when the hiPSC-CM orientation, and EHT conductivity and attachment were varied. 205
6.6 Reentrant activity in LAD pigs. 208
6.7 VT inducibility results as a function of MI location and S2 values. 209
6.8 Changes in proarrhythmicity associated with CS. 210
6.9 Diastolic potential difference between the CS and BiV domains. 211
6.10 IS computed for the least and most inducible pigs of each MI type with and without CS. 212
6.11 Effect of EHT engraftment location on arrhythmogenesis. 213
6.12 Effect of EHT electrical maturation on arrhythmogenesis. 215

7.1 *Cocoro* implementation. 229
7.2 Electrophysiological comparison between *Cocoro* and *openCARP* and experimental and simulated QRS complexes. 233

LIST OF TABLES

3.1 CA and conductivity values used when simulating *in vitro* EHTs or when EHTs were coupled to a slab of MI. 103

3.2 Pore shape, CA and LDC values for different experimentally-based *in silico* EHT models to reproduce *in vitro* AT values. . . . 110

4.1 Preprocessed cine topological priors. 137

4.2 Preprocessed LGE topological priors. 137

4.3 Results of geometrical scores for the MYOSAIQ challenge. 152

4.4 Results of clinical scores for the MYOSAIQ challenge. 152

5.1 Summary of collected and processed experimental data. 158

5.2 Characteristics of DW-CMR data. 160

5.3 Repolarization heterogeneities definition. 171

5.4 Simulation groups (C5GX) and associated configurations. 172

5.5 Results of C5G1 simulations: CS-myocardium coupling. 175

5.6 Results of C5G5 simulations: OM-based CV and APD_{90} tuning for the BZ of MI. 180

A.1 Results of the AIP obtained in the C6G3 simulations. 250

A.2 Results of the AIP obtained in the C6G4 simulations. 251

A.3 Results of the AIP obtained in the C6G5 simulations. 252

A.4 Results of the AIP obtained in the C6G6 simulations. 253
A.5 Results of the characterization of the MI substrate. 253